Colloidal particle-hydrogel interfacial interactions

Amir Sheikhi

Doctor of Philosophy

Department of Chemical Engineering

McGill University

Montreal, Quebec, Canada

2014

A thesis submitted to McGill University in partial fulfillment for the requirements of the degree of Doctor of Philosophy

Abstract

Colloidal adhesion to soft, aqueous interfaces or inside bulk soft materials has drawn much attention recently. Micro and nanoparticle-based drug delivery to soft tissues demands decent knowledge about the colloidal dynamics on soft, sticky tissues. In biomedical engineering, understanding the interfacial deformation and flow properties of soft scaffolds interacting with micron and nano sized cells and drug carriers is of great importance without which proper cell-specific substrates cannot be designed. Moreover, perceiving the mechanism of receptor-ligand type interaction at soft interfaces, biofouling, and cell attachment in microfluidic devices demands characterizing the soft adhesion at a single microparticle scale. In this thesis, silica microspheres are used as sensors reflecting the interaction between the soft materials, including lipid bilayers (mimicking cell surface), grafted polymers (mimicking polymer-coated drug carriers), and hydrogels (mimicking extracellular matrices and soft tissues), through their self-diffusion on a coated flat substrate. The results showed that colloidal particles underwent Brownian or non-Brownian (anomalous) motion. The anomalous interfacial dynamics were observed when entanglement, such as the grafted-polymer interaction with hydrogels, was possible. The dynamics of an optically trapped silica microsphere with various coatings in a polyacrylamide (PA) hydrogel vicinity were resolved in nanometer scale using back-focal-plane interferometry position detection, combined with optical tweezers, from which micro-scale rheological behavior of the interface was ascertained. Various microspherical probes on PA substrates with a controlled stiffness have been used in the absence of external forces (passive microrheology) or under an external oscillatory shear (active microrheology). Passive interfacial microrheology results were interpreted using two approaches, namely a diffusion coefficient-binding stiffness method, developed in this work, and the well-known viscoelasticity formalism of Mason & Weitz (1995). The former fur-

nished substrate elasticity-correlated binding stiffness, and the later suggested that despite significant interfacial attachment, bare and lipopolymer (DSPE-PEG2k)-doped lipid bilayer (DOPC)-coated silica microspheres (termed as DSPE-coated particles) experience almost a thousand times lower elastic stress compared to bulk inclusions. The softer the PA substrate, the lower adhesion stiffness (*i.e.*, an higher long-time Brownian position variance). Interestingly, coating microspheres with phospholipid fluid membranes (DOPC) eliminated the interfacial attachment to PA substrates, despite attractive electrostatic forces, independent of the gel elasticity, providing a non-adhesive probe to characterize fluid properties in the gel contact proximity. Active microrheology with bare, DOPC-coated, and DSPE-coated silica microspheres on PA gels furnished interfacial viscoelastic properties versus PA elasticity, external shear rate, and optical restoring force exerted on the trapped particles, which suggested a substrate stiffness-dependent decrease in the binding stiffness when increasing the exerted force on the particle. The interfacial adhesion phase diagrams were constructed within the Cole-Cole (Nyquist analysis) formalism. The results may help to design biocompatible wet glues for advanced biomedical applications, such as non-intrusive in vivo stitching.

Abrégé

L'adhérence colloïdale aux interfaces molles et aqueuses ou à l'interieur de matériaux mous en vrac, a attiré beaucoup d'attention récemment. La livraison de médicaments basés sur des micro- et nanoparticles aux tissus mous exige une bonne connaissance de la dynamique colloïdale sur les tissus mous et collants. En ingénierie biomédical, il est grandement important de comprendre la déformation aux interfaces et les proprietés de flux de structure molles qui interagissent avec des cellules et des transporteurs de principe actif. En outre, l'investigation du mécanisme d'interaction de type récepteur-ligand aux interfaces moux, le biofouling, et l'attachement de cellules dans des dispositifs microfluidique exigent la caractérisation de l'adhérence douce à l'échelle d'une seule microparticule. Dans cette thèse, des microsphères de silice sont utilisées comme capteurs, reflétant l'interaction entre les matériaux mous, y compris les bicouches lipidiques (imitant la surface cellulaire), les polymères greffés (imitant les transporteurs de médicament revêtu de polymère), et les hydrogels (imitant les matrices extracellulaires et les tissus mous), à travers leur auto-diffusion sur un substrat plat. Les résultats ont démontré que les particules colloïdales subissent un mouvement Brownien ou non-Brownien (anormal). Les dynamiques d'interface anormales ont été observées lorsque de l'enchevêtrement, tels que l'interaction entre des polymères greffés et des hydrogels, était possible. Les dynamiques d'une microsphère de silice optiquement piégé à proximité de divers revêtements dans un hydrogel de polyacrylamide (PA) ont été résolues dans l'échelle nanométrique en utilisant l'interférométrie de plan-focale-arriére pour la détection de la position, combinée avec des pinces optiques, à partir de laquelle le comportement rhéologique de l'interface à micro-échelle a été constaté. Diverses sondes microsphérique sur des substrats de PA avec une rigidité contrôlée ont été utilisées en absence de forces extérieures (microrhéologie passive) ou sous un cisaillement oscillant ex-

terne (microrhéologie actif). Les résultats de la microrhéologie interfaciale passif ont été interprétés en utilisant deux approches, d'une part une méthode de coefficient de diffusion-rigidité d'adhérence, développée dans ce travail, et d'autre part le formalisme bien connu de visco-élasticité de Mason & Weitz (1995). La premiére a fournit les données de l'élasticité du substrat corrélé à la rigidité de liaison, et le second a suggéré que malgré l'attachement interfaciale important, les microsphères de silice enrobées de bicouches lipidique (DOPC) nues et dopées avec un lipopolymère (DSPE-PEG2k), défini en tant que particules enrobées de DSPE, éprouvent un stress élastique presque mille fois plus faible par rapport aux inclusions en vrac. Plus le substrat de PA est mou, plus la rigidité d'adhérence est faible (*i.e.*, une plus grande variance de position Brownienne longue-durée). Fait intéréssant, les microsphères enrobées des membranes fluides de phospholipides (DOPC) ont éliminé l'attachement interfaciale des substrats de PA, et ce malgré les forces électostatiques attractives, indépendantes de l'élasticité du gel, fournissant une sonde non-adhésive pour caractériser les propriétés fluidiques à proximité du contact avec le gel. La microrhéologie actif avec des microsphères de silice nues, enrobées de DOPC, et enrobées de DSPE sur des gels de PA a fournis des propriétés d'interface visco-élastiques versus élasticité de PA, le taux de cisaillement externe et la force de restauration optique exercée sur les particules emprisonnées, ce qui suggère que la rigidité de liaison diminue quand la force exercée sur la particule augmente, le tout dépendant de la rigidité du substrat. Les diagrammes de phase d'adhérence interfaciale ont été élaborés dans le formalisme de Cole-Cole (analyse de Nyquist). Les résultats peuvent aider à concevoir des colles humides biocompatibles pour des applications biomédicales avancées, telles que la couture in vivo non-intrusif.

Acknowledgments

This is a valuable opportunity for me to express my sincere gratitude to Prof. Reghan J. Hill, without whom this work would not be fulfilled. R.J.H.'s scientific support has always been a path-finding torchlight throughout my Ph.D. studies in Chemical Engineering Department, McGill University since September 2010. I am also extremely lucky to be in touch with Dr. J. van Heiningen, an highly knowledgeable yet super humble physicist, who has always been available for my annoying questions about optical tweezers. I gratefully appreciate support from the Centre for Self Assembled Chemical Structures (CSACS), McGill U.; McGill Engineering Doctoral Award (MEDA) through the Lorne Trottier Engineering Graduate Fellowship, Graduate Excellence Award, and Graduate Excellence Fellowship, as well as McGill International Doctoral Awards (MIDAs) to live and study in beautiful Montreal; the Natural Sciences and Engineering Research Council of Canada (NSERC); and the Canada Research Chairs (CRC) program for additional financial support. I cordially acknowledge the helpful discussions with Prof. E. Eiser and T. Yanagishima, Cambridge U., Prof. K. Berg-Sørensen, Technical U. of Denmark, and Prof. S. Jeney and M. Grimm, Ecole Polytechnique Federale de Lausanne (EPFL). Instrumental support by Prof. N. Tufenkji and Prof. T.M. Quinn, Chem. Eng. Dep., McGill U. are much appreciated. Also, special thanks to McGill Chem. Eng. technical staff for their help with my electronic and mechanical designs. I would especially like to thank my family, for their infinite emotional support and sacrifice during the past four years while I was away from home. I will never forget my childhood inspiration about chemistry and physics initiated by my talented uncles, Dr. Alireza Omumi and Shahryar Omumi, without which I am not sure if I was here today. Finally, I would like to dedicate this thesis to my mother, Maryam Omumi, who is the divine of sacrifice and dedication ever.

Contents

List of Figures

List of Tables

Chapter 1

Outline

This thesis is in 8 chapters:

Chapter 1: The overall picture of thesis is depicted here by concisely explaining the content of each chapter.

Chapter 2: The motivation and hypotheses to conduct the current study on various aspects of interfacial soft adhesion are discussed.

Chapter 3: The most relevant literature to various aspects of this thesis is reviewed. Colloidal particles are introduced, and their behavior in dispersions is explained. The chapter continues by introducing hydrogels, one of the most abundantly-used materials for biomedical applications and soft tissue mimics, followed by the interfacial and bulk colloidal particle inclusions with such matter, and the essentials of adhesion theories. Afterwards, the basics of optical tweezers-assisted particle trapping, the main experimental tool in this work, is introduced, and passive and active microrheology are explained.

Chapter 4: The experimental study in the thesis starts with the self-diffusion of silica microspheres on soft interfaces. The inetraction between the soft coating (lipid bilayers or lipopolymer-doped lipid bilayers) on the particle and the coated underlying flat substrate influence the particle diffusion from which the interfacial soft interactions can be characterized.

Chapter 5: A more sophisticated method, passive interfacial microrheology, employing a bare silica microsphere probe at polyacrylamide (PA)-electrolyte interfaces with a controlled PA elasticity is introduced. This chapter explains how the experimental and theoretical methodology is developed to characterize various aspects of these interfacial inclusions, such as short-time diffusion coefficient, binding stiffness, viscoelastic parameters, and adhesion energy.

Chapter 6: Understanding the behavior of a single bare silica microsphere at a PA gel-electrolyte interface while the particle is subjected to an external oscillatory shear is aimed in this chapter. The effort is to elucidate how interfacial inclusion viscoelastic properties are affected by the substrate stiffness, optical trap restoring force, and external shear rate.

Chapter 7: Passive and active microrheology are employed to characterize the interfacial behavior of a coated silica microsphere with phospholipid bilayers (DOPC) or lipopolymer (DSPE-PEG-2k)-doped phospholipid bilayers (DOPC) at gel interfaces to shed light on the interfacial adhesion dynamics of such widely-used colloidal carriers in the contact proximity of a PA gel film. The effect of van der Waals (vdW) forces on such adhesion is highlighted in this chapter by isolating the electrostatic attraction force using the specific particle coatings.

Chapter 8: The main conclusions of the thesis, and how it contributes to knowledge are summarized in this chapter.

Chapter 2

Motivation and objectives

Micro- and nanoparticle adhesion to soft, sticky materials has been always a key interest in many engineering, biomedical, and biological sciences. Despite tremendous effort to characterize particle adhesion to soft substrates in a dry state, little is known about how colloidal particle dynamics are affected by the underlying soft substrate in aqueous media, where the particle and substrate are subjected to thermal fluctuations and draining, respectively. The only available experimental investigation is the very recent attempt of Rose *et al.* (2014) in using silica nanoparticles to attach two pieces of hydrogels. This is a remarkable application, given that the hydrogels (and tissues) are known to be very slippery and non-sticky against each other (Gong, 2006). However, this macro-scale study does not shed light on the mechanism and dynamics of particle adhesion to such interfaces. Thus, single particle studies are necessary to understand microscale local adhesive behavior of soft, wet substrates. Silica microspheres with well-understood dynamics in simple media, such as an electrolyte, are used as sensors to probe the interactions between the soft materials, including lipid bilayers, lipopolymer-doped lipid bilayers, and hydrogels. The interfacial interactions between the coated soft materials on the silica particles and a substrate are reflected in the self-diffusion of the microspheres. The current study seeks to characterize colloidal silica (a widely-used drug carrier) behavior at a polyacrylamide (PA)-electrolyte interface in the absence or pres-

ence of external forces. The effect of substrate stiffness and particle coating on the interfacial adhesion is also investigated in terms of the Brownian diffusion coefficient, binding stiffness, and viscoelastic properties. In this thesis, attempts are made to understand:

1. How a bare silica microsphere interacts with a bilayer or hydrogel-coated flat substrate, and how the dynamics of the particle is affected when it is coated with bilayers or polymers.

2. How bare silica microsphere short-time diffusion coefficient and long-time position variance (and binding stiffness) are affected by an underlying PA gel film in an electrolyte.

3. The interfacial micro-viscoelastic characteristics of bare silica particle-PA hydrogel inclusions.

4. How wet substrate stiffness modifies the interfacial colloidal dynamics.

5. How microsphere coating affects the adhesion at PA-electrolyte interfaces.

6. If the microsphere-PA interfacial inclusion viscoelasticity can be tuned by subjecting the particle to external oscillatory shear and restoring force.

Chapter 3

Literature review

In this chapter, colloidal particles, their stability in terms of DLVO and non-DLVO interactions, and diffusion are introduced. Hydrogels and their inclusions with colloidal particles are explained, and adhesion theories are briefly reviewed. Finally, the essentials of optical tweezers and particle trapping are detailed, and passive and active microrheology are highlighted.

3.1 Colloidal particles

Almost 170 years ago, in the 1840s, colloidal science originated from the pioneering studies of Francesco Selmi, an Italian toxicologist, working on silver iodide and chloride and sulfur pseudo-solutions in water (Ede, 2007; Cosgrove, 2010). Michael Faraday was the next scientist in this newly-born field, who produced dispersions of gold particles in electrolytes (Faraday, 1857). Thomas Graham, a Scottish chemist, who is best recognized today for his gas diffusion law (*Graham's law* of effusion) and the development of dialysis, was the first to suggest the term *colloid*, meaning glue-like in Greek (Cosgrove, 2010). He defined a colloid according to its incapability of passing through a membrane.

The colloidal size spectrum spans a few nanometers to tens of micrometers. Molecular properties, and kinematic and wetting phenomena describe the behavior of the former

and latter systems, respectively (Cosgrove, 2010). A colloidal system includes at least two phases, namely a dispersed phase in a bulk phase. Examples of dispersed phase-bulk phase combinations are solid aerosol (*e.g.*, smoke): solid-gas, sol (*e.g.*, ink): solid-liquid, solid sol (*e.g.*, stained glass): solid-solid, liquid aerosol (*e.g.*, mist): liquid-gas, liquid emulsion (*e.g.*, mayonnaise): liquid-liquid, solid emulsion (*e.g.*, butter): liquid-solid, foam: gas-liquid, and solid foam: gas-solid (Cosgrove, 2010).

Among everyday applications of colloidal systems (Cosgrove, 2010) are surface coatings (*e.g.*, paints, photographic films, and video tapes), cosmetics (*e.g.*, toothpaste, creams, and shampoo), food (*e.g.*, chocolate ice cream and butter), industrial processes (*e.g.*, water clarification, mineral floatation and flocculation, drilling), and pharmaceutics (*e.g.*, aerosol sprays and drug delivery systems).

One of the main motivations of the current thesis is to understand the adhesive behavior of colloidal silica on soft materials; therefore, an important aspect of colloidal dispersions, *i.e.*, stability, is introduced here. The key requirement of a non-aggregating colloidal system is stability. *Colloidal stability* refers to a physically dispersed (non-adhesive) state of a system (Cosgrove, 2010); therefore, an aggregating (adhesive) state is termed as unstable. Colloidal stability is affected by the attractive and repulsive forces among the dispersed phase ingredients. Van der Waals (vdW) interactions and electrostatic (ES) forces are the most well-known contributors to the colloidal stability. In a colloidal dispersion, the adhesion of two particles or a particle to a substrate has been explained by the classical Derjaguin-Landau-Verwey-Overbeek (DLVO) theory (Derjaguin & Landau, 1941; Verwey, 1947; Verwey & Overbeek, 1948).

Within the DLVO theory, the net interaction between two colloidal particles in an electrolyte is the superposition of (usually) attractive van der Waals forces and the repulsive electrostatic interactions of similarly charged objects. The vdW forces originate from the London or dispersion interactions via which non-polar molecules form instantaneous dipoles due to the electron cloud displacement, resulting in correlated temporary dipoles. The time

scale of such a process is comparable to the electron transition (Goodwin, 2004), *i.e.*, visible or ultraviolet (UV) in the electromagnetic spectrum. The so called dispersion interaction energy U_{vdW} between two molecules at separation r (Goodwin, 2004)

$$U_{\mathrm{vdW}}(r) = -\frac{C}{r^6}, \tag{3.1}$$

where C denotes the London constant, which, for a di-molecular interaction, depends on the ionization energy $h\nu$ and the polarizability α

$$C \propto h\alpha_1\alpha_2 \left(\frac{\nu_{11}\nu_{12}}{\nu_{11}+\nu_{12}}\right), \tag{3.2}$$

with Planck constant $h \approx 6.63 \times 10^{-34}$ m^2 kg s^{-1}. To extend this model to multi-atomic systems, such as a colloid, the summation of interactions between all the constituting molecules has to be considered by taking the molecular number density ρ_n and integrating over the interacting volumes, which, in general, leads to

$$U_{\mathrm{vdW}} = C\rho_n^2 f(\mathrm{Geometry}), \tag{3.3}$$

suggesting the vdW force as the multiplication of the material properties function by the geometry function (Hamaker, 1937). As examples, the vdW energy per unit area of a half-space interacting with a different half-space at separation h in a vacuum (Adamczyk, 2006)

$$U_{\mathrm{vdW}} = -C\rho_{n1}\rho_{n2}\frac{\pi}{12h^2}, \tag{3.4}$$

and that of a spherical colloid (radius R) interacting with a half-space

$$U_{\mathrm{vdW}} = -\pi^2 C\rho_{n1}\rho_{n2}\left[\frac{2R(h+R)}{h(h+2R)} + \ln\frac{h}{h+2R}\right] \approx -\pi^2 C\rho_{n1}\rho_{n2}\frac{R}{6h},\ h \ll R. \tag{3.5}$$

It is convenient to write the material properties function as a single constant, known as the

Hamaker constant A. For two interacting bodies in a vacuum,

$$A_{12} = \pi^2 C \rho_{n1} \rho_{n2}. \tag{3.6}$$

When two bodies are interacting through a third medium,

$$A_{132} = A_{12} + A_{33} - A_{13} - A_{23} \approx \left(A_{11}^{0.5} - A_{33}^{0.5}\right)\left(A_{22}^{0.5} - A_{33}^{0.5}\right), \tag{3.7}$$

taking $A_{ij}^2 = A_{ii} A_{jj}$ (van Oss, 2006).

Generally, the vdW interactions attract two bodies (except for certain combinations of materials with $A_{11} > A_{33} > A_{22}$ or $A_{11} < A_{33} < A_{22}$, resulting in a negative Hamaker constant), while the electrostatic interactions prevent similarly-charged bodies adhering. The surface charge, controlling the electrostatic interactions between two objects, results from the ionization of moieties, such as silanol groups, leading, for example, to bare silica particle negative surface charge at high enough pH (Behrens & Grier, 2001). Other important charge regulation mechanisms (Cosgrove, 2010) are the surface adsorption of charged layers, *e.g.*, polyacrylic acid, proteins and surfactants, and isomorphous substitution (Chu & Chang, 1985) of a similar ionic radius element with another element in a mineral (*e.g.*, zeolites), maintaining the crystal structure.

A charged non-porous object, immersed in an electrolyte, attracts oppositely-charged free ions toward its surface, permitting the formation of a double layer (Verwey & Overbeek, 1946; Grahame, 1947) comprising a vanishingly thin adsorbed interfacial ion layer, known as the Stern layer (Stern, 1924), and a diffuse counter ion layer (Gouy, 1910; Chapman, 1913). The Stern layer thickness is affected by the ion type (*e.g.*, monovalent or multivalent) and polarizability, giving rise to potential decrease from surface potential ψ_0 at the solid surface to the Stern potential ψ_{st} at a distance comparable to the ion diameter (Goodwin, 2004). In the Stern layer, the electrostatic attraction between ions and the surface strongly dominates ion diffusion, permitting ion adsorption; however, the decreased electrostatic attraction be-

tween the surface and counter ions at further distances gives rise to a layer in which ion diffusion competes with electrostatic attraction. This layer is called the diffuse (Debye) layer, separated from the Stern layer by a slipping (shear) plane, attaining a potential called the zeta-potential ζ.

The ion number density n, defined as the number of ions in unit volume of the diffuse layer, follows a Boltzmann distribution (Goodwin, 2004)

$$n_i = n_{i,0} e^{\left(\frac{-z_i e \psi}{k_B T}\right)}, \tag{3.8}$$

which can be converted to the charge number density profile

$$\rho_i = n_i z_i e, \tag{3.9}$$

where z and e are the ion valence and elementary charge, respectively, and $k_B T$ denotes the thermal energy.

The electrical potential profile in the diffuse layer is explained by the well-known Poisson equation

$$\nabla^2 \psi = \frac{-\rho}{\epsilon_0 \epsilon_r} = \frac{-\Sigma \rho_i}{\epsilon_0 \epsilon_r}, \tag{3.10}$$

which results in the Poisson-Boltzmann equation when combined with the Boltzmann ion distribution:

$$\nabla^2 \psi = \frac{2 n_0 z e}{\epsilon_0 \epsilon_r} \sinh\left(\frac{z e \psi}{k_B T}\right), \tag{3.11}$$

where ϵ_0 and ϵ_r are the vacuum permittivity and relative permittivity, respectively.

Considering various interacting geometries and operating conditions, this equation furnishes potential distribution between two objects in an electrolyte when proper boundary conditions are applied. As an example, for a flat plate in an $1-1$ electrolyte ($|z| = 1$) at small potentials $\psi < k_B T/e \approx 25$ mV, known as the Debye-Hückel approximation, the

Poisson-Boltzmann equation reduces to a homogeneous, linear ODE, furnishing

$$\psi(x) \approx \psi_{st} e^{-\kappa x}, \tag{3.12}$$

with reciprocal Debye length

$$\kappa = \left(\frac{n_0 e \Sigma z_i^2}{\epsilon \epsilon_0 k_B T} \right)^{\frac{1}{2}}. \tag{3.13}$$

This length for a symmetric electrolyte with ionic strength I(M) at $T = 25°$C, reduces to (Doane *et al.*, 2012)

$$\kappa(\mathrm{nm}^{-1}) \approx 3.3\sqrt{I}. \tag{3.14}$$

As evidenced by Eqns. 3.12 and 3.14, increasing the ionic strength increases κ, which decreases the electrostatic potential. The electrostatic repulsive force per unit area f_{ES} is directly related to the osmotic pressure (Ohshima *et al.*, 1987), originated from the ion gradient between the charged objects and the bulk electrolyte. As an example, for two parallel plates with small potentials located at separation h

$$U_{ES} = 2\kappa \epsilon_r \epsilon_0 \psi_{st}^2 e^{-\kappa h}, \tag{3.15}$$

where $\psi_{st} \approx \zeta$, taking a vanishingly thin shear plane (Cosgrove, 2010).

The electrostatic interactions in complex systems has been studied theoretically by several researchers. For a spherical particle (p) parallel to a rigid flat plate (s) (Hogg *et al.*, 1966)

$$U_{ES} = \pi \epsilon \epsilon_0 R \left[2\psi_p \psi_s \ln \left(\frac{1 + e^{-\kappa h}}{1 - e^{-\kappa h}} \right) + (\psi_p^2 + \psi_s^2) \ln \left(1 - e^{-2\kappa h} \right) \right]. \tag{3.16}$$

The total DLVO interaction energy $U = U_{vdW} + U_{ES}$ controls colloidal stability. Given that the vdW energy is usually negative (attractive), depending on the similarly-charged colloid separation and electrolyte ionic strength, the total energy can be negative or positive. This can result in two energy minima, namely a secondary minimum (reversible adhesion)

or primary minimum (irreversible adhesion). A primary maximum is located between the potential minima (Verwey, 1947). Note that when colloids are oppositely charged, the secondary minimum and primary maximum vanish due to the attractive electrostatic potential.

The extended DLVO (XDLVO) approach takes other types of interactions, such as the Lewis acid-base (AB, arising from hydrogen bonding) into account. The electron donor-electron acceptor mechanism introduces the AB interaction between (polar) moieties in an aqueous solvent, which can be attractive or repulsive (Nguyen *et al.*, 2011). This depends on the hydrophobic or hydrophilic characteristics of the particle (p) and plate (s) (Hoek & Agarwal, 2006)

$$U_{AB} = 2\pi R\lambda\Delta G_{h_0} e^{\frac{h_0-h}{\lambda}}, \tag{3.17}$$

where the acid-base hydrophilic (hydrophobic) interaction decay length $\lambda \approx 0.6$ nm (13 nm) in water (w), the minimum separation distance due to Born repulsion $h_0 \approx 0.158$ nm (van Oss *et al.*, 1988*a*), and the acid-base free energy per unit area

$$\begin{aligned}\Delta G_{h_0} = {} & 2\sqrt{\gamma_w^+}\left(\sqrt{\gamma_s^-}+\sqrt{\gamma_p^-}-\sqrt{\gamma_w^-}\right)+2\sqrt{\gamma_w^-}\left(\sqrt{\gamma_s^+}+\sqrt{\gamma_p^+}-\sqrt{\gamma_w^+}\right) \\ & -2\left(\sqrt{\gamma_s^+\gamma_p^-}-\sqrt{\gamma_s^-\gamma_p^+}\right)\end{aligned} \tag{3.18}$$

with γ denoting the surface tension (mJ m^{-2}), and + (−) indicating the electron acceptor (donor). The electron acceptor (donor) parameter of Lewis acid-base γ^+ (γ^-) can be obtained from contact angle experiments with three different liquids using Young's equation, as suggested by van Oss *et al.* (1988*b*). As an example, for water (silica) at 20°C, $\gamma^+ \approx 25.5$ (1.04) and $\gamma^- \approx 25.5$ (31.72) mJ m^{-2} (Brant & Childress, 2002). Interestingly, Brant & Childress (2004) reported a 5-fold stronger adhesion force between $2R \approx 5$ μm bare silica spheres and hydrophilic membranes than the same size hydrophobic polystyrene microspheres due to the hydrogen bonding of surface γ^+ and γ^- groups. Various aspects of colloid soft adhesion are detailed in section 3.3.

Colloidal particles in a dispersion are subject to thermal forces, arising from solvent molecule collisions. The first observations of Robert Brown in the 1820s (Hida, 1980), who

reported irregular movement of particles, observed by a simple 1 mm focal length microscope, pioneered the field of Brownian motion; however, theoretical understanding of such phenomenon was achieved for the first time by Einstein (1905), relating the diffusion coefficient to the thermal energy k_BT, particle radius R, and medium viscosity η_s:

$$D_x = \frac{k_BT}{6\pi\eta_s R}. \tag{3.19}$$

It can be shown that the particle d-dimensional ($1 \leq d \leq 3$) mean-squared displacement (MSD) in an unbound fluid in the absence of any external force after an elapsed time t is proportional to the time lag τ (Einstein, 1905):

$$\left\langle [X(t+\tau) - X(t)]^2 \right\rangle = 2dD_x\tau \tag{3.20}$$

with mean position displacement $\langle X(t+\tau) - X(t) \rangle = 0$. Various aspects of Brownian motion are detailed by Hida (1980) and Pecseli (2000).

Equations 3.19 and 3.20 immediately suggest that the viscosity of an unknown medium can be acquired by tracking the position of a single particle's centre (known as single or multiple particle tracking: SPT or MPT) and calculating the mean of displacement squares; however, in real systems, diffusion may diverge from the 'normal' behavior due to particle-medium interactions, resulting in anomalous diffusion,

$$\left\langle X^2 \right\rangle \propto \tau^n, \tag{3.21}$$

directed-by-velocity v diffusion,

$$\left\langle X^2 \right\rangle \propto dD_x\tau + (v\tau)^2, \tag{3.22}$$

or confined diffusion (Saxton & Jacobson, 1997). The state-of-the-art trends in the so-called

particle tracking techniques and their performance have been recently gathered by Chenouard *et al.* (2014) through an open worldwide competition among the most active research groups in this field.

A desire to understand the dynamics of complex environments has drawn attention to employ particle tracking to characterize cellular membranes (Saxton & Jacobson, 1997), cytoskeletal compounds (Akhmanova & Steinmetz, 2008), cell-matrix adhesion (O'Toole *et al.*, 2008), intracellular transport Caspi *et al.* (2000) and gene delivery (Suh *et al.*, 2003), and cell-virus interaction (Brandenburg & Zhuang, 2007), conducted by various light microscopy techniques (Stephens & Allan, 2003).

Confinement can attenuate the diffusion coefficient. As an example, a plane wall hydrodynamic interaction with a spherical particle at distance h attenuates the transverse $D_x = D_y$ and vertical D_z diffusion coefficients

$$\begin{pmatrix} D_x \\ D_z \end{pmatrix} = \frac{k_B T}{6\pi R} \begin{pmatrix} 1/\eta_x \\ 1/\eta_z \end{pmatrix}, \tag{3.23}$$

where Faxen (1923) approximate solution for Stokes flow past a stationary sphere near a plane wall for large gaps gives

$$\eta_x = \eta_s \left[1 - \frac{9}{16}(R/h) + \frac{1}{8}(R/h)^3 - \frac{45}{256}(R/h)^4 - \frac{1}{16}(R/h)^5 + O(R/h)^6 \right]^{-1}, \tag{3.24}$$

and for small gaps (Goldman *et al.*, 1967)

$$\eta_x = \eta_s \left[0.9588 - \frac{8}{15} \ln (h/R) \right]. \tag{3.25}$$

Note that an exact solution for normal translation is Cooley & O'Neill (1969)

$$\eta_z = \eta_s \frac{4}{3} \sinh \alpha \sum_{n=1}^{\infty} \frac{n(n+1)}{(2n-1)(2n+3)} \left[\frac{2\sinh(2n+1)\alpha + (2n+1)\sinh 2\alpha}{4\sinh^2(n+\frac{1}{2})\alpha - (2n+1)^2 \sinh^2 \alpha)} - 1 \right] \tag{3.26}$$

with $\alpha = \cosh^{-1}(h/R)$. These bring about an anisotropic diffusion due to the different hindrance in the transverse and perpendicular directions near a wall.

The hydrodynamic behavior of a spherical particle has been studied near various interfaces. Close to a soft wall (Bickel, 2007), *e.g.*, a fluid interface, separating two immiscible, viscous, and incompressible fluids, the particle frequency-dependent mobility couples hydrodynamically to the interface conformation, permitting two main regimes: at low frequencies, the interface acts as a flat wall, and at high frequencies, the particle senses the elastic response of the interface at large particle-interface gap and low oscillation amplitudes due to the memory effect, arising from the interface elastic deformation delay and fluid back-flow. A lift force is exerted on a sphere moving parallel to a rigid (Cherukat *et al.*, 1994) or a soft (Urzay *et al.*, 2007) wall. A porous wall (Brinkman half-space) provides a non-zero velocity at the interface, depending on the hydraulic permeability of the Brinkman medium, which can be used to characterize the wall properties (such as thickness) by tracking the adjacent particles velocity (Damiano *et al.*, 2004). All these fascinating phenomena motivate the use of a colloidal particle as a probe to characterize its surrounding medium.

3.2 Hydrogels

Hydrogels are hydrophilic polymeric networks (Peppas *et al.*, 2000) that can absorb water up to several orders of magnitude more than their polymer mass. They swell [*e.g.*, Kabiri *et al.* (2003)], mimicking biological soft tissues. Among the most important characteristics of hydrogels are their tunable stiffness, structural flexibility, biocompatibility, porous, stimuli-responsive, and transparency, which turned these soft materials into great candidates as substrates and scaffolds for cells and tissues (Lee & Mooney, 2001; Drury & Mooney, 2003; Levental *et al.*, 2007; Macaya & Spector, 2012), microorgans-on-chip (Verhulsel *et al.*, 2014), sensors and actuators (van der Linden *et al.*, 2003; Richter *et al.*, 2008), microfluidics and micro-flow controllers (Beebe *et al.*, 2000; Eddington & Beebe, 2004; Moorthy, 2012),

biomolecular separation (Simhadri *et al.*, 2010), drug delivery systems (Hoare & Kohane, 2008), and contact lenses (Nicolson & Vogt, 2001; Xinming *et al.*, 2008). Comprehensive reviews on novel hydrogel preparation methods are published by Hennink & van Nostrum (2012) and Peak *et al.* (2013).

Combining colloidal particles with soft hydrogels has attracted much attention recently for gel-property modification (Yang *et al.*, 2013*a*) and characterization (Bhosale *et al.*, 2011), particle arraying (Suzuki *et al.*, 2007), to induce colloid-colloid attraction (Di Michele *et al.*, 2011), mimic drug delivery to soft tissues (Lieleg *et al.*, 2010) and bioadhesion (Takeuchi *et al.*, 2001), and to perform wet soft adhesion (Rose *et al.*, 2014).

Silica nanoparticles, providing a high surface area, have shown a promising capability to adsorb polymer chains on their surface, *e.g.*, due to the hydrogen bond formation between silanol groups on silica (Zhuravlev, 2000) and amide groups on polyacrylamide, and to direct the morphology and structure evolution of hydrogels by increasing the energy dissipation rate and particle-gel interfacial rearrangement (Yang *et al.*, 2013*b*, 2014). Recently, Rose *et al.* (2014) have shown that silica nanoparticles readily adhere to polydimethylacrylamide (PDMA) hydrogels, acting as a wet glue within a few seconds. The adhesion energy $\approx$ 6.4 J m^{-2}, which is increased when increasing the particle size. Also, the adhesion energy is reduced by further swelling the gels after synthesis. Note that the adhesion energy is calculated from bulk lap-shear tests, where the disruption force F is related to the adhesion energy

$$W = \frac{3F^2}{2Ehw^2} \tag{3.27}$$

with sample width w and thickness h, and tensile modulus E.

The interaction between silica microspheres has been reported to increase while placed on a very soft polymer template, *e.g.*, polyacrylamide (PA) hydrogels (Di Michele *et al.*, 2011). Depending on the PA substrate stiffness, for a gel with shear modulus $\mu_g \approx 240$ Pa, $R \approx 1$ μm silica particles did not form considerable aggregates, while $\mu_g \approx 12$ Pa resulted in large particle clusters. This is attributed to a possible depletion-mediated particle-particle

interaction and polymer bridging between microspheres. A theoretical explanation for the polymer bridging phenomenon, proposed by Di Michele *et al.* (2012), suggests that the main reason for such an attraction is the increased polymer density between the embedded particles due to the colloid-monomer vdW attraction, instead of the depletion (entropic) effects.

Despite the wide application horizon of such systems, there has been no effort to understand how the dynamics of a single silica particle is affected by the underlying viscoelastic substrate. The interfacial coupling between a bare silica microsphere and PA hydrogels is the focus of chapters 5 and 6. Moreover, the effect of external force stimuli and coatings on the colloidal particle-hydrogel interfacial interaction will be studied in chapters 6 and 7.

3.3 Soft adhesion

Besides the so-called conventional DLVO interactions, which are based on continuum theories, working well for separation gaps greater than a few nanometer, several phenomena can affect the colloidal adhesion to a substrate in nanometer proximity, such as hydration and solvation (repulsion due to the formation of molecular liquid layers between bodies, *e.g.*, between zwitterionic bilayers with decay length ≈ 0.25 nm), steric interactions, and hydrophobic forces (arising from capillary effects, 10-100 times stronger than vdW, with a long decay length ≈ 1 nm). These forces can be attractive, repulsive, or oscillatory (Ninham, 1999; Israelachvili, 2011).

If two objects, prone to any of the discussed forces, come into contact proximity, and the attractive forces prevail, the adhesion takes place. Soft adhesion, *e.g.*, colloid and cell adhesion to substrates, has drawn a lot of attention in various fields. Among numerous examples are the problem of biofouling on membranes due to soft extracellular polysaccharide secretion of microorganisms (Baker & Dudley, 1998), adhesion in microelectromechanical systems (MEMS) (Zhao *et al.*, 2003), gecko adhesion (Autumn *et al.*, 2000), mucoadhesion (the adhesion between a mucus-coated substrate and a targeting agent, such as a colloidal

drug carrier) (Ahuja *et al.*, 1997), and cytoadhesion (cell-specific bioadhesion, demanding engineered ligand-receptor systems) (Vasir *et al.*, 2003), such as the problem of rolling adhesion of a ligand-coated particle on a receptor-covered substrate, studied for various systems by Hammer and co-workers (*e.g.*, Brunk & Hammer (1997); Chang & Hammer (2000); Bhatia *et al.* (2003)).

To understand adhesion phenomena, the evolution of contact models are briefly reviewed here. The motivation from industrial contacting hardware, *e.g.*, train wheels on railways (Shull, 2002), where the adhesive forces are too small to deform the contact area, excited pioneering works of contact mechanics by Hertz & Reine (1882). In their model, which considers no surface interactions, such as vdW attraction, the contact area a is a result of only an external perpendicular load F (Horn *et al.*, 1987)

$$a = \left(\frac{RF}{K}\right)^{1/3}, \tag{3.28}$$

with equivalent radius R of contacting spheres 1 and 2:

$$\frac{1}{R} = \frac{1}{R_1} + \frac{1}{R_2},$$

and reciprocal effective storage modulus:

$$\frac{1}{K} = \frac{3}{4}\Sigma_{i=1}^{2}\frac{1-\nu_i^2}{E_i},$$

where E and ν are shear modulus and Poisson ratio, respectively. Thereby, the normal stress (pressure) distribution over the distance r from the contact centre is

$$P\left(\frac{r}{a}\right) = \frac{3Ka\sqrt{[1-(r/a)^2]}}{2\pi R}. \tag{3.29}$$

Two important results of the Hertz & Reine (1882) model are zero contact area in the

absence of an external force (*i.e.*, zero pull-off force), and 1.5 times greater pressure at the contact centre than the mean pressure over the contact region. This model, however, was unable to predict the adhesion experiments conducted by Johnson *et al.* (1971), in which the contact area of rubber and gelatin spheres with flat rubber and Perspex planes, respectively, was much higher, resulting in finite contact at zero external load. The surface energy contribution, arising from the interfacial molecular attraction, in the elastic contact and fracture was first introduced by Griffith (1921). Taking the effect of surface energy in the contact region, Johnson *et al.* (1971) proposed a model for elastic adhesive contact, now known as the Johnson, Kendall, and Roberts (JKR) contact model. Minimizing the contact total energy, comprising the mechanical load, elastic, and adhesion energies, the JKR contact radius is

$$a = \frac{R}{K}\left[F + 3W\pi R + \sqrt{6W\pi RF + (3W\pi R)^2}\right]^{1/3}, \tag{3.30}$$

where the adhesion energy W between two objects in a third medium can be related to their interfacial energies γ (Israelachvili, 2011)

$$W_{132} = W_{12} + W_{33} - W_{13} - W_{23} = \gamma_{13} + \gamma_{23} - \gamma_{12}, \tag{3.31}$$

which is attractive (repulsive) between 1 and 2 when $W_{132} > 0$ ($W_{132} < 0$).

Adhesive forces in the JKR model (Johnson *et al.*, 1971) bring about a finite contact radius in the absence of an external force ($F = 0$)

$$a = \left(\frac{6\pi W R^2}{K}\right)^{1/3}, \tag{3.32}$$

and the pull-off force ($a = 0$)

$$F = -\frac{3}{2}\pi W R. \tag{3.33}$$

In the JKR model, the normal stress (pressure) distribution has a singularity (*i.e.*, infinite

pressure) at the contact edge ($r = a$) (Horn *et al.*, 1987)

$$P = \frac{3Ka}{2\pi R}\left[1 - \left(\frac{r}{a}\right)^2\right]^{1/2} - \left(\frac{3KW}{2\pi a}\right)^{1/2}\left[1 - \left(\frac{r}{a}\right)^2\right]^{-1/2}. \tag{3.34}$$

This is resolved by the Derjaguin, Muller, and Toporov (DMT) model (Derjaguin *et al.*, 1975), which assumes adhesion originates only from outside contact region (mainly due to vdW interactions) with a Hertzian stress distribution inside the contact area. Note that in this model, the attractive forces outside the contact area are unable to deform it; therefore, the profile where $r > a$ is unchanged, similar to the Hertz model. The contact radius is greater than the Hertz model due to the extra load applied by the attractive interactions outside the contact area (Derjaguin *et al.*, 1975), giving

$$a = \frac{R}{K}\left(F + 2\pi WR\right) \tag{3.35}$$

with pull-off force

$$F = 2\pi WR. \tag{3.36}$$

The DMT theory reduces to the Bradley (1932) model in which the adhesive forces are unable to deform the interface ($a = 0$), *i.e.*, elastic energy is much larger than the intermolecular energy. The Bradley and JKR models have been shown to be two extremes of a unified contact mechanic model by Tabor (1977), which was improved by Maugis (1992) taking a Dugdale intermolecular energy function. The later describes the equilibrium pressure, contact area and profile as functions of a single dimensionless number λ, which reduces to the DMT (JKR) model when $\lambda = 0$ ($\lambda = \infty$). This dimensionless parameter is closely related to the well-known Tabor number μ_T:

$$\lambda = 1.16\mu_T = 1.16\left(\frac{16RW^2}{9K^2z_0^3}\right)^{1/3}, \tag{3.37}$$

where z_0 is the equilibrium interatomic separation between the contacting objects. De-

pending on the Tabor parameter, the adhesion follows the Bradley ($\mu_T \lesssim 0.05$), DMT ($0.05 < \mu_T < 0.1$), Maugis ($0.1 < \mu_T < 5$), or JKR ($\mu_T > 5$) models (Johnson & Greenwood, 1997).

The JKR theory is based on a small contact radius to which the parabolic approximation of a spherical contact profile [$z = r^2/(2R)$] applies. An extension of this model was proposed by Maugis (1995) taking the exact contact profile for a sphere ($z = R - \sqrt{R^2 - r^2}$) into account, resulting in

$$F = \frac{3aK}{2}\left(\frac{R^2 + a^2}{4a}\ln\frac{R+a}{R-a} - \frac{R}{2} - \sqrt{\frac{8\pi W a}{3K}}\right). \tag{3.38}$$

A closely relevant case is the axisymmetric punching of a soft substrate by a hard object, detailed by Boussinesq (1885) for the first time. Since then, several solutions have been proposed, *e.g.*, taking flat-ended (Love, 1929), cylindrical or conical (Love, 1939) punches, or an arbitrary profile, using the Hankel transform and solving the resulting dual integral equations using the Titchmarsh (1937) solution (Harding & Sneddon, 1945), or the elementary solution (Sneddon, 1960, 1965). For a rigid spherical punch, indenting a soft half-space, the well-known Sneddon (1965) method results in penetration depth ϵ

$$\epsilon = \frac{1}{2}a\log\frac{R+a}{R-a}, \tag{3.39}$$

with an equivalent load F to produce such an indentation depth[1]

$$F = \frac{E}{2(1-\nu^2)}\left[\left(a^2 + R^2\right)\log\frac{R+a}{R-a} - 2aR\right]. \tag{3.40}$$

Note that the force at small contact radii is linearly correlated with a^3:

$$F \propto \frac{Ea^3}{(1-\nu^2)\,R} + O\left[(a/R)^5\right],$$

[1]In the original paper [(Sneddon, 1965)], Eqn. 6.15 carries a typo when integrating Eqn. 4.1 to obtain the total load: the second term in the braces misses a factor of 2.

which shows a similar dependency between the load and contact area ($F \propto a^3$) as the Hertz or JKR contact theories (compare to Eqns. 3.28 and 3.30). The difference between the Hertz or JKR and Boussinesq problems is mainly reflected in the adhesive boundary conditions: while the former have no specific constraint on the tangential stress or displacements, the later accompanies zero tangential stress. The slope of the total adhesion force versus the penetration depth furnishes valuable information about each of the aforementioned theories. According to the Hertz model $\epsilon \approx a^2/R$; therefore, $\partial F/\partial \epsilon = 1.5K\sqrt{R\epsilon} = 1.5Ka$, JKR provides $\epsilon \approx a^2/(3R)$ when $F = 0$, thus $\partial F/\partial \epsilon = 1.5Ka$, while for the spherical punch $\partial F/\partial \epsilon = 1.5Ea/(1-\nu^2) = 9Ka/8$ when $a \ll R$. Note that at the same penetration depth, the adhesion (JKR model) increases the contact radius, and, therefore, the spring constant $\partial F/\partial \epsilon$ by a factor of $\sqrt{3}$ compared to a non-adhesive condition (Hertz model).

The adhesion of small glass particles ($4 \leq R \leq 100$ μm) to soft polyurethane substrates ($E \approx 45$ kPa) showed that, in contrast to the JKR prediction, the contact radii have a power law correlation with the particle radius $a \propto R^{3/4}$ (Rimai *et al.*, 1994), which is not predicted by Maugis (1995) or self-consistent surface energy models (Rimai *et al.*, 2001). While Maugis (1995) predicts a range of exponents for contact radius dependency on particle size (2/3–1), Rimai *et al.* (2001) showed that there is a bimodal dependency instead of a range: on polyurethane substrates ($E \approx 5$ MPa), for small particles ($R < 5$ μm), the contact radius $a \propto R^{3/4}$, while for large particles ($R > 5$ μm), the contact radius $a \propto R^{2/3}$. The adhesion work in air for such systems according to JKR theory is reported to be in the range 0.04–0.047 J m^{-2}. In another study, Rimai *et al.* (1992) calculated the adhesion energy between glass microbeads ($R \approx 12$ and 20 μm) and polyurethane substrates with stiffnesses $E \approx 3.83$ and 41.7 MPa to be ≈ 0.12 J m^{-2} using the SEM-acquired contact radii and the JKR theory. Measurements by de Jesus *et al.* (2008) showed that the required centrifugal force to detach half the seven μm silica-coated toner particles from 0.8-22 μm thick bisphenol-A polycarbonate coated nickelized polyethylene terephthalate (PET) surface was 25 nN and independent of the film thickness. This proved that vdW forces govern the adhesion, and

that no long-range electrostatic interaction between the particles and underlying substrates is present. The detachment force increased to 200 nN for the same particles when they were charged 30-55 μC g^{-1} (Rimai *et al.*, 2009).

The detachment force can be time-dependent. An increased force by time, from $\approx$ 80 nN after a few hours of deposition to 200 nN after one day has been reported by de Jesus *et al.* (2007), which is probably due to particle time-dependent rotation, as observed for seven μm silica nanoparticle-coated polyester particles detaching from a compliant ($E \approx$ 850 MPa) ceramer-coated PET support. The detachment force was reduced from $\approx$ 375 nN to $\approx$ 100 nN by increasing the substrate Young's modulus from $\approx$ 80 MPa to $\approx$ 1400 MPa, maintaining the surface energies almost constant (de Jesus *et al.*, 2006). Similar trends for elastomeric substrates with $3.8 \leq E \leq 320$ MPa have been reported (Gady *et al.*, 1998). In another study by Rimai & Quesnel (2002), the detachment force of polystyrene microparticles ($1 \leq R \leq 6$ μm) from a polyester substrate was correlated linearly with the particle radius, resulting in JKR adhesion work $\approx$ 0.01 J m^{-2}, which was mostly due to vdW interactions.

Particle engulfment into soft substrates in a dry state occurs when the particle radius is smaller than a critical radius defined as $R_c = 7\gamma/E$, where γ is the interfacial energy between the particle and substrate (Rimai & DeMejo, 1996). However, the engulfment dynamics can follow a multi-mode process with various embedding rates. As an example, eight μm glass particles were engulfed in plasticized polystyrene substrates by first contacting the substrate following the prediction of JKR model, then sinking at a relatively slow rate, which increased by increasing the contact radius up to the half-particle engulfment, and finally occluding the particle very slowly, permitting the cap to be visible after even several months. This is explained by considering the terminal velocity of the particle in a viscous medium (Rimai *et al.*, 2002). Recently, Style *et al.* (2013) have shown that in case of an high surface tension γ interface, *e.g.*, soft silicone substrate-air, adhesion cannot be explained by the JKR model if the particle size R is smaller than the elastocapillary length $L = \gamma/E$, where E is the substrate Young's modulus. Under this condition, the adhesion process is

similar to the particle adsorption at a fluid interface, obeying the generalized Young's law for liquid wetting. The adhesion model for the penetration length, taking the surface tension into account (Style *et al.*, 2013)

$$\frac{5cER^{1/2}\epsilon^{3/2}}{2(1-\nu^2)} + 2\pi\gamma\epsilon - 2\pi WR, \tag{3.41}$$

which reduces to the JKR prediction for large particles: $c = 8/\left(5\sqrt{3}\right)$, and $\epsilon = WR/\gamma$ for small R.

Rimai *et al.* (1995) calculated the engulfment interfacial energy ≈ 0.029 J m^{-2} for glass spheres ($R \approx 2$ μm) on a styrene butylacrylate substrate film (thickness 25–50 μm) containing 20 % plasticizer ($E \approx 100$ KPa) based on the JKR adhesion theory. For low plasticizer concentrations, *i.e.*, elastomer-like substrates, the theory of Maugis & Pollock (1984), which takes the plastic deformation into account, is suggested by Rimai *et al.* (1995) to be used. Aluminum spheres ranging 60–1500 nm underwent plastic deformation while being deposited on a silicon substrate in air, because the work of adhesion, originated from the van der Waals attractions, was larger than the particle hardness Wang *et al.* (2010).

So far, the static (steady state) adhesion theories and experiments have been reviewed. The soft adhesion from the fracture mechanics point of view is worth being briefly reviewed here due to its relevance to active interfacial microrheology. The term *crack* in the fracture mechanics literature refers to the contact perimeter (Shull, 2002). Experimental results with adhesive elastomers (Shull *et al.*, 1998) have shown that the energy release rate $\mathscr{G}$ (the crack propagation energy, defined as the change in stored elastic energy with contact area decrease, unit energy per contact area) follows a general empirical dependency on the crack velocity $v = -da/dt$ (Shull *et al.*, 1998)

$$\mathscr{G} = \mathscr{G}_0 \left[1 + \left(\frac{v}{v_0}\right)^n\right], \tag{3.42}$$

where $\mathscr{G}_0$ denotes the adhesion energy threshold below which no crack is observed, v_0 is a

characteristic crack velocity at which $\mathscr{G} = 2\mathscr{G}_0$, and n is an experimental exponent. Here, the substrate viscosity is neglected. Interestingly, the thermodynamic adhesion work W is the upper limit of $\mathscr{G}$ in advancing contact (where the adhesion takes place, *i.e.*, increasing a), while W sets the lower limit of $\mathscr{G}$ when the contact is receding (detachment, *i.e.*, decreasing a). For an ideal equilibrium process (either advancing or receding), $\mathscr{G} = W$; therefore, W of real systems attains a value between the acquired $\mathscr{G}$ from advancing and receding experiments. Within the fracture contact formalism, it can be shown that (Shull *et al.*, 1998)

$$\mathscr{G} = -\frac{(\epsilon' - \epsilon)^2}{4\pi a C^2}\frac{\partial C}{\partial a} \tag{3.43}$$

with compliance

$$C = \partial\epsilon/\partial F \approx \frac{\epsilon' - \epsilon}{F' - F},$$

at constant a. This reduces to the well-known JKR model ($a \ll R$):

$$\mathscr{G} = (Ka^3/R - F)^2/(6\pi K a^3), \tag{3.44}$$

taking $C = 2/(3Ka)$. Note that ϵ' and F' refer to the non-adhesive (Hertzian) indenter penetration and load, respectively. The adhesive contact of viscoelastic materials, detailed by Hui *et al.* (1998) for the advancing case, and by Lin *et al.* (1999) for the receding case, cannot be explained by a single-parameter (*i.e.*, W) model; it demands the dependency of the bond breakage and formation to the stress intensity factor. The active interfacial microrheology with (small-amplitude) oscillatory drive can be considered as a simultaneous advancing and receding case: while the bonds are being broken at one edge (receding), the attachment takes place at the other edge (advancing). Direct loading/unloading measurements are necessary to characterize this system.

Despite the importance of lateral forces in defining the behavior of an adhesive soft system, it has not received much attention. If a microsphere, placed on a sticky substrate and pinned at its contact edges due to the adhesion forces, is subjected to a lateral force

smaller than the equivalent detachment moment (rolling resistance moment), it rolls without detachment. Ding *et al.* (2008) acquired the lateral displacement of a subjected microsphere to AFM cantilever lateral forces, and related the force-displacement curve slope ($k = F/\Delta x$) to the adhesion energy

$$W = \frac{k}{6\pi}. \tag{3.45}$$

This approach does not demand the particle size, and relates the rolling resistance moment ($M \approx 6\pi W R^2 \theta$) to k:

$$k = M/(R^2\theta), \tag{3.46}$$

where θ is the rotation angle.

If the applied lateral force is eliminated before reaching the critical rolling force, the particle centre position evolution $\xi = 0.5(a_2 - a_1)$, *i.e.*, the distance between the particle mass centre and the contact centre, with time (Krijt *et al.*, 2014)

$$\ddot{\xi}(t) = \frac{RM}{I} = \frac{RM}{\frac{2}{5}mR^2} = \frac{6\pi\gamma R^2}{I}\xi(t), \tag{3.47}$$

where a_1 is the distance between the receding contact edge and the particle mass centre, and a_2 denotes the distance between the particle mass centre and the advancing contact edge, I is the moment of inertia of a sphere with mass m and density ρ, and M is the torque. Here, the contact radius remains almost unchanged $a = 0.5(a_1 + a_2)$. Note that Eqn. 3.47 describes an harmonic oscillator with the characteristic frequency f_0 (Krijt *et al.*, 2014)

$$f_0 = \frac{3}{4\pi}\left(\frac{5\gamma}{R^3\rho}\right)^{1/2} \approx O(0.1 \text{ MHz}), \tag{3.48}$$

The experimental adhesion work, obtained by Murthy Peri & Cetinkaya (2005*a*) and Murthy Peri & Cetinkaya (2005*b*), with rocking dry spherical polystyrene microspheres on silicon wafer and various metal substrates are satisfactory. Murthy Peri & Cetinkaya (2008) reviewed the current trends of rolling-based particle adhesion characterization.

The rolling dynamics of a sticky particle (*e.g.*, receptor-coated) on a (ligand-covered) substrate depends on the exerted force on the particle (shear rate), receptor number, and the ligand density (Chang & Hammer, 2000). Complex adhesion dynamics simulation methods to predict bioadhesion at interfaces are detailed by Hammer & Tirrell (1996). In simple words, the adhesive, elastic receptors and ligands can attach to (detach from) each other with an association (dissociation) rate k_a (k_d), pertaining to the ligand density, particle-substrate relative velocity, and an intrinsic forward rate constant, defined as $k_{in} = \nu f_s \exp\left[-E/(k_B T)\right]$, with f_s denoting a steric factor, and E as the binding activation energy, which should be lower than the chain vibrational energy at frequency ν to result in an effective binding (Chang & Hammer, 1999, 2000). The dissociation rate is related to the unstressed dissociation rate constant k_{d0}, reactive compliance γ of the receptor-ligand complex, and the applied force F

$$k_d = k_{d0} e^{\frac{F\gamma}{k_B T}}. \tag{3.49}$$

The probability of bond formation P_a and detachment P_d within a short time frame dt (Chang & Hammer, 2000)

$$P_a = 1 - e^{-k_a dt}, \tag{3.50}$$

and

$$P_d = 1 - e^{-k_d dt}, \tag{3.51}$$

which can be simulated using the Monte Carlo method. The force acting on the particle, which is a superposition of tether, interfacial, and hydrodynamic forces, dictates the particle velocity $\underline{u}$ through a mobility matrix $\mathbf{M}$ (Chang & Hammer, 2000)

$$\underline{u} = \mathbf{M}\ \underline{F} \tag{3.52}$$

with $\underline{u}$ including three linear and three angular velocity components, and $\underline{F}$ including three force and three net torque components. Also, the mobility matrix $\mathbf{M}$ for a sphere in a viscous

medium near a plane wall is well-established (Chang & Hammer, 1996). Such a simulation requires extensive time and programming effort.

3.4 Optical tweezers microrheology

Experimental micro- and nanoparticle manipulation to study the adhesion properties has been the focus of many studies. Among the experimental techniques, such as colloidal probe AFM (Kappl & Butt, 2002) and magnetic tweezers (Neuman & Nagy, 2008), optical trapping (Neuman & Block, 2004) provides a non-intrusive characterization method.

3.4.1 Optical tweezers

Optical trapping of microspheres, introduced by Ashkin *et al.* (1986), attracted much attention in various fields. Among the most fascinating examples are the stiffness measurement of bacterial flagella (Block *et al.*, 1989) or red blood cells by exerting pN forces using silica microspheres (Henon *et al.*, 1999), DNA stretching force measurements (Wang *et al.*, 1997), biological filaments (*e.g.*, actin and DNA) molecular knotting (Arai *et al.*, 1999), and DNA unzipping (Bockelmann *et al.*, 2002).

When placed close to a highly-collimated laser beam focus, photons exert two types of forces on a dielectric particle, namely a gradient force, which pulls the particle toward the beam centre (in the light spatial gradient direction) and a scattering force, which pushes the particle in the light propagation direction (out of focus) (Neuman & Block, 2004). Note that if the particle is located far from the trap centre, the scattering force dominates and pushes the particle further (similar to a fire hose). The gradient force originates from the experienced force by a dipole in an inhomogeneous electric field (Neuman & Block, 2004), depending on the particle polarizability and light intensity.

The optical force is similar to a linear Hookean spring force at small displacements ($\approx$ 150 nm) from the trap centre (Neuman & Block, 2004). Depending on the trapped particle

size, the scattering force, from the light absorption and/or reflection by the particle, can be furnished by the well-known ray optics when the particle size R is ($\gtrsim 10$ fold) greater than the laser wavelength λ, *i.e.*, *Mie* scattering. The light momentum change is proportional to the amount of light that is refracted by the sphere, which oppositely acts on the sphere according to Newton's third law. Note that the gradient force is in the same (opposite) direction of the light intensity gradient if the particle refractive index is greater (lower) than the medium. The optical forces are furnished from the conventional ray-optics regime (Ashkin, 1992).

If $R \ll \lambda$, the particle acts as a point dipole in the inhomogeneous field, *i.e.*, *Raleigh* scattering regime. The scattering force F_s is proportional to the incident light intensity I_0, scattering sphere cross section

$$\sigma = \frac{128\pi^5 R^6}{3\lambda^4}(\frac{m^2-1}{m^2+2})^2, \tag{3.53}$$

medium refractive index n_m, speed of light in a vacuum c, and refractive index ratio of the particle to the medium $m = n_p/n_m$ (Neuman & Block, 2004):

$$F_s = \frac{\sigma n_m I_0}{c}, \tag{3.54}$$

and the gradient force F_g is related to the particle polarizability

$$\alpha = n_m^2 R^3(\frac{m^2-1}{m^2+2}), \tag{3.55}$$

and the light intensity gradient ∇I_0,

$$F_g = \frac{2\pi\alpha}{cn_m^2}\nabla I_0. \tag{3.56}$$

To describe the force on the majority of the particles or cells trapped nowadays using optical tweezers, which have sizes comparable to the light wavelength $R \approx \lambda$, electro-

magnetic theories, such as that of Barton *et al.* (1988), are required (Neuman & Block, 2004). To minimize the optical damage at high light intensities, infrared lasers, such as neodymium:yttriumorthovanadate (Nd:YVO_4) with $\lambda \approx 1064$ nm are desirable. Such a laser is used in the current study.

3.4.2 Passive microrheology

Probing the viscoelastic properties of complex materials using small sample volumes (*e.g.*, μl) is possible by optically trapping a micro- or nanoparticle and relating its thermal position fluctuations to the medium properties. While conventional video microscopy techniques can provide spatial accuracy of tens of nanometer (Crocker & Grier, 1996) with tens of milliseconds temporal resolution (Willenbacher & Oelschlaeger, 2007), back-focal-plane interferometry furnishes nanometer spatial resolution and tens of nanoseconds temporal resolution (Gittes & Schmidt, 1998). Within this technique, the collimated optical beam exiting a high numerical aperture (NA) microscope objective, passing through a specimen to trap a particle, is directed onto a quadrant photo diode (QPD) placed in the back-focal plane (BFP) through a set of aligned microscope condenser, dichroic mirror, and focusing lens. Light angular (phase) intensity changes, due to the interference of the scattered light and transmitted beam, furnishes the position displacement (in Volts) relative to the trap centre. Here, the position detection accuracy is independent of the trap location within the specimen plane when the trapping and detection lasers are the same, and the particle displacements are small (Neuman & Block, 2004). The voltage time series are converted to accurate position time series by calibrating the position (and force) using established methods, *e.g.*, Berg-Sørensen & Flyvbjerg (2004). Details of the calibration method used in this work are presented in chapter 5. The most recent advances in optical trapping are collected by Moffitt *et al.* (2008).

Tracking the probe particle motion while it is subjected only to the thermal forces, and relating it to the deformation and flow behavior of the medium, is known as passive

microrheology. One extreme is when the probe particle is optically trapped in a pure viscous medium. In this condition, the bead is kicked by the solvent molecules followed by a complete memory loss before the next position variation step, bringing about a non-correlated random motion, known as Brownian motion. As discussed earlier (Eqn. 3.20), the effective medium viscosity is readily calculated from the particle position mean-squared displacements. In the one-dimensional case,

$$\eta = \frac{k_B T \tau}{3\pi R \left\langle [X(t+\tau) - X(t)]^2 \right\rangle}. \tag{3.57}$$

The storage modulus of such a system $G' = 0$, and the loss modulus $G'' = \omega\eta$, where $\omega = \tau^{-1}$. A biological example of this case is a highly viscous ($\eta \approx 1$ Pa) and non-elastic cytoplasm of *Caenorhabditis elegans* (a soil worm) embryos (Daniels *et al.*, 2006). The other extreme is when the particle is in an elastic medium. In this case, the mean-squared displacements become independent of the time lag (Wirtz, 2009)

$$G' = \frac{k_B T}{3\pi R \left\langle [X(t+\tau) - X(t)]^2 \right\rangle}, \tag{3.58}$$

which furnishes elasticity measurements as large as ≈ 1 kPa, taking the position detection resolution ≈ 2 nm and trappable particle size limit $R \approx 100$ nm. For such a system, $G'' \approx 0$. An intermediate state, *i.e.*, a viscoelastic medium, is evidenced by a non-constant slope of the mean-squared displacement versus time lag. For the first time, Mason & Weitz (1995) proposed a method to relate the probe position mean-squared displacements to the storage and loss moduli of a complex fluid. The complex modulus $G^*(\omega) = G'(\omega) + iG''(\omega)$ is readily attained from the unilateral Fourier transform $\mathscr{F}$ of the MSD (Mason & Weitz, 1995; Mason *et al.*, 1997; Wirtz, 2009)

$$G^*(\omega) = \frac{k_B T}{3\pi R i\omega \mathscr{F} \left\langle [X(t+\tau) - X(t)]^2 \right\rangle}, \tag{3.59}$$

which furnishes

$$G'(\omega) = |G^*(\omega)| \cos\left[\frac{\pi\alpha(\omega)}{2}\right] \tag{3.60}$$

with

$$|G^*(\omega)| = \frac{k_B T}{3\pi R \left\langle [X(t+\tau) - X(t)]^2 \right\rangle \Gamma\left[1 + \alpha(\omega)\right]}. \tag{3.61}$$

Here, Γ is the gamma function, and the local MSD logarithmic slope at a desired ω furnishes $\alpha(\omega)$. The loss modulus is, however, not independent of the storage modulus according to the Kramers and Kronig relation (Winter & Chambon, 1986)

$$\frac{G'(\omega)}{\omega^2} = \frac{2}{\pi} \int_0^\infty \frac{G''(x)}{x\left(\omega^2 - x^2\right)} dx. \tag{3.62}$$

An open source Matlab routine is available to convert the MSD data to the viscoelastic moduli (Crocker, 1999). Trapped in an ideal viscoelastic material (shear modulus μ and viscosity η), the MSD of a probe particle, subjected to stress σ (Cicuta & Donald, 2007) is

$$\left\langle [X(t+\tau) - X(t)]^2 \right\rangle = \sigma \left(\frac{1}{\mu} + \frac{\tau}{\eta}\right), \tag{3.63}$$

where the viscoelastic moduli, according to the Maxwell model, are related to the material relaxation time τ and shear modulus μ:

$$G' = \mu \frac{(\omega\tau)^2}{1 + (\omega\tau)^2}, \tag{3.64}$$

and

$$G'' = \mu \frac{\omega\tau}{1 + (\omega\tau)^2}. \tag{3.65}$$

This will be discussed later for active interfacial characterization. Weihs *et al.* (2006) thoroughly reviewed biomicrorheology, and Squires & Mason (2010) conducted a comprehensive review on the fluid mechanics of microrheology.

3.4.3 Active microrheology

The central idea of active microrheology is to apply an external force (usually an oscillatory shear) to an optically trapped dielectric particle, embedded in a target material, and probe the particle position response while locally deforming the material (Brau *et al.*, 2007). Active microrheology can be conducted at a constant velocity (optical tweezers) or constant forcing (magnetic tweezers) (Wilson & Poon, 2011). The focus of this section is on optical tweezers active microrheology at interfaces.

To follow the sticking dynamics of a microsphere at an interface, a probe particle is brought into contact with the interface while subjected to an external force. An oscillatory shear force can be applied to the substrate via the probe particle by harmonically translating a substrate that is attached to microscope's digitally-controllable stage. A sinusoidal strain $\epsilon = \epsilon_0 \exp(i\omega t)$ exerted on a viscoelastic material results in a sinusoidal stress response $\sigma = \sigma_0 \exp[i(\omega t + \delta)]$ with a phase lag δ, termed as the loss angle (Malkin, 1994). The complex viscoelastic modulus

$$G^* = G' + iG'' = \sigma/\epsilon, \tag{3.66}$$

furnishing storage $G' = |G^*| \cos\delta$ and loss $G'' = |G^*| \sin\delta$ moduli, with $|G^*| = \sqrt{G'^2 + G''^2}$. Accordingly, the loss tangent $\tan\delta = G''/G'$, and the complex viscosity

$$\eta^* = \frac{\sigma}{\dot{\epsilon}} = \frac{|G^*|}{\omega}(\sin\delta - i\cos\delta) = \eta' - i\eta'', \tag{3.67}$$

introducing the dynamic viscosity $\eta' = G''/\omega$ and out-of-phase viscosity $\eta'' = G'/\omega$. For a linear viscoelastic material, (i) the loss angle does not depend on the strain amplitude, and (ii) changing the strain amplitude changes the stress amplitude linearly and vice versa (Malkin, 1994). Also, the area under the stress-strain curve furnishes the dissipation work W_d per cycle per unit volume ($V = A\ell_0$ with A denoting the sample cross-sectional area, and ℓ_0

representing the sample initial length, and strain is shown with ϵ_0):

$$W_d = \frac{1}{V}\int_0^{\ell} F dx = \int_0^{\ell} \frac{F}{A}\frac{dx}{\ell_0} = \int_0^{\epsilon_{cycle}} \sigma d\epsilon = \pi G'' \left|\epsilon_0\right|^2 . \tag{3.68}$$

In the active microrheology, however, the probe particle position response $x_p = \hat{x}_p \exp(i\omega t)$ to the external drive $x_s = \hat{x}_s \exp(i\omega t)$ (having complex amplitudes) is obtained experimentally (instead of the stress and strain), which is related to the storage and loss moduli as suggested by Sharma *et al.* (2008), and derived in Appendix 6.B. The phase angle (lag) between the particle position response and the external drive ϕ is directly related to the particle diffusion coefficient if the particle is trapped in a viscous fluid (Ghosh *et al.*, 2007; Sharma *et al.*, 2010*a*) or in a viscoelastic medium, as described in Appendix 6.B.

When an optically trapped particle is in a viscous fluid, the imaginary part of the response is expected to dominate the real part, because the particle viscous response is out-of-phase with the position disturbance. The real part of the response is, however, directly affected by the medium elasticity, because the particle response to an elastic perturbation is in-phase with the perturbation. The phase lag between a probe particle and an external drive when the particle is coupled to a viscous (elastic) medium is, therefore, high (low). The exact dependency of the phase lag to the medium viscoelastic properties and trap stiffness is explained in Appendix 6.B. Briefly, the phase lag is attenuated by increasing medium dynamic and out-of-phase viscosity, trap stiffness, and drive frequency. Note that, if the particle is subject to an oscillatory optical force, for example by an acousto-optic deflector (AOD), the phase lag increases when increasing the optical drive frequency.

Conducting active interfacial microrheology with silica and polystyrene (PS) microspheres on a glass plate, Sharma *et al.* (2008) reported that, in case of a hard microsphere, *i.e.*, silica, adhesion takes place abruptly, while for a soft microsphere (PS), the adhesion strength depends on the operating parameters, namely trap stiffness, drive frequency, and ionic strength. They showed that for a PS (silica) microsphere, in a 20 mmol l^{-1} NaCl electrolyte, the dy-

namics are attenuated within a long time-scale ≈ 0.5 h (abruptly within a few seconds). In these experiments, the particles were subject to 33 nm drive amplitude and 251 rad s^{-1} drive frequency, contacting the underlying glass substrate. Such an aging behavior of PS particles on a glass substrate has been hypothesized to be related to polymer tether formation within the particle-substrate gap (Sharma *et al.*, 2010*b*).

The gradual bond formation between a PS probe particle and a glass substrate (Sharma *et al.*, 2008, 2010*b*), resulting in the aging of viscoelastic properties from a loss modulus dominant ($G'' > G'$) to a storage modulus dominant ($G' > G''$) coupling provides a multi-time scale transition within the Cole-Cole formalism that was successfully modeled as a single Maxwell material. Such multi-time scale transition is attributed to the existence of discrete potential minima, manifested in the clustered data points in the G''-G' Cole-Cole plots. Well-fitted viscoelastic moduli to a simple Maxwell model imply that while the relaxation time and viscosity increases with time (aging), their ratio remains almost constant, suggesting that the relaxation time distribution is a sharply-peaked (high kurtosis) function of Maxwell relaxation time τ.

A colloidal particle at an interface can undergo weak or strong adhesion, depending on the surface energy. If the interfacial adhesion is assumed to be the result of n discrete spatially-ordered pinning sites in a correlation volume V (*i.e.*, structural correlation area ξ^2 multiplied by a perpendicular inter-atomic length scale ℓ) (Kumar *et al.*, 2013), the adhesion energy U_a depends on the adhesive force f and the adhesion potential range u: $U_a = fu\sqrt{n/(\xi^2\ell)}$, and the elastic energy U_e is directly related to the cohesive stiffness $k_c = G'\ell$: $U_e = 0.5(k_c/\ell)(u/\xi)^2$. Minimizing the elastic and adhesion energy difference with respect to ξ results in a characteristic structural length scale $\xi_0 = k_c u/(f\sqrt{n\ell})$, which is readily related to the critical interfacial stress to induce a plastic deformation $\sigma_c \approx \gamma_c k_c/\ell = \gamma_c f(\xi_0/\ell)\sqrt{n\ell/u^2}$, where γ_c is the critical tensile strain. Accordingly, strong adhesion is the result of a small ξ_0 and large $fn^{0.5}$ and σ_c (Kumar *et al.*, 2013). This occurs when the adhesive coupling is stronger than the cohesive coupling. A recent theory (Mani

et al., 2012) relates the sticking process of a colloidal particle to a soft polymer tether-coated substrate, which describes the adhesion with the binding kinetics, bond elasticity, and fluid drainage in terms of three dimensionless ratios, namely (i) viscous drainage time to the binding kinetics, (ii) elastic to thermal energies, and (iii) particle size to the polymer tether length. This permits adhesion susceptibility to the instabilities parallel to the substrate.

The possibility of tuning the equilibrium adhesion properties, despite the adhesion of a silica microsphere to a gel-electrolyte interface, often takes place abruptly, will be discussed in this thesis.

Chapter 4

Video particle tracking to quantify colloidal dynamics at soft interfaces

4.1 Preface

Amir Sheikhi designed, conducted, and analyzed the experiments. In this chapter, video microscopy is used to perform particle tracking for characterizing the colloidal dynamics at soft interfaces, such as lipid bilayers, lipopolymer-doped lipid bilayers and hydrogels. Soft interactions are important in biological systems, where the cells with lipid bilayer wall, extra cellular matrices with hydrogel-like structure, and polymer chain-grafted drug agents interact with each other. The dynamics of coated silica microspheres at a soft interface reflect the interaction between the coating and the soft substrate, providing valuable information about the potential landscapes.

4.2 Abstract

Particle-based drug and gene delivery systems have gained tremendous importance due to their simplicity in design, production, and controllability. Micron and sub-micron size drug agents are usually coated with various polymeric layers to increase circulation time, improve

colloidal stability, or achieve targeted delivery and binding. However, due to the complicated nature of soft interfaces, little is known about how colloidal drug agents behave at biological interfaces (*e.g.*, cell membrane, brush-coated surfaces, and porous tissues). To help understand the interaction forces, a series of surface self-diffusion experiments were conducted involving surface-functionalized colloidal spheres on lipid bilayers (DOPC), lipopolymer-doped phospholipid bilayer membranes (DSPE-PEG/DOPC, termed as DSPE), hydrogels, and glass. The analysis of stochastic particle trajectories, obtained using digital image processing and optical microscopy, qualifies how the motion is influenced by the surface coatings and electrolyte ionic strength. The results showed that colloidal particles underwent Brownian or non-Brownian (anomalous) motion. The anomalous interfacial dynamics were observed when entanglement, such as the grafted-polymer interaction with lipid membranes or hydrogels, was possible. Moreover, from these studies, the key interfacial characteristics that tune particle adhesion were identified. It is also discussed how the findings may enable control over the interaction forces in applications.

4.3 Introduction

Soft interactions play an important role in many biological systems where, for example, cells comprising lipid bilayer membrane exterior (Plant, 1999; Tanaka & Sackmann, 2005), drug carriers with conjugated polymer chain coatings (Storm *et al.*, 1995), and soft tissues interact. Given the difficulty of studying real biological systems, satisfactory model systems are necessary to study soft interfacial interactions.

Cell adhesion [*e.g.*, (Kloboucek *et al.*, 1999)] and immune reaction [*e.g.*, (Grakoui *et al.*, 1999)] are well correlated with the interactions between the cell-wall and the surrounding environment. Lipid bilayers, as the major external part of the cell, provide a good mimic of cell surface (Simons & Vaz, 2004). To maintain their mechanical stability while benefiting from their two-dimensional fluidity, they need to be supported (Castellana & Cremer, 2006).

The substrate can be rigid (Richter *et al.*, 2006) or soft (Sackmann & Tanaka, 2000; Tanaka & Sackmann, 2005), planar (Richter *et al.*, 2006) or curved (Mornet *et al.*, 2005), each providing unique characteristics. A comprehensive review on the lipid bilayer structure was conducted by Nagle & Tristram-Nagle (2000).

Important examples of particular soft interactions involving supported interfaces are as follows: (i) nanoparticles, contacting supported lipid bilayers, may penetrate, disrupt, thin, or bend the membrane, depending on their size and surface properties (Leroueil *et al.*, 2007, 2008), (ii) exchange of species between two contacting supported lipid bilayers [*e.g.*, oppositely-charged supported planar or spherical fluid membranes target each other selectively and exchange lipids (Sapuri *et al.*, 2003), and contacting lipid-coated microspheres exchanging fluorophores (Kendall *et al.*, 2010)], (iii) lignad-receptor bonding by applying external forces on ligand-coated particles interacing with receptor-coated substrates to explain cell rolling (Marshall *et al.*, 2003), and (iv) reducing non-specific binding of particle-based sensors to coated surfaces, *e.g.*, control over protein-coated particles in a polymer-coated surface vicinity by a magnetic field (Kemper *et al.*, 2012).

In a closely-related recent work, Everett & Bevan (2014) studied the interaction potential between a variety of supported lipid bilayers, including those coated on a silica microsphere and a flat substrate interacting with each other or with a bare substrate, using total internal reflection microscopy (TIRM). They showed that for PEG-grafted particle-supported lipids interacting with a substrate with the same coating, the particle-substrate binding is regulated by the particle size, PEG concentration, and lipid composition. Larger particles, lower PEG molecular weight, and lower conjugate PEG concentration resulted in stronger adhesion. Interestingly, bilayer deformation in the gap between a bilayer-coated silica microsphere and a bilayer-coated substrate resulted in wider potential well compared to bare surfaces in an high ionic strength medium (150 mmol l^{-1} NaCl). Various mechanisms, such as neck formation, and bilayer exchange and fusion, modified the soft interactions in these systems (Everett & Bevan, 2014).

Furthermore, an ultimate objective of this thesis is to shed light on the interfacial properties of soft hydrophilic polymer networks, termed hydrogels, which, despite their wide variety of applications, are not well understood. A desire to understand the interaction at such soft interfaces motivated tracking the position of silica microspheres with soft coatings on a flat substrate coated with another soft material. Combining inverted microscopy with image processing, video particle tracking furnishes the position time-series of microspheres diffusing on a flat substrate while the interacting surfaces are bare, or coated with DOPC, DSPE, or hydrogel, providing an ensemble representation of surface interactions.

4.4 Materials and methods

4.4.1 Bilayer preparation

Small unilamellar vesicles (SUV) were prepared according to Zhang & Hill (2011). Briefly, a phospholipid mixture, containing 2 mg 1,2-dioleoyl-sn-glycero-3-phosphocholine (DOPC, Avanti Polar Lipids, Alabaster, AL, U.S.A.) and lipopolymer 1,2-distearoyl-sn-glycero-3-phosphoethanolamine-N-[amino(polyethylene glycol)2000] (DSPE-PEG2k-Amine, Avanti Polar Lipids, Alabaster, AL, U.S.A.) in chloroform was dried under nitrogen. Then, it was desiccated under a vacuum for at least 1 h, followed by reconstitution in 1X PBS buffer (pH $\approx$ 7.4) to 2 mg ml^{-1} to form giant multilamellar vesicles (GMV), which were extruded through 100 nm and 50 nm polycarbonate membranes (Avanti Polar Lipids, Alabaster, AL, U.S.A.) at least 20 times each, to form SUVs, as identified by a change from an opaque to a transparent solution. SUVs were stored in a fridge (4°C) and used freshly within one day. The chemical structure of DOPC and DSPE-PEG2k-Amine molecules is presented in figure 4.4.1.

4.4.2 Substrate preparation and coating

Prior to coating, rectangular cover glasses (60×24 mm, thickness No. 2, VWR microcover glass, U.S.A.) were cleaned by boiling for 30 min in 7X solution (MP Biomedical, Solon, OH, U.S.A.) followed by rinsing with reverse osmosis (RO) water. They were then dried under nitrogen and immersed in a freshly-prepared Piranha solution (3:1 v/v concentrated sulphuric acid and 30 % hydrogen peroxide) for 20 min. Etched cover glasses were rinsed with RO water extensively and dried under nitrogen. The ζ-potential of a cleaned cover glass is ≈ -20 mV in TAE buffer (see Appendix 7.B).

For bilayer coating, small unilamellar vesicles were fused on a cleaned cover glass by sandwiching a droplet of the SUV solution between the cover glass and the bottom of a crystallization dish (Cremer & Boxer, 1999) followed by gently washing the cover glass in RO water. To coat a cleaned cover glass with PEG hydrogel (polyethylene glycol diacrylate, Mw = 575, Sigma-Aldrich, MO, U.S.A.), it was allowed to contact 0.5 mol l^{-1} sodium hydroxide solution followed by a silanization agent (3-aminopropyltrimethoxysilane, 97 %, Sigma-Aldrich, MO, U.S.A.) according to the protocol of Wang & Pelham (1998) with intermediate gentle rinses with RO water. To covalently bind to the gel film, finally, the cover glass was incubated with 0.7 % glutaraldehyde (70 % EM Grade, Polysciences, Inc., PA, U.S.A.) in phosphate buffered saline (PBS, pH $\approx$ 7.4) at room temperature for 30 min, and then rinsed thoroughly with RO water. PEG monomers were mixed with PBS buffer to achieve a desired monomer concentration. The solution was blanketed with nitrogen to prevent oxygen absorption during crosslinking. The gel was formed by sandwiching the pre-gel solution between the functionalized cover glass and a cleaned but non-functionalized cover glass followed by $\approx$ 10 min curing with $\approx$ 0.001% w/v ammonium persulphate (APS, Sigma-Aldrich, MO, U.S.A.) initiator and 0.1% v/v N,N,N′,N′-tetramethylethylenediamine (TEMED, GE Healthcare, Uppsala, Sweden). To achieve an equilibrium swollen state, the thin film was incubated in RO water for at least one day at the ambient temperature ($\approx 23^{\circ}$C). If the cover glass is not functionalized, the gel layer cannot be deposited uniformly, and surface instabilities oc-

cur. Gel-coated functionalized and unfunctionalized cover glasses are depicted in figure 4.4.2. The Young's modulus (density) of 20 % and 5 % PEG hydrogels prepared by photoinitiation has been reported $\approx$ 228.9 kPa (1.0062 g ml^{-1}) and $\approx$ 2.8 kPa (1.0248 g ml^{-1}), respectively, via AFM indentation (Corbin *et al.*, 2013). The ζ-potential of free-standing PEG hydrogel films have been reported to be close to zero and slightly negative at pH $\gtrsim$ 3.5 and 10 mmol l^{-1} NaCl solution (Sagle *et al.*, 2009). The agarose gel was prepared by adding a desired amount of agarose powder (IEF garde, Formula Weight 306.12, gelling temperature 34–45°C, Fisher, N.J., U.S.A.) to PBS buffer at room temperature with magnetic stirring to disperse and hydrate, followed by the hot plate heating in a sealed container to boil while preventing evaporation (Johansson, 1972). The resulting clear solution was then cooled to $\approx$ 70°C, and the cover glass surface gently dipped into the warm gel solution, removed, and allowed to cool down before immersing in RO water to swell. An estimate of the agarose elasticity comes from the compression elastic modulus $\approx 1.5 \pm 0.7$ kPa for a 0.3 % w/w agarose hydrogel (Normand *et al.*, 2000).

4.4.3 Colloidal particle preparation, coating, and tracking

Bare silica microspheres (diameter $2R \approx 1.97$ μm, 10–15% coefficient of variation, Bangs Laboratories, Inc., IN, U.S.A.) were cleaned by at least two centrifugations in RO water (pH $\approx$ 5.8). To coat silica microspheres with lipid bilayers, they were mixed (Baksh *et al.*, 2004) with the lipid solution at particle (10 w%):lipid ratio 1:3 v/v and stirred for at least 10 min. To eliminate infused SUVs, the particle-lipid mixture was three times pulse-centrifuged from which the supernatant was separated, followed by dilution in TAE buffer. Finally, coated particles were diluted in RO water to be used in interfacial self-diffusion experiments. The SUVs or supported lipid bilayers have been reported to be stable for more than a month at 4°C (Mornet *et al.*, 2005). The ζ-potential of bare, DOPC-coated, and DSPE-coated silica microspheres in TAE buffer is ≈ -52 mV, ≈ -30 mV, and ≈ -30 mV, respectively (see Appendix 7.B). The coatings on the particles were ascertained by doping the

bilayers with fluorescent PEG lipids, 1,2-distearoyl-sn-glycero-3-phosphoethanolamine-N-[poly(ethylene glycol)2000-N'-carboxyfluorescein] (DSPE-PEG2k-CF, Avanti Polar Lipids, Alabaster, AL, U.S.A.), and performing fluorescent microscopy using a Zeiss 510 META NLO confocal microscope equipped with a plan-Neofluar 20X (numerical aperture= 0.5) objective. Green coating around the $2R \approx 4.74$ μm DSPE-PEG-CF-coated silica microspheres is demonstrated in the top left panel of figure 4.4.2. To perform self-diffusion experiments, the microspheres were injected into a sealed flow cell (FC 81-AL, BioSurface Technologies Corporation, Mont., U.S.A.) with approximate length 50 mm, width 13 mm, and height 2.35 mm, including the coated cover glass (170–250 μm thick, bottom) and a glass microscope slide (25×75 mm, ≈ 1 mm thick, top). Particle trajectories were acquired by capturing snapshots at a desired frequency, as controlled by the image analysis software interface (MetaMorph, Molecular Devices, CA, U.S.A.) using an inverted optical microscope (TE-2000U, Nikon, NY, U.S.A.) equipped with a charge coupled device (CCD) camera (CoolSNAP HQ, Roper Scientific, AZ, U.S.A.). At each time, the particle positions (pixel) were detected using a free source image processing Matlab routine (Kilfoil, 2007), shown in the bottom right panel of figure 4.4.2, and converted to distance using the calibration micro-ruler provided by the microscope manufacturer. The position time-series were post-processed in Matlab to furnish particle mean-squared displacements, from which the lateral diffusion was analyzed.

4.5 Results and discussion

4.5.1 Bare silica microspheres

As a baseline for the particle tracking experiments with coated particles on soft supports, the behavior of bare silica microspheres on a cleaned bare glass cover slip was studied. The number of tracked particles in the CCD camera field of view was 22. In this sample, no particle has less than approximately 3 min residence time in the field. An example of X- and Y-position fluctuations of a microsphere is shown in figure 4.5.1. The particle X- and Y-

positions fluctuate randomly, furnishing a time-series of the particle centre at each time point. The 2D trajectory of a bare silica microsphere diffusing freely on a bare glass slide is shown in figure 4.5.1, left panel. The position time-series furnishes the mean-squared displacement from which the lateral diffusion coefficient D_x and anomalous time-lag exponent n is acquired by fitting the MSD to a function of the form

$$\left\langle [r\,(t+\tau) - r(t)]^2 \right\rangle = 4D_x\tau^n, \tag{4.1}$$

where

$$\left\langle [r\,(t+\tau) - r(t)]^2 \right\rangle = \left\langle [X\,(t+\tau) - X(t)]^2 \right\rangle + \left\langle [Y\,(t+\tau) - Y(t)]^2 \right\rangle. \tag{4.2}$$

The mean-squared displacements of bare silica microspheres on bare cover glass are shown in figure 4.5.2. While the MSD of particles grows linearly at short time lags ($\tau \lesssim 20$ s), the long-time anomalous growth of the MSD is mainly due to the particle local confinement, for example due to contamination and surface heterogeneity, particle-particle interaction, and local drift flow; however, this does not affect the short-time diffusion coefficient. Fitting the MSD at short time lags is necessary to prevent long-time artifacts (Saxton, 1997). The diffusion coefficient and time-lag exponent are ascertained from fitting the MSD to Eqn. 4.1 up to $\tau \approx 19.3$ s, representing free Brownian motion $n \approx 1$ with a reduced ensemble average diffusion coefficient $D_x/D_0 \approx 0.43$ due to the presence of the rigid glass wall, as predicted by the hydrodynamic theories. The individual particle Brownian diffusion coefficient and time-lag exponent, furnished from fitting each of the MSDs (figure 4.5.2, panel a) to Eqn. 4.1, gives the average diffusion coefficient $D_x/D_0 \approx 0.41 \pm 0.06$ of total particle number N_t with standard error $0.06/\sqrt{N_t} \approx 0.01$, excluding the outliers ($D_x/D_0 < 0.2$ or $D_x/D_0 > 0.6$), and average exponent $n \approx 1.0 \pm 0.1$.

The accuracy of the video particle tracking was tested by capturing the position time-series of firmly-attached silica microspheres to a cover glass. The position of 41 attached silica particles to glass (one example is presented in figure 4.5.3) in an high ionic strength medium

(physiological condition: 150 mmol l^{-1} NaCl and 10 mmol l^{-1} HEPES buffer, pH $\approx$ 7, after one day equilibration) was processed to obtain the MSDs, which are shown in figure 4.5.4. The noise is associated with a 80 nm $\times$80 nm region in both X- and Y-directions with drift in the positive direction, as evident in figure 4.5.3, resulting in MSD plateau $\lesssim$ 1000 nm^2, followed by anomalous diffusion when $\tau \gtrsim$ 150 s due to thermal and mechanical drift of the stage. Accordingly, the position and MSD below $\approx$ 100 nm and 1000 nm^2, respectively, are below the noise limit of the video particle tracking.

Increasing the ionic strength, decreases the Debye length, permitting the negatively-charged interacting surfaces to explore closer separation, which may lead to partial (secondary potential minimum) or permanent (primary energy minimum) attachment. The medium ionic strength was systematically increased by increasing the HEPES buffer concentration. In 0.5 mmol l^{-1} HEPES buffer, shown in figure 4.5.5, the MSDs fall into two main groups: a Brownian group, similar to the same system in RO water; and a non-Brownian group, comprising significantly slower particles. The diffusion coefficient (figure 4.5.5, left panel b) is bimodal comprising approximately 35 % particles undergoing hindered diffusion and $\approx$ 65 % freely diffusing. The time-lag exponent (figure 4.5.5, panel b) suggests that while most particles are Brownian ($n \approx 1$), $\approx$ 30 % have sub-diffusive exponent $n \lesssim 0.5$. Note that almost all the MSDs are above the noise threshold. Further increase of the ionic strength to 50 mmol l^{-1} HEPES buffer resulted in permanent particle attachment, bringing the MSD to the noise level (not shown here).

Bare colloidal silica dynamics on PEG hydrogels in any ionic strength were attenuated below the noise limit (not shown here), suggesting that negative charge, such as that born by agarose (0.33 % w/v) may promote diffusion. Therefore, a cover glass coated with thermally-prepared agarose hydrogel was used to support bare silica microspheres. The MSDs, shown in figure 4.5.6, suggest free diffusion for most particles, as evidenced by the MSD linear growth versus time lag; however, confinement, identified by the MSD plateau at $\tau \gtrsim$ 20 s for some particles, is a result of weak local attachment. The diffusion coefficient distribution

(figure 4.5.6, left panel b) is wider than on a glass substrate due to the gel surface heterogeneity, which includes $\approx$ 10 % particles with $D_x/D_0 < 0.01$. Interestingly, sub-diffusive particle dynamics are reflected in $0.5 \lesssim n < 1$. Prevention of non-specific adhesion of bare silica microspheres to agarose is a key characteristic of this interfacial inclusion enabling it to be employed as a soft system to investigate bilayer or polymer coating interactions with gels.

4.5.2 DOPC-coated silica microspheres

The silica microsphere ζ-potential is suppressed by coating it with DOPC lipid bilayers (mentioned in section 4.4.3). These sphere-supported lipid bilayers (SLBs) resemble the interaction at the cell-surface 'level'. The MSD of DOPC-coated particles diffusing on a bare cover glass, presented in figure 4.5.7, shows that most particles have unconfined diffusion with local attachment at long times for a few particles. All the MSDs are well above the noise limit. The diffusion coefficients are more widely distributed than for bare particles on gel, mostly attaining high (close to the bare-bare system) values. The particle interaction with the substrate is repulsive as coating the bare silica microspheres with DOPC maintains the negative ζ-potential. Less significant bimodality is observed in the time-lag exponent, which is mainly distributed around $n = 1$ with a few populations ($\lesssim$ 20 %) adopting $n < 0.5$. Accordingly, although the diffusion is slightly hindered, it follows a close-to-normal Brownian behavior on glass.

The sensitivity of the DOPC-glass interaction to the electrostatic surface potentials was examined by increasing the ionic strength using 0.5 mmol l^{-1} HEPES buffer. The mean-squared displacement and diffusion characteristics are presented in figure 4.5.8. Panel (a) shows that while the MSD increases linearly for some particles, a large number of particles with small MSD lowers ensemble average. Accordingly, the distribution of diffusion coefficient is sharply peaked at $D/D_x \lesssim 0.003$, including more than 50 % of the particles, while the second peak occurs at $D_x/D_0 \approx 0.17$ involving less than 10 % of the particles.

Obviously, compared to the same system in RO water (larger Debye length and accordingly higher electrostatic potentials), diffusion is hindered in the HEPES buffer. Interestingly, n becomes bimodal with the probability of sub-diffusivity ($n \lesssim 0.5$), opposite to the behavior in RO water (see figure 4.5.7) where n was distributed mainly around one.

To further suppress the cover glass ζ-potential, the substrate was coated with DOPC. The MSD and diffusion characteristics are summarized in figure 4.5.9. While no significant binding to the surface is observed (MSDs are large and do not have any plateau), the diffusion coefficient becomes almost normally distributed around $D_x/D_0 \approx 0.1$ (corresponding to an implausibly small particle-substrate gap, suggesting diffusion at close proximity) showing lower values than the DOPC-bare case (figure 4.5.7). This is mainly attributed to the DOPC coating bearing zero effective charge. Note that the super-diffusive diffusion modes $n > 1$ may be an artifact related to drift. Increasing the ionic strength decreased the diffusion coefficients to the system noise level, similar to the DOPC-bare glass system (not shown here).

Coating a glass substrate with DSPE provides a means to study the interaction between the conjugated PEG chains and the apposing lipid bilayers coated on a silica microsphere. The MSD and diffusion properties of DOPC-coated silica microsphere contacting a DSPE (5 mol %)-coated glass substrate in RO water is presented in figure 4.5.10. Again, particle diffusion is in two main groups: free and hindered. The short-time diffusion coefficient from fitting the ensemble average MSD to Eqn. 4.1 at $\tau \lesssim 22$ s furnishes $D_x/D_0 \approx 0.06$ and $n \approx 1.09$. Despite ≈ 25 % of the particles adopt high diffusion coefficients ($D_x/D_0 \gtrsim 0.1$), the majority of particles (75 %) have $D_x/D_0 \approx 0.05 \pm 0.05$. The time-lag exponent is distributed around one, suggesting close-to-normal diffusion, including some super diffusion. Accordingly, while the short-time diffusion behavior of DOPC-DSPE is similar to DOPC-DOPC system, at long times, the DOPC-coated particles can attach to the PEGylated substrate due to polymer adsorption to, penetration into, or exchange between the lipid bilayers. Stick-slip behavior of the particles with tendency to become locally attached to

the substrate (stick) between long displacements (slip) is observed in the position time-series (shown in figure 4.5.11).

Next, the interacion between DOPC-coated silica microspheres and PEG hydrogel (20 %)-coated glass substrate is studied. The MSDs (figure 4.5.12) suggest that the dynamics of most particles are severely attenuated, limiting particle diffusion to an area on the order of $0.001 - 0.1$ μm^2. Within the temporal resolution of the video particle tracking, the full spectrum of MSD versus time lag is almost a plateau, from which no diffusion coefficient can be calculated. Important is that despite the confined interfacial motion of the particles on the PEG gel, their displacements are detectable. Interestingly, the dynamics on the gel are faster than for particles immobilized on glass substrate (compare to the stuck particle portion in figure 4.5.8). An example of the position fluctuation of a DOPC-coated particle on a PEG gel is shown in figure 4.5.12 (b).

Finally, it is hypothesized that by introducing negative charge to the gel, *e.g.*, by using an agarose hydrogel, fast dynamics would be promoted. The MSD of DOPC-coated silica microspheres undergoing Brownian motion on an agarose (0.33 % w/v)-coated glass cover slip are shown in figure 4.5.13. Interestingly, no significant particle attachment to the gel surface is observed. The diffusion coefficients are mainly distributed around $D_x/D_0 \approx 0.4$, a value corresponding to free Brownian diffusion near a rigid wall. The time lag is also distributed around one, showing a normal diffusion. Note that some particles experience local drift ($n \gtrsim 1$).

4.5.3 DSPE-coated silica microspheres

Doping DOPC lipid bilayers with DSPE lipopolymer (PEG conjugated lipid bilayers) results in a bilayer coating with grafted PEG polymer chains, hereafter termed DSPE. Diffusion of DSPE-coated silica microspheres on a bare cover glass is presented in figure 4.5.14. While most of the particles undergo free diffusion, a portion are confined by attachment. The diffusion coefficient distribution suggest that ≈ 25 % of the particles have $D_x/D_0 \lesssim 0.03$.

Bimodality shows that the fast-diffusing particles ($D_x/D_0 \gtrsim 0.03$) have an average diffusion coefficient $D_x/D_0 \approx 0.17 \pm 0.03$, which is slightly lower than the DOPC-coated particles (see figure 4.5.7). The confinement of DSPE-coated particles on glass may be due to PEG adsorption. The time-lag exponent is mainly centred around one, identifying a Brownian diffusion; however, the wide, equally-weighted $n < 0.5$ identifies attachment.

PEG coatings have been used as a steric layer to prevent non-specific attachment of proteins (Owens III & Peppas, 2006) and cells (Zhang *et al.*, 1998) to drug carriers or substrates. The adhesion sensitivity of DSPE-coated particles to ionic strength is tested by varying HEPES buffer concentration. The MSD and diffusion coefficient in 0.5 mmol l^{-1} HEPES buffer are presented in figure 4.5.15, showing that most particles attain slow diffusion involving MSDs comparable to the noise level. More than 70 % of the particles have $D_x/D_0 \lesssim 0.03$ and the time-lag exponent is mainly smaller than 0.5, suggesting an highly-sub-diffusive behavior, *i.e.*, localized dynamics. The diffusion coefficient of the fast particles (approximately 30 % of particle with $D_x/D_0 \gtrsim 0.03$) $D_x/D_0 \approx 0.29 \pm 0.12$ with $n \approx 0.9 \pm 0.2$ for $n \gtrsim 0.5$. The ensemble average diffusion coefficient is not reported, because the MSDs are close to the noise level or do not increase with time, *i.e.*, confined motion. No mobile particles were observed in 50 mmol l^{-1} HEPES buffer.

When the substrate was coated with DOPC, no significant DSPE-coated particle adhesion was observed (results not shown) and the diffusion was close to the free Brownian diffusion at a rigid wall. This system was, however, susceptible to the ionic strength, and more than 80 % of the particles attached permanently to the DOPC-coated substrate at an high ionic strength (200 mmol l^{-1} HEPES buffer). Interestingly, coating the substrate with PEG (20 % or 5 %) hydrogels resulted in firm particle attachment in a way that the position fluctuations decreased to the noise level, as shown in figure 4.5.16. Although the DOPC-coated particles undergo confined diffusion (see figure 4.5.12), DSPE-coated microspheres experience more localized interfacial attachment, which may be due to the grafted polymer interaction with the gel surface. Accordingly, PEG hydrogels can be used as biocompatible templates to

separate bare or bilayer-coated silica microspheres. This is a significant application for drug carrier elimination from body. Moreover, PEG hydrogels can have promising ability as a soft cushion to form ordered colloidal arrays, *e.g.*, by pattering a glass with PEG and directing a silica sphere suspension through them in a microfluidic device.

Introducing negative charge to the gel layer using agarose hydrogel, the effect of electrostatic repulsion on the particle diffusion was studied. Video microscopy observations by eye indicated that although the DSPE (2.5 % mol)-coated silica microspheres were locally-bound to agarose (0.33 % w/v), their position fluctuations were larger (compared to, for example, on PEG hydrogels). The MSD and diffusion characteristics are presented in figure 4.5.17. Despite the low MSDs compared to, for example, the diffusion on a bare substrate, most particles attain MSD values above the particle-tracking noise level. Calculating the diffusion coefficient within the temporal resolution of the particle tracking does not seem plausible as the MSDs already reached plateaus. However, for comparison, the MSDs were fitted to Eqn. 4.1 to furnish time-lag exponents, which are presented in figure 4.5.17 (b). As Expected, the exponents adopt very small values, and ≈ 95 % of the particles undergo anomalous diffusion wih $D_x/D_0 < 0.1$. Compared to bare silica microspheres on agarose (figure 4.5.6), diffusion coefficients are severely hindered and the particle motion is localized. This is due to the conjugated PEG chain interactions (entanglement and/or adsorption) with agarose. Recall, in the absence of PEG, DOPC-coated particles undergo free Brownian diffusion on agarose (see figure 4.5.13).

The effect of conjugated PEG concentration and the medium ionic strength on the interfacial dynamics of DSPE-coated particles studied by increasing the DSPE concentration to 9.2 mol % in physiological ionic strength. The MSD and diffusion properties of this interfacial system are presented in figure 4.5.18. Compared to 5 % DSPE in RO water, no significant difference in MSDs are observed. This suggests that the MSD hindrance of the DSPE-coated particles on agarose gel has an upper limit, and does not increase proportionally to the increase of adhesive moieties. The diffusion coefficient and time-lag exponent from individual

MSDs are $D_x/D_0 \approx 0.035 \pm 0.046$ and $n \approx 0.27 \pm 0.29$ when fitting up to $\tau \approx 3.7$ s. The large standard deviation shows a wide distribution of the diffusion coefficients.

The ensemble-averaged diffusion and time-lag exponent of all the studied cases are summarized in Table 4.1. This table shows that by coating the particle and/or substrate and consequently changing the surface potential and vdW attraction, interfacial diffusion can be tuned. For instance, coating the surfaces with bilayers decreases the diffusion coefficient when bare particles are coated with DOPC, and the diffusion coefficient further decreases when both particles and substrate are coated. The results also provide examples of possible PEG conjugate interaction with lipid bilayers, reducing the interfacial diffusion coefficient. Furthermore, a neutral hydrogel, *e.g.*, PEG, promotes adhesion significantly, while a charged hydrogel repels bare and DOPC-coated particles, keeping their diffusion coefficient comparable to the diffusion coefficient on glass. Interestingly, despite a free diffusion of bilayer-coated particles on agarose hydrogel, introducing grafted PEG chains to the bilayer binds the particles to the gel. Future work seeks the single-particle adhesion dynamics at hydrogel soft interfaces using more sophisticated methods, such as optical tweezers microrheology.

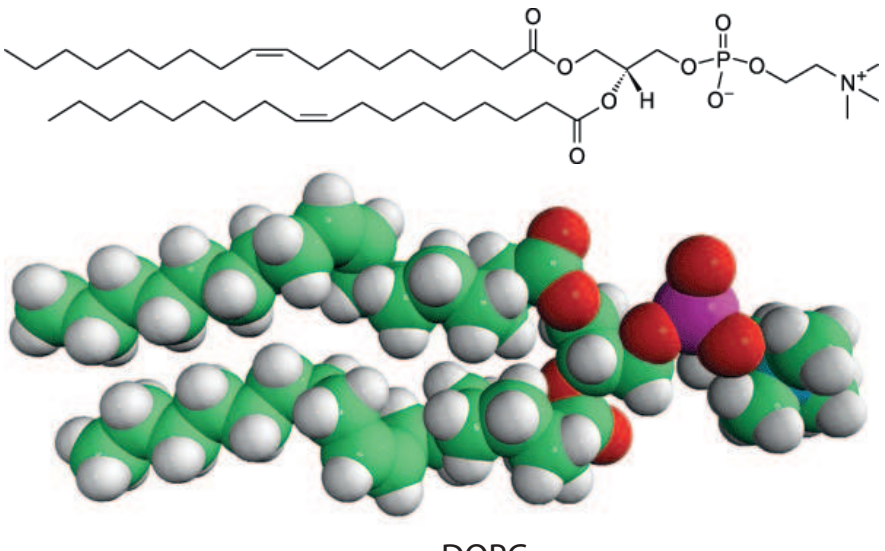

DOPC

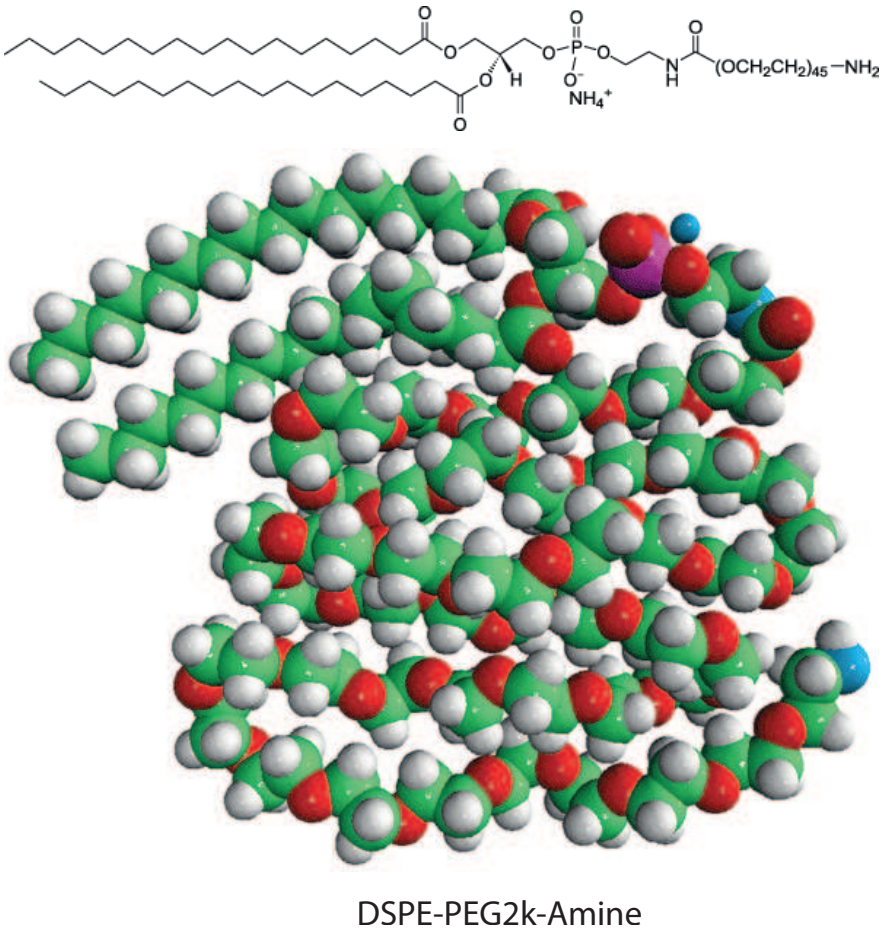

DSPE-PEG2k-Amine

Figure 4.4.1: DOPC and DSPE-PEG2k-Amine chemical structure. Note that DOPC molecular formula is $C_{44}H_{84}NO_8P$, and DSPE-PEG-2k-Amine has a molecular formula as $C_{132}H_{266}N_3O_{54}P$. Image courtesy of Avanti Polar Lipids (Alabaster, AL, U.S.A.).

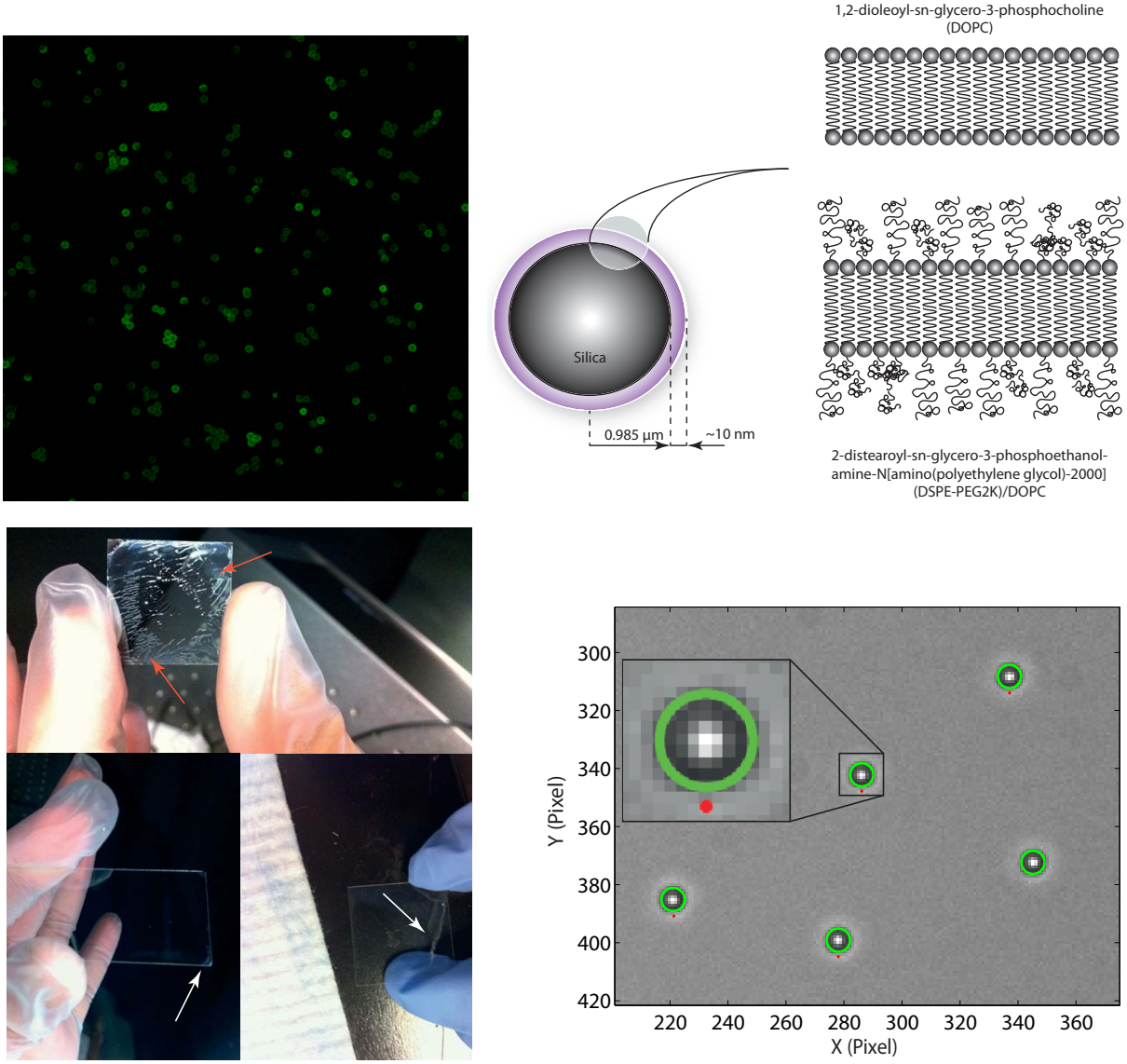

Figure 4.4.2: (top left panel) Fluorescence microscopy of DSPE-PEG-CF-coated $2R \approx 4.74$ μm bare silica microspheres, (top right panel) schematic of a bilayer-coated particle, (bottom left panel) PEG gel-coated unfunctionalized cover glass, bearing surface instabilities (shown with red arrows), and functionalized cover glasses, bearing uniform gel layer (shown with white arrows), and (bottom right panel) an example of $2R \approx 1.97$ μm microsphere centre detection via the image processing Matlab routine (Kilfoil, 2007). The algorithm performance is shown with green circles adopting the detected particle centre and diameter.

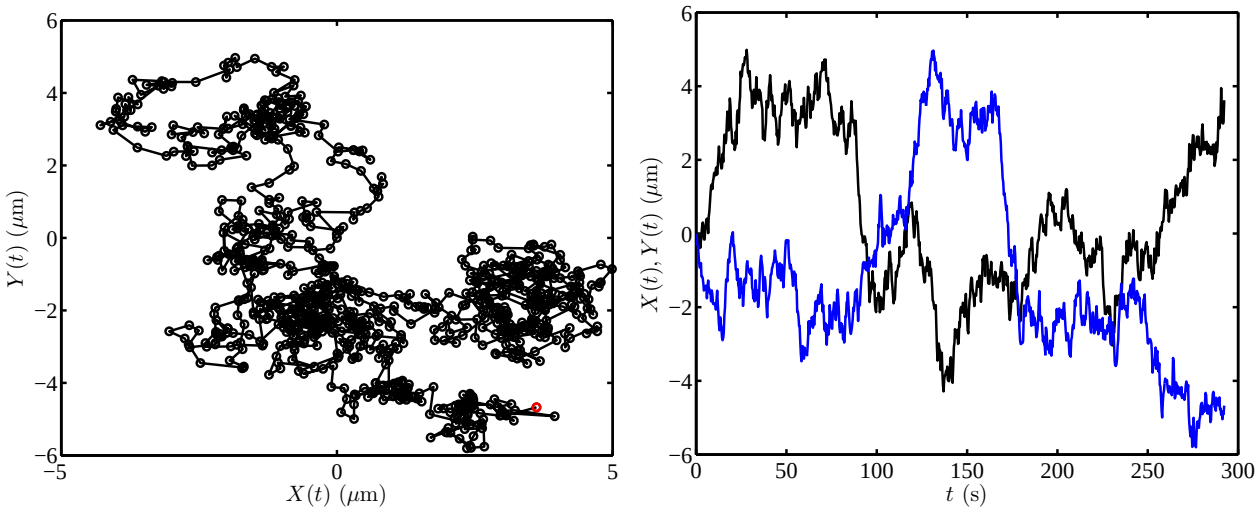

Figure 4.5.1: Position fluctuations of a silica microsphere on glass, acquired using video particle tracking: (left panel) Y-position versus X-position with the initial position (X,Y)=(0,0) and the last position indicated with red symbol. (right panel) X- (black color) and Y- (blue color) position time-series. Note that the particle exits the CCD camera detection field of view after approximately 5 min. The diffusion coefficient associated with this position time-series $D_x/D_0 \approx 0.32$ with anomalous time-lag exponent $n \approx 1.07$, furnished from the mean-squared displacements fit to Eqn. 4.1 up to a time lag $\tau \approx 19.3$ s. This diffusion coefficient is equivalent to a bare silica microsphere touching the glass substrate according to the Faxen (1923) theory, or with gap $z \approx 17$ nm based on the Goldman *et al.* (1967) theory.

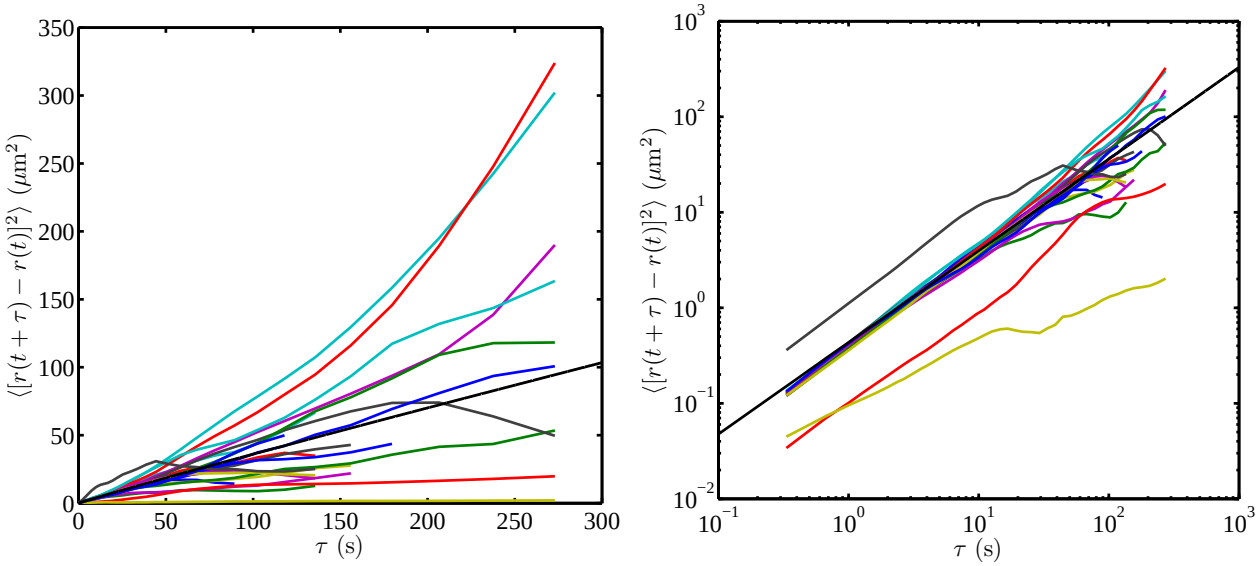

(a) Bare silica microsphere on glass in RO water.

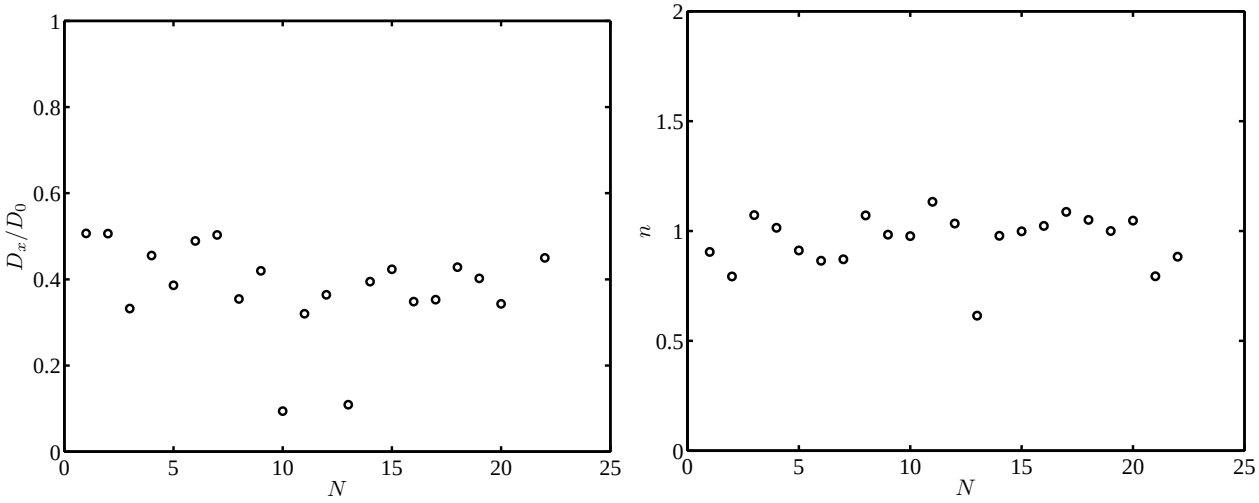

(b) Diffusion coefficient and time-lag exponent from the time-series in (a).

Figure 4.5.2: Mean-squared displacements (panel a) and diffusion coefficient and time-lag exponents versus particle number N (panel b) of bare silica microspheres on glass, acquired from video particle tracking. Each curve in (a) corresponds to one particle. Right panel (a) is the logarithmic representation of the MSD from which the linear growth of the MSD versus time lag at short τ is clear. The black line in panel (a) indicates the ensemble-averaged MSD fit to Eqn. 4.1, furnishing the ensemble-averaged diffusion coefficient $D_x/D_0 \approx 0.43$ and $n \approx 0.96$, suggesting free Brownian diffusion close to a rigid wall with elevation $z \approx 106$ nm according to the Faxen (1923) theory, and $z \approx 76$ nm according to the Goldman *et al.* (1967) theory. The individual particle Brownian diffusion coefficient and time-lag exponent, from fitting each MSD in panel (a) to Eqn. 4.1, furnishes an average diffusion coefficient $D_x/D_0 \approx 0.41 \pm 0.06$ with standard error $0.06/\sqrt{N_t} \approx 0.01$, excluding the outliers ($D_x/D_0 < 0.2$ or $D_x/D_0 > 0.6$), and average exponent $n \approx 1.0 \pm 0.1$. Note that $D_0 \approx 0.25$ μm^2 s^{-1} is the unbound microsphere diffusion coefficient in water at $T = 296$ K.

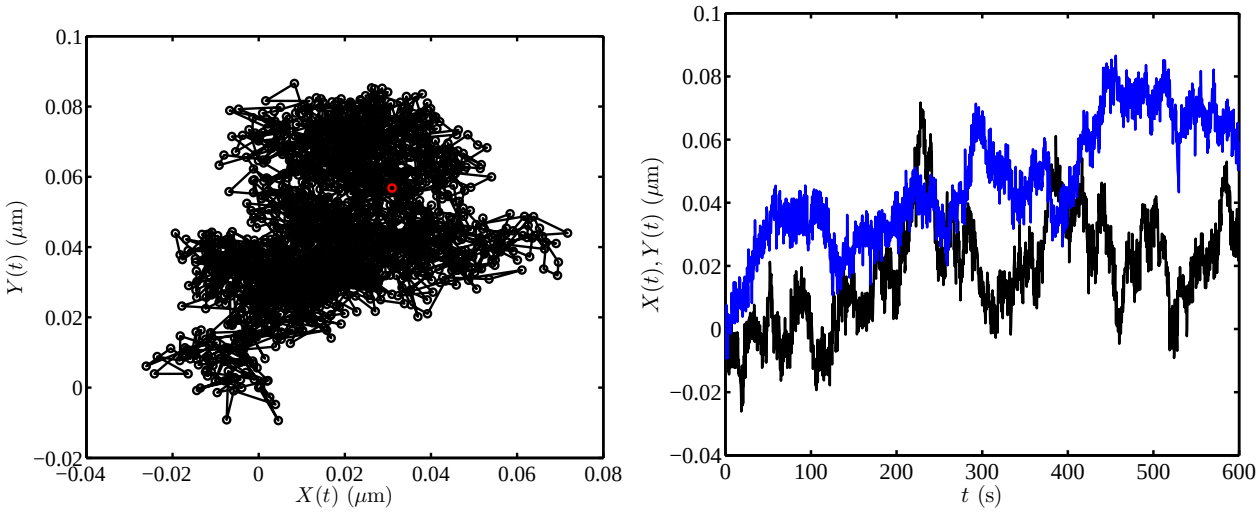

Figure 4.5.3: Immobilized silica microsphere position fluctuations acquired from video particle tracking: (left panel) Y-position versus X-position with the initial position (X,Y)=(0,0) and the last position indicated with red symbol. (right panel) X- (black color) and Y- (blue color) position time-series. Note that the particles are firmly adhered to glass in physiological ionic strength. The particle is localized to an approximately 80×80 nm^2 area. Particle position drift in both directions is observed in the right panel, which is responsible for high-time lag MSD increase.

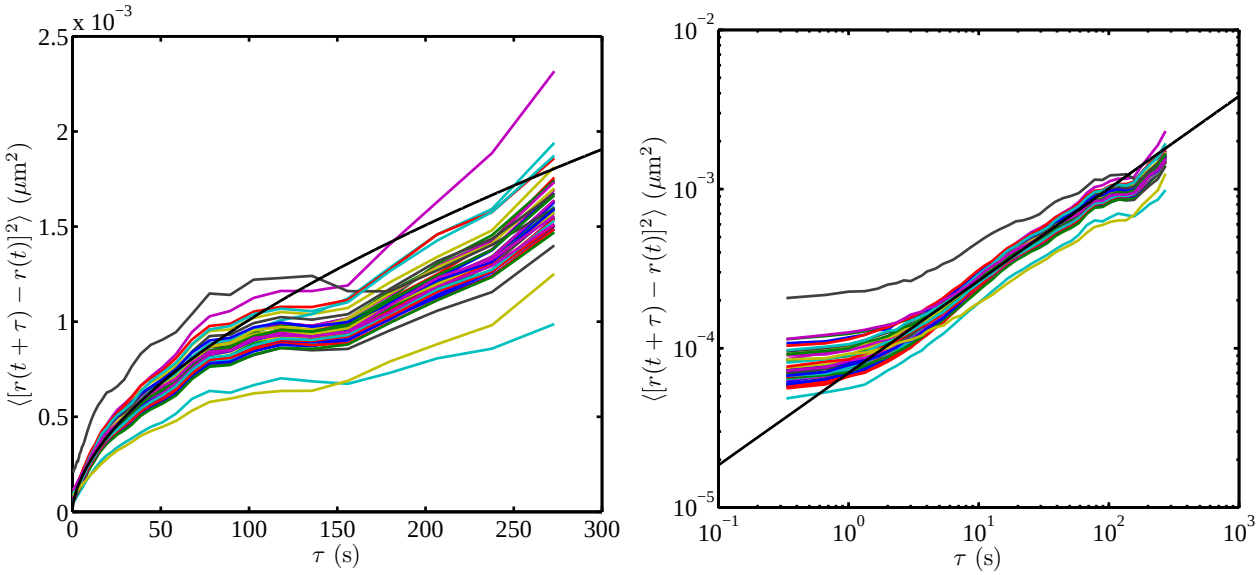

(a) Bare silica microspheres immobilized on glass in physiological ionic strength.

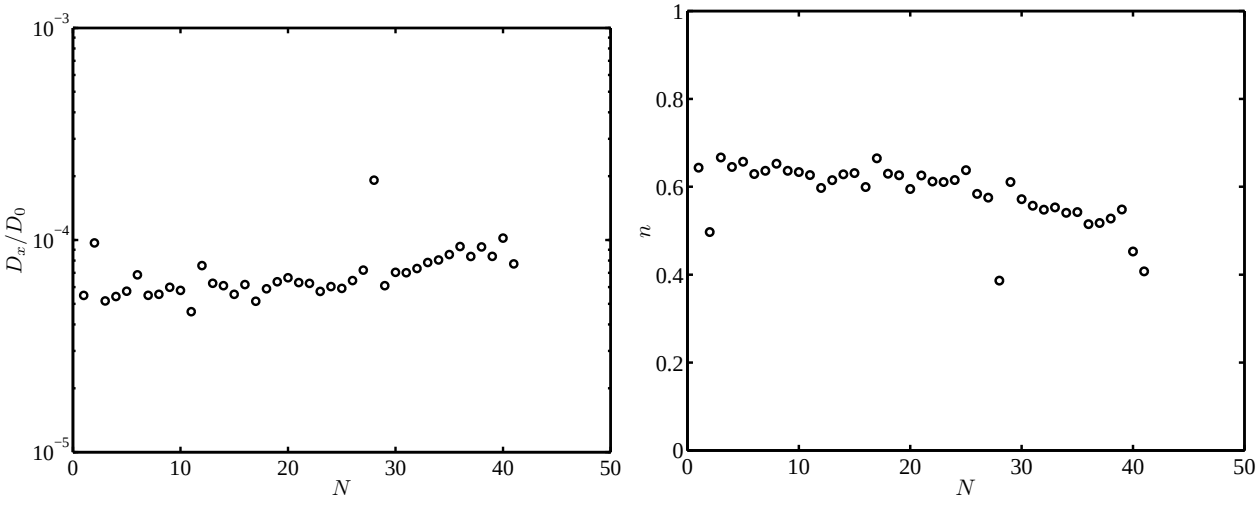

(b) Diffusion coefficient and time-lag exponent from the time-series in (a).

Figure 4.5.4: Mean-squared displacements (panel a) and diffusion coefficient and time-lag exponent versus particle number N (panel b) of immobilized bare silica microspheres on glass in physiological ionic strength, acquired from video particle tracking. Each curve in (a) corresponds to one particle, and right panel (a) is the logarithmic representation of the MSD. MSD plateau ≈ 100 nm^2 at intermediate time lags $60 \lesssim \tau \lesssim 150$ s indicates the spatial resolution, which is followed by the thermal and mechanical drift of the stage when $\tau \gtrsim 150$ s. The black line in (a) indicates the ensemble-averaged MSD fit to Eqn. 4.1 up to $\tau \approx 19.3$ s, furnishing the ensemble-averaged diffusion coefficient $D_x/D_0 \approx 7 \times 10^{-5}$ and $n \approx 0.58$, suggesting particle confinement to a region with area ≈ 1000 nm^2, indicating the highest possible accuracy in MSD measurements.

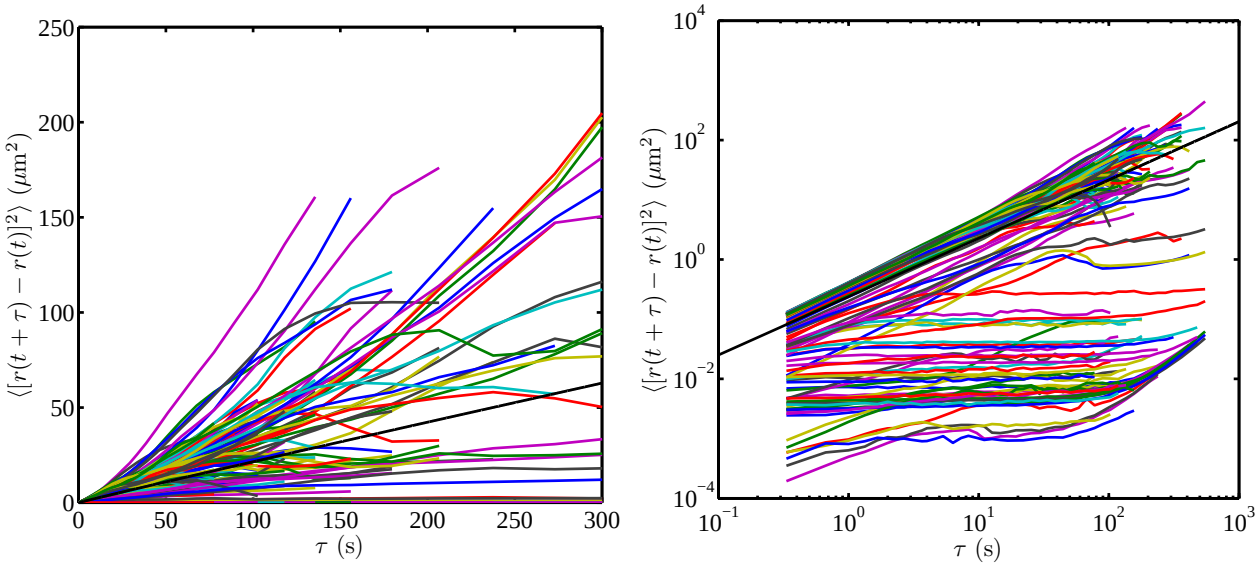

(a) Bare silica microspheres on glass in 0.5 mmol l^{-1} HEPES buffer.

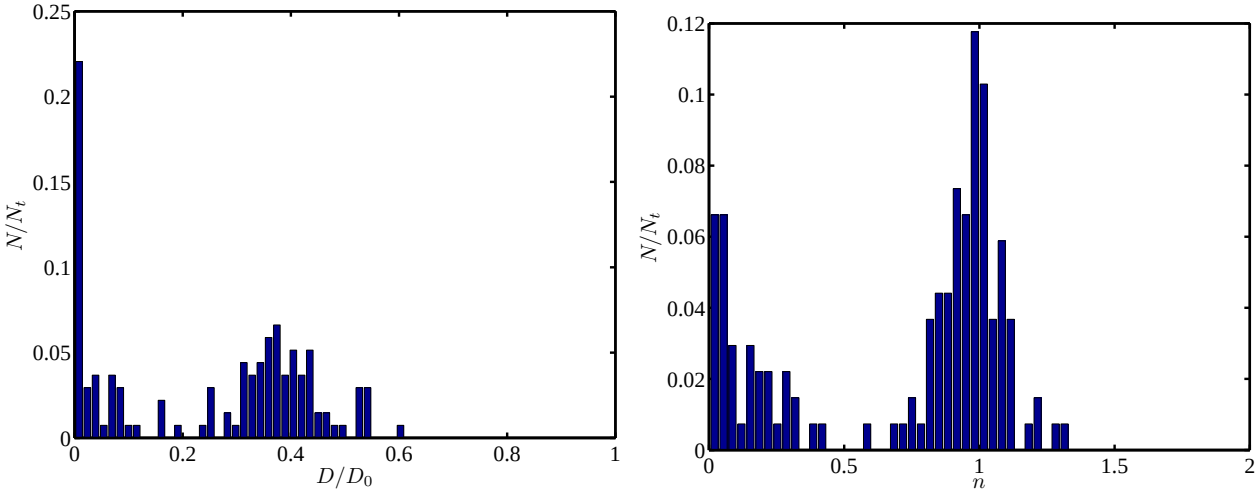

(b) Diffusion coefficient and time-lag exponent distribution from the time-series in (a).

Figure 4.5.5: Mean-squared displacements (panel a) and diffusion coefficient and time-lag exponent distribution versus normalized particle number N/N_t (panel b) of bare silica microspheres on glass, acquired from video particle tracking. Each curve in (a) corresponds to one particle, and right panel (a) is the logarithmic representation of the MSD. The black line in (a) indicates the ensemble-averaged MSD fit to Eqn. 4.1 up to $\tau \approx 22$ s, furnishing the ensemble-averaged diffusion coefficient $D_x/D_0 \approx 0.24$ and $n \approx 0.98$. The bimodal distribution of D_x/D_0 and n suggests that the particle-substrate interactions remain negligible (for ≈ 65 % of the microspheres with $D_x/D_0 \approx 0.39 \pm 0.08$) or hinder the diffusion significantly ($D_x/D_0 \approx 0.037 \pm 0.048$).

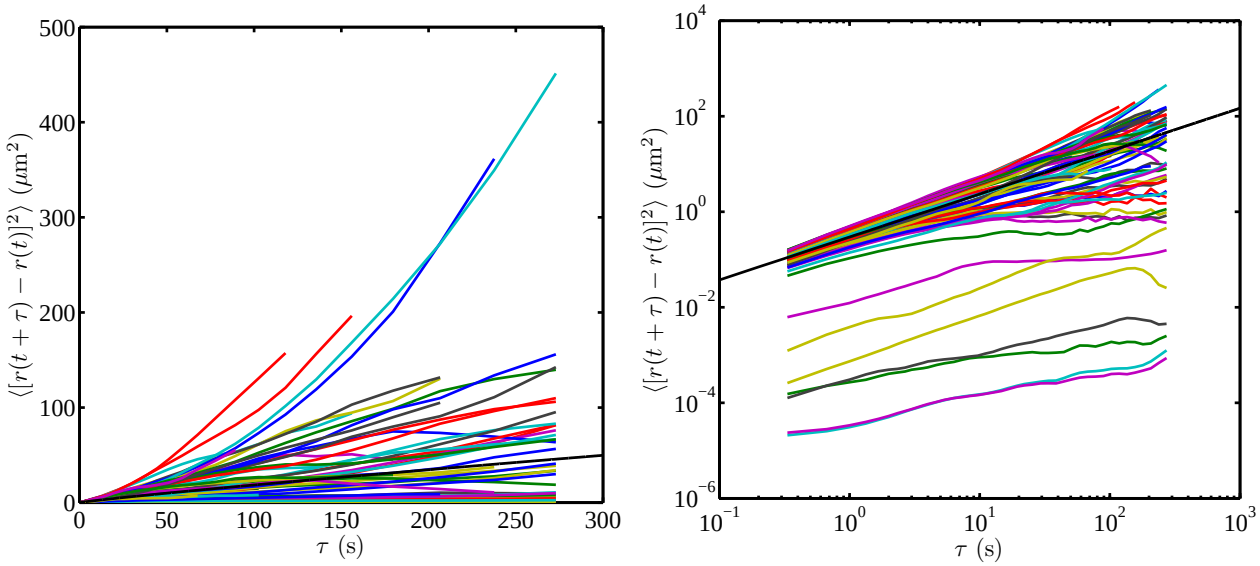

(a) Bare silica microspheres on agarose (0.33 % w/v) in RO water.

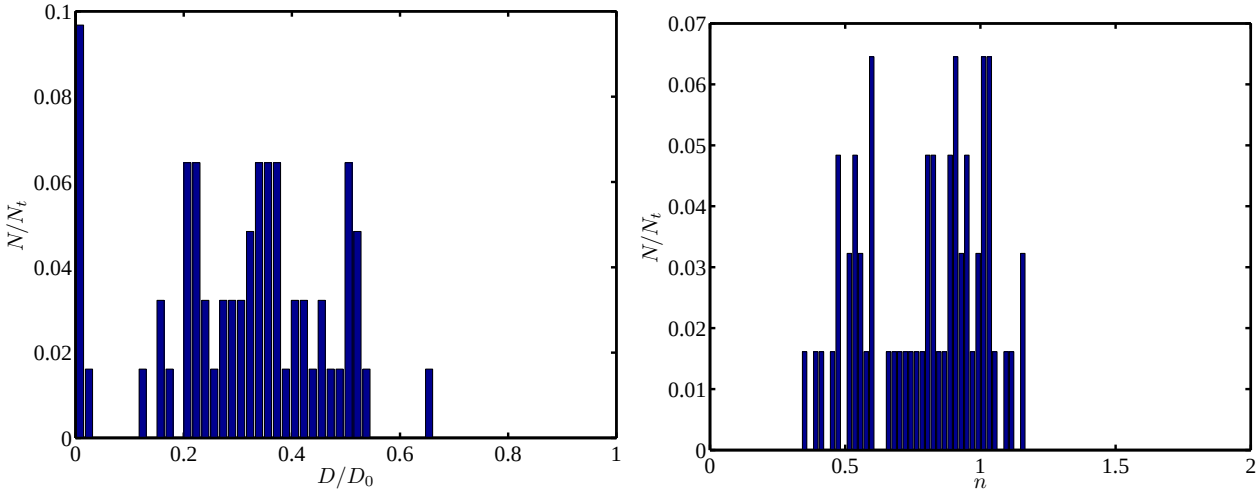

(b) Diffusion coefficient and time-lag exponent distribution from the time-series in (a).

Figure 4.5.6: Mean-squared displacements (panel a) and diffusion coefficient and time-lag exponent distribution versus normalized particle number N/N_t (panel b) of bare silica microspheres on agarose hydrogel, acquired from video particle tracking. Each curve in (a) corresponds to one particle, and right panel (a) is the logarithmic representation of the MSD. The black line in (a) indicates the ensemble-averaged MSD fit to Eqn. 4.1 up to $\tau \approx 19.3$ s, furnishing the ensemble-averaged diffusion coefficient $D_x/D_0 \approx 0.3$ and $n \approx 0.9$. The wide distribution of D_x/D_0 ($\approx 0.31 \pm 0.16$) and n ($\approx 0.79 \pm 0.22$) suggests that the particle-substrate interaction potential is evenly distributed, which may be due to the evenly-distributed charge patches (with various charge densities) on the gel.

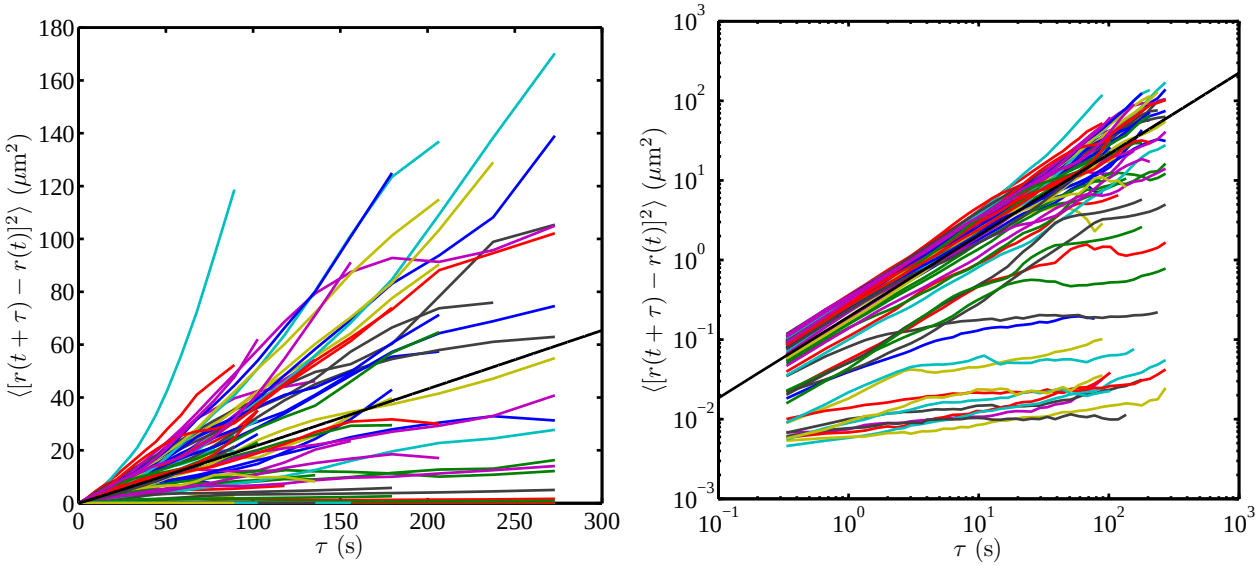

(a) DOPC-coated silica microspheres on glass in RO water.

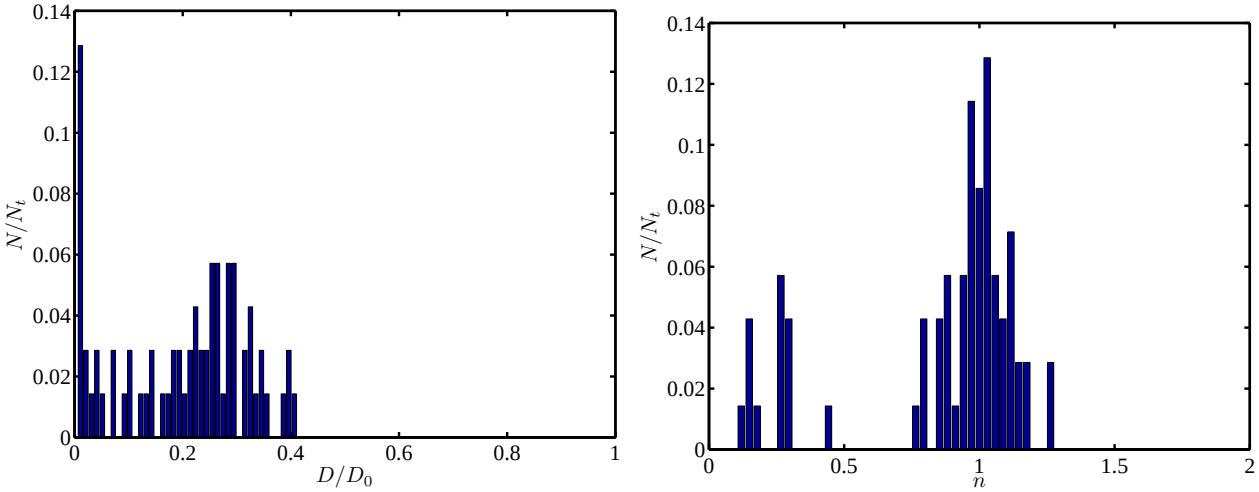

(b) Diffusion coefficient and time-lag exponent distribution from the time-series in (a).

Figure 4.5.7: Mean-squared displacements (panel a) and diffusion coefficient and time-lag exponent distribution versus normalized particle number N/N_t (panel b) of DOPC-coated silica microspheres on glass, acquired from video particle tracking. Each curve in (a) corresponds to one particle, and right panel (a) is the logarithmic representation of the MSD. The black line in (a) indicates the ensemble-averaged MSD fit to Eqn. 4.1 up to $\tau \approx 19.33$ s, furnishing the ensemble-averaged diffusion coefficient $D_x/D_0 \approx 0.19$ and $n \approx 1.02$. The bimodal distribution of D_x/D_0 and distribution of $n \approx 1$ suggest that although the particle-substrate interaction is stronger than a bare silica microsphere (mainly due to the reduced electrostatic repulsion), the diffusion remains Brownian. The diffusion coefficient and time-lag exponent from individual particles $D_x/D_0 \approx 0.2 \pm 0.1$ and $n \approx 0.9 \pm 0.3$, respectively. The average n when $n > 0.5$ represents the majority of the particles: $n \approx 1.0 \pm 0.1$, showing a normal diffusion.

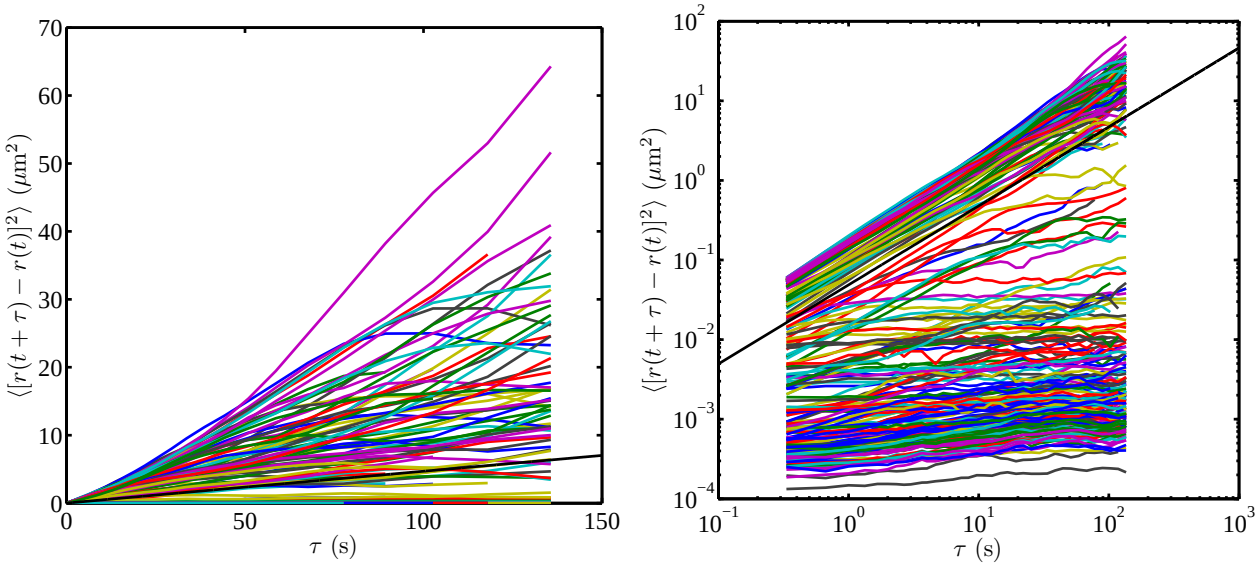

(a) DOPC-coated silica microspheres on glass in 0.5 mmol l^{-1} HEPES buffer.

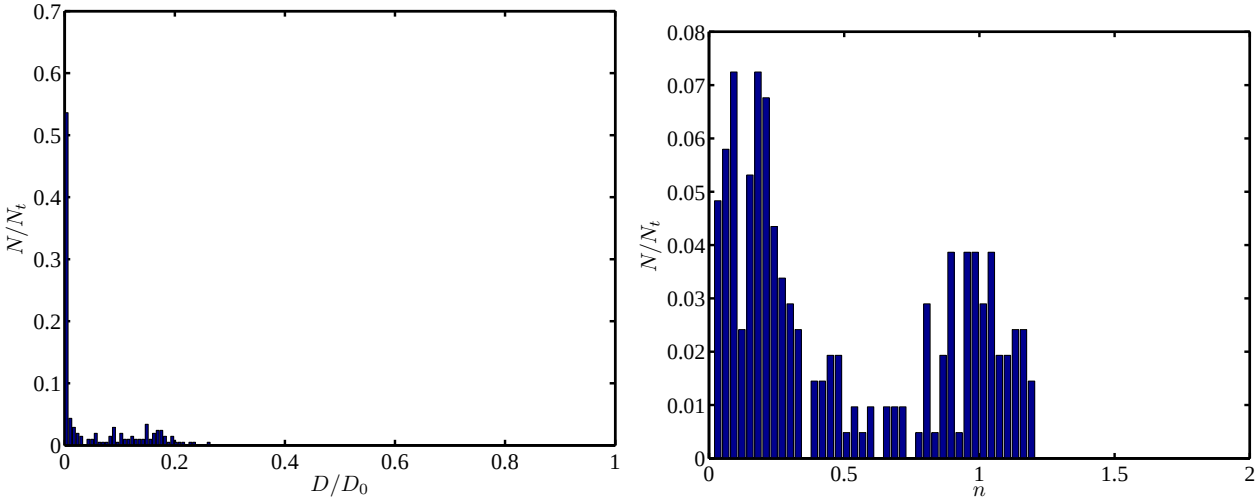

(b) Diffusion coefficient and time-lag exponent distribution from the time-series in (a).

Figure 4.5.8: Mean-squared displacements (panel a) and diffusion coefficient and time-lag exponent distribution versus normalized particle number N/N_t (panel b) of DOPC-coated silica microspheres on glass, acquired from video particle tracking. Each curve in (a) corresponds to one particle, and right panel (a) is the logarithmic representation of the MSD. The black line in (a) indicates the ensemble-averaged MSD fit to Eqn. 4.1 up to $\tau \approx 19.3$ s, furnishing the ensemble-averaged diffusion coefficient $D_x/D_0 \approx 0.05$ and $n \approx 0.99$. The bimodal distribution of D_x/D_0 is strongly weighted by the slow particles ($D_x/D_0 \lesssim 0.003$), and the bimodal distribution of n suggests that the particle-substrate interaction is stronger than in RO water due to the attenuated electrostatic repulsion. The diffusion coefficient and time-lag exponent from individual particles $D_x/D_0 \approx 0.05 \pm 0.07$ and $n \approx 0.5 \pm 0.4$, respectively. Note that some of the slowly-diffusing particles have MSDs comparable to the system noise level.

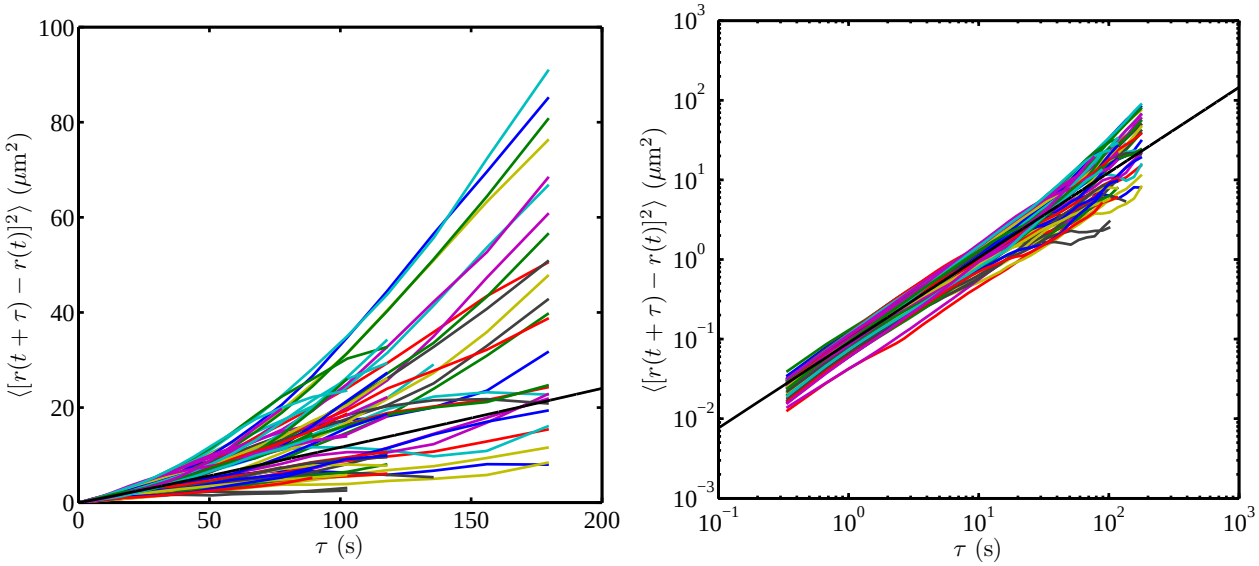

(a) DOPC-coated silica microspheres on DOPC-coated glass in RO water.

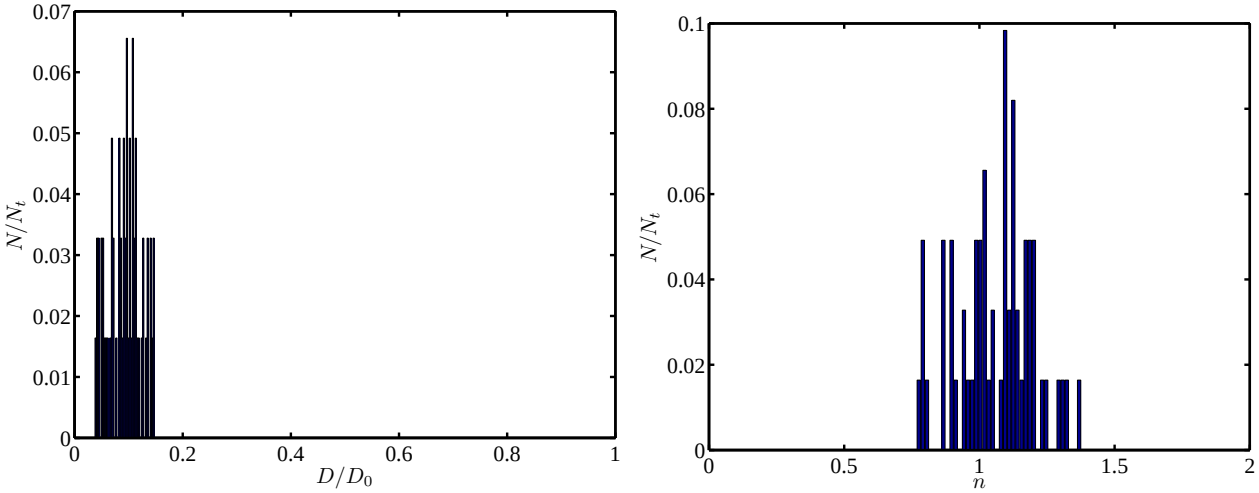

(b) Diffusion coefficient and time-lag exponent distribution from the time-series in (a).

Figure 4.5.9: Mean-squared displacements (panel a) and diffusion coefficient and time-lag exponent distribution versus normalized particle number N/N_t (panel b) of DOPC-coated silica microspheres on DOPC-coated glass, acquired from video particle tracking. Each curve in (a) corresponds to one particle, and right panel (a) is the logarithmic representation of the MSD. The black line in (a) indicates the ensemble-averaged MSD fit to Eqn. 4.1 up to $\tau \approx 12.7$ s, furnishing the ensemble-averaged diffusion coefficient $D_x/D_0 \approx 0.09$ and $n \approx 1.05$. The diffusion coefficient and time-lag exponent from individual particles $D_x/D_0 \approx 0.10 \pm 0.02$ and $n \approx 1.0 \pm 0.1$, respectively. The diffusion coefficient is lower than the DOPC-coated particles on glass.

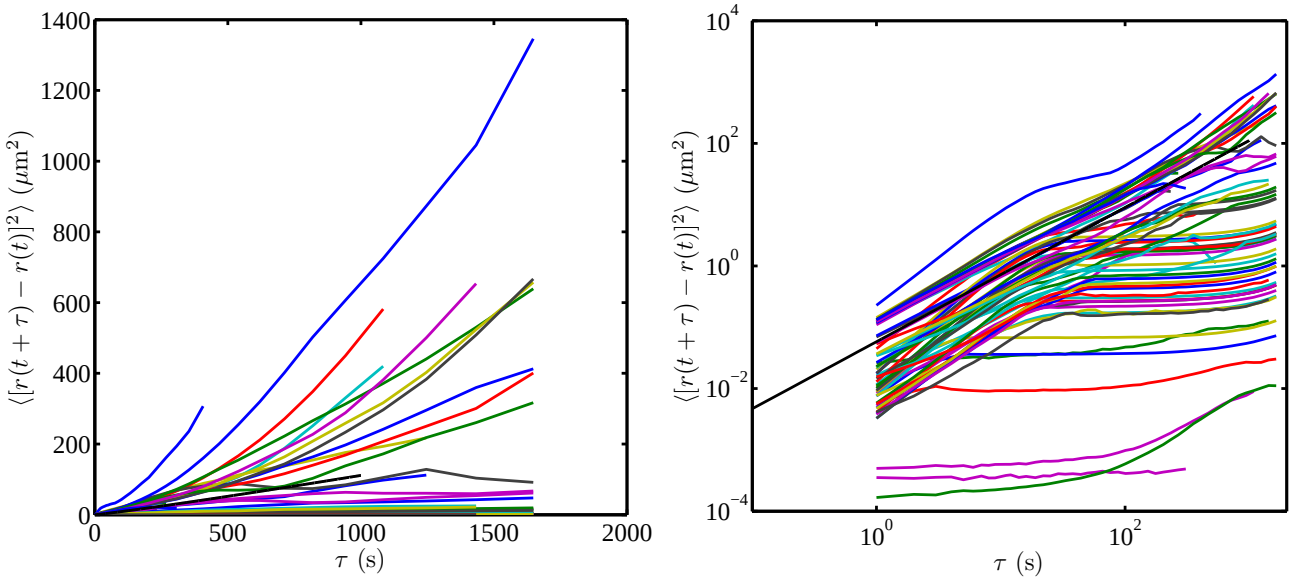

(a) DOPC-coated silica microspheres on DSPE (5 mol %)-coated glass in RO water.

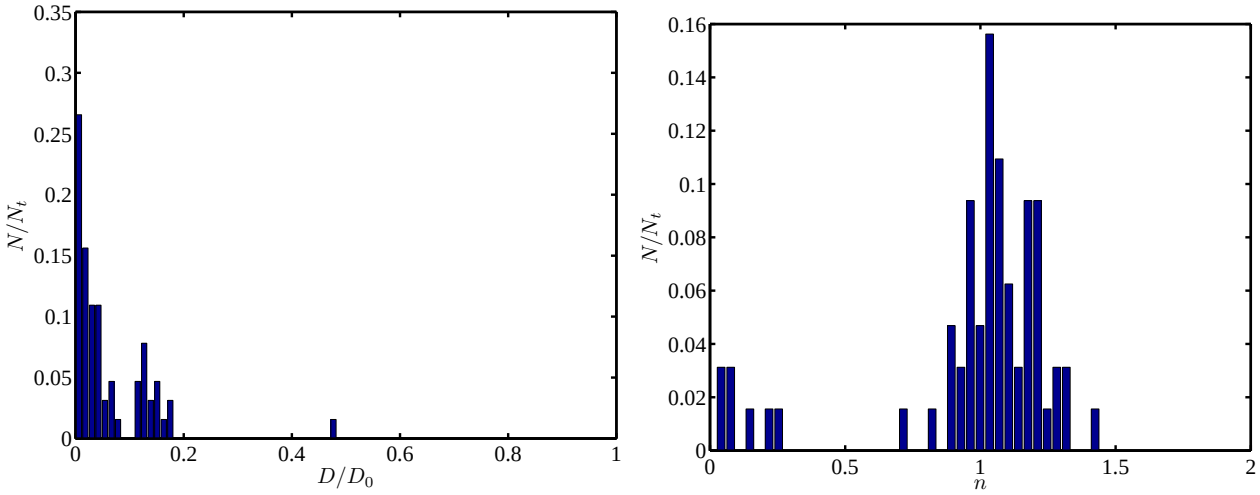

(b) Diffusion coefficient and time-lag exponent distribution from the time-series in (a).

Figure 4.5.10: Mean-squared displacements (panel a) and diffusion coefficient and time-lag exponent distribution versus normalized particle number N/N_t (panel b) of DOPC-coated silica microspheres on DSPE (5 %)-coated glass, acquired from video particle tracking. Each curve in (a) corresponds to one particle, and right panel (a) is the logarithmic representation of the MSD. The black line in (a) indicates the ensemble-averaged MSD fit to Eqn. 4.1 up to $\tau \approx 22$ s (to prevent long-time plateau), furnishing the ensemble-averaged diffusion coefficient $D_x/D_0 \approx 0.06$ and $n \approx 1.09$. The diffusion coefficient and time-lag exponent from individual particles $D_x/D_0 \approx 0.06 \pm 0.08$ and $n \approx 0.98 \pm 0.33$, respectively. The diffusion coefficient is lower than DOPC-coated particles on glass.

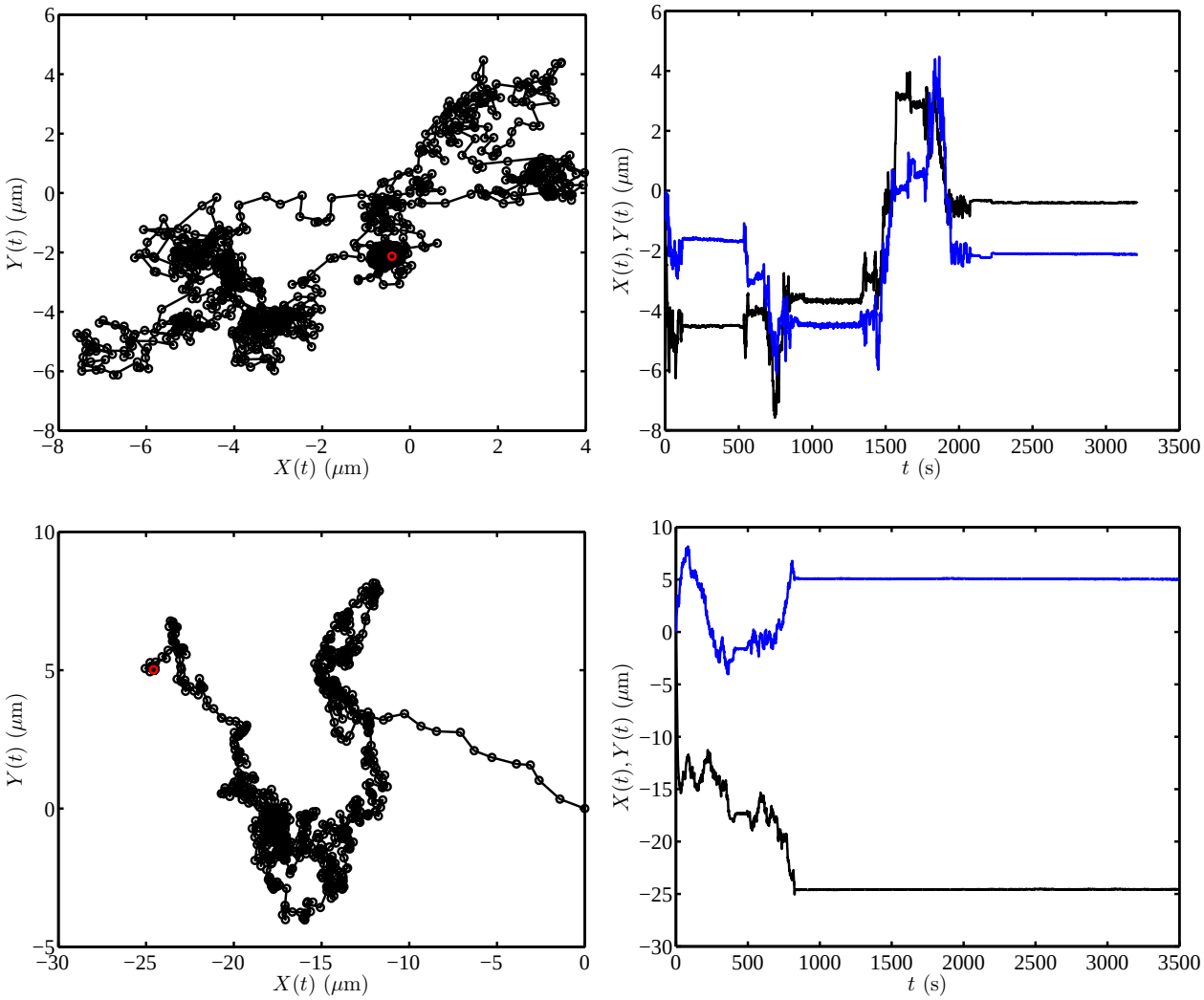

Figure 4.5.11: Stick-slip dynamics of two DOPC-coated silica microspheres diffusing on DSPE (5 mol %)-coated glass in RO water. (left panel) Y-position versus X-position with the initial position (X,Y)=(0,0) and the last position indicated with red symbol. (right panel) X- (black color) and Y- (blue color) position time-series. While the particles adopt fast dynamics at some time intervals (slip), they become periodically localized (stick) followed by a permanent adhesion, *e.g.*, when $t \gtrsim 800$ s in the lower panel.

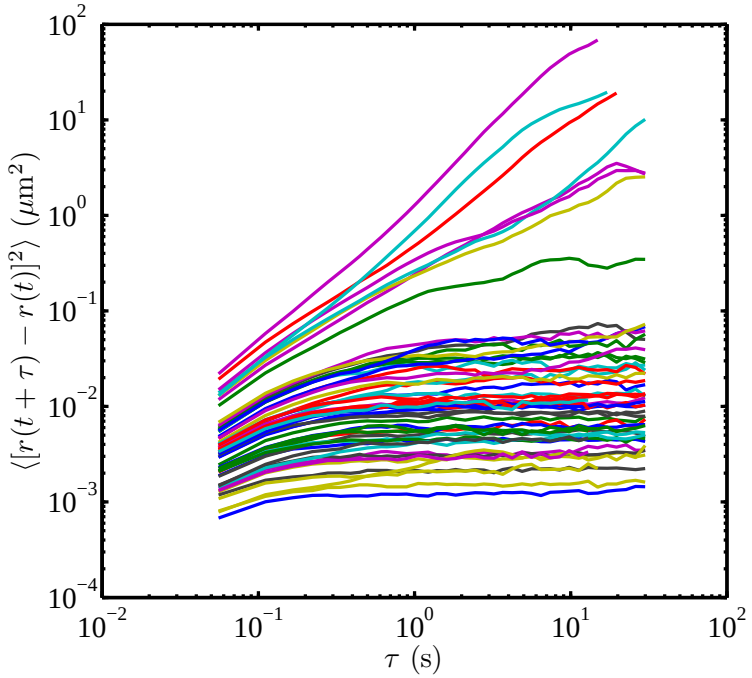

(a) DOPC-coated silica microspheres on PEG hydrogel (20 % v/v)-coated glass in RO water.

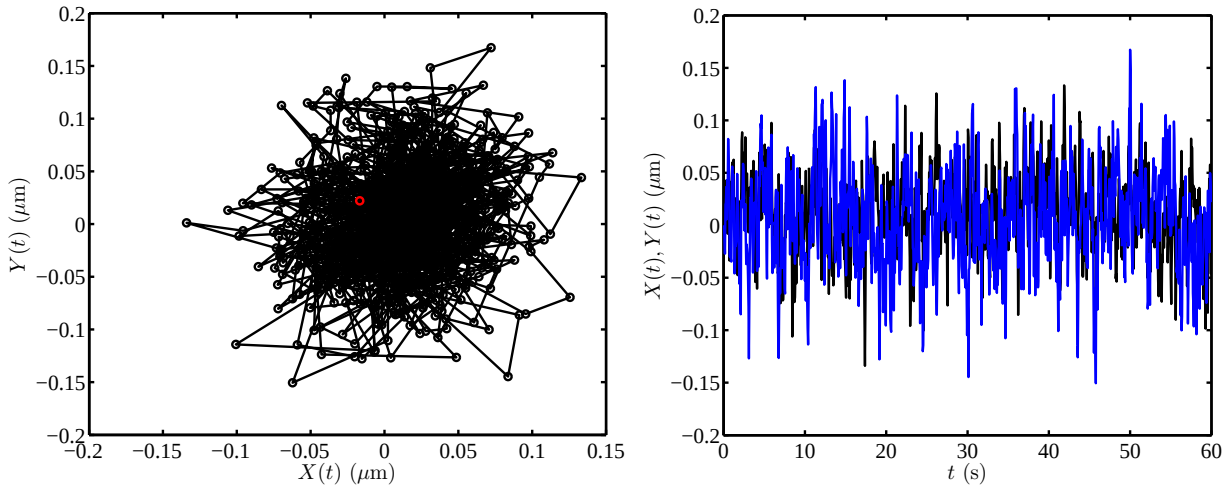

(b) An example of localized position trajectory related to (a).

Figure 4.5.12: Mean-squared displacements (panel a) and localized position trajectory (panel b) of DOPC-coated silica microspheres on PEG hydrogel (20 %)-coated glass, acquired from video particle tracking. Each curve in (a) corresponds to one particle. Although the colloidal dynamics become locally restricted within the spatial and temporal resolution of the measurements, the position fluctuations are larger than an immobilized particle on glass (compare to figure 4.5.8a). Note that the initial position in (b) is (0,0), and the last position is shown with red symbol in the left panel.

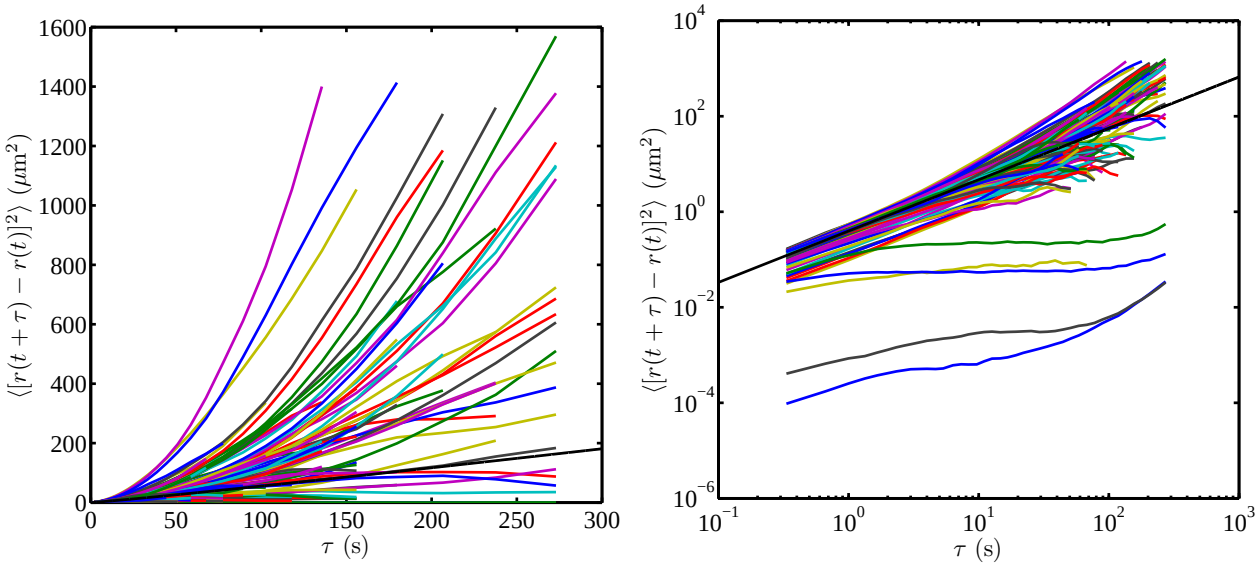

(a) DOPC-coated silica microspheres on agarose (0.33 % w/v)-coated glass in RO water.

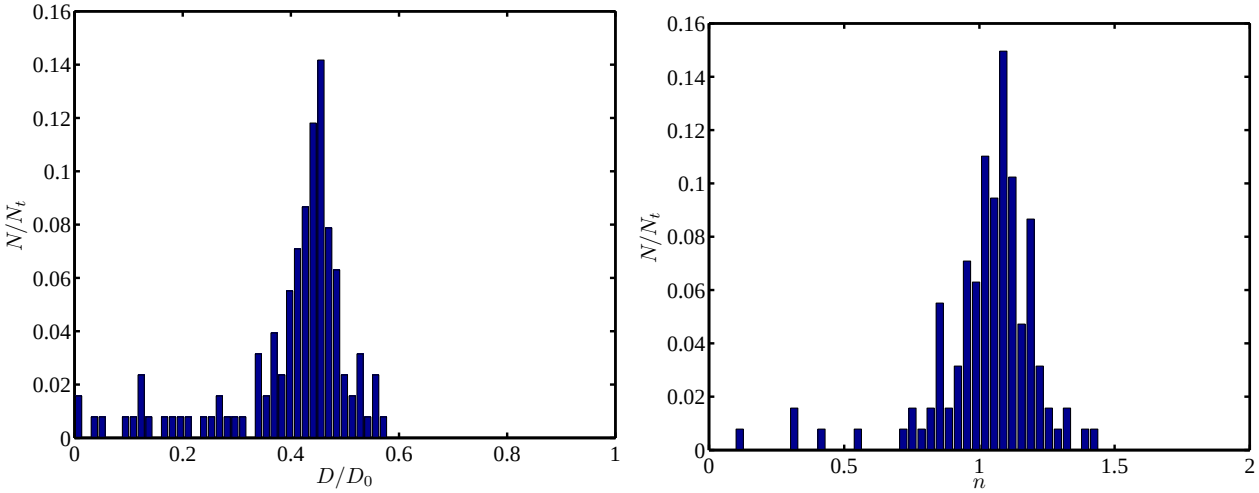

(b) Diffusion coefficient and time-lag exponent distribution from the time-series in (a).

Figure 4.5.13: Mean-squared displacements (panel a) and diffusion coefficient and time-lag exponent distribution versus normalized particle number N/N_t (panel b) of DOPC-coated silica microspheres on agarose (0.33 % w/v)-coated glass, acquired from video particle tracking. Each curve in (a) corresponds to one particle, and right panel (a) is the logarithmic representation of the MSD. The black line in (a) indicates the ensemble-averaged MSD fit to Eqn. 4.1 up to $\tau \approx 7.3$ s (to prevent long-time plateau), furnishing the ensemble-averaged diffusion coefficient $D_x/D_0 \approx 0.04$ and $n \approx 1.07$. The diffusion coefficient and time-lag exponent from individual particles $D_x/D_0 \approx 0.40 \pm 0.12$ and $n \approx 1.03 \pm 0.19$, respectively. The diffusion coefficient is similar to the diffusion on glass.

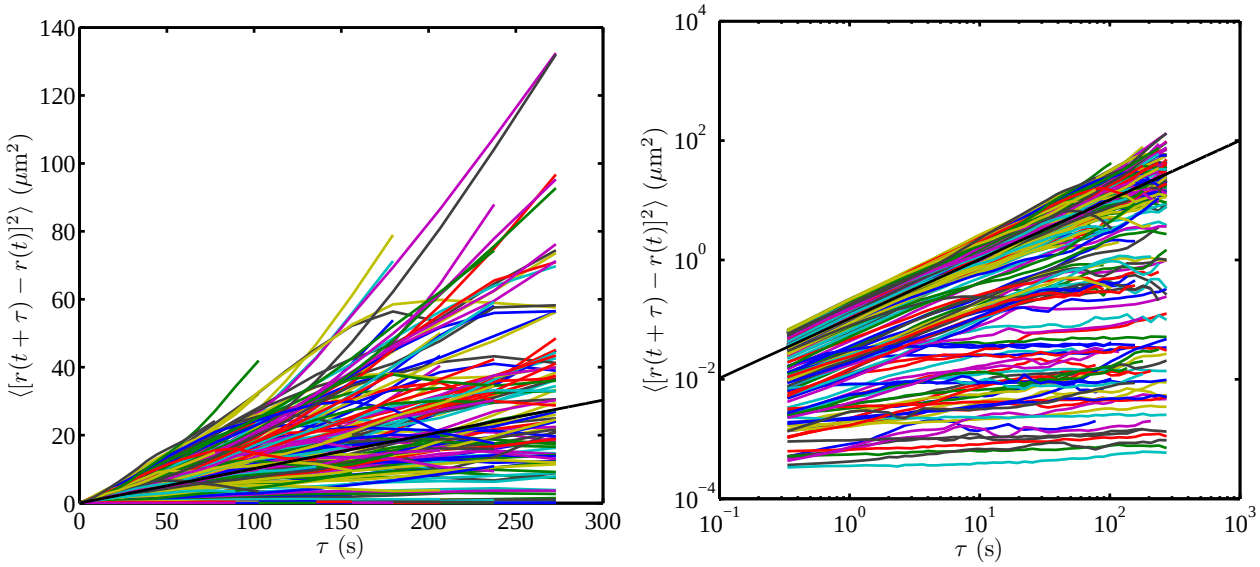

(a) DSPE (5 mol %)-coated silica microspheres on glass in RO water.

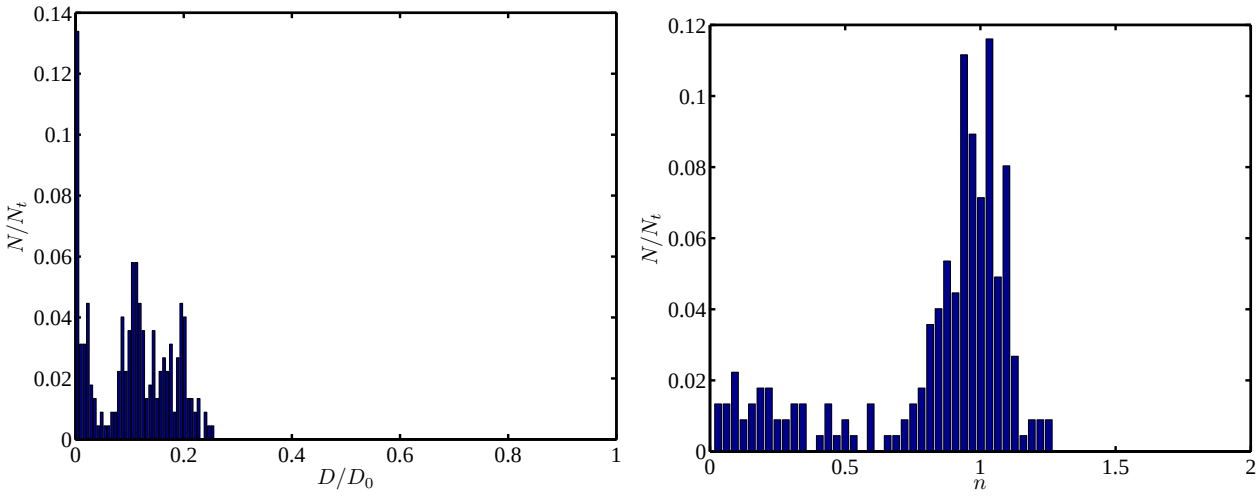

(b) Diffusion coefficient and time-lag exponent distribution from the time-series in (a).

Figure 4.5.14: Mean-squared displacements (panel a) and diffusion coefficient and time-lag exponent distribution versus normalized particle number N/N_t (panel b) of DSPE (5 %)-coated silica microspheres on glass, acquired from video particle tracking. Each curve in (a) corresponds to one particle, and right panel (a) is the logarithmic representation of the MSD. The black line in (a) indicates the ensemble-averaged MSD fit to Eqn. 4.1 up to $\tau \approx 19.3$ s (to prevent long-time plateau), furnishing the ensemble-averaged diffusion coefficient $D_x/D_0 \approx 0.10$ and $n \approx 0.995$. The diffusion coefficient and time-lag exponent from individual particles $D_x/D_0 \approx 0.11 \pm 0.07$ and $n \approx 0.83 \pm 0.31$, respectively. The ensemble comprises ≈ 75 % fast-diffusing particles with $D_x/D_0 \approx 0.17 \pm 0.03$, adopting diffusion coefficients lower than the DOPC-coated particles on glass. The adsorption of PEG chains on glass may be responsible for the confined and slow dynamics of these particles.

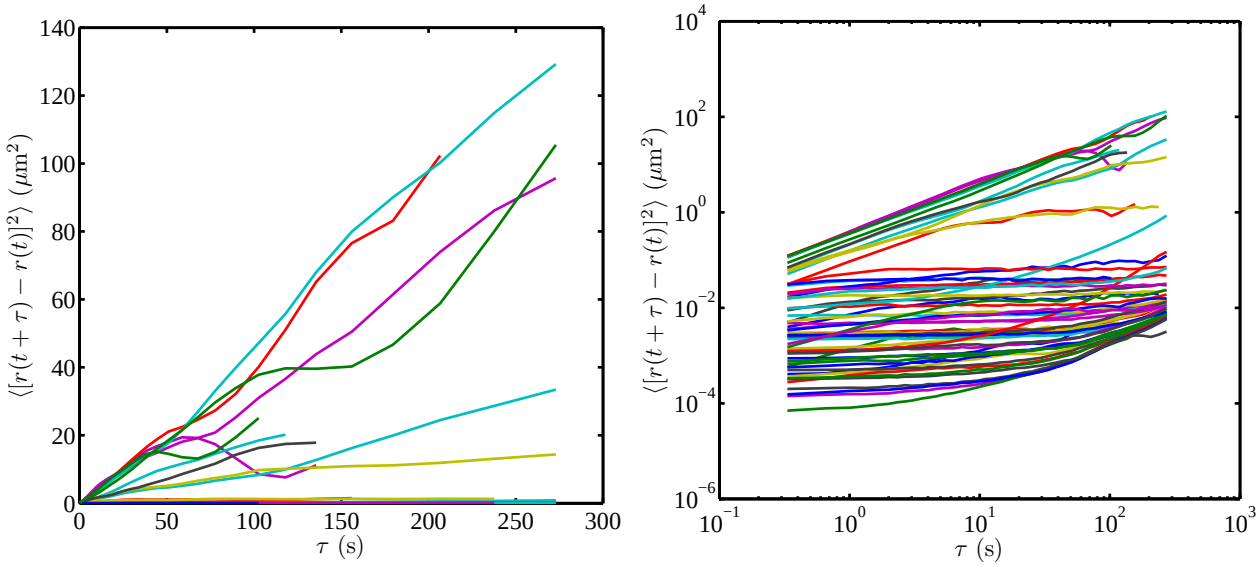

(a) DSPE (5 mol %)-coated silica microspheres on glass in 0.5 mmol l^{-1} HEPES buffer.

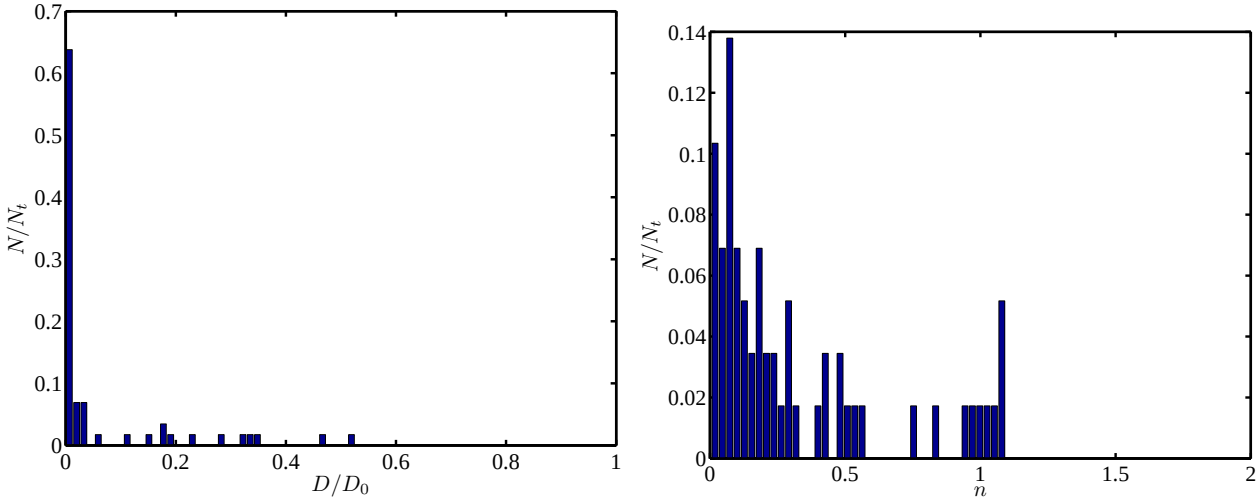

(b) Diffusion coefficient and time-lag exponent distribution from the time-series in (a).

Figure 4.5.15: Mean-squared displacements (panel a) and diffusion coefficient and time-lag exponent distribution versus normalized particle number N/N_t (panel b) of DSPE (5 %)-coated silica microspheres on glass, acquired from video particle tracking. Each curve in (a) corresponds to one particle, and right panel (a) is the logarithmic representation of the MSD. The The diffusion coefficient and time-lag exponent from individual particles $D_x/D_0 \approx 0.06 \pm 0.12$ and $n \approx 0.32 \pm 0.34$, respectively. The ensemble comprises ≈ 70 % slow-diffusing particles with $D_x/D_0 \lesssim 0.03$, adopting diffusion coefficients lower than in RO water due to the screened diffuse layer. The adsorption of PEG chains on glass may facilitate the particle deposition, as compared to a bare silica microsphere (figure 4.5.5).

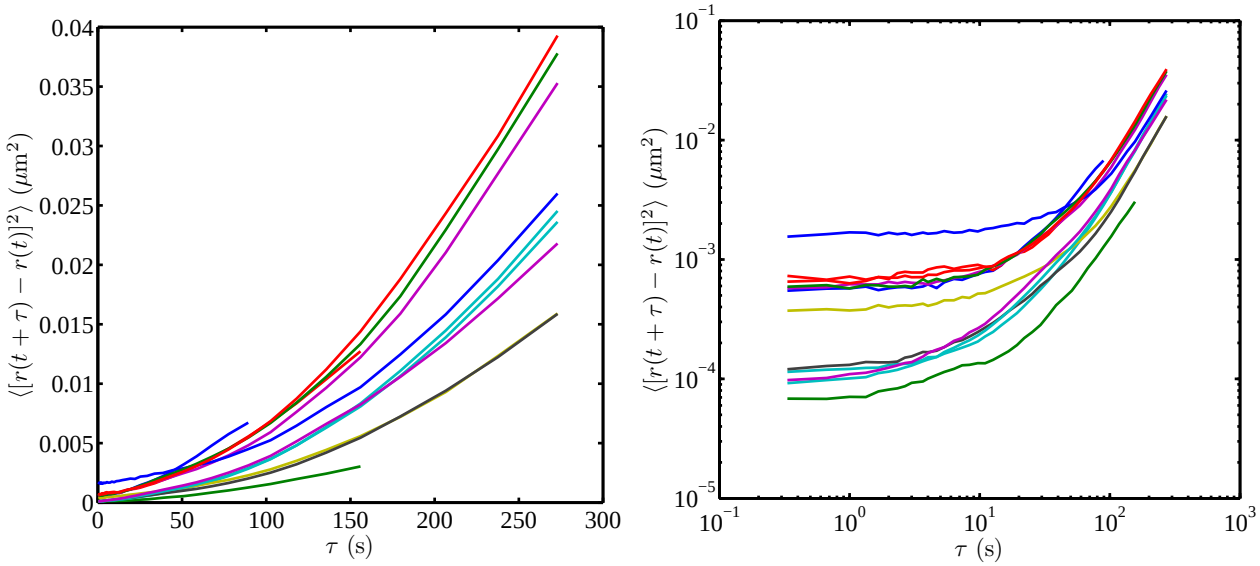

(a) DSPE (5 mol %)-coated silica microspheres on PEG (20 % v/v)-coated glass in RO water.

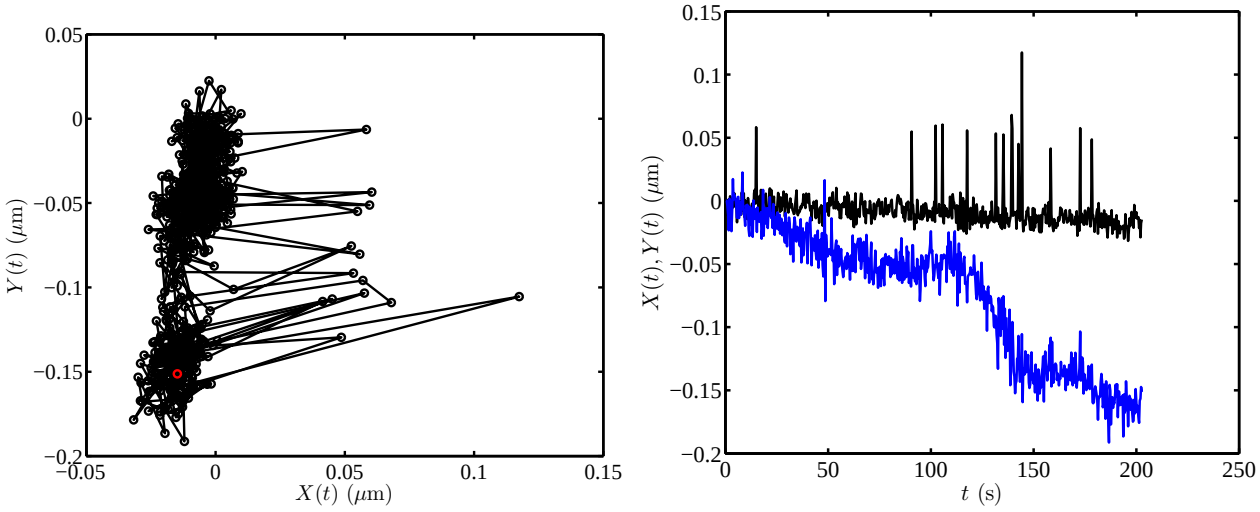

(b) An example of localized position trajectory related to (a).

Figure 4.5.16: Mean-squared displacements (panel a) and an example of localized position trajectory (panel b) of DSPE (5 %)-coated silica microspheres on PEG (20 % v/v)-coated glass, acquired from video particle tracking. Each curve in (a) corresponds to one particle, and right panel (a) is the logarithmic representation of the MSD. The long-time MSD increase is due to the mechanical and thermal drift of stage. PEG hydrogel is able to restrict the DSPE-coated silica microsphere dynamics to a very small region, comparable to the particle tracking noise level. The PEG ability of particle adsorption can have advanced applications such as high-yield drug carrier separation platforms.

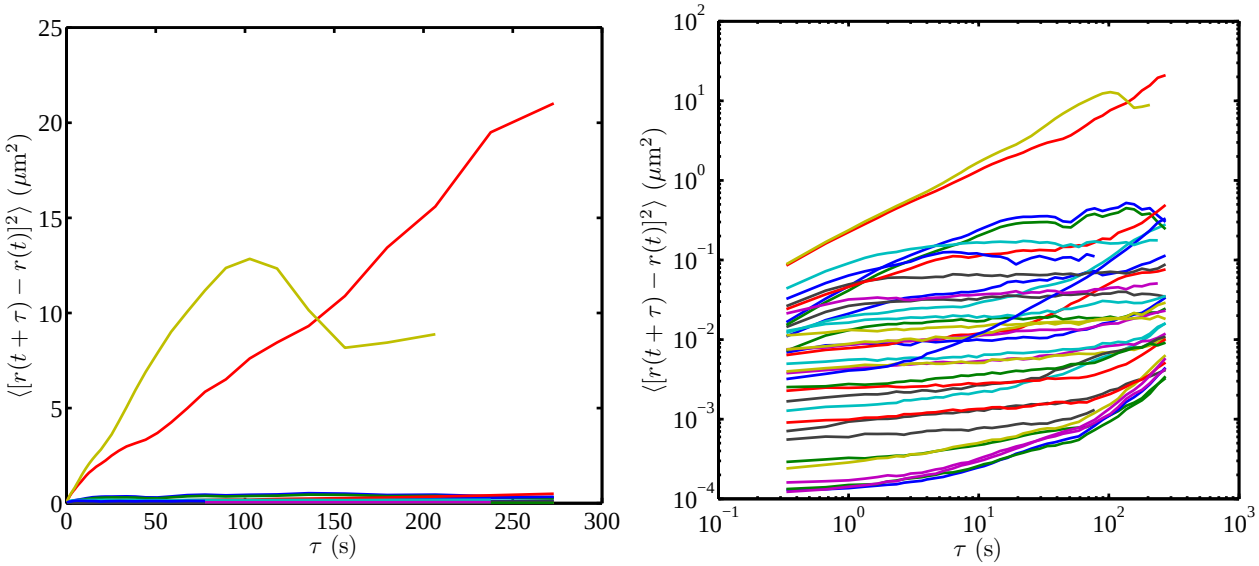

(a) DSPE (2.5 mol %)-coated silica microspheres on agarose (0.33 % w/v)-coated glass in RO water.

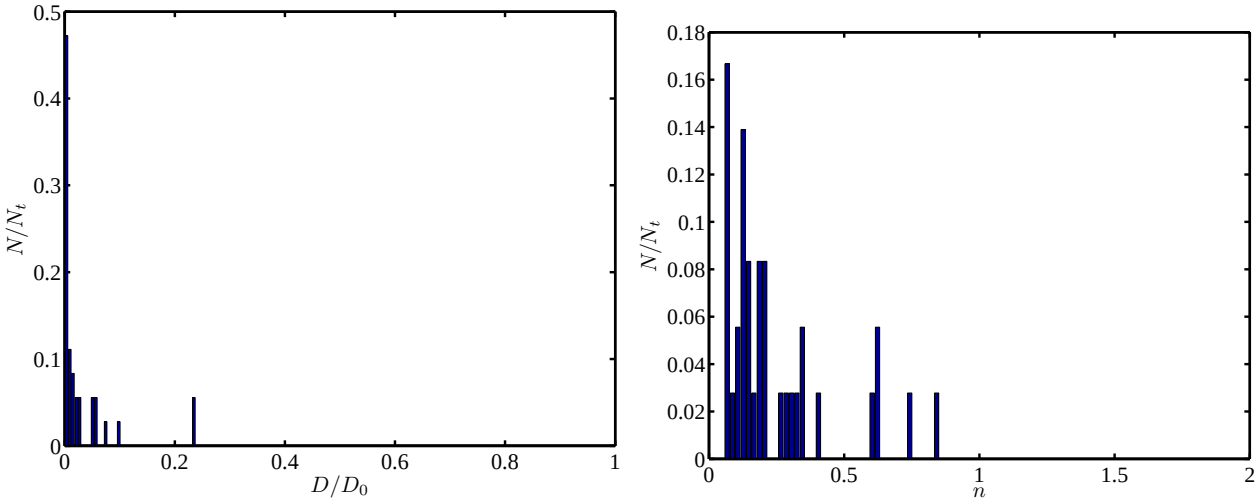

(b) Diffusion coefficient and time-lag exponent distribution from the time-series in (a).

Figure 4.5.17: Mean-squared displacements (panel a) and diffusion coefficient and time-lag exponent distribution versus normalized particle number N/N_t (panel b) of DSPE (2.5 %)-coated silica microspheres on agarose (0.33 % w/v)-coated glass, acquired from video particle tracking. Each curve in (a) corresponds to one particle, and right panel (a) is the logarithmic representation of the MSD. The ensemble comprises $\approx$ 95 % slow-diffusing particles with $D_x/D_0 \lesssim 0.1$, adopting diffusion coefficients lower than on glass due to the PEG-agarose interactions. Both PEG conjugates and agarose gel are negatively charged, suggesting that the grafted polymer entanglement with agarose structure may be the main reason of the attenuated dynamics.

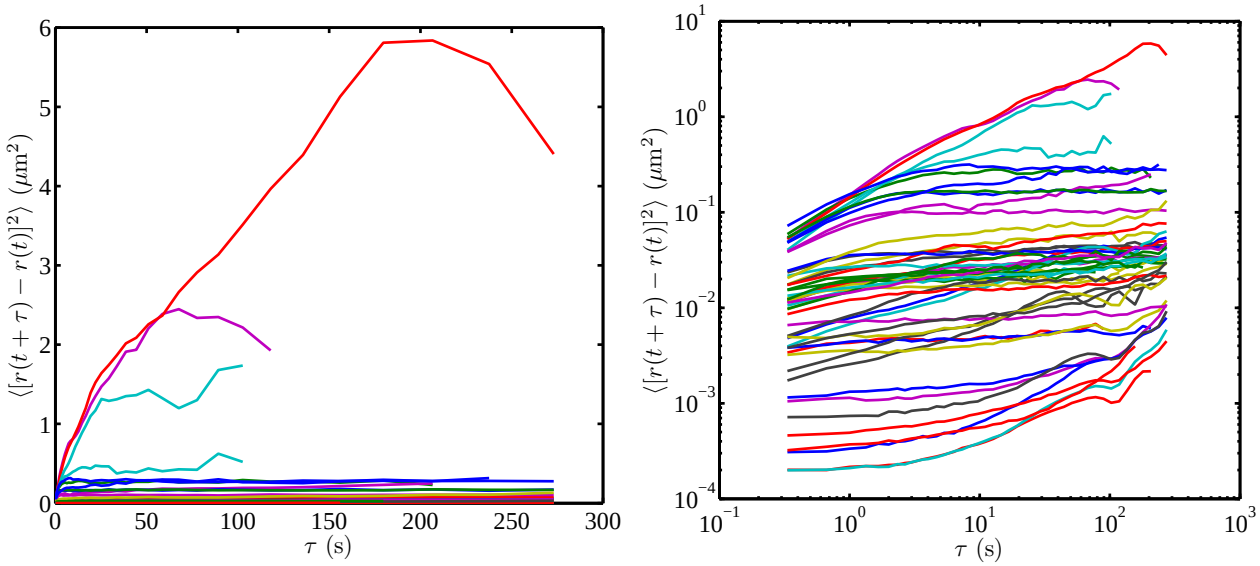

(a) DSPE (9.2 mol %)-coated silica microspheres on agarose (0.33 % w/v)-coated glass in physiological ionic strength.

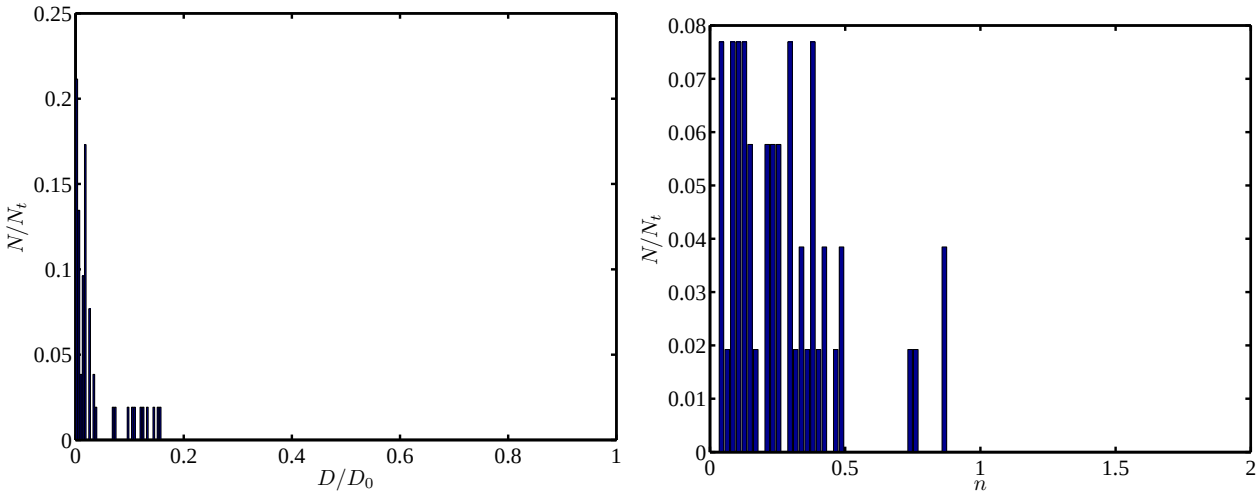

(b) Diffusion coefficient and time-lag exponent distribution from the time-series in (a).

Figure 4.5.18: Mean-squared displacements (panel a) and diffusion coefficient and time-lag exponent distribution versus normalized particle number N/N_t (panel b) of DSPE (9.2 %)-coated silica microspheres on agarose (0.33 % w/v)-coated glass, acquired from video particle tracking. Each curve in (a) corresponds to one particle, and right panel (a) is the logarithmic representation of the MSD. The ensemble comprises $\approx$ 85 % slow-diffusing particles with $D_x/D_0 \lesssim 0.1$, adopting diffusion coefficients comparable to DSPE (5 %)-agarose in RO water.

Table 4.1: Silica microsphere diffusion on soft interfaces.

Particle coating	Cover glass coating	Medium	D_x/D_0	$\sigma^{\mathrm{i}}_{D_x/D_0}$	n	σ_n	N_t
Bare	Bare	RO	0.41	0.06	0.96	0.12	20
Bare	Bare	HEPES[ii]	0.25	0.19	0.72	0.4	135
Bare	Agarose[iii]	RO	0.31	0.16	0.79	0.22	60
DOPC	Bare	RO	0.2	0.12	0.86	0.32	70
DOPC	Bare	HEPES[ii]	0.05	0.07	0.50	0.39	200
DOPC	DOPC	RO	0.10	0.02	1.04	0.10	60
DOPC	DSPE[iv]	RO	0.06	0.08	0.98	0.33	60
DOPC	PEG[v]	RO	0.04	0.08	0.38	0.22	44
DOPC	Agarose[iii]	RO	0.40	0.12	1.04	0.19	127
DSPE[iv]	Bare	RO	0.11	0.07	0.83	0.31	224
DSPE[iv]	Bare	HEPES[ii]	0.06	0.12	0.32	0.34	58
DSPE[vi]	Agarose[iii]	RO	0.03	0.06	0.24	0.20	36
DSPE[vii]	Agarose[iii]	Phys.[viii]	0.03	0.05	0.27	0.20	52
[ix]Bare	Bare	Phys.[viii]	7.0×10^{-5}	2.4×10^{-5}	0.59	0.07	40

(i) σ is the standard deviation over all the particles N_t. In the literature, it is conventional to report the standard error $\sigma/\sqrt{N_t}$. Here, σ is reported to show the distribution width.
(ii) 0.5 mmol l^{-1}
(iii) 0.33 % w/v
(iv) 5 mol %
(v) 20 % v/v
(vi) 2.5 mol %
(vii) 9.2 mol %
(viii) Physiological ionic strength: 150 mmol l^{-1} NaCl and 10 mmol l^{-1} HEPES buffer.
(ix) This is the particle-tracking noise level in the physiological ionic strength.
Note that the following systems (particle coating, substrate, medium) had comparable MSDs to the noise level: (Bare or DSPE 2.5 or 9.2 %, PEG 20 or 5 %, RO or high ionic strength), and (DSPE 2.5 %, Agarose 0.33 %, high ionic strength), suggesting that PEG hydrogels attenuate the particle dynamics, and, secondly, that the dynamics on a charged hydrogel (agarose) can be tuned by changing the ionic strength.

4.6 Conclusions

Silica microspheres are employed as sensors to study the interaction between soft interfaces by coating the colloidal particles and permitting them to diffuse on the underlying substrate

with soft coatings and studying their random motion. A wide variety of soft interfaces, including lipid bilayers (mimicking cell wall), lipopolymer-doped lipid bilayers (mimicking polymer-coated drug carriers), and hydrogels (mimicking extracellular matrices and soft tissues) were chosen, and the interfacial dynamics of silica microspheres were studied using video-particle-tracking. It is shown that by systematically reducing the electrical surface potential and Hamaker constant by coating them with lipid bilayers (DOPC) or decreasing the Debye length by increasing the ionic strength, the interfacial diffusion coefficient could be decreased due to the reduced particle-substrate distance. The attractive PEG-chain interactions with DOPC lipid bilayers were evidenced by the attenuated diffusion coefficient of DSPE-coated particles diffusing on DOPC-coated glass. PEG hydrogels were found to be an excellent platform to adsorb bare, DOPC-coated, and DSPE-coated silica microspheres regardless of the medium ionic strength. To shed light on the interaction between grafted polymer chains and hydrogels, negatively-charged agarose hydrogels were employed to firstly show that they repel bare silica, then, to promote DOPC-coated silica microspheres diffusion, and finally to present their ability to specifically hinder the dynamics of DSPE-coated silica microspheres significantly upon contact: a process similar to the glass transition of many-body systems upon reaching the glass transition point. The gel experiments in this chapter encourage single-particle level studies, which will be followed in the next chapters.

Chapter 5

Passive microrheology for quantifying bare silica microsphere adhesion to polyacrylamide hydrogels

5.1 Preface

Amir Sheikhi designed, conducted, and analyzed the experiments. Reghan J. Hill contributed to the theory. This chapter provides the passive microrheology results for a bare silica microsphere at an electrolyte-polyacrylamide (PA) hydrogel interface with a specified shear modulus. Understanding the stiffness-mediated adhesion at such soft micro-interfaces is vital in many chemical, biomedical, and biological fields, such as drug delivery to soft tissues, phagocytosis, and membrane biofouling.

5.2 Abstract

The dynamics of a colloidal microsphere adhering to soft films, such as tissues, biofilms, and hydrogels have been an important question in soft-contact science. This work is motivated by colloidal-based drug delivery and a desire to better understand how colloidal

dynamics are modulated by interacting with soft interfaces. As a model system, the transverse Brownian position fluctuations of a bare silica microsphere, whether in the vicinity of a polyacrylamide (PA) hydrogel film with a specified elastic modulus or when it contacts the substrate, are measured using a novel optical tweezers passive interfacial microrheology technique. The substrate stiffness effect on the colloidal contact dynamics is investigated by modulating the substrate elasticity using a chemically-crosslinked polyacrylamide hydrogel with a bulk elastic modulus $\approx$ 10.9 (gel A), 6.3 (gel B), or 3.2 kPa (gel C). The time-dependent mean-squared displacements are well described by a single exponential relaxation, furnishing measures of the transverse interfacial binding stiffness (spring constant) and mobility (diffusion coefficient), suggesting that the former (latter) increases (decreases) when increasing the substrate stiffness. Theoretical interpretation suggests that the interfacial adhesion and substrate compliance play significant roles in attenuating the particle dynamics. Using gel macroscopic properties, the theory for interfacial soft adhesion suggests that silica microsphere-PA hydrogel interfacial binding energy $\pi a^2 U$ is fairly small on the order of $10^{-5} k_B T$ (with contact radius $a \approx 10$ nm from the theory). Comparing such a low adhesion energy to firm attachments observed in the experiments, it is hypothesized that the particle adhesion is affected by several phenomena, which are not considered in the model, namely hydrogen bonding, entanglement with interfacial dangling polymer chains, softer-than-bulk gel surface, the intrinsic hydrogel surface roughness occurred during gelation and/or confined swelling, gel thermal fluctuations, van der Waals (vdW)-induced gel interfacial instabilities arising from a close-contact proximity of a solid particle to the gel surface, and roughness-mediated tangential vdW forces. This work paves the way toward engineering colloidal dynamics at soft, deformable interfaces.

5.3 Introduction

Silica particle-based drug delivery has gained tremendous attention during the past decade due to its promising thermal and chemical stability and the ability to become stealth from the immune system (Barbe *et al.*, 2004; Knopp *et al.*, 2009; Yu *et al.*, 2011). In rat intravenous delivery, when the particle size is higher than $\approx$ 300 nm, more than 90 % of them become trapped in lung and liver (Barbe *et al.*, 2004). An example of particle trapping by a soft matter is the filtration of sub-micron particles by salps, a pelagic tunicate, which are able to trap particles (even up to hundred times) smaller than their mesh size using their soft, sticky net under a laminar flow (Sutherland *et al.*, 2010). Another interesting case is the recent effort to design micro- and nano-carriers to penetrate mucus, a slippery discharge of mucous membranes, for drug delivery purposes (Ensign *et al.*, 2012; Schuster *et al.*, 2013), or to adhere to it (Md *et al.*, 2012). Although a lot of experimental observations have been conducted on such phenomenon, the single-particle behavior upon contact with soft substrates is poorly understood. A decent model system to study microhydrodynamics of a rigid body interacting with soft substrates is silica microsphere-hydrogel interfacial inclusions.

Hydrogels, as hydrophilic polymer networks which can absorb water up to thousands times of their dry weight (Hoffman, 2002), have been introduced as model systems for biological tissues and extracellular matrices (Ju *et al.*, 2007; Plant *et al.*, 2009; Reed *et al.*, 2009; Choi *et al.*, 2013). Tunable elasticity of such soft materials provides a promising infrastructure to study substrate stiffness effect on the cell attachment (Sunyer *et al.*, 2012), migration (Ng *et al.*, 2012), secretion (Petersen *et al.*, 2012), differentiation (Liu *et al.*, 2012; Eroshenko *et al.*, 2013), and shape (Tee *et al.*, 2011). Polyacrylamide hydrogels with customizable elasticity and nanometer root-mean-square surface roughness (Suzuki *et al.*, 1996) have been widely used to regulate the top-sitting species behavior (Ulrich *et al.*, 2009; Moshayedi *et al.*, 2010; Sant *et al.*, 2010; Ghosh *et al.*, 2013) given their excellent transparency (at low enough monomer concentrations), which is compatible with optical-based

techniques. Numerous advantages of this gel are reviewed by Yang (2008).

On length and time scales relevant to micron sized particles, such interfaces are subject to hydrodynamic draining and deformation, which impact kinetic and thermodynamic adhesion factors Mani *et al.* (2012). The problem becomes intriguing given no adhesive moieties on a bare silica microsphere and the probability of polymer chain presence on an hydrogel surface. Recently, the soft adhesion dynamics has been studied theoretically between a bare colloidal particle and a polymer-coated rigid substrate (Gopinath & Mahadevan, 2011; Mani *et al.*, 2012). Such adhesion can adopt a stepwise mechanism starting with long-bond formation between the surfaces followed by short-bond establishment (Mani *et al.*, 2012). Recent experiments with a colloidal particle interacting with a rigid glass substrate shows that the dynamics of a bare silica particle follows a rapid attenuation at high (low) enough medium ionic strength (restoring force and/or shear rate exerted on the particle) while a soft microsphere, such as a polystyrene bead, is able to adhere to the stiff substrate gradually at a specified combination of medium ionic strength, trap stiffness, and external drive frequency (Sharma *et al.*, 2008, 2010*a*,*b*; Kumar *et al.*, 2012). This is attributed to the dynamic formation of bonds between the soft particle and the rigid substrate; however, details about how such bonds appear only under a specified operating condition are not discussed, nor the behavior is associated with the physical properties of interacting bodies.

In this chapter, optical tweezers and back-focal-plane interferometry are applied to measure the Brownian fluctuations of a silica microsphere at positions close to and when attached to a PA hydrogel film. Two closely-related methods are adopted to explain the acquired results: (i) diffusion and adhesion behavior and (ii) storage and loss moduli interpretation. The former is achieved using the theory developed in this work, which paves the way toward understanding how particle short- and long-time dynamics are modulated by the underlying substrate stiffness, and the latter is accomplished using standard passive interfacial microrheology routines. These help furnish valuable information about the soft, wet adhesion at an hydrogel sticky interface, such as apparent interfacial contact area, energy, and viscoelastic

properties.

5.4 Materials and methods

5.4.1 Hydrogel preparation

Prior to hydrogel coating, square cover glasses (22 × 22 mm, thickness No. 1, Fisher Scientific, ON, Canada) were cleaned by 30 min boiling in 7X solution (MP Biomedical, Solon, OH, U.S.A.) followed by reverse osmosis (RO) water rinses. They were, then, dried under nitrogen and immersed in a freshly-prepared piranha solution (3:1 v/v concentrated sulphuric acid and 30 % hydrogen peroxide) for 20 min. Etched cover glasses were rinsed with RO water extensively and dried under nitrogen and allowed to contact 0.5 mol l^{-1} sodium hydroxide solution followed by a silanization agent (3-aminopropyltrimethoxysilane, 97 %, Sigma-Aldrich, MO, U.S.A.) according to the protocol of Wang & Pelham (1998) with intermediate gentle rinses in RO water. To be ready to covalently bind to the gel film, finally, the cover glass was incubated with 0.7 % glutaraldehyde (70 % EM Grade, Polysciences, Inc., PA, U.S.A.) in phosphate buffered saline (PBS, pH ≈ 7.4) at room temperature for 30 min and rinsed thoroughly with RO water. The stiffest hydrogel (termed A) pre-gel solution was prepared by mixing ≈ 5 % w/v acrylamide solution diluted with PBS from a 40 % w/v stock solution of 19:1 w/w acrylamide to bis-acrylamide crosslinker (Fisher BioReagents, NJ, U.S.A.) resulting in a final crosslinker concentration ≈ 0.25 % w/v, and the semi-stiff (termed B) and soft (termed C) hydrogels were formed by manually mixing and diluting an acrylamide solution (40 % w/v) with bis-acrylamide solution (2 % w/v) in PBS buffer to final mixtures of 5 % w/v acrylamide and 0.15 % w/v bis-acrylamide (33.3:1 w/w acrylamide to bis-acrylamide) and 0.049 % w/v bis-acrylamide (102:1 w/w acrylamide to bis-acrylamide), respectively. The solutions were blanketed with nitrogen for at least 15 min to prevent oxygen absorption during crosslinking. The gel was formed by sandwiching $\lesssim 1$ μl of pre-gel solution between the functionalized cover glass and a cleaned, but non-functionalized

cover glass followed by ≈ 10 min curing with ≈ 0.001% w/v ammonium persulphate (APS, Sigma-Aldrich, MO, U.S.A.) initiator and 0.1% v/v N,N,N′,N′-tetramethylethylenediamine (TEMED, GE Healthcare, Uppsala, Sweden). To achieve an equilibrium swollen state, the thin film was incubated in tris-acetate-EDTA (TAE, pH ≈ 8.3 with 40 mmol l^{-1} ionic strength tris-acetate and 1 mmol l^{-1} EDTA, Sigma, MO, U.S.A.) buffer for at least one day at the ambient temperature (≈ 23°C). The AFM (atomic force microscopy) Young's modulus of hydrogels A, B, and C ≈ 8, 4.47, and 1 kPa, respectively, are adopted from Tse & Engler (2010) and Engler *et al.* (2004). Hydrogels A, B, and C also mimic the softness of human thyroid/mouse skeletal muscle, human breast tumor/guinea pig lung, and human liver, respectively (Levental *et al.*, 2007).

5.4.2 Colloidal particle preparation and flow cell

Bare silica microspheres (diameter $2R \approx 1.97$ μm, 10–15% coefficient of variation, Bangs Laboratories, Inc., IN, U.S.A.) were cleaned by at least two centrifugations in TAE buffer. To perform experiments, the microspheres were injected into a custom-built sealed channel including the gel-coated cover glass (150–200 μm thick, bottom), glass microscope slide (≈ 1 mm thick, top), and ≈ 3 mm thick plexiglas spacer, as shown in figure 5.4.1, at a particle concentration ≈ 40 μl^{-1}.

5.4.3 Optical tweezers calibration

An optically trapped silica microsphere behavior is investigated in a gel-free (to show the calibration procedure in this section) and a gel-coated (to show the hydrodynamic effect in section 5.6) channel. Also, to estimate the instrumental noise level, silica microspheres are immobilized on a glass cover slip by increasing ionic strength up to the physiological condition, *i.e.*, 150 mmol l^{-1} NaCl and 10 mmol l^{-1} HEPES buffer (pH ≈ 7, Invitrogen, NY, U.S.A.) and allowing to equilibrate for one day followed by position fluctuations measurement and analysis. The voltage signal is quantified by scanning the stuck particle position while si-

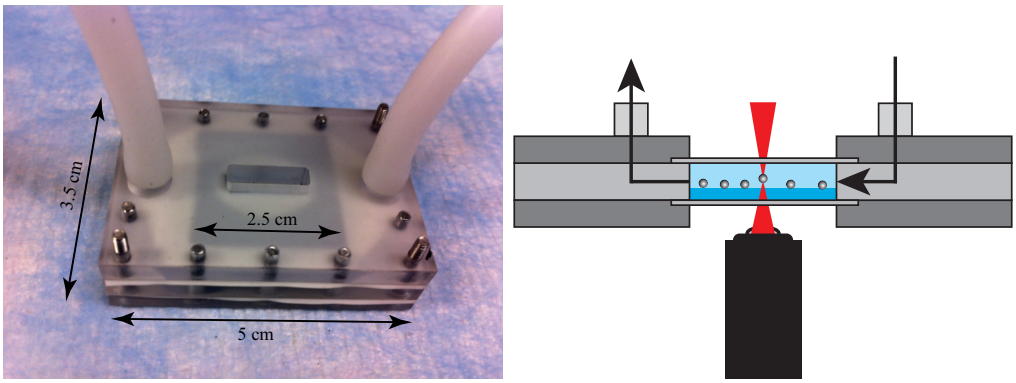

Figure 5.4.1: Custom-built flow cell (left panel) and schematic (not to scale) (right panel). Colloidal microspheres in buffer solution are injected into the chamber, and one particle is trapped using the optical tweezers at various heights $z \lesssim 1$ μm above the hydrogel-electrolyte interface, assisted by a nano-positioning stage; the glass microscope slide (top) and an hydrogel-coated cover glass (bottom) are separated by a plexiglas spacer. In this work, the height above the bottom cover glass $h \sim 20-45$ μm is comparable to the hydrogel thickness.

nusoidally translating the nano-positioning stage to measure the QPD voltage-to-nanometer position conversation factor, which enables immobilized particle position fluctuation measurements while the stage is fixed.

A single colloidal microsphere is trapped using custom-built optical tweezers instrument (van Heiningen *et al.*, 2010), shown schematically in figure 5.4.2. This comprises a steerable high-power 1064 nm ND-YVO_4 laser (BL-106C, Spectra-Physics, U.S.A.) collimated and directed through the high numerical aperture (NA) 100X objective lens of an inverted optical microscope (TE-2000U, Nikon, NY, U.S.A.). The sample (figure 5.4.1) is translated vertically using a nano-positioning stage (NPXYZ100B, nPoint, WI, U.S.A.) in 20 nm increments, and the optically trapped microsphere position fluctuations are recorded using back-focal-plane interferometry whereby the transmitted and scattered light are directed through the microscope condenser lens onto a quadrant photodiode detector (QPD, Spot-9dmi, OSI Optoelectronics, CA, U.S.A.). QPD voltage time series are amplified using a dual-axis position-sensing amplifier (501C, UDT Instruments, CA, U.S.A.) and filtered at 10 kHz (half the sampling frequency) for 10 s time periods. These time series are propor-

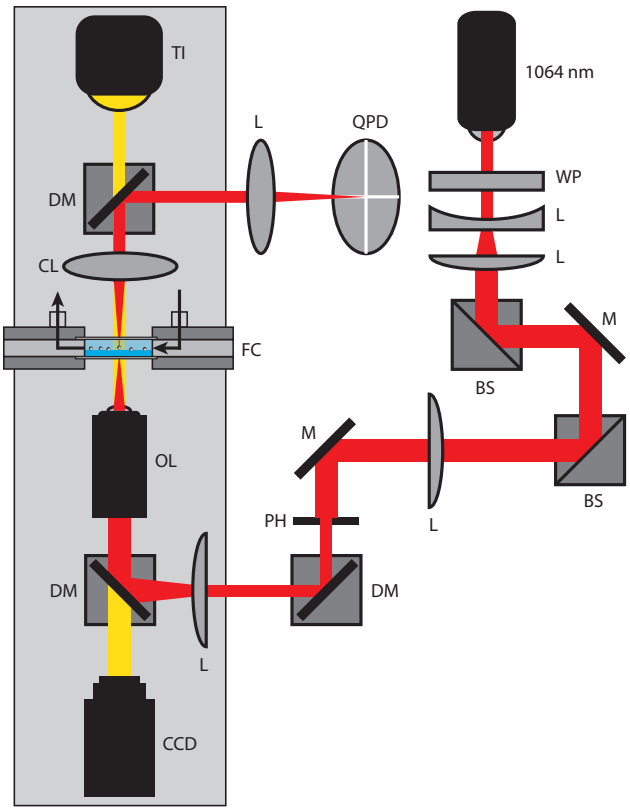

Figure 5.4.2: Optical tweezers interfacial microrheology setup schematic: 1064 nm ND-YVO_4 laser, lenses (L), condenser lens (CL), half waveplate (WP), pinhole (PH), polarizing beam splitters (BS), beam dump (BD), mirrors (M), dichroic mirrors (DM), CCD camera, high numerical aperture objective lens (OL), flow cell (FC) mounted on a piezoelectric nano-positioning stage, quadrant photodiode detector (QPD), and tungsten illuminator (TI). Components internal to the Nikon TE-2000U inverted microscope are within the box on the left. Absent in the box on the right are details pertaining to a secondary imaging laser and acousto-optical deflector, which are not used in this work.

tional to the particle displacement from the centre of the optical trap, and, as demonstrated below, can be calibrated to ascertain the trap stiffness and voltage-to-displacement scaling factor using power spectrum analysis (Berg-Sørensen & Flyvbjerg, 2004).

A silica microsphere with the same diameter as in the experiments with a gel was optically trapped at an elevation $h \approx 20$ μm from the bottom cover glass wall (see figure 5.4.1, right panel). Voltage time series corresponding to the Brownian fluctuations around the trap centre were post-processed in Matlab to compute the power spectrum shown in figure 5.4.3 to which fitting a Lorentzian function furnished the corner frequency $f_c \approx 105.9$ Hz, voltage-

to-displacement scaling factor $\alpha \approx 479$ nm V^{-1} and trap spring constant $k_{x,t} \approx 11.5$ μN m^{-1}. For an $\approx$ 1 μm increase in elevation, these values changed by less than $\approx$ 10 % ($\alpha \approx 446 \pm 24$ nm V^{-1}, $k_{x,t} \approx 10.5 \pm 0.7$ μN m^{-1}). The calibration parameters are checked by performing in-situ calibration using the optically trapped particles in the gel-coated channel before gel experiments and taking the hydrodynamic diffusion coefficient attenuation caused by the coating into account. This assures that the effect of trap height on the calibration factors is considered in various experiments. It is extremely important that the stuck particle method is not accurate when calibrating the detector response for gel-attached particles, because the particles are not attached to the gel as firm as they do to a rigid glass substrate. Figure 5.4.4 illustrates a gel-attached bare silica particle drift towards the optical trap centre resulting in a finite particle elastic displacement on the hydrogel. Such drift is finite and elastic meaning that the amplitude by which the particle centre moves is not necessarily as large as the trap-particle centre spacing, and the particle returns to its initial position when the trap is turned off. Such an elastic drift could cause up to 50 % error in the detector response characterization using the stuck particle method.

When an optically trapped particle inside TAE buffer comes in contact with the hydrogel, it sticks on the soft substrate, which could sometimes result in particle movement out of the trap centre. An example in figure 5.4.5 shows that a bare silica particle travels out of laser focus upon attachment to the gel, which is manifested in the position average drift from zero. To perform accurate position measurements using back-focal-plane interferometry, the particle should be necessarily located as close to the trap centre as possible (within 100 nm from the trap centre) to ascertain detector linear response. To maintain the particle detectable by the QPD and to eliminate any possible drift, before each sampling, the microsphere position is centred in three directions x, y, and z using a custom-developed control system operated in LabVIEW environment. Details of the control system are presented in Appendix 5.A.

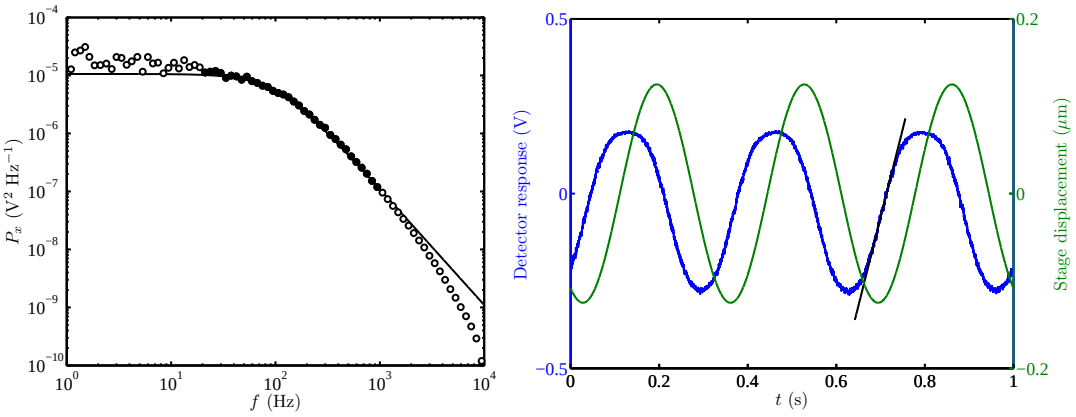

Figure 5.4.3: The power-spectrum $P_x(f)$ of a microsphere position fluctuations $X(t)$, used to calibrate the optical trap (left panel). The fitted Lorentzian (line) furnishes a voltage-to-displacement scaling factor $\alpha \approx 479$ nm V^{-1} and an optical trap spring constant $k_{x,t} \approx 11.5$ μN m^{-1} corresponding to $\langle X^2 \rangle \approx 350$ nm^2. Note that the Lorentzian is fitted only in the intermediate range of frequencies (20–1000 Hz) identified with filled symbols. Detector response to a sinusoidal position scan over an immobilized silica microsphere on a cover glass in physiological condition, *i.e.*, 150 mmol l^{-1} NaCl and 10 mmol l^{-1} HEPES buffer, pH ≈ 7, after one day equilibration (right panel). This furnishes a voltage-to-displacement scaling factor $\alpha \approx 591$ nm V^{-1}. Note that the solid black line in figure 5.4.3, right panel, shows a linear regression in the linear region of the detector response, *i.e.*, less than 100 nm displacement. The phase difference between the input signal and the detector response in the right panel is arbitrary, which depends on the sampling start time.

5.5 Theory

The problem of colloidal soft adhesion to an elastic, sticky plane (shown schematically in figure 5.5.1) is addressed theoretically in this section (Hill & Sheikhi, 2014). Half-space Green's functions (Landau & Lifshitz, 1986) relate the surface displacements (u_x, u_y, u_z) to surface tractions $\boldsymbol{f} = (f_x, f_y, f_z)$:

$$u_x = \frac{3}{4\pi E\rho}\left[f_x + \frac{x}{\rho^2}\left(xf_x + yf_y\right)\right], \tag{5.1}$$

$$u_y = \frac{3}{4\pi E\rho}\left[f_y + \frac{y}{\rho^2}\left(xf_x + yf_y\right)\right], \tag{5.2}$$

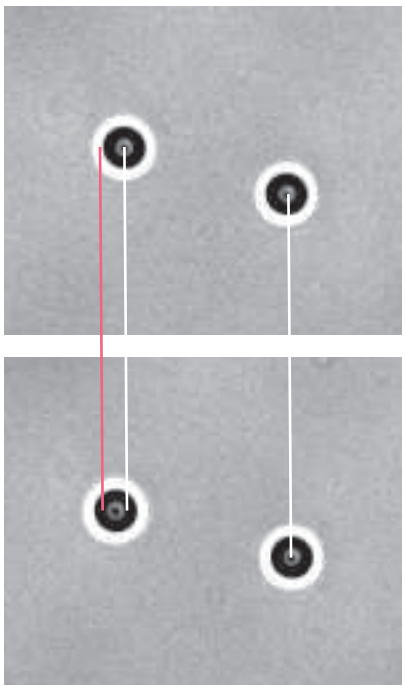

Figure 5.4.4: Particle drift (elastic rolling) on PA hydrogel B film induced by the optical force. Two locally bound bare silica microspheres on the hydrogel surface are shown when the optical trap is off (upper picture) and on (lower picture). Trap centre in xy plane is shown with the red line, and white lines show the initial particle centres. While the right-side particle shows a slight centre displacement (because of the localized Brownian diffusion on the gel), left-side particle could be dragged hundreds of nanometers employing the trap restoring force. Particle size is $2R \approx 1.97$ μm, imaging region is maintained fixed, and the trap is at the same height as the particle centres. Such behavior is never observed for a particle sitting on a rigid glass substrate.

$$u_z = \frac{3}{4\pi E\rho} f_z, \tag{5.3}$$

where $\rho = (x^2 + y^2)^{1/2} = [r^2 + r'^2 - 2rr'\cos(\theta - \theta')]^{1/2}$ with $x = r\cos\theta - r'\cos\theta'$ and $y = r\sin\theta - r'\sin\theta'$, and the contact profile $z = R + \epsilon - (R^2 - r^2)^{1/2}$, where ϵ is the normal particle displacement from an undisturbed interface. Also, a point force $\boldsymbol{f}$ is applied at $r = r'$.

The transverse displacement X:

$$X_i = \int_0^{2\pi} \int_0^a A_{ij}(r - r') f_j(r') r' dr' d\theta' \tag{5.4}$$

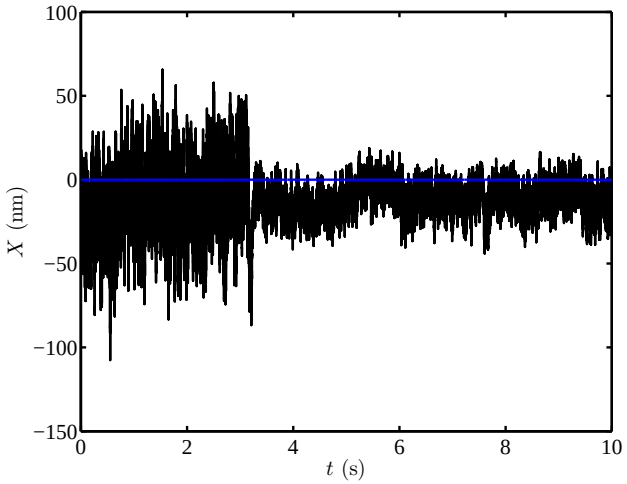

Figure 5.4.5: Deviation of a bare silica particle centre from trap centre upon attachment to PA hydrogel B. Here, hydrogel attraction brings the particle ≈ 25 nm out of the trap focus. To correct such binding drift, a feed-back control system is developed, which maintains the particle at the trap centre. The blue line shows $X = 0$, *i.e.*, trap centre.

with

$$A_{ij} = \frac{3}{4\pi E\rho} \begin{pmatrix} 1 + x^2/\rho^2 & xy/\rho^2 \\ xy/\rho^2 & 1 + y^2/\rho^2 \end{pmatrix}. \tag{5.5}$$

This results in a Fredholm integral equation (calculation details are presented elsewhere) as:

$$\frac{4\pi E}{18} = \int_0^a \frac{K(\alpha)}{|r + r'|} r' \left[f_1(r') - f_1(r) \right] dr' + f_1(r) \int_0^a \frac{K(\alpha)}{|r + r'|} r' dr', \tag{5.6}$$

where K is the first kind complete elliptic integral, $\alpha = 4rr'/(r + r')^2$, and f_1 denotes the traction in-plane component, which is solved numerically for $f_1(r')$ to furnish the transverse force $F_x = 2\pi X \int_0^a f_1(r')dr'$:

$$F_x = \frac{16}{9} aEX, \tag{5.7}$$

resulting in a transverse spring constant

$$k_x = \frac{16}{9} aE = \frac{2}{3} k_z, \tag{5.8}$$

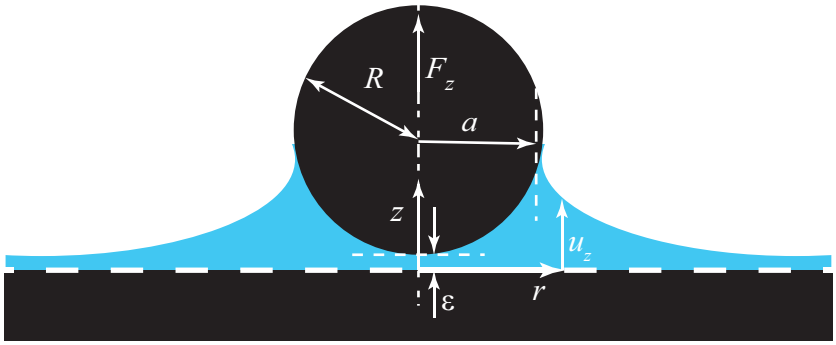

Figure 5.5.1: Schematic of a colloidal microsphere, adhered to a soft, sticky elastic plane. A perpendicular positive force F_z is applied to the particle, *e.g.*, from thermal z-direction fluctuations, which results in a positive perpendicular particle displacement ($\epsilon > 0$). Absence of a perpendicular force furnishes $\epsilon < 0$ originated from the interfacial adhesion. Similarly, transverse fluctuations induce in-plane X displacements affected by the sticky contact area.

furnishing the long-time transverse particle position variance $\langle X^2 \rangle$

$$\langle X^2 \rangle = k_B T / k_x = \frac{9 k_B T}{16 a E}. \tag{5.9}$$

Knowledge of substrate interfacial elasticity is vital in using Eqn. 5.9; however, employing bulk Young's modulus, an estimation of the contact radius a can be acquired using the position variance.

For a given interfacial adhesion energy U, the theory of Maugis (1995) furnishes the contact radius dependency on the substrate Young's modulus

$$\frac{U}{RE} = \frac{2R}{3\pi a}\left[\frac{1}{2} - \frac{1}{4}\left(\frac{a}{R} + \frac{R}{a}\right)\log\left(\frac{1+\frac{a}{R}}{1-\frac{a}{R}}\right)\right]^2. \tag{5.10}$$

Assuming a constant interfacial adhesion energy for a bare silica microsphere on gels A, B, and C, the particle position variance is related to the substrate elasticity (will be discussed in figure 5.6.5, right panel a). Note that in the developed theory, hydrodynamic draining and substrate compressibility are not included.

5.6 Results and discussion

To shed light on the colloidal behavior at soft interfaces, and to understand the effective interfacial viscoelastic properties of a polyacrylamide hydrogel, a bare colloidal silica probe is brought in contact with hydrogels A, B, and C with three specified stiffnesses. The goal is to understand how adhesion affinity and dynamics are affected by the soft substrate stiffness.

Keeping the environment stagnant, the only forces exerted on an elevated particle ($z > 0$) are stochastic Brownian force dictating the short-time lag diffusion coefficient of the probe and the optical trap restoring force partaking the long-time lag position fluctuation plateau. As an example, the microsphere position fluctuations time series $X(t)$ when the particle is in bulk electrolyte (black), at hydrogel-electorlyte interface (blue), and stuck on a glass cover slip (red) are shown in figure 5.6.1 from which the mean-squared displacements $\langle [X(t+\tau) - X(t)]^2 \rangle$ are directly computed. Here, τ is the time lag. The mean-squared displacement data are shown in figure 5.6.2 with accompanying fits to the two-parameter model (Clercx & Schram, 1992)

$$\langle [X(t+\tau) - X(t)]^2 \rangle = 2\langle X^2 \rangle [1 - \exp(-\tau D_x / \langle X^2 \rangle)], \tag{5.11}$$

where D_x is the diffusion coefficient and $\langle X^2 \rangle$ is the particle position variance. From the Stokes-Einstein relationship and equipartition theorem, respectively, $D_x = k_B T / \gamma_x$ and $\langle X^2 \rangle = k_B T / k_x$, where $k_B T$ is the thermal energy, γ_x is the friction coefficient, and k_x is the spring constant.

Under conditions where the particle is trapped far from a cover glass or gel, $\gamma_x \to 6\pi\eta R$ and $k_x \to k_{x,t}$, where $k_{x,t}$ is the optical trap spring constant. Accordingly, fitting Eqn. (5.11) to the data in figure 5.6.2 with $h \approx 20$ μm furnishes $D_x \approx 0.24$ μm^2 s^{-1} and $\langle X^2 \rangle \approx 370$ nm^2, giving $2R = \gamma_x / (3\pi\eta) \approx 2$ μm and $k_x \approx k_{x,t} \approx 11$ $\mu\text{N m}^{-1}$, which are both in good agreement with the values associated with the foregoing power-spectrum analysis.

Next, assuming that $k_{x,t}$ and α are independent of the trap height h over the range

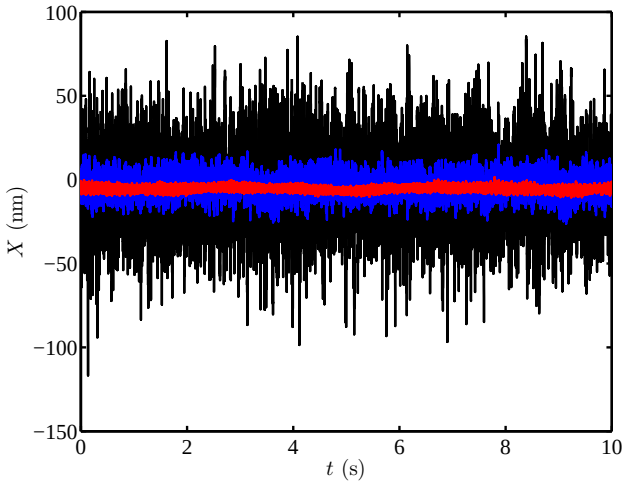

Figure 5.6.1: Time series of the detector response $X(t)$ to the thermal fluctuations of an optically trapped silica microsphere with a specified diameter $2R \approx 1.97$ μm at an elevation $z \approx 20$ μm from the bottom wall of a gel-free channel (black), when attached to the PA gel A (blue), and while immobilized on a cover glass in an high ionic strength solution (red). The voltage-to-position scale factor and optical trap spring constant for an elevated (stuck) particle are furnished by the power spectrum (stuck particle calibration method), explained in figure 5.4.3. Note that the time series corresponding to an elevated particle trapped in a gel-coated channel is not shown here (mean-squared displacement is provided with gray color in figure 5.6.2) as it covers the particle fluctuations in the gel-free channel, *i.e.*, they have comparable fluctuation amplitudes.

of heights in experiments with particles interacting with a gel ($z \lesssim 1$ μm, figure 5.4.1, right panel), D_x and $\langle X^2 \rangle$ are obtained at various positions z above the apparent hydrogel-electrolyte interface. As the particle is brought closer to the interface, hydrodynamic coupling to the gel attenuates D_x, and particle contact is identified by a discontinuous change in D_x and $\langle X^2 \rangle$ over a distance that is less than the ≈ 20 nm vertical displacement increment of the nano-positioning stage. Once the particle attaches to the gel, k_x ($\langle X^2 \rangle$) increases (decreases) substantially, because the particle dynamics become dominated by the viscoelastic coupling to the gel, which overwhelms the optical force. Accordingly, the data in figure 5.6.2 with a particle attached to the gel A (blue symbols) furnish $D_x \approx 0.014$ μm^2 s^{-1} and $\langle X^2 \rangle \approx 31$ nm^2 following attachment.

Dynamic behavior of a bare silica particle in the vicinity of hydrogels A, B, and C is shown in figure 5.6.3 in terms of height (time)-dependent diffusion coefficient, left panel, and long-time position variance as an indication for binding stiffness, right panel, for an elevated (adhered) particle. An elevated particle ($z > 0$) diffusion coefficient reduces when decreasing the particle height from the substrate due to the wall hydrodynamic effect. The symmetry breakage increases the effective (hydrodynamic) particle size resulting in an increased hydrodynamic friction, which tends to lower the diffusion coefficient. The data are compared with Faxen (1923) (blue), O'Neill (1964) (green), and Goldman *et al.* (1967) (red) theories at various heights. Given an almost-constant trap stiffness within such a small height change, the diffusion coefficient hindrance is mostly attributed to the wall effect. Although the wall is soft and porous with 95 % bound water content, the effect is similar to a rigid wall. This suggests that at length scales $\gtrsim 100$ nm, the hydrogel attenuates the free Brownian diffusion coefficient in the same way as a rigid wall. To the best of the author's knowledge, this is the first experimental report on the colloidal diffusion in close vicinity of a soft, deformable and porous wall. Linear short-time behavior of the particle mean-squared displacement (see figure 5.6.2a) suggests no anomalous diffusion near the soft walls and while attached to the gels.

Once the particle touches the hydrogel, its diffusion coefficient undergoes an abrupt reduction, reflecting a much viscous drag on the probe, arising from becoming partially embedded at the interface. The diffusion coefficient attenuation resulted from the contact with a soft substrate is more pronounced for the stiffest hydrogel (gel A). While hydrogel A attenuates particle diffusion coefficient down to 5 % of bulk diffusion in water, softer hydrogels B and C reduce the equilibrium short-time diffusion coefficient to ≈ 10 % of the bulk value. Also, the diffusion attenuation occurs abruptly for hydrogels A and B suggesting that the bond formation between the particle and the interface is spontaneous, and the bonds are possibly similar in length and stickiness. To understand the nature of attraction, the ζ- and streaming potentials of the bare silica microspheres in TAE buffer and PA gel-coated cover glasses are measured, respectively (details are available in Chapter 7, Appendix 7.B). Opposite ζ-potentials of silica microspheres ($\zeta \approx -52$ mV) and a gel-coated slide (27 mV) facilitates the adhesion, which is further pronounced at short particle-gel film separation gaps (*e.g.*, $z \lesssim 10$ nm) by van der Waals attraction forces. An estimation of force dependency on the particle-gel vertical distance is presented in Appendix 7.B.

Using a low crosslinker concentration, *i.e.*, almost five times smaller than the amount used to prepare gel A, the softest gel C has much distant crosslinking nodes and lower crosslinking density, which decreases the chance of having more partially attached polymer chains (dangling chains) at the interface. Seen in panel (c) of figure 5.6.3, the diffusion coefficient (left panel) and position variance (right panel) of a bare probe particle decreases gradually by time suggesting the possibility of continuous increase in the adhesion strength on the interface, which can be a result of multi-length adhesive bonds at the gel surface, as suggested by Mani *et al.* (2012). This also suggests a gradual penetration of the colloidal microsphere into the gel in an $\approx$ 1500 s time span. Similar behavior is reported for a sticking transition of a polystyrene microsphere on a rigid glass substrate (Sharma *et al.*, 2008); however, they argue that no aging can be observed for a silica microsphere on a glass substrate, because there is no possibility for an hard particle to deform.

The position fluctuations variance is a good representative of the particle-surrounding environment binding stiffness; the lower the variance, the stiffer is the potential in which the particle is trapped. As the experiments are conducted on gels with different (but close) thicknesses (20-50 μm), the optical trap stiffness, which dictates the particle position variance in the bulk electrolyte, is different from one experiment to another. Calibrating the trap before each experiment, the variance is normalized with the corresponding variance of the optical trap, resulting in an average $k_{x,t}/k \approx 1$ for an elevated particle (see figure 5.6.3, right panel, for $z > 0$). Once the particle is trapped at the hydrogel interface, the position variance is attenuated, which furnishes $\langle X^2 \rangle^{1/2} \approx 5$, 6.4, and 9.2 nm for the stiff (A), semi-stiff (B), and soft (C) gels, respectively. Comparing gels C with A and B, the softest gel reduces a bare silica microsphere-PA gel inclusion stiffness in an exponential manner, which can be a result of gradual binding enhancement by time.

The experiments are repeated with randomly chosen bare silica microspheres on random gel regions, and the interfacial microrheology results are presented in terms of position variance and diffusion coefficient in figure 5.6.4 left panel, and right panel, respectively, shown with various colors. The difference observed in similar experiments in each panel is explained by how a particle rests on a gel surface. Depending on the gel local properties, *e.g.*, nano-scale roughness, the particle dynamics behave differently; however, as can be seen in figure 5.6.4 right panel, short-time diffusion coefficient decreases when increasing the substrate stiffness. Also, the Brownian position fluctuations variance decreases when increasing the substrate stiffness as seen in figure 5.6.4, left panel, which indicates that a stiff substrate enhances the binding stiffness.

These experiments furnish average values for the diffusion coefficient and position variance, which are shown in figure 5.6.5 (a). The average normalized diffusion coefficients (position variance) versus the substrate bulk elastic modulus (blue symbols) and AFM elastic modulus from literature (black symbols) are presented in the left panel (right panel). Theoretical predictions of position variance using predicted contact area by the DMT (Der-

jaguin *et al.*, 1975), Maugis (Maugis, 1995), and JKR (Johnson *et al.*, 1971) theories with a constant surface energy [$\pi a^2 U \approx 10^{-5} k_B T$, calculated based on Maugis (1995)], are presented with red, black, and green solid lines, respectively. The adhesion region depends on a single dimensionless parameter, called Tabor parameter (Johnson & Greenwood, 1997). In case of a very large (very small) Tabor parameter, the adhesion is reported to be described better by Johnson *et al.* (1971) (Bradley, 1932) models as two extremes. Tabor parameter for interatomic distances $z_0 \approx 0.2$, 0.5, and 1 nm are plotted versus substrate elasticity in figure 5.6.5, left panel (b), from top to bottom. The interatomic distance between the particle and the gel is not accurately known; however, considering that both hydrophilic surfaces have a layer of water molecules on them, $0.2 \leq z_0 \leq 1$ nm is an acceptable estimation. The dashed black and red lines show the relevant Tabor parameter values corresponding to the adhesion regime changes from Maugis (1995) to Derjaguin *et al.* (1975), and from Derjaguin *et al.* (1975) to Bradley (1932), respectively. This shows that altering the interatomic distance of such an interfacial inclusion by only a fraction of nanometer can change the adhesion region easily. Given that the Maugis (1995) prediction results in a good fit, the adhesion energy versus Maugis contact area of a $R \approx 1$ μm sphere on gels A, B, and C is also plotted in figure 5.6.5, right panel (b). The small adhesion energy furnished from the theory suggests that the theory needs to be improved to take other interfacial phenomena, such as surface roughness into account. Comparing this energy with the typical sphere-polymer film adhesion energies in a dry state (thoroughly reviewed in section 3.3) and also noting the firm silica particle attachment on PA gels show that the observed particle position fluctuations are larger than expected, suggesting a superimposed motion on the probe. The thermal fluctuations of the gel surface dangling chains may be the main source of the enhanced dynamics.

One hypothesis to explain the realistic adhesion energy is that the adhesion area a comprises n small-scale domains, similar to the adhesion of a gecko on a wall (Arzt *et al.*, 2003). These sub-contact units of radius $a/\sqrt{n}$ increase the effective adhesion area by a factor of $\sqrt{n}$. Both Derjaguin *et al.* (1975) and Johnson *et al.* (1971) theories predict $a \propto U^{1/3}$; there-

fore, the sub-contact units increase the adhesion energy by a factor of $n^{3/2}$. As an example, if contact radius $a \approx 10$ nm, with only 1000 sub-contact units of radius ≈ 0.3 nm, the effective adhesion energy increases by a factor of 3×10^4, which, compared to the predicted value by Maugis (1995), brings the adhesion energy closer to a realistic and acceptable value. The presence of sub-contact unit on the gel surface can be a result of roughness and swelling instabilities induced during the gel preparation, swelling, or even bringing the gel to a close proximity of the approaching colloidal probe (vdW-induced surface instabilities).

Passive interfacial microrheology is able to furnish storage and loss moduli of a viscoelastic material (Wirtz, 2009). The viscoelastic properties of the microsphere-PA gel interfacial inclusions are calculated from the bare particle mean-squared displacements using the general formalism of Mason & Weitz (1995) via a Matlab routine provided by Crocker (1999). Storage (black symbols) and loss (blue symbols) moduli versus frequency calculated from the position time series of a bare silica microsphere trapped at an elevation $z \approx 200$ nm or 1360 nm above a gel film is shown in figure 5.6.6, panels (a) and (b), respectively. The low-frequency elastic contribution from the trap restoring force adopts a constant value ≈ 0.2 Pa over a wide frequency range while the loss modulus increases linearly between $10^2 \leq \omega \leq 10^4$ s^{-1}, which furnishes solvent viscosity $\eta_s \approx 2.3$ cP ($z \approx 200$ nm) and 1.3 cP ($z \approx 1360$ nm); a reasonable value for water considering the effective particle size in a rigid wall vicinity according to Faxen (1923) ($R/R_{z=200} \approx 0.5$ and $R/R_{z=1500} \approx 0.8$). This results in bulk water viscosity $\approx$ 1.15 cP at $z = 200$ nm and $\approx$ 1.04 cP at $z = 1360$ nm. The crossover frequency $\omega_c \approx 172$ s^{-1} ($z \approx 200$ nm) and $\omega_c \approx 227$ s^{-1} ($z \approx 1360$ nm).

The interfacial viscoelastic properties of gels A, B, and C are calculated by averaging the mean-squared displacements over the acquisition time for one set of data points (corresponding to figure 5.6.4), which are presented in figure 5.6.7. Following the same procedure for an elevated particle, for gels A, B, and C, the storage modulus $G' \approx 17.3 \pm 3$, 6 ± 1, and 1.7 ± 0.3 Pa, and $\eta \approx 0.0156$, 0.0081, and 0.0045 Pa s, respectively. The crossover frequency of gels A, B, and C, $\omega_c \approx 1150$, 690, and 400 s^{-1}, respectively. The error bars in the

right-hand-side figures reflect the dynamics of property change once the particle touches the hydrogel up to a desired sampling time, shown with magenta color in panel (a), blue color in panel (b), and black color in panel (c) for gels A, B, and C, respectively, in figure 5.6.4. Normalizing the storage moduli with the bulk elastic moduli ($E/1000$) (see Appendix 5.B) results in 1.6, 0.96, and 0.53, respectively. Interestingly, performing the same normalization with the AFM elasticities ($E/1000$) furnishes closer values 2, 1.3, and 1.1, respectively, for gels A, B, and C. Storage moduli and viscosity, measured by passive interfacial microrheology, are averaged over all sampling particles over all sampling times in figure 5.6.4 and presented in figure 5.6.8). Results show that $1000G'/E \approx 1$ for all of the gels suggesting that a bare silica microsphere trapped at PA gel-TAE electrolyte interface, and while subjected to the ambient-temperature thermal forces, experiences almost three orders of magnitude lower elastic stresses from the substrate compared to the case when the particle is fully embedded inside the gel. Accordingly, PA gels seem to be promising as interfacial scaffolds when small stresses are needed to ascertain cell growth and differentiation. It is, therefore, necessary to study the properties of such inclusions under external forces, which is followed in chapter 6.

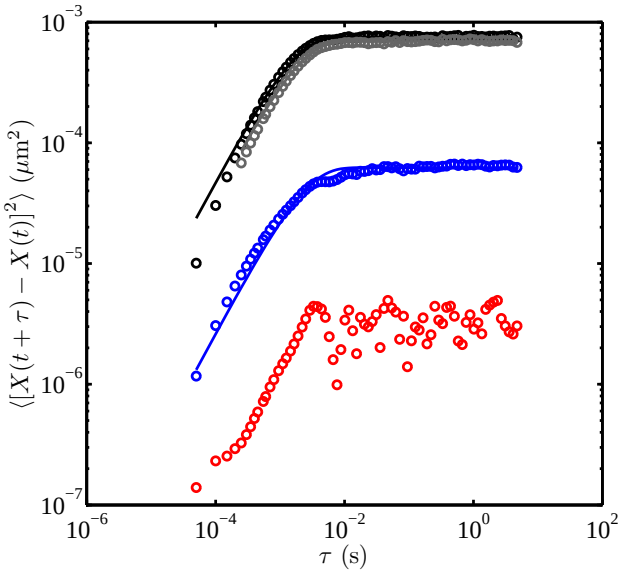

(a)

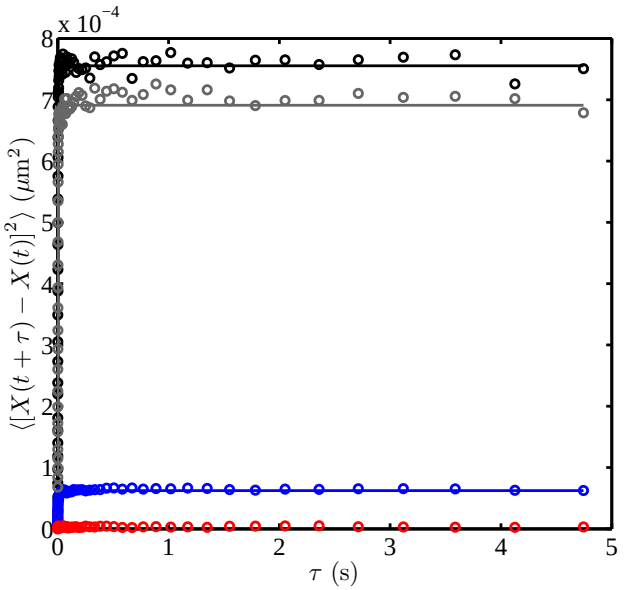

(b)

Figure 5.6.2: Mean-squared displacement $\langle [X(t+\tau) - X(t)]^2 \rangle$ of bare silica microspheres in a gel-free channel (black), gel-coated channel (gray), when attached to a PA gel A film (blue), and while immobilized on a cover glass (red) in an high ionic strength condition. The corresponding time series are presented in figure 5.6.1. Fitting Eqn. (5.11) to the data furnishes $D_x \approx 0.24$ μm^2 s^{-1} and $\langle X^2 \rangle \approx 370$ nm^2 with goodness of fit $R^2 \approx 0.997$ (black); $D_x \approx 0.178$ μm^2 s^{-1} and $\langle X^2 \rangle \approx 346$ nm^2 with goodness of fit $R^2 \approx 0.995$ (gray); and $D_x \approx 0.014$ μm^2 s^{-1} and $\langle X^2 \rangle \approx 31$ nm^2 with goodness of fit $R^2 \approx 0.97$ (blue). Note the logarithmic and linearly scaled axes in panels (a) and (b), respectively.

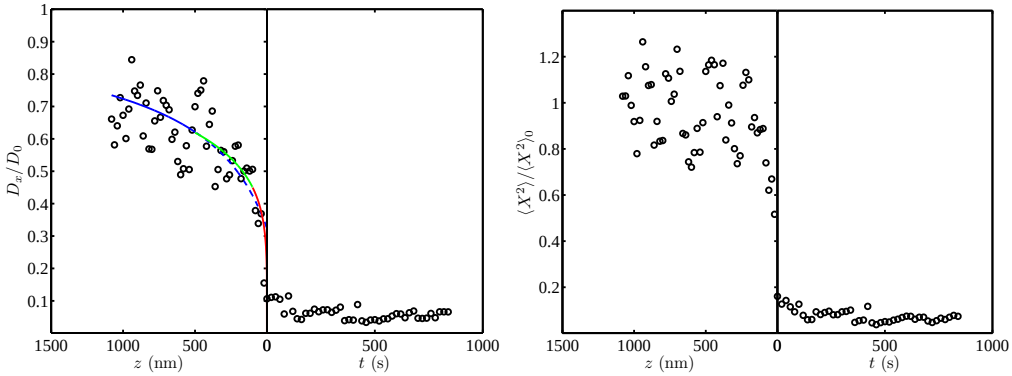

(a) Bare silica microsphere on PA hydrogel A.

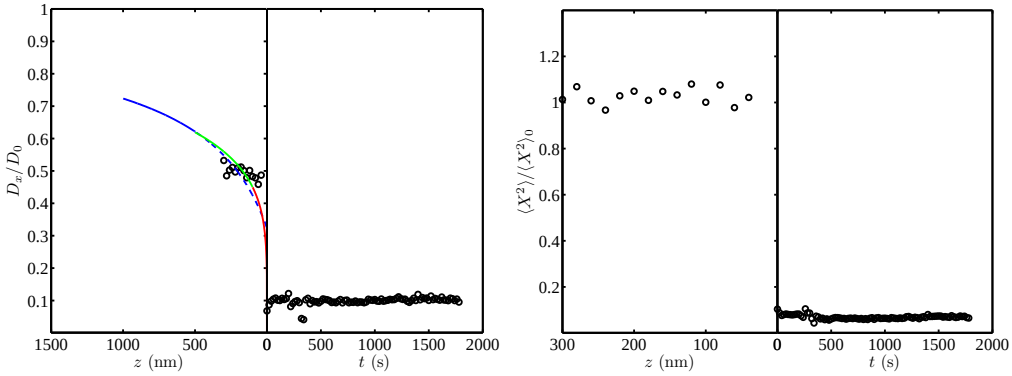

(b) Bare silica microsphere on PA hydrogel B.

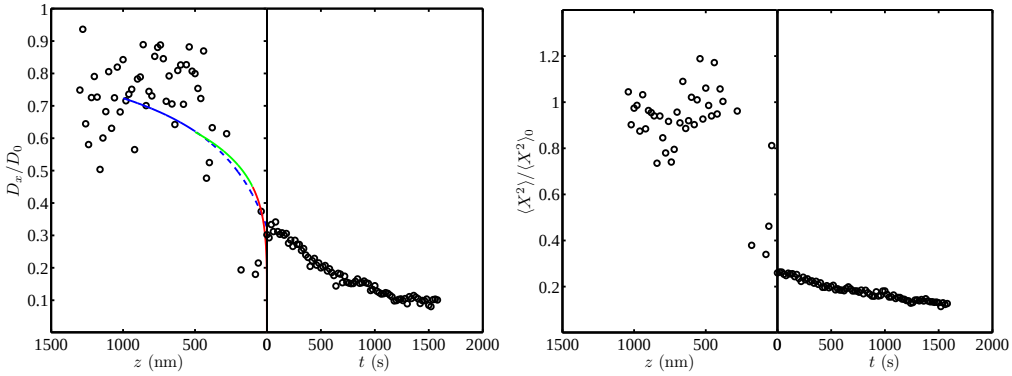

(c) Bare silica microsphere on PA hydrogel C.

Figure 5.6.3 *(previous page)*: Short-time diffusion coefficient (left panel) and long-time position variance (right panel) obtained from passive interfacial microrheology with optical tweezers and back-focal-plane interferometry position detection employing a bare silica microsphere on the surface of the stiff PA hydrogel A (panel a), semi-stiff PA hydrogel B (panel b), and soft PA hydrogel C (panel c). The particle ($2R \approx 1.97$ μm) is brought in contact with PA hydrogels by vertically translating the sample in 20 nm increments using a piezoelectric nano-positioning stage. The diffusion coefficients D_x (left panel) and the (long-time) variance of the transverse Brownian position fluctuations $\langle X^2 \rangle$ (right panel) are plotted versus the particle-hydrogel gap height z and time t when the particle is elevated and once it adheres to the interface, respectively. Lines in the left panel are the Faxen (1923) (solid and dashed, blue), O'Neill (1964) (green), and Goldman *et al.* (1967) (red) hydrodynamic theories for the translation of a sphere parallel to a plane wall. Note that $\langle X^2 \rangle$ and D_x were obtained by fitting a single exponential relaxation to plots of $\langle [X(t+\tau) - X(t)]^2 \rangle$ versus the time lag τ: $D_0 \approx 0.25$ μm^2 s^{-1} and $\langle X^2 \rangle_0 \approx 350$ (panel a), 520 (panel b), and 780 nm^2 (panel c). These furnish equilibrium $\langle X^2 \rangle^{1/2} \approx 5$, 6.4, and 9.2 nm for the stiff (A), semi-stiff (B), and soft (C) gels, respectively.

5.7 Conclusions

Optical tweezers combined with back-focal-plane interferometry provided a means to perform passive interfacial microrheology, employing a bare silica microsphere probe at PA hydrogel-TAE electrolyte interfaces with controlled Young's moduli to shed light on the stiffness-mediated colloidal particle adhesion at soft interfaces as model systems for particle-based drug delivery to tissues. The substrate elastic moduli ranged from $\approx 1 - 10$ kPa, mimicking the elasticity of several organs, such as lung and liver. The back-focal-plane interferometry position detection resolves the microsphere position fluctuations with nanometer accuracy, which is further used to furnish the position mean-squared displacements. To analyze the acquired mean-squared displacement data, two methods, namely a newly-developed diffusion coefficient-binding stiffness method in this work and a well-known viscoelasticity analysis technique are adopted. A single relaxation time fitted the experimental mean-squared displacements well suggesting that the transverse interfacial short-time diffusion coefficient and long-time position variance decrease when increasing the substrate stiffness, which were both significantly smaller than the bulk electrolyte. Using Maugis (1995) interfacial adhesion energy, the theory suggests an adhesion energy $\pi a^2 U \approx 10^{-5} k_B T$ J with contact radius $a \approx 10$ nm. This is implausibly lower than common interfacial adhesion energies (reviewed in 3.3), which suggests the possibility of interactions not included in the theory, such as the formation of sub-contact units increasing the contact area, interfacial effective elasticity, dangling chain-particle entanglement and adsorption, and gel surface instabilities and roughness. The elastic moduli furnished by the second method confirm that the probe particle experiences ≈ 1000 times lower elastic stress compared to a particle trapped in the bulk gel. Future theoretical studies should consider the influences of polymer chain adsorption and thermal fluctuations, hydrogen bonding, hydrogel viscosity and drainage, and experiments should be undertaken to study the effect of shear rate on the adhesion dynamics, *i.e.*, active interfacial microrheology.

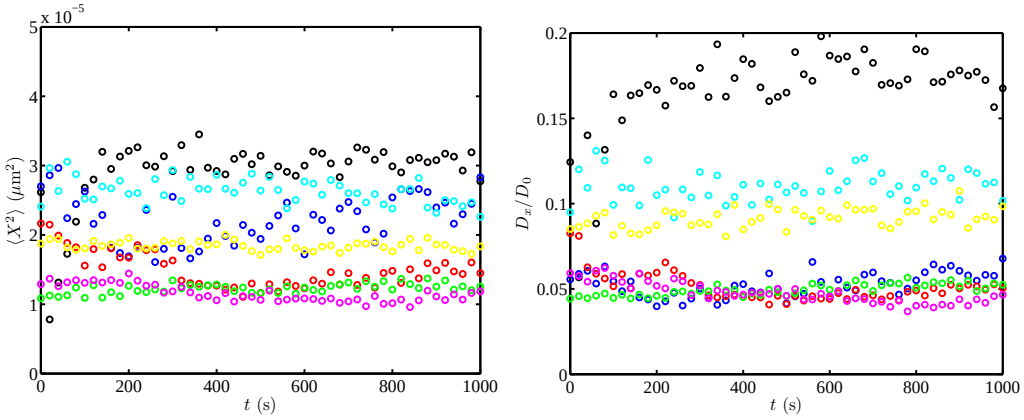

(a) Bare silica microsphere on PA hydrogel A.

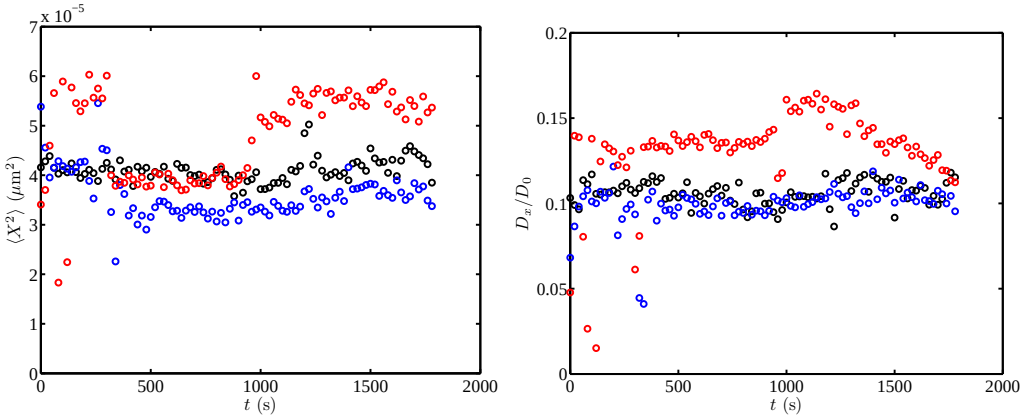

(b) Bare silica microsphere on PA hydrogel B.

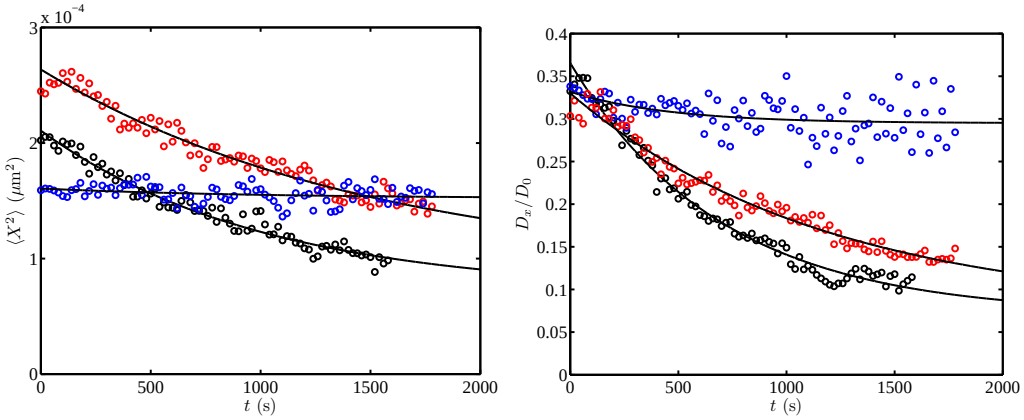

(c) Bare silica microsphere on PA hydrogel C.

Figure 5.6.4 *(previous page)*: long-time position fluctuation variance (left panel) and short-time diffusion coefficient (right panel) of bare silica microspheres on various hydrogels obtained from passive interfacial microrheology. In case of aging with time (gel C), single relaxation fit $C_1 + C_2 \exp(-t/\tau)$ (black lines) furnishes equilibrium values well. The position variance fit coefficients C_1, C_2, and τ are 88.4 nm^2, 175.3 nm^2, 1510 s for red symbols, 71.4 nm^2, 139.4 nm^2, and 1010 s for black symbols, and 152 nm^2, 8.6 nm^2, and 1000 s for blue symbols, respectively, furnishing equilibrium position variances 88.4, 71.4, and 152 nm^2 for these data points, respectively. The diffusion coefficient fit parameters C_1, C_2, and τ are 0.075, 0.255, and 1171 s for red symbols, 0.071, 0.295, and 695 s with $R^2 \approx 0.98$ for black symbols, and 0.294, 0.037, and 456 s for red symbols, respectively, furnishing equilibrium $D_x/D_0 \approx 0.075$, 0.071, and 0.29 for these data points, respectively. The fitting to Eqn. 5.11 are conducted up to $\tau \approx 0.05$ s for gels A and B, and 0.1 s for gel C, to prevent any possible long-time position drift. The same colors represent properties acquired in one experiment on each gel. Cumulative results are presented in figure 5.6.5.

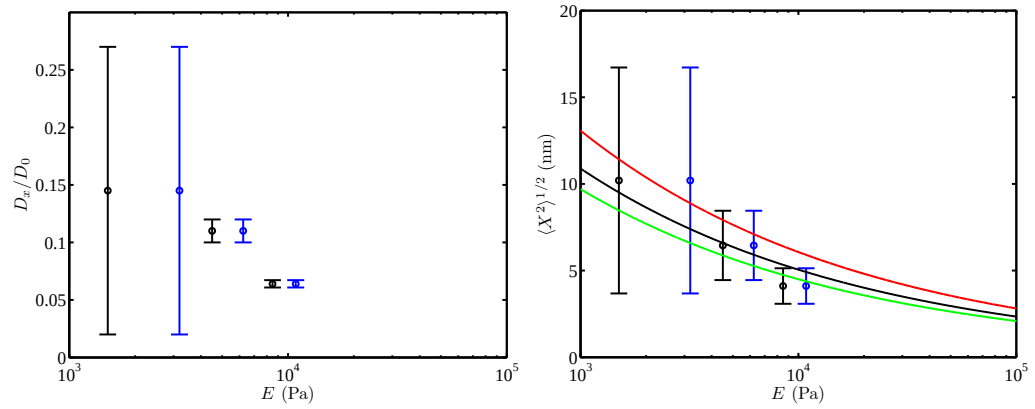

(a)

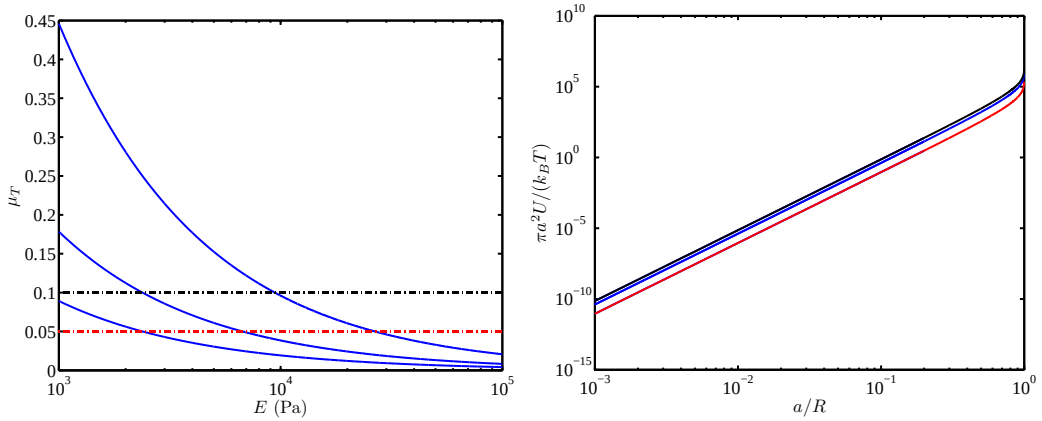

(b)

Figure 5.6.5: The effect of substrate stiffness (elastic modulus E) on the short-time diffusion coefficient (left panel a) and Brownian position fluctuation variance (right panel a) of a bare silica microsphere adhered to PA hydrogel films with controlled elasticities. Data points represent average values of particle steady state behavior. Theoretical values based on the contact area predicted by Johnson *et al.* (1971), Maugis (1995), and Derjaguin *et al.* (1975) are plotted with green, black, and red colors, respectively, using Maugis (1995) adhesion energy per unit area, furnished from a least-squared regression on the experimental data employing the AFM Young's moduli, *i.e.*, $U \approx 7.1 \times 10^{-10}$ J m^{-2}. This results in adhesion energy $\pi a^2 U/(k_B T) \approx 5.45 \times 10^{-5}$, taking the contact radius $a \approx 10$ nm (Refer to section 5.5 for details). Tabor parameter, $\mu_T^3 = (9/16) R u^2/(z_0^3 E^2)$, versus substrate stiffness (left panel b) for three equilibrium atomic distances (respectively from top) $z_0 = 0.2$, 0.5, and 1 nm. The black and red dashed lines show the corresponding Tabor parameter to change the adhesion from Maugis (1995) to Derjaguin *et al.* (1975), and from Derjaguin *et al.* (1975) to Bradley (1932), when decreasing μ_T, respectively (Johnson & Greenwood, 1997). Maugis (1995) adhesion energy versus contact area is shown in the right panel (b) for gels A (black line), B (blue line), and C (red line).

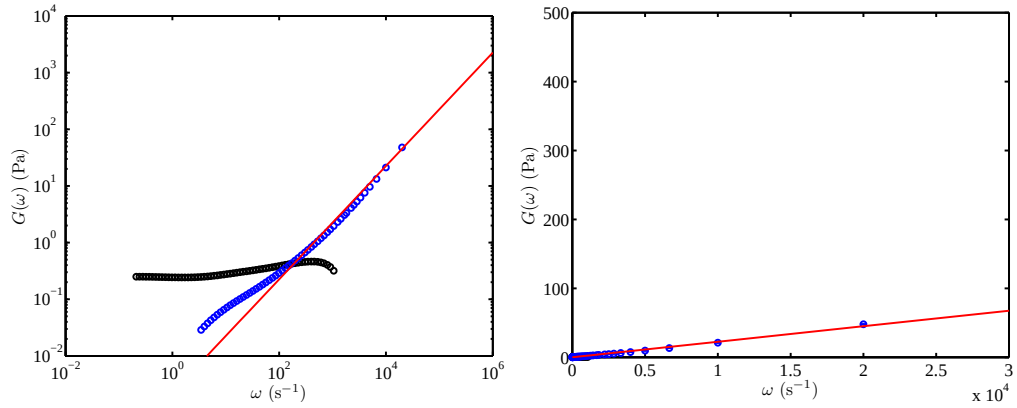

(a) Bare silica microsphere at $z \approx 200$ nm above PA hydrogel A.

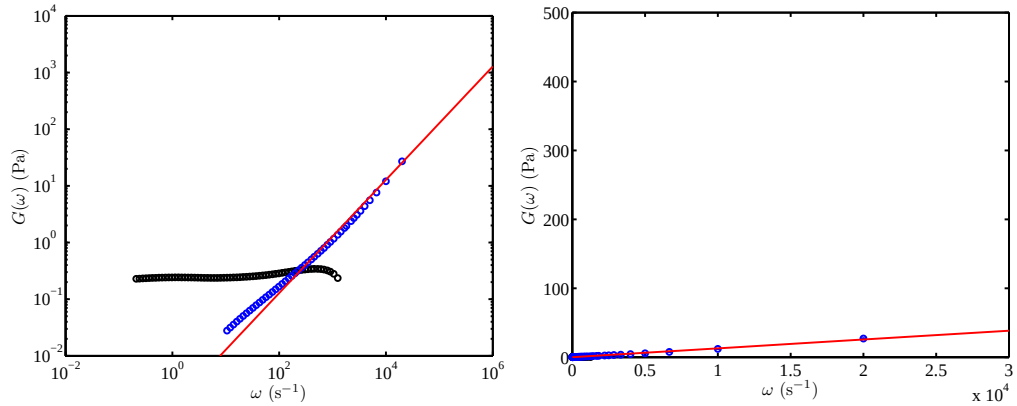

(b) Bare silica microsphere at $z \approx 1360$ nm above PA hydrogel A.

Figure 5.6.6: Storage (black symbols) and loss (blue symbols) moduli, furnished from the mean-squared displacements of an optically trapped bare silica microsphere at an elevation $z \approx 200$ nm (panel a) or $z \approx 1360$ nm (panel b) above a PA hydrogel-coated cover slip inside the TAE electrolyte. The storage modulus ($G' \approx 0.2$ Pa) corresponds to the optical restoring force applied to the trapped microsphere, and the high-frequency linear fit to the loss modulus, shown with solid red line, furnishes the solvent viscosity $\eta_s \approx 0.0023$ Pa s and 0.0013 Pa s at $z \approx 200$ nm and $z \approx 1360$ nm, respectively. The corssover frequency, $\omega_c \approx 171$ and 227 s^{-1} at $z \approx 200$ nm and $z \approx 1360$ nm, respectively. Note that the wall hydrodynamic friction effect on the effective particle radius is not considered in calculating the viscosity; therefore, the viscosity increases by approaching the gel by a factor of ≈ 2, which is consistent with Faxen (1923) hydrodynamic theory. Left panel is logarithmic presentation of the data, and right panel is scaled such to allow comparison with the gel results in figure 5.6.7 and show error bars. Noteworthy is that the $G'(\omega)$ and $G''(\omega)$ are clipped at least $0.03G(s)$ according to Mason & Weitz (1995); Crocker (1999), and high (low)-frequency $G'(G'')$ does not bear physical meaning. More details about the calculation algorithm are presented in section 3.4.2.

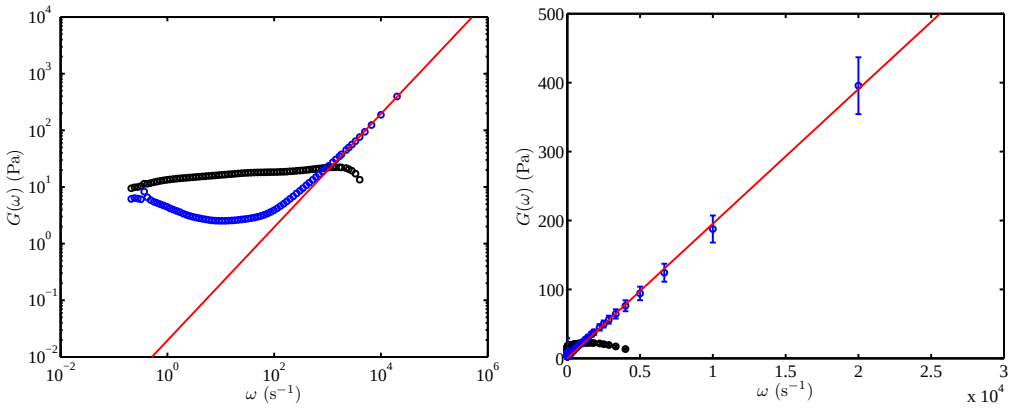

(a) Bare silica microsphere on PA hydrogel A.

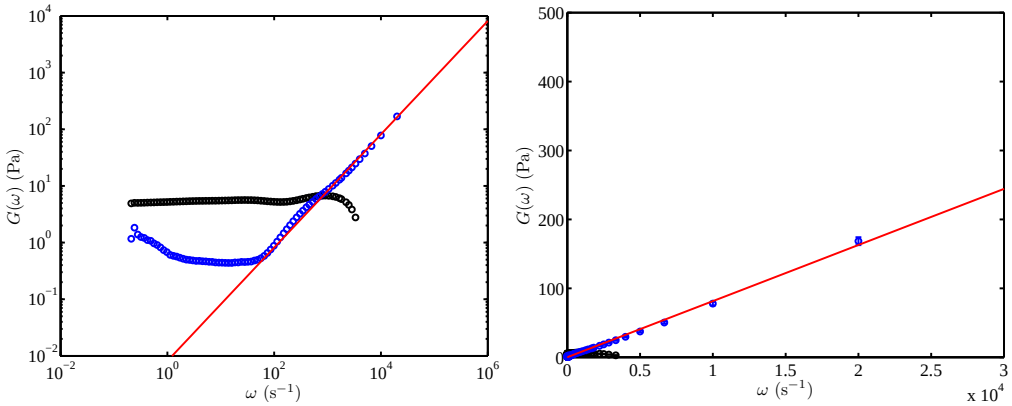

(b) Bare silica microsphere on PA hydrogel B.

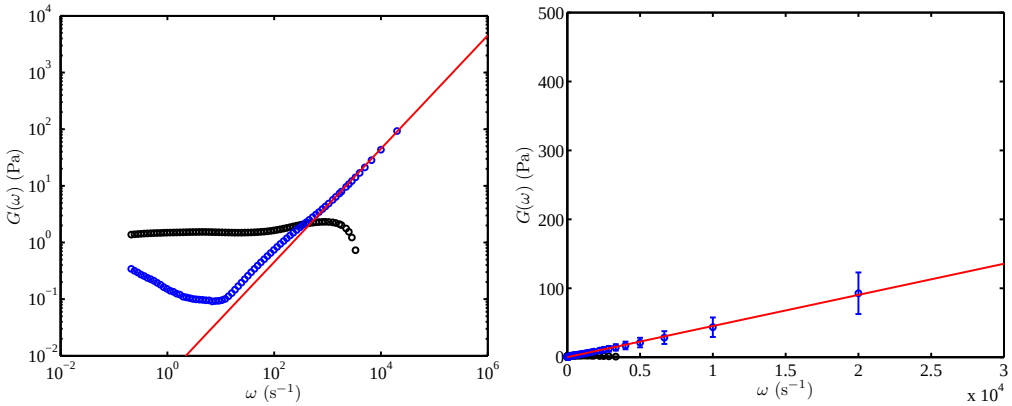

(c) Bare silica microsphere on PA hydrogel C.

Figure 5.6.7: Storage (black symbols) and loss (blue symbols) moduli obtained from passive interfacial microrheology with an optically trapped bare silica microsphere at polyacrylamide hydrogel-TAE electrolyte interfaces. The storage moduli for hydrogels A, B, and C are $G' \approx 17 \pm 3$, 6 ± 1, and 1.7 ± 0.3 Pa, respectively. The linear fits, shown with solid red lines, furnish viscosity $\eta \approx 0.0195$, 0.0081, and 0.0045 Pa s, respectively. Also, the crossover frequency $\omega_c \approx 1150$, 690, and 400 s^{-1} for gels A, B, and C, respectively.

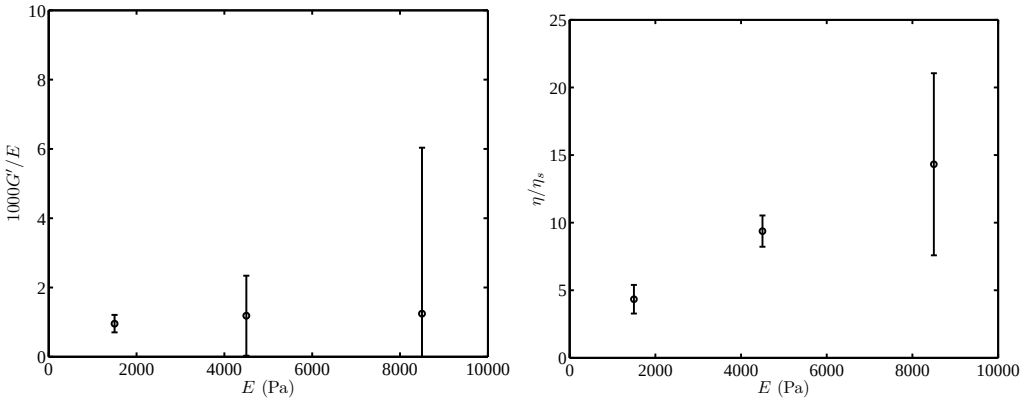

Figure 5.6.8: Storage modulus (left panel) and viscosity (right panel) versus substrate AFM elastic modulus E, obtained from passive microrheology with bare silica microspheres at PA gel-electrolyte interfaces. Normalizing the storage moduli with gel AFM Young's modulus results in $1000G'/E \approx 1$ for all the gels. The viscosity is normalized with solvent (water) viscosity $\eta_s \approx 0.0009$ Pa s, which increases when increasing gel stiffness. Note that the data points (error bars) in both panels reflect the average (standard deviation) over all the samplings over all sampling times in figure 5.6.4. Stokes-Einstein theory suggests $D_x = k_BT/(6\pi\eta R)$ resulting in $D_x/D_0 \propto \eta_s/\eta$; therefore, the corresponding diffusion coefficients to the viscosity data (right panel) $D_x/D_0 \approx 0.2$, 0.1, and 0.07 for gels C, B, and A, respectively, which are in close agreement with figure 5.6.5, left panel (a): $D_x/D_0 \approx 0.15$ (gel C), 0.1 (gel B), and 0.06 (gel A). Also, the furnished storage moduli (left panel) for gels C, B, and A, $G' \approx 1.5$, 4.5, and 8.5 Pa bring about $\langle X^2 \rangle^{1/2} = (k_BT/6\pi RG')^{1/2} \approx 12$, 7, and 5 nm, respectively, which agree with figure 5.6.5, right panel (a).

Appendix

5.A Control system

To eliminate any possible drift (*e.g.*, figure 5.4.5) within the particle position measurement pause times, position signals were recorded for 10 s using the interferometry and, simultaneously, the deviation from the set point, *i.e.*, trap centre, was calculated inside a custom-built LabVIEW interface to furnish the three-dimensional error vector. Tuning proportional, integral, and derivative gains, the optimum correction factor to achieve the fastest possible control response was obtained and fed to the nano-positioning stage to compensate the drift. The gains were set in a way that the control system becomes neither unstable nor underdamped. This methodology furnished proportional ($K_{c,x}$), integral ($\tau_{i,x}$), and derivative ($\tau_{d,x}$) in-plane gains ≈ 1, 2 s, and 10^{-5} s, respectively, which were employed simultaneously with the Z-direction controller adopting $K_{c,z} = 1$, $\tau_{d,z} = 10^{-6}$ s, and $\tau_{i,z} = 0$ s. To tune the PID controller, the integral and derivative gains were first set to zero and the proportional gain was tweaked to achieve the fastest response without instability. This resulted in the control variable (*i.e.*, particle position) oscillations in response to a stage step change (see figure 5.A.1, left panel). Then, by tuning the integral part with trial and error, the steady state error was reduced as much as possible and the resulting overshoot was corrected using the derivative part (see figure 5.A.1, right panel). An acceptable sensitivity was achieved in the perpendicular (Z) direction without using the integral part of the PID controller. To show the accuracy and sensitivity of the Z-controller, a large-step change of 1 μm (fig-

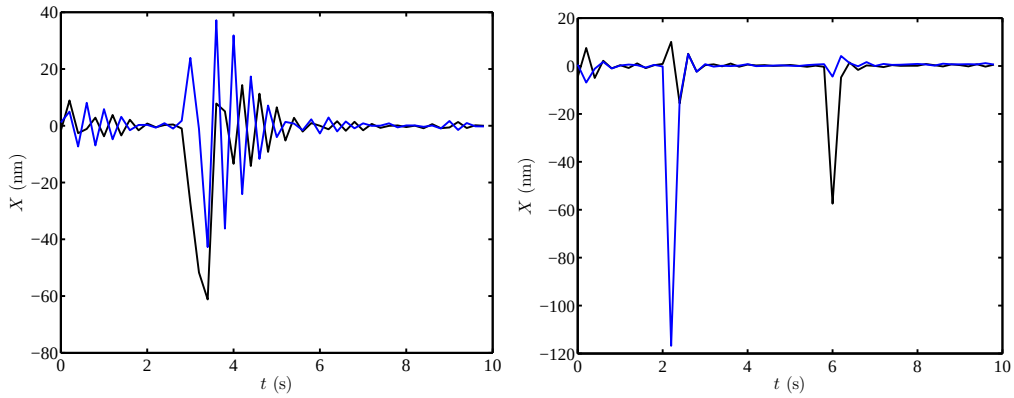

Figure 5.A.1: Colloidal microsphere centre position control using a proportional (left panel) and PID (right panel) controller. At a desired time, a position step change is introduced to the nano-positioning stage holding the sample with an attached particle on a glass substrate at physiological condition, and the response of the feed-back control system is recorded in terms of the control variable, *i.e.*, particle position. Proportional gains employed to observe oscillations are 1 and 0.6 for X and Y directions, respectively (left panel). Optimum gains to achieve a tuned feed-back control system in X, shown with black color (Y, shown with blue color) direction are: $K_p = 1$ (0.6), $\tau_i = 2$ s (0.1 s), and $\tau_d = 10^{-5}$ s. The same gains are used for gel experiments but with a proper position calibration factor.

ure 5.A.2, left panel) or -1 μm (figure 5.A.2, right panel) was introduced to the stage while the control system was running, and the control system performance was recorded in terms of the three-dimensional particle position. The particle holograms were captured at $z \approx 0$ before and after the step changes were applied, and when $z \approx 1$ or -1 μm, which were further processed to obtain the intensity profiles across the particle diameter (see insets in figure 5.A.2). Image analysis assured that the particle is brought back to the trap centre precisely by matching the intensity profiles before and after the step changes, which are shown in figure 5.A.2 insets.

5.B Bulk gel characterization

To understand bulk hydrogel rheological characteristics, *i.e.*, elastic (Young's) and shear moduli, compression tests were conducted on several hydrogel samples with various crosslinker concentrations while maintaining the monomer concentration fixed at 5 %. Using a custom-

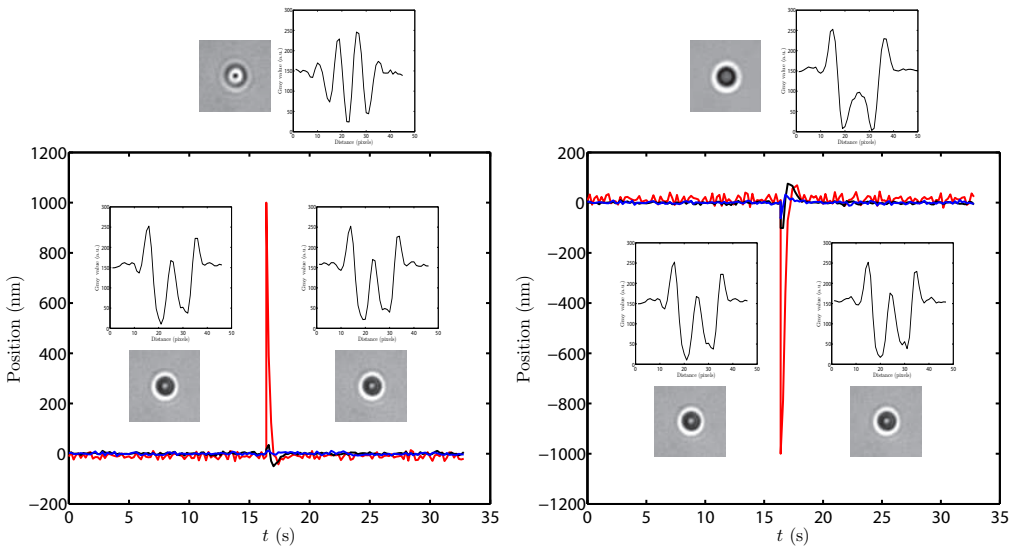

Figure 5.A.2: Z-direction dynamic particle position controller performance coupled with the in-plane (XY) controller before and after introducing a perpendicular position step input ≈ 1 μm (left panel) or ≈ -1 μm (right panel) to the stage while the goal is to maintain the particle at the trap centre in three dimensions (Z: red, X: black, and Y: blue). The insets are the holograms of a particle adhered to gel A while it is in the trap centre (position ≈ 0) or perpendicularly out of trap (left panel: trap is 1 μm below the particle, right panel: trap is 1 μm above the particle), and corresponding intensity profiles across the particle diameter. The background gray value is ≈ 150 a.u. The controller is able to accurately bring the particle to the trap centre quickly ($t \approx$ 0.6 s) even at large position drifts.

built material testing machine comprising a load cell (Model 31, Honeywell) and a displacement actuator (LTA-HL, Newport) (Chin *et al.*, 2011), perpendicular force was measured when a cylindrical gel sample was compressed, kept compressed, and got unloaded. Polyacrylamide hydrogels were synthesized using a fixed acrylamide concentration ≈ 5 % w/v mixed with various amounts of the corsslinker, bis-acrylamide. The stiffest gel, called A, was prepared by diluting a 40 % acrylamide:bis-acrylamide 19:1 stock solution. Semi-stiff, B, and soft, C, gels were synthesized by mixing the monomer and the crosslinker with ratios 33.3 : 1 w/w and 102 : 1 w/w, respectively. The pre-gel solution was chemically crosslinked according to the standard procedure noted earlier in 5.4 to assemble cylindrical hydrogel samples (diameter ≈ 10 mm, height ≈ 10 or 5 mm). A gel cylinder was placed on the instrument impenetrable unlubricated and unconfined sample holder (circle shape) and compressed at

Table 5.B.1: n^{th}-order polynomial fitting parameters for the stress-strain curve (figure 5.B.1, panel a) of 10 mm thick hydrogel A at compression speed 10 μm s^{-1}

n	ϵ_0	a_1	a_2	a_3	a_4	a_5	$E_{\epsilon\to 0}$ (kPa)
2	-0.0006	13778	16478	-	-	-	13.8
3	-0.3058	-16512	66915	-41395	-	-	12.8
4	-0.3009	-16855	70807	-50103	6133.6	-	12.8
5	-0.1808	-5537.3	-47076	779600	-2293800	2191500	11.4

a constant slow (10 μm s^{-1}) or fast (100 μm s^{-1}) rate. The whole setup was mounted on a floating antivibration table (Newport) and enclosed in a plexiglas box to minimize the environmental noise. Acquired force-displacement data were converted to stress-strain curves considering the compression area (6 mm diameter circle), sample height, and cell displacements. An example of compression and unloading stress-strain curves for hydrogel A is shown in figure 5.B.1, left panel, at a stage velocity 10 (panel a) or 100 (panel b) μm s^{-1}. As can be seen in this figure, when the gel is compressed or unloaded, its behavior is slightly different due to different structural responses. Also, stress-time plots (figure 5.B.1, right panel), show the hysteresis and a negligible relaxation while the gel is compressed.

To furnish elastic moduli at small strains, the stress-strain curves are fitted with polynomials of various orders at specified strain spans: $\sigma = \sum_{i=1}^{n} a_i(\epsilon - \epsilon_0)^i$. Quadratic, cubic, quartic, and quintic fits on the stress-strain curve at $\epsilon \leq 0.2$ for hydrogel A (figure 5.B.1, left panel), shown in black, red, green, and yellow solid lines, respectively, results in an average $E = 13.3$ kPa ($R^2 \geq 0.99$) when $\epsilon \to 0$. The fitting coefficients are presented in Table 5.B.1 and 5.B.2 for compression speeds 10 μm s^{-1} and 100 μm s^{-1}, respectively.

Another important finding is the non-draining behavior of gel A at the slow (10 μm s^{-1}) or fast (100 μm s^{-1}) compression/unloading speeds for a total sampling time of 20 or 200 s, respectively. More than 10 compression experiments on various samples of hydrogel A furnished an elastic modulus $E = 13 \pm 2$ kPa. It is noteworthy that reducing the gel thickness to 5 mm did not have any significant effect on the sample elasticity.

The effect of crosslinker (bis-acrylamide) concentration on the hydrogel stiffness was also investigated. Semi-stiff, B, and soft, C, PA gel samples with thickness $\approx$ 10 or 5 mm

Table 5.B.2: n^{th}-order polynomial fitting parameters for the stress-strain curve (figure 5.B.1, panel b) of 10 mm thick hydrogel A at compression speed 100 μm s^{-1}

n	ϵ_0	a_1	a_2	a_3	a_4	a_5	$E_{\epsilon\to 0}$ (kPa)
2	0.0017	13870	14682	-	-	-	13.8
3	−0.1632	−13868	103890	−112070	-	-	11.1
4	−0.3492	0.93	−55387	225760	191230	-	11.3
5	0.0011	16484	−117790	1803800	−9236700	231430	16.8

were prepared with the same procedure as before using ≈ 2 and 5 times lower crosslinker concentrations than gel A, respectively: ≈ 0.15 w/v % (gel B) and ≈ 0.05 w/v % (gel C). Examples of strain-stress curves (figure 5.B.2, left panel, for gel B and figure 5.B.3, left panel, for gel C) and time-stress curves (figure 5.B.2, right panel, for gel B and figure 5.B.3, right panel, for gel C) for these gels show that similar to gel A, no significant draining at low compression speeds and while compressed can be distinguished. Fitting the curves with the same various-order polynomials as for gel A results in elastic moduli $E \approx 7.4$ and 3.7 kPa with fitting accuracies $R^2 \geq 0.99$, for gels B and C, respectively. The elastic modulus of hydrogels A, B, and C versus crosslinker concentration, obtained from more than 10 tests for each gel, is plotted in figure 5.B.6. The bulk compression tests show greater elasticities compared to the reported shear modulus for gel C ($\mu_g \approx 240$ Pa) by Di Michele *et al.* (2011), and AFM nanoindentation experiments for gels A ($8.44 \leq E \leq 8.73$ kPa), B ($E \approx 4.47 \pm 1.19$ kPa), and C ($1 \leq E \leq 1.8$ kPa) (Tse & Engler, 2010). Other reported experimental data as well as the bulk rheology experiments are presented in figure 5.B.6.

To understand the gelation dynamics and the steady bulk rheological properties of PA gels, the storage and loss moduli of the pre-gel solution during gelation are measured at a constant low frequency $\omega = 10$ rad s^{-1} using an ARES-G2 rheometer, TA Instruments. The mixture of pre-gel solution and APS was nitrogen purged, and upon addition of the initiator (TEMED), a desired amount of the liquid was placed on a 4 cm diameter rheometer plate to form a circular layer of 1 mm thickness. Oscillating the sample at the constant low frequency, the storage and loss moduli versus time were measured, which are shown in figure 5.B.4. To acquire the steady moduli, a function with a general form as equation 5.12 was fitted to

the data, which furnished $G'_{t\to\infty} = A + B \approx 3617$, 2080, and 1060 Pa for gels A, B, and C, respectively:

$$G' = A \exp\left(\frac{-\tau_1}{t - t_0}\right) + B \exp\left(\frac{-\tau_2}{t - t_0}\right); A, B \geq 0 \tag{5.12}$$

These results are compared to the available literature for the closest gels to this study, which are presented in Table 5.B.3. Also, according to figure 5.B.4, the average $G'' \approx 0.1$ Pa for gels A and B at $\omega = 10$ rad s^{-1} results in a dynamic viscosity $\eta' = G''/\omega \approx 0.01$ Pa s, while gel C has $G'' \approx 12$ Pa resulting in $\eta' \approx 1.2$ Pa s. For gel A, the frequency sweep tests showed $\eta' \approx 20.24$ Pa s at $\omega = 0.126$ rad s^{-1} which decreased monotonically to $\eta' \approx 0.035$ Pa s at $\omega = 1.58$ rad s^{-1}. This follows a power-law dependency on the angular frequency $\eta' \approx 10^{-0.84}\omega^{-2.4}$. The frequency-dependent dynamic viscosity of gels A, B, and C are shown in figure 5.B.5.

Table 5.B.3: Storage (G') or Young's (E) moduli for polyacrylamide hydrogels.

G' (Pa)	E (Pa)	A %	bis-A %	Method	Reference
1060	-	5	0.05	Oscillatory shear	This work
-	3289	5	0.05	Compression	This work
-	1000	5	0.03	AFM nanoindentation	Tse & Engler (2010)
-	1800	5	0.06	AFM nanoindentation	Tse & Engler (2010)
-	1100	5	0.03	AFM nanoindentation	Engler *et al.* (2004)
-	2200	5	0.06	AFM nanoindentation	Engler *et al.* (2004)
400	-	5.5	0.05	Oscillatory shear	Yeung *et al.* (2005)
2080	-	5	0.15	Oscillatory shear	This work
-	7874	5	0.15	Compression	This work
-	4470	5	0.15	AFM nanoindentation	Tse & Engler (2010)
1800	-	5.5	0.15	Oscillatory shear	Yeung *et al.* (2005)
-	6000	5	0.15	AFM nanoindentation	Engler *et al.* (2004)
3617	-	5	0.25	Oscillatory shear	This work
-	12832	5	0.25	Compression	This work
2000	-	5.5	0.2	Oscillatory shear	Yeung *et al.* (2005)
-	7000	5	0.225	Tension	Engler *et al.* (2004)
-	7000	5	0.225	AFM nanoindentation	Engler *et al.* (2004)
-	8440	5	0.225	AFM nanoindentation	Tse & Engler (2010)
-	8730	5	0.3	AFM nanoindentation	Tse & Engler (2010)

*A and bis-A stand for "acrylamide" and "bis-acrylamide" contents, respectively.

The swelling ratio of gels A and B versus time was characterized by cutting cylindrical samples of known size upon gelation and measuring their weight change in TAE buffer by time (figure 5.B.7). Before weighing the samples, the surface water was dried using a cotton piece to prevent any mass error. Dry samples weight, m_0, was obtained by letting the hydrated gels dry for several weeks. As can be seen in figure 5.B.7, softer gel (B) reaches an higher swelling ratio, implying that it can accommodate more water inside its structural pores due to better network stretching capability ($m/m_0 \approx 20$) compared to gel A ($m/m_0 \approx 17$). Also, the non-equilibrium region, $t \lesssim 30$ h is diffusion dependent; the smaller the sample the higher the slope of swelling ratio versus time, while the equilibrium swelling is independent of the sample size. Swelling ratio of gel C could not be measured due to a very low elasticity and high stickiness.

Considering a 1D expansion of a surface-bound hydrogel and an equilibrium gel height $h \approx 25$ μm, the height of dry gel, h_0, is directly correlated with the mass swelling ratio (m/m_0), which is proportional to the volume swelling ratio λ_h:

$$\begin{aligned} \lambda_h \ &= \frac{V}{V_0} = \frac{h}{h_0} = \frac{m_0/\rho_0 + m_w/\rho_w}{m_0/\rho_0} = 1 + (m_w/m_0)(\rho_0/\rho_w) = \\ &1 + (\rho_0/\rho_w)(\frac{m - m_p}{m_0}) = 1 + (\rho_0/\rho_w)(\frac{m}{m_0} - 1), \end{aligned} \tag{5.13}$$

where subscript 0 denotes dry gel. For polyacrylamide [partial molar volume $\nu \approx 49.2$ cm^3 mol^{-1} (Day & Robb, 1981)], $\rho_0 \approx 1.44$ g cm^{-3} taking $M_w = 71.08$ g mol^{-1}:

$$\lambda_h = 1.44(m/m_0) - 0.44. \tag{5.14}$$

Accordingly, $\lambda_{h,A} = h_A/h_{0,A} \approx 24.5$ and $\lambda_{h,B} = h_B/h_{0,B} \approx 28.4$. These result in $h_{A,0} \approx 1.02$ μm and $h_{B,0} \approx 0.88$ μm. According to Kang & Huang (2010*a*), for the homogeneous swelling of gels with the assumption of an ideal polymer network, *i.e.*, shear modulus G' is linearly proportional to the effective number of polymer chains per hydrogel unit volume N, $G' = Nk_BT$; therefore, for gels A and B with AFM shear moduli $G'_A = E_A/3 \approx 2.7$ kPa and $G'_B = E_B/3 \approx 1.5$ kPa (given that the Poisson ratio of gels $\nu = 0.5$), Flory-Huggins free energy (Kang & Huang, 2010*a*),

$$\ln(1-1/\lambda_h)+1/\lambda_h+\chi/\lambda_h^2+N\nu\left(\lambda_h-1/\lambda_h\right)-\frac{\hat{\mu}-p\nu}{k_BT}=0, \tag{5.15}$$

demands an homogenous swelling: $\lambda_{h,A}\approx 12.2$ and $\lambda_{h,B}\approx 14.1$. In this calculation, the effective number of polymer chains per unit volume of gel A, $N_A\approx 6.6\times10^{23}$ m^{-3}, of gel B, $N_B\approx 3.67\times10^{23}$ m^{-3}, chemical potential $\hat{\mu}=0$ at equilibrium, solvent equilibrium vapor pressure $p=p_0\approx 2.8\times10^3$ pa at 23°C, and $\chi\approx 0.49$ (Li *et al.*, 2012*b*). Predicted volume swelling ratios by the Flory-Huggins theory furnishes smaller-than-usual values, which can be because of uncertainties in PA density, χ-parameter, and/or shear moduli. As an example, taking the density of acrylamide (1.13 g cm^{-3}), and $\chi\approx 0.45$ with the same shear moduli, swelling ratios are predicted 15.1 and 17.9 for gels A and B, which are closer to the experimental values, 19 and 22, respectively; however, according to the literature, $\chi\approx 0.49$ and $\rho_0\approx 1.44$ g cm^{-3}, which demand a much lower shear moduli than that obtained from the AFM tests.

For instance, with 1/10 of bulk shear moduli, and using $\rho_0\approx 1.44$ and $\chi\approx 0.49$, volume swelling ratios for gels A and B are predicted to be 20.8 and 23.2, respectively. Taking $\chi\approx 0.49$ and $Nv\approx 2\times10^{-5}$ and 1.1×10^{-5} for gels A and B, respectively, they fall within the "unstable" region for substrate-confined gel layers provided by Kang & Huang (2010*b*). Here, $v\approx 3\times10^{-29}$ m^3 is the volume per solvent (water) molecule. If the gel thickness is considered as the only governing length scale, the onset of wrinkling and the corresponding wavelength cannot be determined from any physical properties of the gel and solvent due to the paucity of characteristic lengths (Li *et al.*, 2012*a*). Finite values for wrinkle wavelength is resulted by taking gel surface tension, strain gradients, substrate curvature, or electrostatic forces (Li *et al.*, 2012*a*) into account. For the constraint gel swelling without considering any approaching external object (*e.g.*, a silica microsphere), gel surface tension can be used to define an elastocapillary length $L=\gamma/\mu$ (Li *et al.*, 2012*a*), where μ is gel shear modulus. Unrealistically approximating gel surface tension as water surface tension 0.073 N m^{-1}, L_A, L_B, and $L_C\approx 27$, 49, and 146 μm, respectively. Accordingly, the instability wavelengths are

calculated Li *et al.* (2012*a*) from

$$\lambda = \frac{4\pi h}{\ln(44.953h/L)}, \tag{5.16}$$

which results in wavelengths 84, 100, and 215 μm for gels A, B, and C, respectively. As the gel thicknesses are smaller than or comparable to the elastocapillary length, which is the case in this study, elastocapillary-affected interfacial instabilities are expected (Chakrabarti & Chaudhury, 2013); however, the instability wavelengths are two orders of magnitude larger than microspheres. Performing the calculation with more realistic gel surface tension, *e.g.*, $\gamma \approx 0.00075$ N m^{-1} for poly(acrylonitri1e-acrylamide-acrylic acid) hydrogels after 8 h hydrolysis (Hu & Tsai, 1996), with $\mu \approx 2.7$ kPa, elastocapillary length and wrinkle wavelength ≈ 280 nm and 38 μm, respectively. It is noteworthy that no directional alignment of particles on the gel were observed, and, instead, spontaneous local attachments took place.

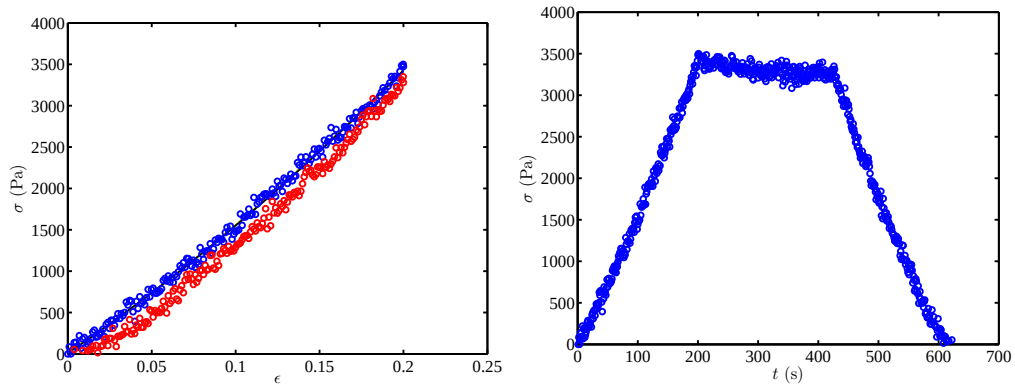

(a) Compression and unloading tests on PA gel A at 10 μm s^{-1}.

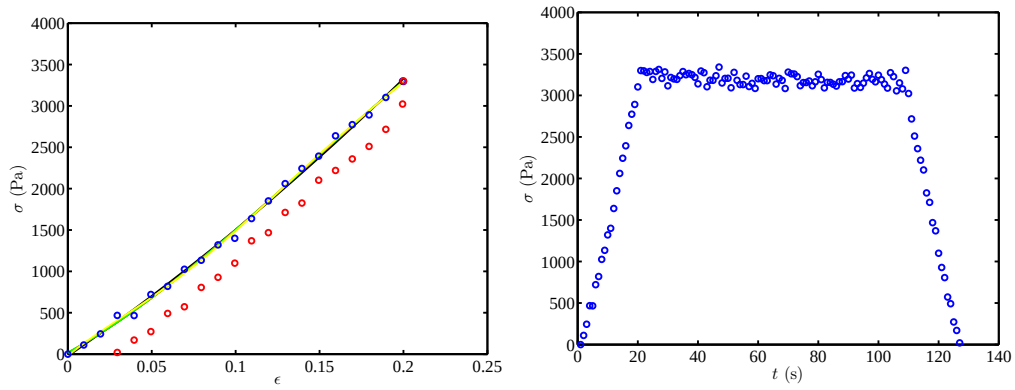

(b) Compression and unloading tests on PA gel A at 100 μm s^{-1}.

Figure 5.B.1: Compression and unloading stresses σ (blue symbols: compression, red symbols: unloading) versus strain ϵ for a 10 mm thick cylindrical PA hydrogel A comprising 5% polyacrylamide, diluted from a 19:1 w/w acrylamide:bis-acrylamide stock solution using PBS (1X) solution, at compression speeds 10 μm s^{-1} (left panel a) and 100 μm s^{-1} (left panel b), and stress σ versus time t at compression speeds 10 μm s^{-1} (right panel a) and 100 μm s^{-1} (right panel b). Fitting the data with n^{th}-order polynomials ($n = 2$, 3, 4, and 5, shown with black, red, green, and yellow solid lines, respectively) in figure 5.B.1, left panel a, furnishes the low-strain elastic modulus $E \approx 13$ kPa when $\epsilon \to 0$ with regression accuracies $R^2 \geq 0.99$. While compressed, no significant draining or relaxation can be observed. The hysteresis is obvious in figure 5.B.1, left panel.

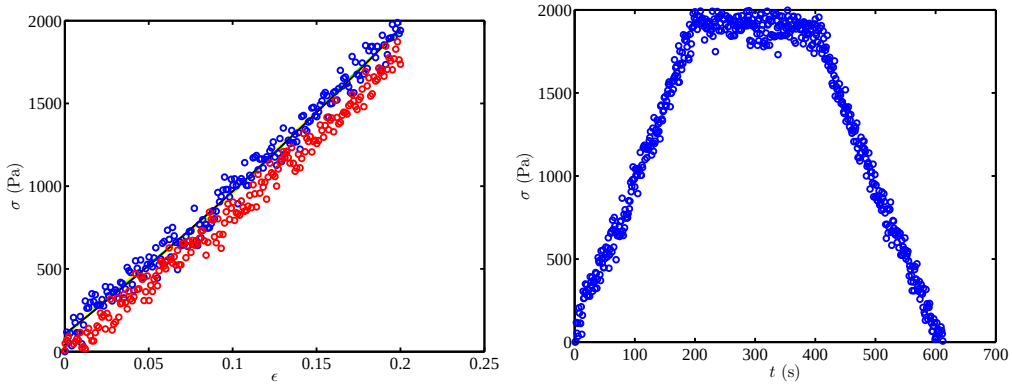

(a) Compression and unloading tests on PA gel B at 10 μm s^{-1}.

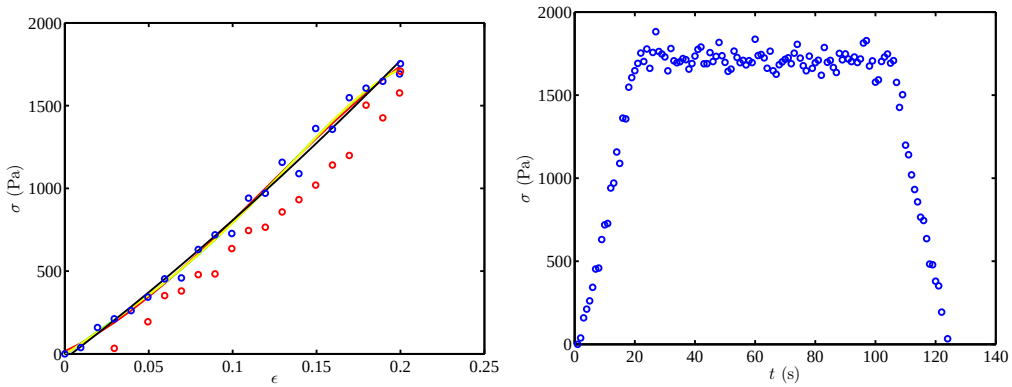

(b) Compression and unloading tests on PA gel B at 100 μm s^{-1}.

Figure 5.B.2: Compression and unloading stresses σ (blue symbols: compression, red symbols: unloading) versus strain ϵ for a 10 mm thick cylindrical hydrogel B sample comprising 5% polyacrylamide and 33.3:1 w/w acrylamide:bis-acrylamide in PBS (1X), at compression speeds 10 μm s^{-1} (left panel a) and 100 μm s^{-1} (left panel b), and stress σ versus time t at compression speeds 10 μm s^{-1} (right panel a) and 100 μm s^{-1} (right panel b). Fitting the date with n^{th}-order polynomials (in figure 5.B.2, left panel a, with $n = 2$, 3, 4, and 5, shown with black, red, green, and yellow solid lines, respectively) results in $E \approx 7.7$, 4.6, 7.6, and 6.8 kPa, respectively. Low-strain average elastic modulus (over all fittings) $E \approx 7 \pm 1$ kPa at the fast compression speed (figure 5.B.2b) and $E \approx 8$ kPa at the slow compression speed (figure 5.B.2a) when $\epsilon \to 0$ with regression accuracies $R^2 \geq 0.99$. While compressed, no significant draining and relaxation can be observed.

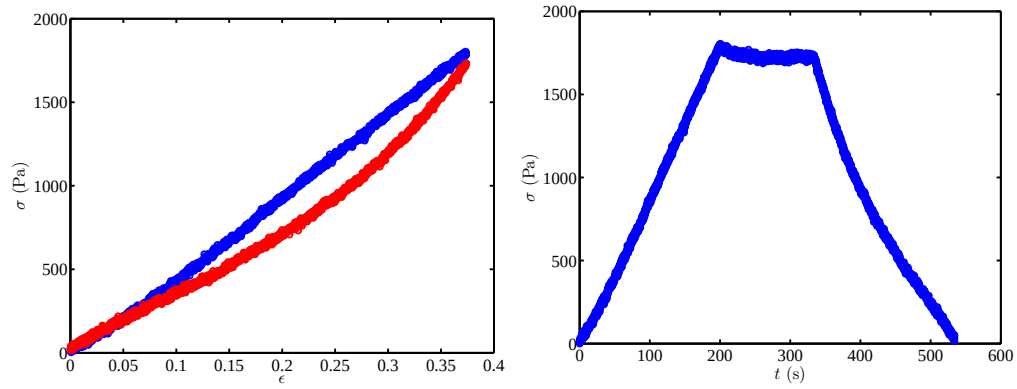

(a) Compression and unloading tests on PA gel C at 10 μm s^{-1}.

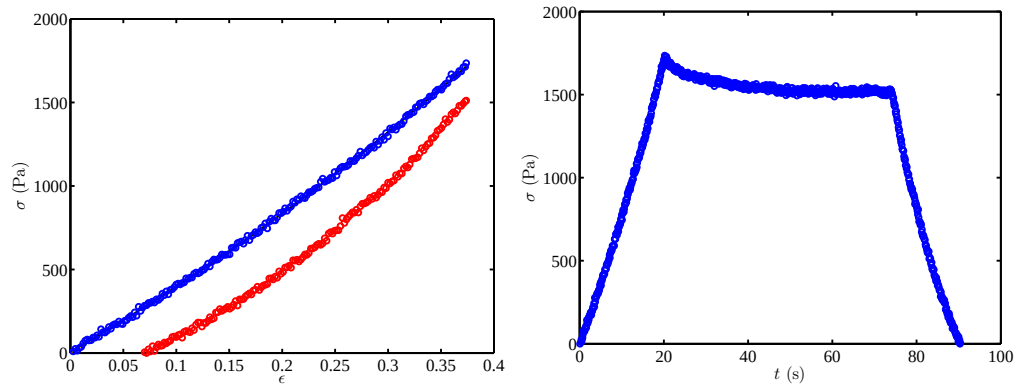

(b) Compression and unloading tests on PA gel C at 100 μm s^{-1}.

Figure 5.B.3: Compression and unloading stresses σ (blue symbols: compression, red symbols: unloading) versus strain ϵ for a 5.35 mm thick cylindrical hydrogel C sample comprising 5 % polyacrylamide and 102:1 w/w acrylamide:bis-acrylamide in PBS (1X) solution at compression speeds 10 μm s^{-1} (left panel a) and 100 μm s^{-1} (left panel b), and stress σ versus time t at compression speeds 10 μm s^{-1} (right panel a) and 100 μm s^{-1} (right panel b). Fitting the data with n^{th}-order polynomials in figure 5.B.3, left panel a (with $n = 2$, 3, 4, and 5 shown with black, red, green, and yellow solid lines, respectively) results in $E \approx 4.4$, 3.7, 3.3, and 3.4 kPa, respectively, and in figure 5.B.3, left panel b, with $n = 2$, 3, 4, and 5, $E \approx 3.6$, 3.8, 3.4, and 3.8 kPa, respectively. In figure 5.B.3, left panel, the low-strain average elastic modulus $E \approx 3.7 \pm 0.5$ kPa at the fast compression speed and $E \approx 3.7 \pm 0.2$ kPa at the slow compression speed are calculated when $\epsilon \to 0$ with regression accuracies $R^2 \geq 0.99$. While compressed, a slight decrease in the stress is obvious in figure 5.B.3, right panel. Hysteresis and the relaxation can be due to the drainage or slippage.

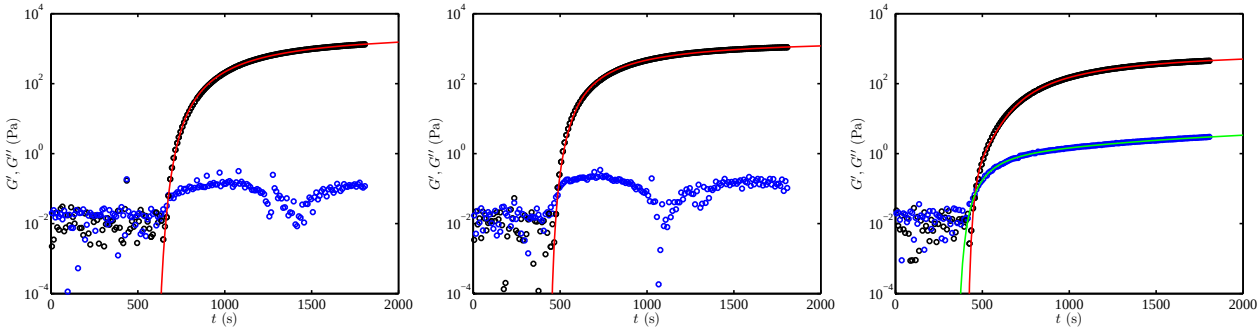

Figure 5.B.4: Storage G' (black symbols) and loss G'' (blue symbols) moduli evolution of a PA hydrogel including 5 % acrylamide in PBS buffer and various monomer:crosslinker ratios (gels A; 19 : 1, B; 33.3 : 1, and C; 102 : 1, from left to right) during gelation versus time t. Fitting the experimental G' with $A\exp\left(\frac{-\tau_1}{t-t_0}\right) + B\exp\left(\frac{-\tau_2}{t-t_0}\right)$ results in a steady shear modulus $G'_{t\to\infty} \approx 3617$, 2080, and 1060 Pa, respectively, with $R^2 \approx 0.999$. Fitting parameters are as follows: gel A: $A \approx 3145$ Pa, $B \approx 472$ Pa, $\tau_1 \approx 1252$ s, $\tau_2 \approx 1074$ s, and $t_0 \approx 566$ s, gel B: $A \approx 1928$ Pa, $B \approx 152$ Pa, $\tau_1 \approx 900$ s, $\tau_2 \approx 550$ s, and $t_0 \approx 416$ s, and gel C for G': $A \approx 396$ Pa, $B \approx 18$ Pa, $\tau_1 \approx 1217$ s, $\tau_2 \approx 345$ s, and $t_0 \approx 396$ s, and gel C for G'': $A \approx 3$ Pa, $B \approx 10$ Pa, $\tau_1 \approx 484$ s, $\tau_2 \approx 3427$ s, and $t_0 \approx 328$ s resulting in $G''_{t\to\infty} \approx 12.33$ Pa.

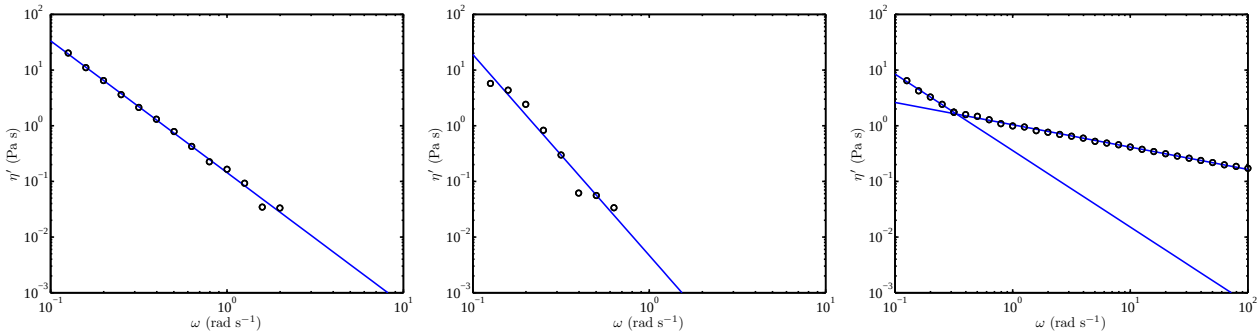

Figure 5.B.5: Shear viscosity η' versus frequency ω for PA hydrogels A, B, and C (from left to right) after ≈ 30 minutes from gelation. The dependency is well correlated by a power-law function: gel A; $\eta' \approx 10^{-0.84}\omega^{-2.4}$, gel B; $\eta' \approx 10^{-2.33}\omega^{-3.61}$, and gel C, low-frequency region; $\eta' \approx 10^{-0.45}\omega^{-1.37}$ and gel C, high-frequency region; $\eta' \approx 10^{0.017}\omega^{-0.4}$ with $R^2 \approx 0.999$.

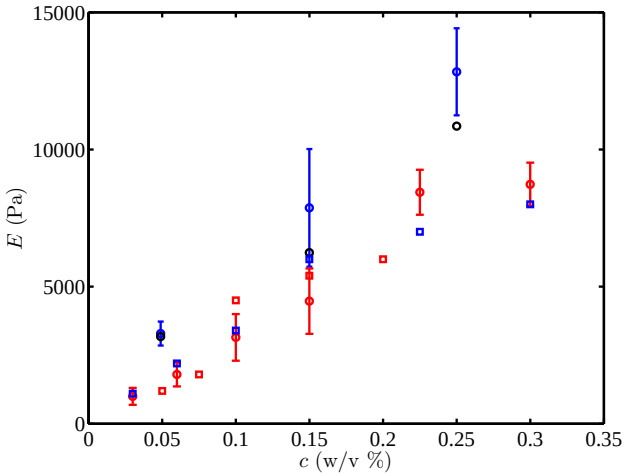

Figure 5.B.6: Effect of crosslinker (bis-acrylamide) concentration c on the elastic modulus of 5 % polyacrylamide hydrogels, obtained from compression tests (blue symbols) and bulk rheology (assuming Poisson ratio $\nu \approx 0.5$, black symbols). In compression experiments, the gels are allowed to swell in TAE buffer (pH ≈ 8.3) for at least one day before the experiments, and the moduli acquired from bulk rheology are steady ($t \to \infty$) values. Linear dependency of gel stiffness on the crosslinker concentration shows a close-to-ideal behavior. For an 8 % PA hydrogel crosslinked with various bis-A:A ratios, Calvet *et al.* (2004) reported 1261 Pa offset in G' when $c \to 0$, which is compatible with the trend of the compression tests. Red circles show the elastic moduli measured from AFM nanoindentation experiments by Tse & Engler (2010). Red squares depict elastic moduli of 5.5 % PA calculated from the shear moduli (G') reported by Yeung *et al.* (2005) considering $\nu = 0.5$, and blue squares present the Young's moduli of 5 % PA reported by Engler *et al.* (2004). As an example of the discrepancy between bulk and interfacial elasticities, for 10 % acrylamide and 0.08 % bis-A gels with thicknesses 18.3 and 165.6 μm attached to cover slips, aspiration method (Boudou *et al.*, 2006) results in $E = 7595.6 \pm 3966.2$ Pa (value exactly quoted from the reference; however this should be reported as $E = 8 \pm 4$ kPa) while tensile tests show $E \approx 12545$ Pa, and AFM-based nanoindentation provides $E \approx 3100$ Pa.

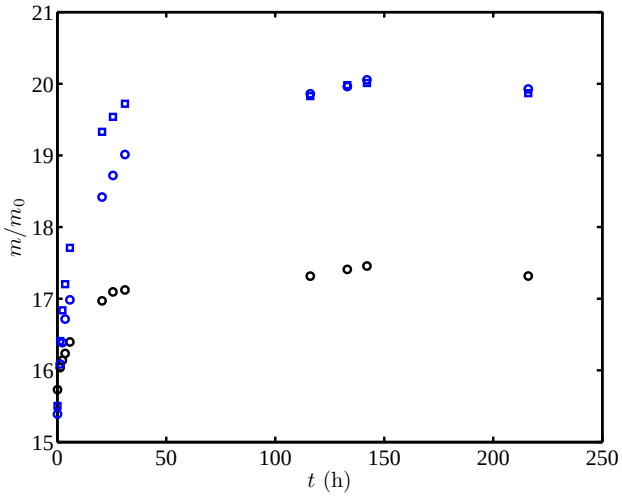

Figure 5.B.7: Mass swelling ratio (hydrogel mass at time t, m, divided by its dry mass, m_0) for gels A (black symbols, sample size $\approx 11.6 \times 8 \times 8$ mm^3, $m_{0,A} \approx 0.0482$ g) and B (blue symbols, circles: sample 1 size $\approx 16.6 \times 8 \times 8.6$ mm^3, $m_{0,B1} \approx 0.0712$ g, squares: sample 2 size $\approx 16.6 \times 8 \times 4.5$ mm^3, $m_{0,B2} \approx 0.0383$ g) versus time. The gels are allowed to swell in TAE buffer (pH $\approx$ 8.3), and surface water was wiped off with a non-sticky cotton piece before mass measurements. Four important results are: (*i*) a stiffer gel (A) has a lower equilibrium swelling ratio than a softer one (B); (*ii*) the slope of non-equilibrium region depends on the sample size: the larger the sample, the smaller the slope (*i.e.*, diffusion-controlled swelling); (*iii*) both gels reach their equilibrium state after $\approx$ 1 day; (*iv*) right after the gelation ($t < 1$ h), the hydrogels already absorbed water $\approx$ 15 times their initial mass.

Chapter 6

Active microrheology for quantifying bare silica microsphere adhesion to polyacrylamide hydrogels

6.1 Preface

Amir Sheikhi designed, conducted, and analyzed the experiments. This chapter focuses on the interfacial behavior of bare silica microspheres on swelled PA hydrogel films in TAE buffer while the probe particle is subject to an oscillatory shear. The goal is to understand how colloidal binding on a PA hydrogel with a controlled elasticity is affected by the external stimuli, such as shear rate and optical restoring force. Understanding the soft adhesion dependency on the external stimuli can help design more efficient adhering drug carriers.

6.2 Abstract

The sticking of a bare silica microsphere to PA hydrogel films with controlled elastic moduli in TAE bufer (pH $\approx$ 8.3) is studied using an optical tweezers interfacial active microrheology method in which the response of the colloidal probe to a small-amplitude oscillatory shear

is used to furnish interfacial viscoelasticity of such inclusions through phase-sensitive measurements. Depending on the substrate stiffness and external stimuli, the colloidal particle adopts one of the three possible types of viscoelastic behavior, namely elastic coupling (*i.e.*, prevailing storage modulus, also called stuck regime), viscous coupling (*i.e.*, prevailing loss modulus, also called non-stuck regime), and aging from viscosity to elasticity dominated coupling. Three PA hydrogels (A, B, and C) with the same monomer concentration (≈ 5 %) and a specified crosslinker content (bulk Young's moduli $E \approx 10.9$, 6.3, and 3.2 kPa, respectively) are used. A softer substrate is able to shift the adhesion process from elastic to viscous binding. Moreover, on the same substrate, increasing the external force on the probe increases the viscous-to-elastic moduli ratio for a stuck particle, *i.e.*, at low enough shear rates. The dissipation force per cycle is higher for a softer gel if the elastic adhesion is dominant; however, at high enough external stimuli (*e.g.*, high shear rate), such dissipation becomes independent of the substrate stiffness. Interestingly, the interfacial storage modulus (G') of a bare silica microsphere on various PA gels is correlated with the bulk gel shear modulus μ_g, resulting in $G'/\mu_g \approx (0.1 - 1) \times 10^{-3}$.

6.3 Introduction

Microorganism and cell mobility on soft substrates has been the focus of many recent experimental (Lo *et al.*, 2000; Haga *et al.*, 2005; Yeung *et al.*, 2005; Lee, 2007; Janmey *et al.*, 2009; Jannat *et al.*, 2010; Angelini *et al.*, 2011; Murrell *et al.*, 2011; Perschmann *et al.*, 2011; Hrning *et al.*, 2012; Kim *et al.*, 2012) and theoretical (Lin, 2010; Sarvestani, 2011; Zeng & Li, 2012) investigations. Colloidal particle dynamics at soft interfaces is of great importance in various fields, such as drug delivery (Wang *et al.*, 2011; Ensign *et al.*, 2012), biomedical (Lai *et al.*, 2010; Nance *et al.*, 2012) and microfluidic (Usta *et al.*, 2008) sciences, environmental engineering (Leon-Morales *et al.*, 2004; Tripathi *et al.*, 2012), and biology (Lamblet *et al.*, 2008).

When a colloidal particle approaches a soft planar interface, its dynamics are affected not only by the fluid environment, but also by the viscoelastic properties of the soft substrate. Among the most important examples are colloidal dynamics at an extracellular matrix (ECM) interface (Moshayedi *et al.*, 2010), microparticle diffusion into a bioadhesive system, *e.g.*, mucoadhesion processes (Gniewek & Kolinski, 2012), and phagocytosis (Patel *et al.*, 2012), the process of colloidal occlusion by cells. Moreover, substrate viscoelasticity plays a vital role in the mechanobiology by regulating cell behavior, *e.g.*, growth, migration, and differentiation (Wang *et al.*, 2012), response (Engler *et al.*, 2004), and occlusion (Beningo & Wang, 2002).

Mobility attenuation plays an important role in defining the behavior of freezing, pinning, and jamming systems (Sharma *et al.*, 2008). Freezing of a colloidal dispersion into a crystalline or a glassy state through an equilibrium or non-equilibrium pathway, respectively, is accompanied by the particle mobility attenuation as a response to an external stimulus, such as temperature. Altering freezing rates, Anderson & Worster (2012) were able to modify the periodic ice banding, affected by the cryosuction, a tension induced by a frozen layer on its adjacent environment. Supercooled molecular fluids tend to undergo a glass transition, and highly-concentrated colloidal dispersions tend to adopt a jamming state through which the dynamics are slowed (Ballesta *et al.*, 2008). A simple system undergoing a similar transition is the adhesion of a colloidal particle to a glass substrate, which has been characterized by Sharma *et al.* (2008) using a novel interfacial microrheology method.

While a silica microsphere adheres abruptly to a glass plate in a 20 mmol l^{-1} NaCl solution, a soft polystyrene (PS) particle adopts an aging transition from a non-stuck region to a elasticity-dominant stuck mode Sharma *et al.* (2008). Such behavior can be tailored by changing the trap stiffness, drive frequency, and ionic strength such that a PS particle undergoes a sticking, non-sticking, or aging transition on a glass substrate (Sharma *et al.*, 2008, 2010*b*). Tracking the phase lag between a sinusoidal stage displacement and an optically trapped particle inside a fluid environment, (Sharma *et al.*, 2010*a*) were able to precisely cor-

relate the lateral Brownian diffusion coefficient to the particle height: $\tan\phi = k_t D_x/(\omega k_B T)$, where ω is the drive angular frequency; however, in contact proximity to a sticky substrate, the phase lag is also affected by the restoring force from the elastic substrate.

Acquiring an optically trapped particle response (x_p) to an external oscillatory shear, introduced by the sinusoidal movement of a stage (x_s), Kumar *et al.* (2012) suggested two parameters, namely elastic (k') and viscous (k'') coupling factors, relating the binding viscoelasticity to the imaginary $\mathrm{Im}(x_p)$ and real $\mathrm{Re}(x_p)$ parts of the response:

$$k' = G'\xi = k_t \frac{\mathrm{Re}(x_p)\,|x_s| - |x_p|^2}{[|x_s| - \mathrm{Re}(x_p)]^2 + \mathrm{Im}(x_p)^2}, \tag{6.1}$$

$$k'' = G''\xi = k_t \frac{\mathrm{Im}(x_p)\,|x_s|}{[|x_s| - \mathrm{Re}(x_p)]^2 + \mathrm{Im}(x_p)^2}, \tag{6.2}$$

where ξ is a phenomenological length scale representing the hydrodynamic and adhesive properties of the contact region. Dynamics of these coupling factors furnish Cole-Cole plots in which G'' is plotted versus G' by taking $\xi = 6\pi R$, where R is the particle radius, to track the viscoelastic evolution of PS particle-glass substrate binding (Sharma *et al.*, 2010*b*) originated from the gradual formation of polymer tethers between the surfaces.

In this chapter, the passive interfacial microrheology is extended by subjecting an optically trapped bare silica microsphere to an external small-amplitude oscillatory shear while bringing it to the contact proximity of a PA hydrogel film to achieve active interfacial microrheological properties. The goal is to understand the particle mobility and coupling as a function of separation, while elevated, and as a function of time when it is allowed to contact the gel. The effort is to characterize the viscoelastic coupling between the microsphere and the deposited planar hydrogel layer using the particle response to the substrate in-plane oscillatory movements by means of phase-sensitive measurements. Viscous and elastic components of the particle response are calculated accordingly, and the coupling is expressed within a generalized viscoelastic response theme, which is further employed to establish

adhesion phase diagrams.

6.4 Materials and methods

Bare silica microspheres and hydrogels were prepared using the same methods detailed in chapter 5. The same optical tweezers setup as in chapter 5 was modified to conduct active interfacial microrheology experiments. Briefly, the customized gel-coated channel is placed tightly on the microscope stage, which is vertically translated with desired nanometer-precision increments to control the nano-spacing between the optically trapped microsphere and the hydrogel layer. The optically trapped microsphere position fluctuations were acquired by directing the interference of the transmitted and scattered light through the microscope condenser onto a quadrature photo diode (QPD, Spot-9dmi, OSI Optoelectronics, CA, U.S.A.). This is known as the back-focal plane interferometry. The QPD voltage signals were amplified using a dual-axis position-sensing amplifier (501C, UDT Instruments, CA, U.S.A) and fed to a phase-sensitive lock-in amplifier (SR830, Stanford Research Systems, CA, U.S.A.). Simultaneously, a small-amplitude sinusoidal signal is generated using a signal generator (AFG310, Tektronix, Inc., OR, U.S.A.) and used to drive the nano-positioning stage, which is further employed as the reference input to the lock-in amplifier to be compared with the particle response. The setup is similar to (Mohammadi, 2011).

The acquired particle position is compared to the reference signal using the lock-in amplifier to furnish the real and imaginary parts of the particle position response to the external oscillatory shear. Note that the generic nanostage phase lag and amplitude attenuation were independently identified at the working frequencies (shown in Table 6.1), and the furnished phase lags in the gel experiments were corrected accordingly.

To obtain the frequency response of nanostage, it was driven sinusoidally with a fixed amplitude ($|x_{s,0}| \approx 28.3$ nm) and variable frequencies. The drive was swept from the lowest ($f = 8$ Hz) to the highest ($f = 256$ Hz) desired frequency, and the steady state response, in

Table 6.1: Stage response phase ϕ_s and amplitude $|x_s|$ at various sinusoidal input frequencies f, normalized with the nominal input amplitude $|x_{s,0}| \approx 28.3$ nm.

f (Hz)	8	16	32	64	128
$\|x_s\| / \|x_{s,0}\|$	1	1	0.985	0.923	0.725
$-\phi_s$ (degrees)	4.05	10.80	23.11	46.10	85.73

terms of the magnitude and phase lag, was acquired using the lock-in amplifier by comparing the drive input to the stage controller with the stage controller output. The corresponding state-space model to the stage response (Ljung, 1999)

$$\dot{x} = ax(t) + bu(t);\ y(t) = cx(t) + du(t), \tag{6.3}$$

where x is the state of system, $\dot{x}$ is the state time change of system, y denotes the system output, and u presents the system input. Coefficients a, b, c and d are state-space matrices, which are obtained using *fitfrd* provided by the Robust Control Toolbox in Matlab. These coefficients in Eqn. 6.3, $a = (-4458,\ 2371;\ -3902,\ 1667)$, $b = (11.96;\ 35.31)$, $c = (198.9,\ -99.44)$, and $d = (0.0842)$. The state-space function is, then, converted to its equivalent transfer function using *ss2tf* syntax. The transfer function in terms of the Laplace transform is readily furnished in the frequency domain

$$G(s) = \frac{Y(s)}{X(s)} = c(sI - a)^{-1}b + d = \frac{0.0842s^2 - 897.3s + 1.828 \times 10^6}{s^2 + 2791s + 1.822 \times 10^6}, \tag{6.4}$$

where $G(s)$ is the system transfer function, *i.e.*, the Laplace form of the system output $Y(s)$ over input $X(s)$, I is the identity matrix, and $s = i\omega$. The experimental data and modeled response magnitude and phase are plotted in figure 6.4.1. Note that, such a transfer function in the frequency domain corresponds to the summation of two exponential functions in the time domain.

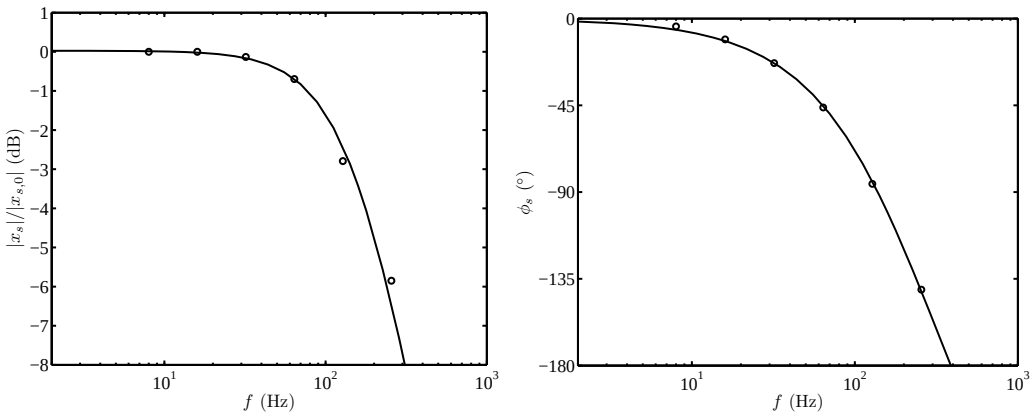

Figure 6.4.1: Bode plots: the nanostage frequency response to sinusoidal drive inputs with a fixed amplitude $|x_{s,0}| \approx 28.3$ nm in terms of the magnitude (left panel) and phase lag (right panel). The corresponding transfer function $G(s) = \frac{0.0842s^2-897.3s+1.828\times10^6}{s^2+2791s+1.822\times10^6}$ to the experimental data (symbols) is obtained using a state-space fit to the data and converting it to the frequency-domain transfer function in Matlab. Note that the response magnitude (left panel) is presented in decibel: $20 \times \log_{10}(|x_s|/|x_{s,0}|)$.

6.5 Theory

Neglecting the inertial and Brownian forces, the equation of motion for an optically trapped particle in a viscoelastic medium is

$$-k_t x_p - \gamma^*(\dot{x}_p - \dot{x}_s) = 0, \tag{6.5}$$

where x_p and x_s are the particle and substrate positions, respectively, k_t is the optical trap stiffness, and γ^* is the (complex) friction coefficient. With harmonic forcing, $x_s = \hat{x}_s \exp(i\omega t)$, the particle response $x_p = \hat{x}_p \exp(i\omega t)$; therefore,

$$\gamma^* = \frac{k_t}{i\omega}\frac{S^*}{1-S^*}, \tag{6.6}$$

where $S^* = \hat{x}_p/\hat{x}_s = S' + iS''$ is the experimentally measured quantity termed the dynamic susceptibility. Note that $\tan\phi = S''/S'$, where ϕ is the phase lag.

It is expedient to present the friction coefficient in terms of either a complex shear vis-

cosity $\eta^* = \eta' - i\eta''$ or shear modulus $G^* = G' + iG'' = i\omega\eta^*$ via

$$\gamma^* = 6\pi R\eta^* = 6\pi RG^*/(i\omega). \tag{6.7}$$

Thus, the complex viscosity is defined above so that $G' = \omega\eta''$ and $G'' = \omega\eta'$. For example, if the particle is positioned far from the substrate, then $\eta^* \to \eta'$ and $G^* \to G'' = \omega\eta'$; and if the particle is completely embedded in the substrate, then $G^* \to \mu$ and $\eta^* \to -i\eta'' = \mu/i\omega$. Here η' is the solvent shear viscosity, η'' shows the substrate out-of-phase viscosity, and μ is the substrate shear modulus.

Dimensional analysis permits the complex viscosity to be expressed as

$$\eta^* = \eta f(\Pi_1, ..., \Pi_7) \tag{6.8}$$

where f is a dimensionless function of the following 7 dimensionless parameters, depending on 11 dimensional parameters involving 4 dimensions: $\mu^*(\omega)$, η, h, w, R, $\hat{x}_s$, ω, k_t, $\Delta\rho_p g$, and $k_B T$. Here, h is the gap between the particle and the interface (a more precise definition for h should consider the distance between the trap centre and the substrate, because the probe particle undergoes perpendicular fluctuations while it is optically trapped), w is the interfacial adhesion energy per unit area, $\Delta\rho_p g R^3$ scales the buoyancy force, and $k_B T$ is the thermal energy. Thus, a set of independent dimensionless parameters is: $\Pi_1 = \omega\eta/\mu^*(\omega)$, $\Pi_2 = k_t/[\mu^*(\omega)R]$, $\Pi_3 = h/R$, $\Pi_4 = \hat{x}_s/h$, $\Pi_5 = k_B T/(wR^2)$, $\Pi_6 = \Delta\rho g R^2/k_t$, and $\Pi_7 = k_B T/[\mu^*(\omega)R^3]$. η^*/η is independent of the trap stiffness by normalizing it by the dimensionless number $k_t/(\omega R\eta)$. The complete adhesion phase diagram can be constructed by sweeping all these dimensionless groups in a desired range of operating condition, which is experimentally unfeasible.

Rheological behavior of a viscoelastic material can be explained by a simplified physical model, comprising a spring (stress $\sigma = k_m\epsilon$), to impart the elastic response, and a dash pot (stress $\sigma = \eta_m\dot{\epsilon}$), to express the viscous response, in series, known as the single-mode

Maxwell model (Ferry, 1980). The constitutive equation governing the stress and strain ϵ for such system (Drozdov, 1998) is

$$\frac{1}{\tau}\sigma_m + \dot{\sigma}_m = k_m\dot{\epsilon}, \tag{6.9}$$

where m denotes the Maxwell model with relaxation time $\tau = \eta/k_m$ and spring stiffness per unit length k_m (*i.e.*, material shear modulus μ). The derivation of Eqn. 6.9 is presented in Appendix 6.A.

The Maxwell model can fit the viscoelastic response of a material under a small-amplitude oscillatory shear (SAOS); however, for an interfacial inclusion, when the drive frequency is increased, the shear force on the particle increases, which may result in complete particle detachment from the substrate. In this case, the relaxation time decreases rapidly, resulting in decreased and non-zero dimensionless relaxation time $\omega\tau = G'/G''$, which corresponds to a non-zero storage modulus when $\omega\tau \to 0$. However, according to the Maxwell model, $G' \to 0$ when $\omega\tau \to 0$. This shortcoming in the Maxwell model can be compensated by considering a system of a parallel spring (denoted with subscript e) with the standard Maxwell system (denoted with subscript m), known as the standard linear solid (SLS) model. The schematic of the SLS system is shown in figure 6.5.1, left panel.

In the SLS model,

$$\sigma = \sigma_m + \sigma_e, \tag{6.10}$$

and

$$\epsilon = \epsilon_e = \epsilon_m, \tag{6.11}$$

where

$$\sigma_e = k_e\epsilon. \tag{6.12}$$

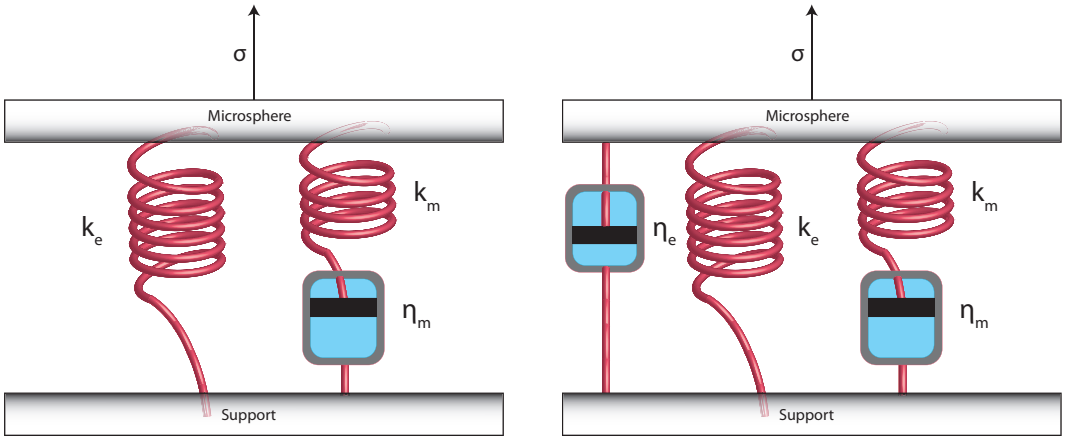

Figure 6.5.1: (left panel) The standard linear solid (SLS) viscoelastic model, comprising a standard Maxwell system (shown with subscript m) parallel to a spring (shown with subscript e). (right panel) The extended standard linear solid (ESLS) viscoelastic model comprising the standard Maxwell system parallel to the Kelvin-Voigt model.

A sinusoidal strain $\epsilon = \epsilon_0 \exp(i\omega t)$ results in $\sigma = \sigma_0 \exp(i\omega t)$, giving rise to

$$\sigma = \frac{k_m \epsilon i\omega}{i\omega + \frac{1}{\tau}} + k_e \epsilon, \tag{6.13}$$

and

$$G^* = \sigma/\epsilon = k_e + \frac{k_m \left[i\omega\tau + (\omega\tau)^2\right]}{1 + (\omega\tau)^2}, \tag{6.14}$$

so

$$G' = k_e + k_m \frac{(\omega\tau)^2}{1 + (\omega\tau)^2}, \tag{6.15}$$

and

$$G'' = k_m \frac{\omega\tau}{1 + (\omega\tau)^2}. \tag{6.16}$$

Note that $\lim_{\omega\tau\to 0} G' = k_e$ and $\lim_{\omega\tau\to\infty} G' = k_e + k_m$. Equations 6.15 and 6.16, termed as the SLS model, are used to fit the active interfacial data in the next section.

When probing the viscoelastic properties of a gel layer at a fluid interface, it is expected that in case of an extreme external force, the probe microsphere is decoupled from the interface, which results in probing the properties of the fluid in the contact proximity of the

gel layer. Therefore, the SLS model, which suggests $\lim_{\omega\tau\to 0} G'' = 0$ breaks down (this will be experimentally investigated in this chapter, *e.g.*, see figure 6.6.12). To compensate the SLS model shortcoming, arising from the fluid effect at the interface, an extended model, keeping the storage modulus the same as Eqn. 6.15, is suggested:

$$G'' = k_m \frac{\omega\tau}{1+(\omega\tau)^2} + \frac{k_e}{\omega\tau_e}, \tag{6.17}$$

in which, $\lim_{\omega\tau\to 0} G'' = k_e/(\omega\tau_e) = G'_t/(\omega\tau_e) = G''_s$, where, subscripts t and s stand for the optical trap and the solvent, respectively. The physical interpretation of this model is a system of a parallel dash pot and the SLS, *i.e.*, parallel Maxwell and Kelvin-Voigt models. The extended SLS model (ESLS) is employed to fit the viscoelastic data, which is compared to the SLS model in the next section.

6.6 Results and discussion

In this section, first, the possible coupling modes between a bare silica microsphere and PA hydrogel are discussed in sub-section 6.6.1, and, then, the comprehensive active microrheology results are presented and discussed in sub-section 6.6.2.

6.6.1 Typical behavior of a stuck, aging, and non-stuck bare particle in PA gel vicinity

To present a general perspective of active interfacial microrheology, three possible types of soft adhesion modes, namely elastic (stuck, $G' > G''$), aging (viscous-to-elastic transition, $G'' > G'$ to $G' > G''$), and viscous (non-stuck, $G'' > G'$) coupling are explained in terms of measurable parameters in the active interfacial microrheology experiments with a bare silica microsphere at a PA hydrogel interface in TAE buffer. To achieve these regimes, combinations of gel stiffness, drive frequency, and optical trap stiffness are selected. Phase

lag $\tan\phi$, particle position real $\mathrm{Re}(x_p)$ and imaginary $\mathrm{Im}(x_p)$ responses, storage G' and loss G'' moduli, dynamic viscosity η', out-of-phase viscosity η'', zero-shear viscosity $\eta_0 = \eta'\left[1+(\omega\tau)^2\right]$, and the Maxwell relaxation time $\tau = \eta''/G''$ are presented versus particle height (defined as the gap size between the optically trapped particle and the deposited hydrogel film surface) for an elevated particle ($z > 0$), and versus time when the particle adheres to the gel ($z = 0,\ t \geq 0$).

To study the diffusivity of a bare silica microsphere near a planar hydrogel layer deposited on a glass cover slip, the phase lag between an optically trapped particle and an external oscillatory shear drive is recorded at various particle heights z (for an elevated particle) or times t (for an adhered particle to the gel), as shown in figure 6.6.1, left panel. Specified combinations of trap stiffness, external drive frequency, and bulk substrate Young's modulus (k_t, f, E) are used to achieve stuck (case 1, black symbols: 24 μN m^{-1}, 8 Hz, 10.9 kPa), aging (case 2, red symbols: 9 μN m^{-1}, 32 Hz, 6.3 kPa), and non-stuck (case 3, yellow symbols: 18 μN m^{-1}, 64 Hz, 6.3 kPa) regimes.

For an elevated particle, considering a constant trap stiffness within a 1 μm particle-hydrogel gap, the phase lag decreases by a factor of ≈ 0.6 from $z \approx 1$ μm to $z \approx 20$ nm. This is the result of an increased effective particle size due to the wall hydrodynamic friction. Such a reduction is predicted by the Faxen (1923) theory $D_{x(z=20\text{ nm})}/D_{x(z=1000\text{ nm})} \approx 0.47$ for a rigid wall. The difference can be because of slip-flow over the microsphere, arising from the neighboring Brinkman medium (porous hydrogel) (Damiano *et al.*, 2004). Upon touching the hydrogel, the normalized phase lag with the bulk value at $z \approx 20$ nm reduces immediately to ≈ 0.01, 0.2, and 0.3, for cases 1, 2, and 3, respectively. While the phase lag remains almost constant with time for cases 1 and 3, it decreases to ≈ 0.15 of the bulk value for case 2 (aging) in ≈ 200 s. Note that if a microsphere is completely stuck to a substrate, the phase lag between its response and the stage displacement adopts values ≈ 0, resulting in a complete in-phase response of the microsphere to the external drive, *e.g.*, for a silica microsphere adhered to a glass slide in an high ionic strength electrolyte.

The phase lag is an indirect indication of the transverse Brownian diffusion coefficient (Eqns. 6.53 and 6.57). The normalized diffusion coefficient D_x with the bulk diffusion coefficient $D_0 \approx 0.25\ \mu\text{m}^2\ \text{s}^{-1}$ versus height (for an elevated particle) and time (for an adhered particle to a gel) is shown in figure 6.6.1, right panel. While the normalized diffusion coefficient D_x/D_0 decreases with decreasing particle height z to ≈ 0.5 at $z \approx 20$ nm, it is immediately attenuated to 0.2, 0.6, and 0.0015, for cases 1, 2, and 3, respectively, suggesting that the microsphere interfacial transverse diffusion coefficient can be tuned by changing the operating conditions mentioned earlier. The large phase lag fluctuations of an elevated particle at a low frequency ($f = 8$ Hz, black symbols) do not permit accurate diffusion coefficient measurements in the unbound electrolyte.

Besides the phase lag, the amplitude of microsphere response to an external drive indicates the extent to which the particle is displaced by the oscillatory shear exerted by the fluid. Real $\text{Re}(x_p)$ and imaginary $\text{Im}(x_p)$ parts of a bare silica microsphere response for the same cases as in figure 6.6.1 are calculated from the acquired phase lag and amplitude using the phase-sensitive measurements, which are demonstrated in figure 6.6.2. When the microsphere is in the bulk solution, it experiences viscous drag from the fluid environment and an elastic restoring force from the optical trap. The former results in a frequency-dependent imaginary (out-of-phase) response, and the later takes the real (in-phase) part of the response. When a silica microsphere contacts the hydrogel, depending on the adhesion strength, the real part increases immediately, suggesting an elastic coupling between the probe particle and gel. Such an increase is approximately one order of magnitude for the stuck (elastic coupling) case (black symbols), and three times for the non-stuck (viscous coupling) case (yellow symbols). The normalized imaginary response with the drive amplitude (figure 6.6.2, right panel) decreases versus time for the aging case, adopting a steady value ≈ 0.1. The non-stuck case is associated with no significant change in the imaginary response, while in the stuck case, the imaginary response decreases upon touching the gel surface. Real and imaginary responses furnish the interfacial viscoelasticity of the soft inclusion.

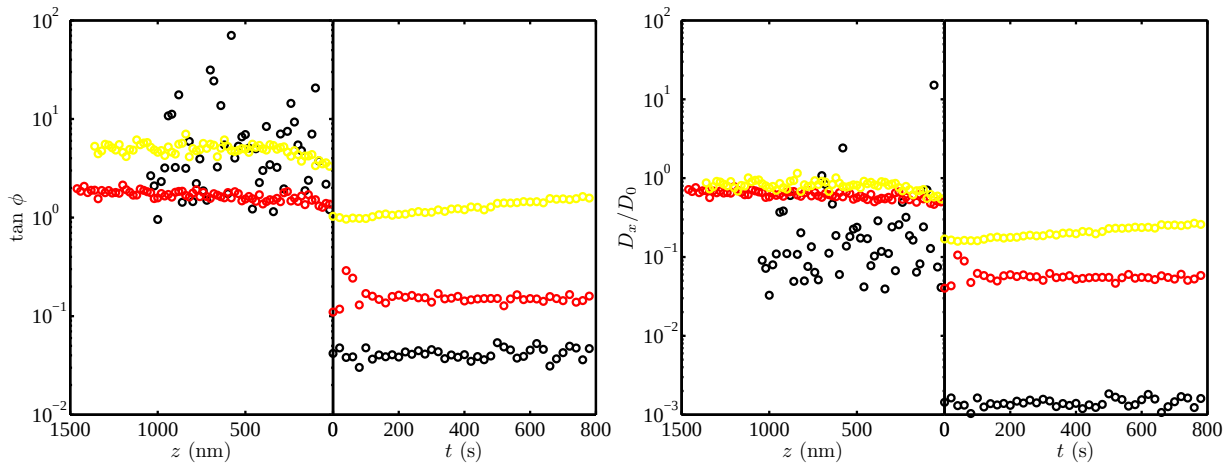

Figure 6.6.1: Examples of viscous, aging, and elastic soft coupling of a bare silica microsphere to a PA gel film in terms of the phase lag (left panel) and effective transverse diffusion coefficient $D_x = 2\pi f k_B T \tan(\phi)/k_t$ (right panel). An optically trapped bare silica microsphere (at an specified trap stiffness k_t) is brought in contact with a gel film (Young's modulus E), and the phase lag is furnished when approaching ($z > 0$) and while attached ($t > 0$) to the substrate. The microsphere response to an external oscillatory shear (with a specified drive frequency f) is recorded when it is brought to the hydrogel vicinity in 20 nm increments using a 3D nano-positioning stage coupled with a feed-back control system. Upon touching the substrate, the stage height is fixed, and the particle response in terms of phase lag and amplitude is acquired using the phase-sensitive measurements. The solution comprised TAE buffer: pH $\approx$ 8.3 and ionic strength 41 mmol l^{-1}. For an attached particle to a gel, depending on the optical trap stiffness, oscillatory shear frequency, and substrate stiffness, three coupling modes, namely elastic (case 1: black symbols, $k_t \approx 24$ μN m^{-1}, $f = 8$ Hz, $E \approx 10.9$ kPa), aging (case 2: red symbols, $k_t \approx 9$ μN m^{-1}, $f = 32$ Hz, $E \approx 6.3$ kPa), and viscous (case 3: yellow symbols, $k_t \approx 40$ μN m^{-1}, $f = 64$ Hz, $E \approx 6.3$ kPa) are observed. The phase lag on the hydrogel surface is reduced by more than one order of magnitude for the elastic case, resulting in $D_x/D_0 \approx 10^{-3}$, while gels B and C attenuate the interfacial transverse diffusion coefficient $D_x/D_0 \approx 0.05$ and ≈ 0.2, respectively. Note that the diffusion coefficient attenuation when approaching the interface ($z = 0$) is a result of an increased hydrodynamic drag on the microsphere originated from the gel wall.

To express the real and imaginary responses as physical parameters, storage modulus G' (black, red, and yellow symbols, for cases 1, 2, and 3, respectively) and loss modulus G'' (blue, green, and magenta symbols, for cases 1, 2, and 3, respectively), are calculated from Eqns. (6.39) and (6.40) and presented in figure 6.6.3. For an optically trapped microsphere in the bulk fluid and far from a gel layer, loss modulus attains values higher than the storage modulus, suggesting a viscous environment, *i.e.*, the electrolyte, with an elastic response

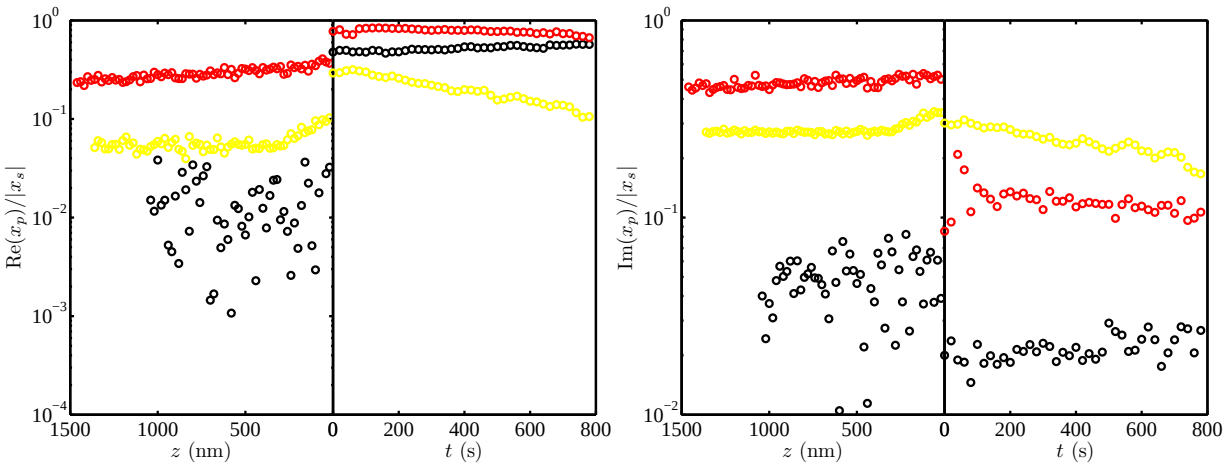

Figure 6.6.2: Examples of viscous, aging, and elastic soft coupling of a bare silica microsphere to a PA gel film in terms of the (left panel) real (in-phase) and (right panel) imaginary (out-of-phase) parts of the particle position response to an external oscillatory shear, normalized with the stage small-amplitude sinusoidal input ($|x_s| \approx 30$ nm, see Table 6.1). The color legend is the same as figure 6.6.1. As soon as the particle contacts the hydrogel, depending on the gel elastic modulus, optical trap stiffness, and drive frequency, the real response increases up to an order of magnitude for the elastic adhesion (black symbols) or only three times for the viscous coupling (yellow symbols). The imaginary part of the response shows a dynamic decay for the aging microsphere-hydrogel adhesion (red symbols, $t > 0$), while it abruptly decreases in the case of an elastic adhesion (black symbols, $t > 0$) and remains within the same range of the bulk values for the viscous coupling (yellow symbols, $t > 0$). The dynamic behavior implies the time change of interfacial viscoelastic properties.

that is only originated from the optical restoring force trapping the microsphere. Once the probe particle is attached to a gel, for the elastic adhesion (case 1), G' (black symbols) is immediately saturated to values approximately two orders of magnitude higher than the bulk values, while G'' (blue symbols) does not change significantly, maintaining G' always higher than G''. Such inclusion attains an interfacial storage modulus $G' \approx 1$ Pa, considering an effective length scale that is equal to the particle radius $R \approx 1$ μm; however, G' seems to be much higher than this value due to a nanometer scale adhesion length scale ($\xi \ll 1$ μm) according to Eqn. 6.1. For the viscous adhesion (case 3), the storage modulus (magenta symbols) remains the same order as the bulk fluid while the loss modulus (yellow symbols) increases several times upon touching the gel, maintaining $G'' > G'$ at $t > 0$ s. The aging case is associated with a dynamic change in the viscoelastic moduli, such that the storage

modulus (red symbols) increases to plateau, and the loss modulus (green symbols) increases to cross over the storage modulus at $t \approx 200$ s, then, decreases by time, producing a transition from viscous to elastic binding. Note that the crossover of the storage and loss moduli, for the aging case, takes place when the storage modulus reaches its maximum value $\approx$ 1 Pa.

To investigate whether the particle-gel adhesion at a specified operating condition follows the Maxwell viscoelastic material model (a spring and dash pot connected in series), G' and G'' are plotted versus $\omega\tau$ $(= G'/G'')$ in figure 6.6.4. For the aging case, G' (red symbols) and G'' (green symbols) cross over at $\omega\tau = 1$, when G' is maximum, showing that the adhesion follows a Maxwell viscoelastic model. On the other hand, for a non-stuck case (viscous coupling), not only the storage (yellow symbols) and loss (magenta symbols) moduli never cross, they also do not show significant aging within $\omega\tau < 1$, showing that the loss modulus always attains higher values than the storage modulus. The main characteristic of a stuck case (elastic adhesion) is that both G' (black symbols) and G'' (blue symbols) remain in the $\omega\tau > 1$ region, so that interfacial storage modulus is always higher than the loss modulus.

Moreover, taking an adhesion length scale $\xi \approx 6\pi R$, and using the storage and loss moduli, the dynamic η' and out-of-phase η'' viscosity are presented in figure 6.6.5. When the particle is optically trapped in an unbound fluid, the dynamic viscosity attains values close the viscosity of water, which increases when decreasing the particle height because of the gel-wall hydrodynamic interaction. Upon particle-gel contact, η' undergoes small changes with time, remaining comparable to the bulk values for the case 1 (black symbols) and 3 (yellow symbols); however, in the aging case (red symbols), a rise-and-fall is observed. The resulting values of dynamic viscosity are smaller than obtained from passive interfacial microrheology. The out-of-phase viscosity, however, saturates to $\approx$ 1, $\approx$ 10, and $\approx$ 30 times the solvent viscosity for the viscous (yellow symbols), aging (red symbols), and elastic (black symbols) coupling cases, respectively.

The zero-shear viscosity (calculated from the Maxwell model: $\eta_0 = G''/\omega + G''\tau^2\omega$) and the Maxwell relaxation time $\tau = G'/(G''\omega)$ are presented in figure 6.6.6. While the actual

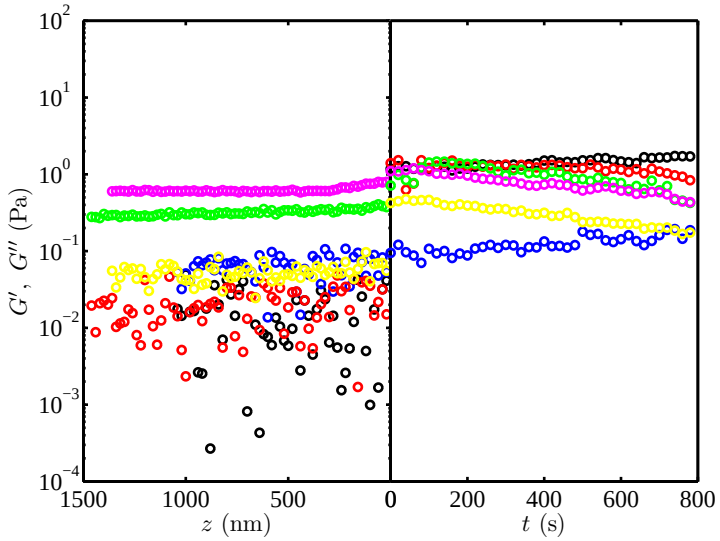

Figure 6.6.3: Examples of viscous, aging, and elastic soft coupling of a bare silica microsphere to a PA gel film in terms of the interfacial storage G' (shown with black symbols: case 1, red symbols: case 2, and yellow symbols: case 3) and loss G'' (shown with blue symbols: case 1, green symbols: case 2, and magenta symbols: case 3) moduli, furnished from active interfacial microrheology. The experimental parameters are the same as figure 6.6.1. The figure presents the viscoelastic coupling between a bare silica microsphere and the environment (*i.e.*, electrolyte and optical trap at $z \geq 0$, and hydrogel-electrolyte interface at $t \geq 0$). For an elastic adhesion, *e.g.*, case 1, the interfacial storage modulus (black symbols) increases abruptly upon touching the gel by two orders of magnitude and remains unchanged and greater than the loss modulus (blue symbols) versus time. An aged adhesion, case 2, is accompanied by an increase in the storage modulus (red symbols) versus time until it crosses the loss modulus (green symbols) at $t \approx 200$ s. For a viscous coupling, case 3, the loss modulus (magenta symbols) remains greater than the elastic modulus (yellow symbols) at $t > 0$, and G'' adopts values close to its bulk values.

zero-shear viscosity depends on the adhesion length scale ($\eta_0 \propto \xi^{-1}$), τ is independent of ξ; however, by taking a constant length scale $\xi = 6\pi R$ for all cases, they can be compared. As expected, the zero-shear viscosity when a probe microsphere is far from the substrate, $z > 0$, $\eta_0 \approx$ 1.7 mPa s, which is an acceptable value for the viscosity of water at the ambient temperature close to a plane wall. By moving toward the gel, η_0/η_s increases to ≈ 2 when the particle-gel gap is $\approx$ 20 nm. As soon as the particle touches the gel, η_0/η_s saturates to ≈ 300, ≈ 10, and ≈ 3 for the elastic (black symbols), aging (red symbols), and viscous (yellow) adhesion, respectively. Acquiring the actual values of the interfacial viscosity does not seem to be plausible, because of the unknown adhesion length scale;

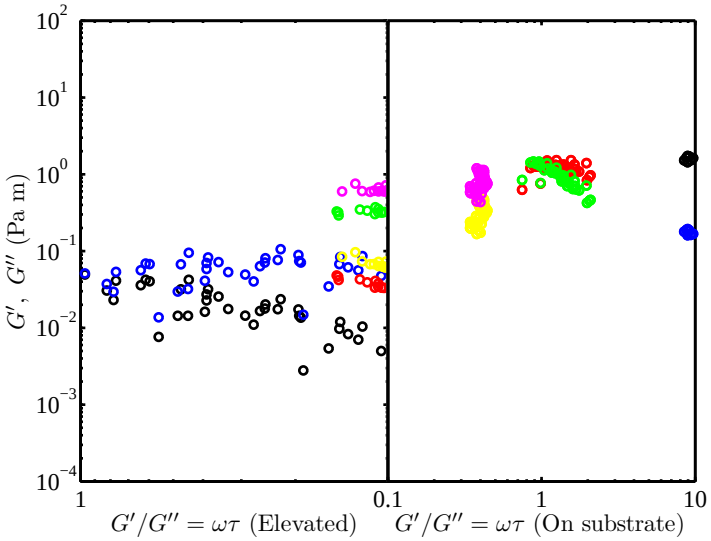

Figure 6.6.4: Examples of viscous, aging, and elastic soft coupling of a bare silica microsphere to a PA gel film in terms of storage G' and loss G'' moduli versus the dimensionless Maxwell relaxation time $G'/G'' = \omega\tau$, furnished from active interfacial microrheology. An elastic adhesion, case 1, is characterized by $G' > G''$ (black and blue symbols), maintaining $\omega\tau > 1$. An aged adhesion, case 2, takes place when $\omega\tau \approx 1$, in which the storage modulus (red symbols) crosses the loss modulus (green symbols) at $\omega\tau = 1$. This shows an expanded G' and G'' from $\omega\tau < 1$ (viscous coupling) to $\omega\tau > 1$ (elastic coupling) with a crossover ($G' = G''$) at $\omega\tau \approx 1$, which is compatible with the Maxwell viscoelastic model. The viscous coupling is associated with $G'' > G'$ or $\omega\tau < 1$ (magenta and yellow symbols).

however, comparing them can be useful for understanding the relative interfacial properties. The slight decrease in η_0 for the non-stuck case (yellow symbols) can be due to the possible alteration of interfacial inclusion properties at an high external drive frequency ($f = 64$ Hz). The Maxwell relaxation time τ, shown in figure 6.6.6, right panel, follows a similar trend as the η_0, resulting in higher values for a stronger adhesion case (elastic adhesion, black symbols). While the viscous coupling relaxation time (yellow symbols) is ≈ 1 ms, τ for the elastic adhesion is ≈ 20 s, which is more than two orders of magnitude greater. Multi time-scale adhesion is evident by the non-constant τ for the aging (red symbols) case.

6.6.2 Bare particle-PA hydrogel active interfacial microrheology

Similar to the glass transition in many-body systems in which transition takes place from a viscous to an elastic state either by increasing the frequency or decreasing temperature (Ngai,

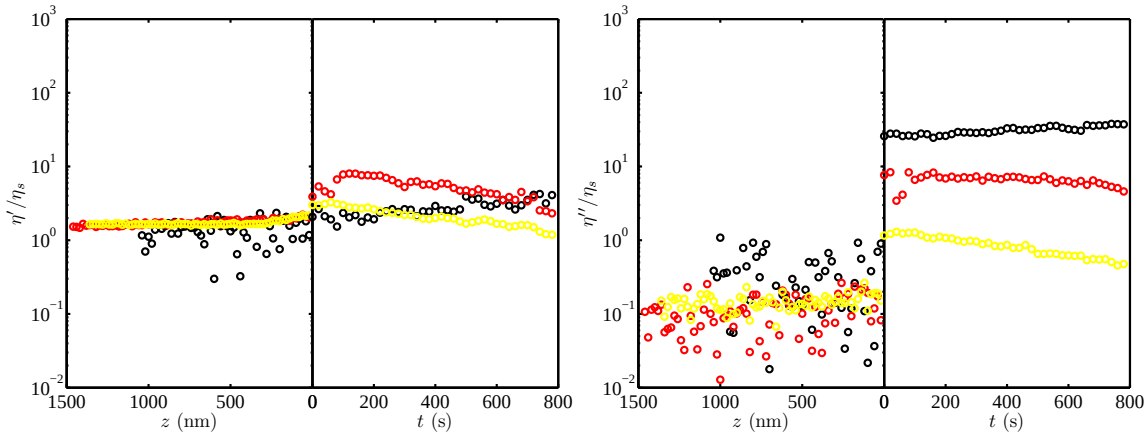

Figure 6.6.5: Examples of viscous, aging, and elastic soft coupling of a bare silica microsphere to a PA gel film in terms of dynamic viscosity $\eta' = G''/\omega$ (left panel), and out-of-phase viscosity $\eta'' = G'/\omega$ (right panel), furnished from active interfacial microrheology. For an elevated microsphere from a gel surface ($z > 0$), the interfacial dynamic viscosity adopts values close to the solvent viscosity ($\eta_s \approx 0.9$ cP), which increases by approaching the interface ($z = 0$) due to the gel-wall hydrodynamic effect, while the out-of-phase viscosity is mainly affected by the trap stiffness, which remains independent of the particle height. As soon as the particle adheres to a gel, η' undergoes small changes for the elastic adhesion to gel A (black symbols, case 1) and viscous coupling with gel B (yellow symbols, case 3), while it adopts a rise-and-fall trend for the aging adhesion to gel B (red symbols, case 2). The out-of-phase viscosity, which is directly affected by the interfacial storage modulus, is higher for the elastic adhesion than the viscous coupling. Note that the hydrodynamic effect of the wall as well as the adhesion length scale is not considered in calculating the viscosity.

2000; Sharma *et al.*, 2010*b*), viscoelastic transitions can be identified by plotting loss modulus G'' versus storage modulus G', known as Cole-Cole plots. Within this framework, such a process results in a shift from $G'' > G'$ (viscous coupling region) to $G' > G''$ (elastic adhesion region), indicating a transition from a viscous fluid to an elastic solid through a viscoelastic (G' and $G'' \neq 0$) pathway. For an ideal single relaxation transition (Sharma *et al.*, 2010*b*), the viscoelastic evolution pathway follows a semicircle with radius $\mu/2$, centred at $(G'', G') = (0, \mu/2)$. The maximum $G'' = \mu/2$ at $G' = \mu/2$, and the maximum $G' = \mu$, where μ is shear (rigidity) modulus. Such an ideality is not the case for most of the real transitions (Sharma *et al.*, 2010*b*).

To understand the dynamics of elastic and viscous coupling between a bare silica microsphere and an hydrogel, experimental Cole-Cole plots at various combinations of gel stiffness,

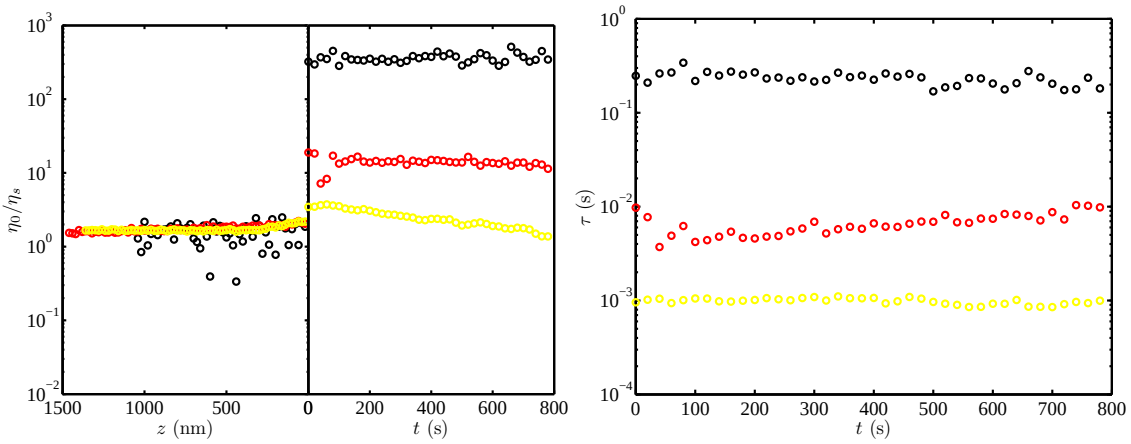

Figure 6.6.6: Examples of viscous, aging, and elastic soft coupling of a bare silica microsphere to a PA gel film in terms of zero-shear viscosity $\eta_0 = \eta' \left[1 + (\omega\tau)^2\right]$ (left panel) and Maxwell relaxation time $\tau = G'/G''\omega$ (right panel), furnished from active interfacial microrheology. For an elevated particle from the gel surface ($z > 0$), the zero-shear viscosity adopts values close to the solvent viscosity ($\eta_s \approx 0.9$ cP); however, adhering to a gel film, it increases abruptly by two orders of magnitude for the elastic adhesion (case 1, black symbols), while it only increases ≈ 2 times for the viscous adhesion (case 3, yellow symbols). The aging adhesion (case 2, red symbols) includes a dynamic increase in the zero-shear viscosity. The Maxwell relaxation time is higher for a stronger adhesion: $\tau_{\text{elastic}} > \tau_{\text{aging}} > \tau_{\text{viscous}}$.

drive frequency, and optical trap stiffness are studied. This is also called the Nyquist analysis scheme, which is frequently used in the impedance spectroscopy (Macdonald, 1992), where the imaginary impedance is plotted versus the real impedance. Experiments cover three gel stiffnesses: gel A, gel B, and gel C, and several frequencies and trap stiffnesses. The layout of this section provides the results at a fixed trap stiffness to discuss the effect of substrate stiffness and drive frequency.

Figure 6.6.7 demonstrates viscous versus elastic coupling in terms of loss modulus versus storage modulus, normalized with the solvent (water) dynamic viscosity $\eta_s \approx 0.9$ cP (left panel) or bulk hydrogel shear modulus μ_g (right panel), acquired from active interfacial microrheology with an adhered bare silica microsphere to gels A (panel a), B (panel b), and C (panel c) while subjected to an external oscillatory shear at frequencies $f = 8$ Hz (black symbols), 16 Hz (blue symbols), 32 Hz (red symbols), 64 Hz (green symbols), and 128 Hz (yellow symbols), in a relatively weak ($k_t \approx 9$ μN m^{-1}) trap. To distinguish the dynamics,

the experimental data for $t \leq 180$ s, $180 < t \leq 360$ s, and $t > 360$ s are shown with triangles, squares, and pentagons, respectively.

When a bare silica microsphere is in a weak trap (figure 6.6.7, $k_t \approx 9$ μN m^{-1}), it adheres abruptly to gels A, B, and C if subjected to a low-frequency shear (*e.g.*, $f = 8$ Hz, black symbols). The maximum drag force at this condition $F_m = 6\pi R\eta_s |x_s| \omega \approx 0.024$ pN if the particle is assumed to be in an unbound (bulk) fluid. The force on an interfacialy trapped particle on a gel $G'\pi a^2 \approx 0.0003$ pN with interfacial $G' \approx 1$ Pa (figure 6.6.7), and ≈ 0.3 pN with bulk gel shear modulus $\mu_g \approx 1$ kPa (figure 5.B.4), taking the contact radius $a \approx 10$ nm (see section 5.6). These are lower (higher) than the maximum drag force by 2 (1) orders of magnitude. With $a \approx 100$ nm, the interfacial elastic force becomes comparable to the drag force. The theory for passive interfacial microrheology, discussed in chapter 5, furnishes an adhesion force (in the absence of external drive) $\approx 10^{-19}$ N, taking the bulk gel stiffness into account. Despite the small passive adhesion force, the external drive force cannot detach the microsphere from the substrate completely; therefore, the attachment cannot be a pure viscous coupling, and remains viscoelastic binding instead. The dynamics of binding viscoelastic properties (loss and storage moduli) depend on the interfacial bond formation evolution, which is also affected by the unknown local surface patterns and properties, as well as intermolecular forces.

By increasing the drive frequency, the shear force on the probe particle is increased ($F_{s,m} \propto f$), which weakens the elastic coupling by decreasing the interfacial out-of-phase viscosity (figure 6.6.7, left panel a) or increasing the loss modulus (figure 6.6.7, right panel a). This slightly shifts the adhesion towards the viscosity-dominant (non-stuck) region; however, gel A prevents the adhesion from taking place in the viscous coupling region at this operating condition, *i.e.*, low k_t. The interfacial bond formation and breakage dictate the viscoelastic pathway for the soft, sticky inclusions. For a bare particle on gel A while subjected to such external forces, the binding viscoelasticity seems to cover a narrow range of loss and storage moduli, suggesting a robust non-equilibrium adhesion state. Normalizing

the interfacial loss and storage moduli with the drive frequency and solvent viscosity (left panel a) distinguishes the data at different frequencies, furnishing normalized interfacial dynamic viscosity versus out-of-phase viscosity. This suggests a decreasing trend in the out-of-phase viscosity while the dynamic viscosity is almost constant, which is a typical behavior of a firmly-sticking system in which the viscoelastic moduli are not affected by the external stimuli. Note that the effective particle size is considered to be equal to the nominal microsphere radius ($2R \approx 1.97$ μm) when reporting the moduli here.

Decreasing the bulk gel shear modulus by a factor of $\approx 4/7$ (gel B) reduces (increases) the binding storage modulus (loss modulus), as evidenced by figure 6.6.7 (b). This is particularly reflected in the similar (higher) storage modulus (loss modulus) range as (than) gel A if normalized with μ_g ($\omega\eta_s$). The adhesion viscoelasticity is more susceptible to the shear rate for gel B, as indicated in panel (b): increasing the shear rate, obviously, shifts the adhesion towards the viscous-binding region, resulting in an aging process at $f = 32$ Hz (red symbols), in which the adhesion starts from the viscous region ($G'' > G'$) and settles in the elastic region ($G' > G''$). Higher shear rates ($f \geq 64$ Hz) keep the particle in the viscosity-dominant region, and do not allow firm elastic adhesion to take place. Note that achieving the viscous coupling region through the passive interfacial microrheology is not feasible, because an equivalent passive (thermal) force ($k_BT/|x_s|$) to the active drag force exerted on the optically trapped particle $F_m \approx 1.9 \times 10^{-13}$ N requires an implausibly high temperature ($T \approx 120$°C).

The frequency at which the adhesion resides in the viscous region decreases when decreasing the gel stiffness: $32 \leq f \leq 64$ Hz for gel B compared to $16 \leq f \leq 32$ Hz for gel C, shown in figure 6.6.7, panels (b) and (c), respectively. Not only Gel C maintains the adhesion elasticity (viscosity) lower (higher) than the other substrates, it also facilitates particle detachment from the gel at high enough frequencies. Results for various gels suggest that the interfacial elasticity is well correlated with the bulk gel shear modulus: $G'/\mu_g \approx (0.2-0.6)\times 10^{-3}$. Note that all the gels have the same monomer concentration (5%) resulting in the same van der

Waals attraction; therefore, from the fact that decreasing the crosslinker density alters the adhesion viscoelasticity, it can be inferred that the softer the interface the more susceptible it is to the interfacial stresses, such as oscillatory shear rate. To elucidate this, experiments with a doubled oscillatory amplitude are conducted on gel C and illustrated in figure 6.6.7 (d). Interestingly, the interfacial loss (storage) moduli are increased (decreased), permitting the adhesion to reside in the close-to-pure viscous region. The reason that increasing the external shear rate has similar effect on the viscoelastic moduli as decreasing the gel stiffness may be due to the reduced number of adsorbed polymer chains on the bare silica probe in both cases.

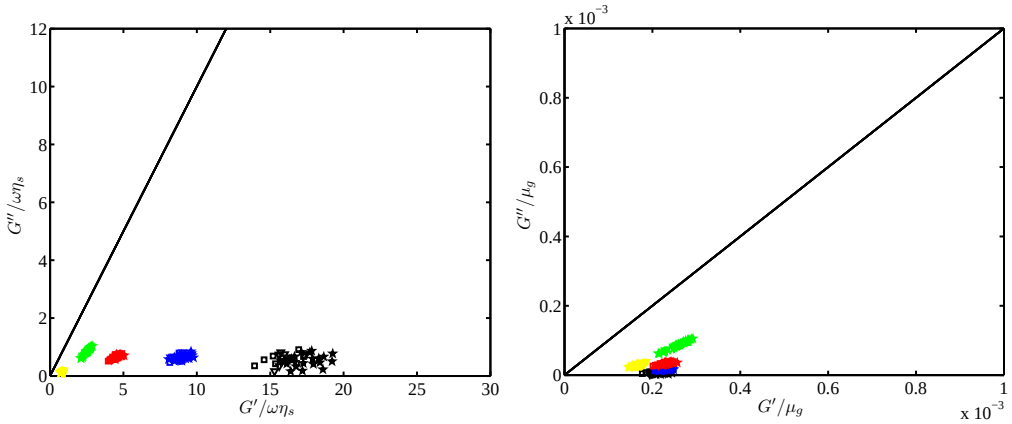

(a) Bare silica microsphere on PA hydrogel A, $k_t \approx 9$ μN m^{-1}.

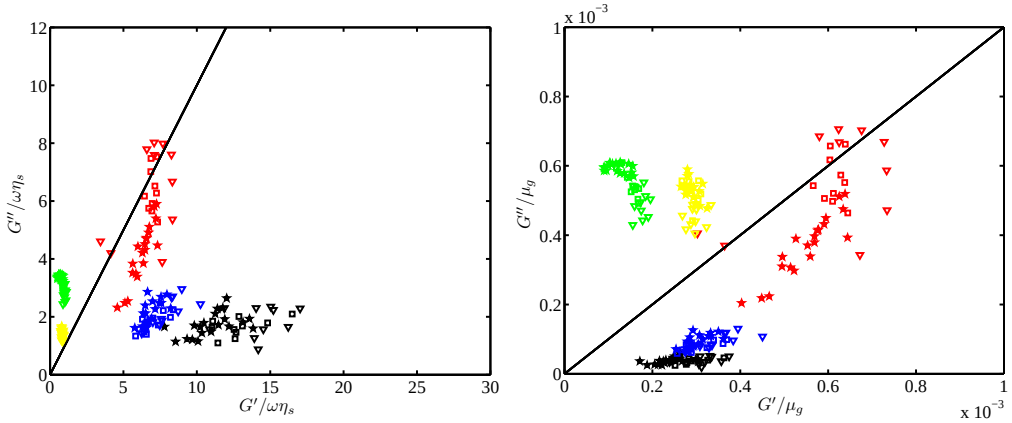

(b) Bare silica microsphere on PA hydrogel B, $k_t \approx 9$ μN m^{-1}.

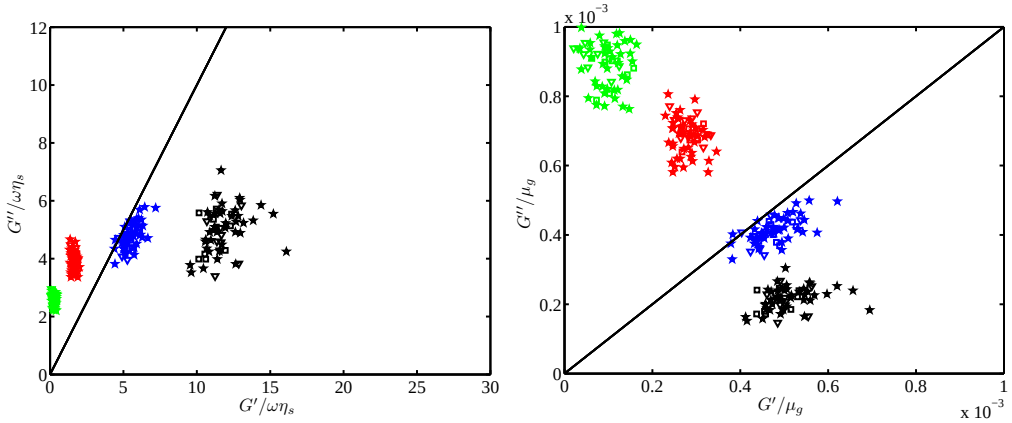

(c) Bare silica microsphere on PA hydrogel C, $k_t \approx 9$ μN m^{-1}.

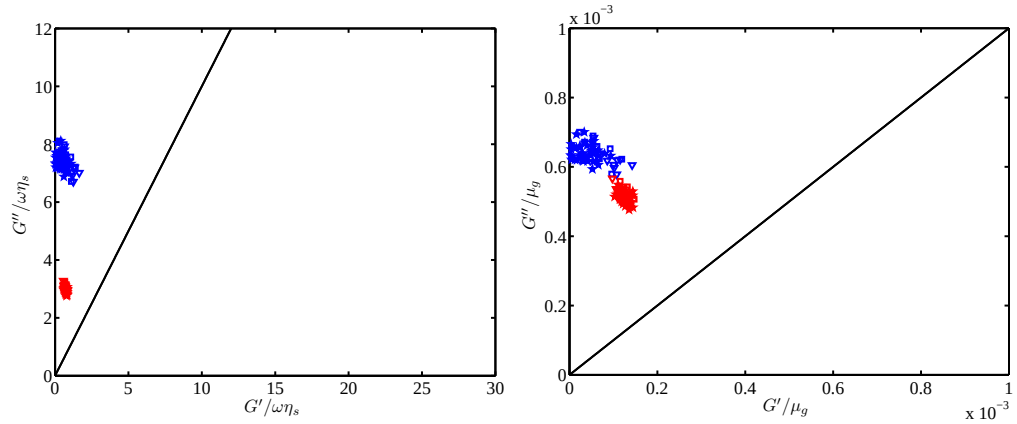

(d) Bare silica microsphere on PA hydrogel C, $k_t \approx 9$ μN m^{-1}, $|x_s| \approx 60$ nm.

Figure 6.6.7 *(previous page)*: Loss modulus G'' versus storage modulus G' (Cole-Cole plots) normalized with solvent viscosity ($\eta_s \approx 0.9$ cP, left panel) or bulk gel shear modulus μ_g (right panel) for a bare silica microsphere adhered to PA hydrogels A (panel a), B (panel b), and C (panel c for the same drive amplitude as panels a and b, and panel d with a doubled amplitude) in TAE buffer (pH = 8.3, ionic strength 41 mmol l^{-1}), obtained from active interfacial microrheology. The probe particle is trapped using an optical tweezers with stiffness $k_t \approx 9$ μN m^{-1} and brought in contact with the gels. The boundary for the viscous ($G'' > G'$)-to-elastic ($G' > G''$) transition (*i.e.*, $G'' = G'$) is shown with the solid line. The stage (and consequently the probe particle) is subject to a small-amplitude ($|x_s| \approx 30$ nm in panels (a), (b), and (c), see table 6.1) sinusoidal displacement with an oscillatory shear frequency $f \approx 8$ Hz (black symbols), 16 Hz (blue symbols), 32 Hz (red symbols), 64 Hz (green symbols), and 128 Hz (yellow symbols) shown with triangles ($t \leq 180$ s), squares ($180 < t \leq 360$ s), and pentagons ($t > 360$ s). An high enough drive frequency or amplitude or low enough substrate stiffness can shift the coupling towards the viscous region. Increasing shear rate, in case of a firm adhesion (*e.g.*, in panel a), mostly affects the loss modulus, while in case of a relatively weak adhesion (*e.g.*, in panel c), it affects both loss and storage moduli.

The acquired frequency-dependent loss and storage moduli furnish the dynamic viscosity ($\eta' = G''/\omega$) and out-of-phase viscosity ($\eta'' = G'/\omega$), which are presented in figure 6.6.8, left and right panels, respectively, for gels A (panel a), B (panel b), and C (panels c and d). Interfacial dynamic viscosity at low frequencies $\eta'/\eta_s \approx 0.8$, 2, and 4 for gels A, B, and C, respectively, which are almost independent of the frequency. The furnished η' are smaller than obtained from the passive interfacial microrheology (figure 5.6.8) for gels A and B, but the same as gel C, because the loss modulus for gels A and B from the active experiments is smaller than obtained from passive interfacial microrheology. The viscosity in the absence

of oscillatory flow, furnished via passive interfacial microrheology from the microsphere interfacial diffusion coefficient, is higher (see figures 5.6.8). This suggests that the oscillatory shear on the particle may weaken the adhesion by partially pulling the particle out of the gel asperities and increasing (decreasing) the interfacial diffusion coefficient (interfacial dynamic viscosity). Note the rapid decrease of the bulk shear viscosity of gels A and B by increasing the frequency compared to gel C (see figure 5.B.5), is compatible with the interfacial dynamic viscosity, furnished from active experiments, being smaller than acquired by the passive method.

Beside the gel stiffness, the dynamic viscosity increase can also be a result of increasing the shear strain by increasing the drive amplitude (panel d) if the gel (adhesion) is soft (weak) enough. As seen in panel (d), for instance at $f = 16$ Hz (blue symbols), the dynamic viscosity $\approx 7\eta_s$ while $|x_s| \approx 30$ nm (panel c) results in $\eta' \approx 4\eta_s$ (blue symbols). At $f = 32$ Hz, the interfacial dynamic viscosity does not change significantly when increasing the drive amplitude, because the particle is already in the viscous adhesion region at the lower drive amplitude. It should, however, be noted that the viscoelastic moduli are calculated considering an effective particle size $\approx R$.

In contrast to the dynamic viscosity, the imaginary part of the complex viscosity (figure 6.6.8, right panel) is much frequency-dependent for all gels, and decreases when increasing the drive frequency. The results suggest that the lower (higher) the shear rate (gel stiffness), the higher is the out-of-phase viscosity $\eta'' = G'/\omega$. For uncrosslinked materials, it is expected that the low-frequency oscillatory rheology results in steady-flow viscosity (Franklin & Krizek, 1969). Although crosslinked materials can adopt infinite viscosity, they usually have finite dynamic viscosity at low frequencies (Franklin & Krizek, 1969; Ferry, 1980). The bulk rheology experiments (figure 5.B.5) suggest that at $f \approx 0.016$ Hz, the bulk dynamic viscosity for gels A, B, and C is ≈ 30 Pa s, ≈ 20 Pa s, and ≈ 8 Pa s, respectively. These are $\approx 30 \times 10^3$, 10×10^3, and 2×10^3 times higher than the interfacial dynamic viscosity furnished by the active interfacial microrheology (figure 6.6.8), and $\approx 2 \times 10^3$, 1×10^3, and

1×10^3 times higher than the passive interfacial microrheology experiments (figure 5.6.8). Considering that the bulk dynamic viscosity decreases when increasing the frequency, the active interfacial results show a plausible trend; however, the bulk dynamic viscosity at such high frequencies cannot be measured. Interestingly, the interfacial dynamic viscosity is lower than the bulk value by the same factor (≈ 1000) as the storage modulus.

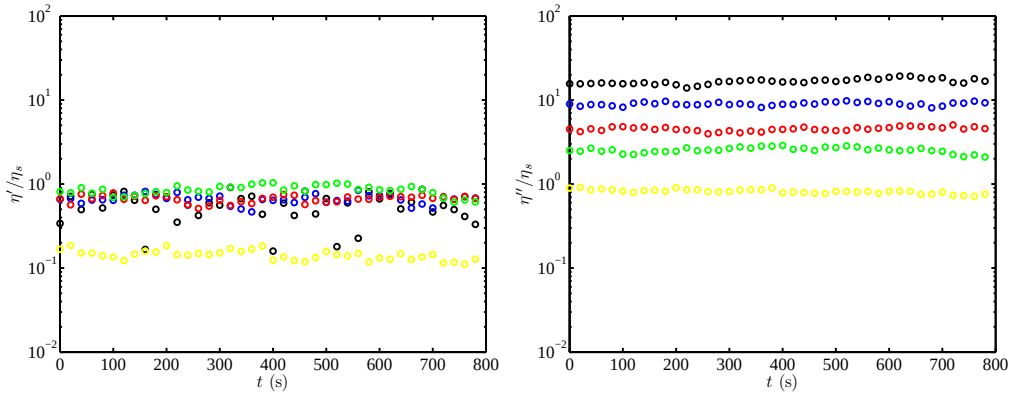

(a) Bare silica microsphere on PA hydrogel A, $k_t \approx 9$ μN m^{-1}.

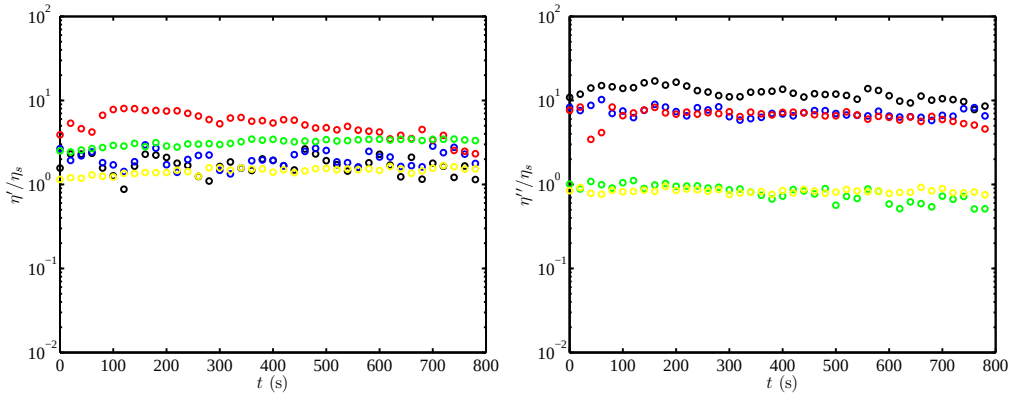

(b) Bare silica microsphere on PA hydrogel B, $k_t \approx 9$ μN m^{-1}.

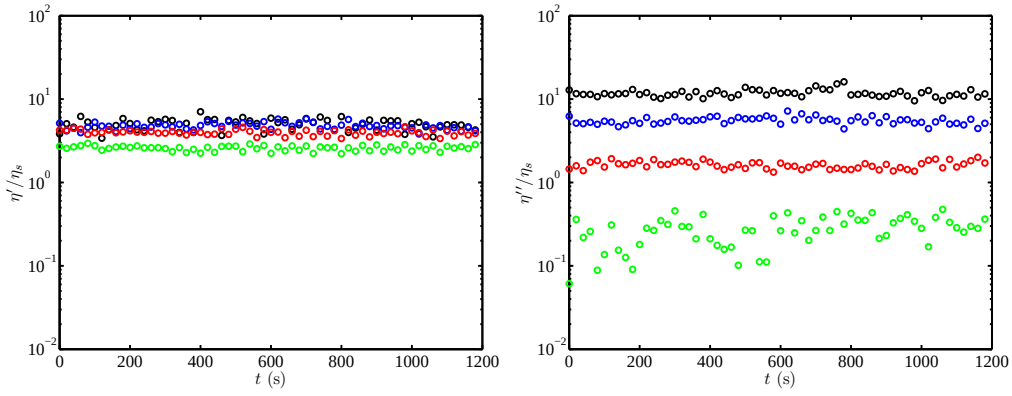

(c) Bare silica microsphere on PA hydrogel C, $k_t \approx 9$ μN m^{-1}.

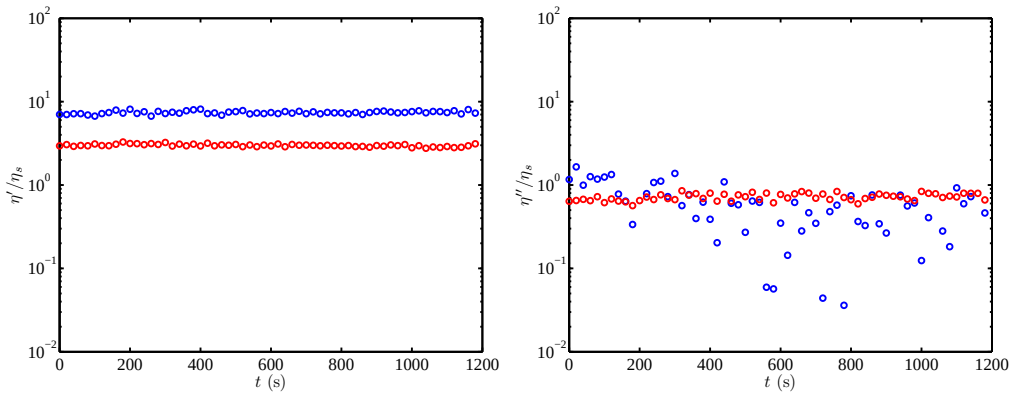

(d) Bare silica microsphere on PA hydrogel C, $k_t \approx 9$ μN m^{-1}, $|x_s| \approx 60$ nm.

Figure 6.6.8 *(previous page)*: Interfacial dynamic viscosity $\eta' = G''/\omega$ (left panel) and out-of-phase viscosity $\eta'' = G'/\omega$ (right panel) versus time for a bare silica microsphere on PA hydrogels A (panel a), B (panel b), and C (panel c for the same drive amplitude as panels (a) and (b), and panel (d) with a doubled amplitude) in TAE buffer (pH = 8.3, ionic strength 41 mmol l^{-1}), obtained from active interfacial microrheology. All experimental parameters are the same as figure 6.6.7. The oscillatory shear frequency $f \approx 8$ Hz (black symbols), 16 Hz (blue symbols), 32 Hz (red symbols), 64 Hz (green symbols), and 128 Hz (yellow symbols). If the particle is in the elastic adhesion region (see Cole-Cole plots, figure 6.6.7), the acquired interfacial dynamic viscosity fluctuates around $\eta'/\eta_s \approx 0.8$, 2, and 4 for gels A, B, and C, respectively. Compared to the dynamic viscosity of water close to the gels (figure 6.6.5, left panel), the firm elastic coupling between gel A and the microsphere furnishes a small η', while for gel B, the dynamic viscosity is close to that of the solvent, and gel C gives rise to ≈ 2 times higher η' than the solvent dynamic viscosity. These are smaller than the values obtained from the passive interfacial microrheology (figure 5.6.8). The out-of-phase viscosity decreases systematically when increasing the drive frequency. Moreover, the stiffer the substrate, the greater the out-of-phase viscosity at a given frequency (compare right panels).

Employing the dynamic and out-of-phase viscosity, the Maxwell zero-shear viscosity $\eta_0 = \eta' [1 + (G'/G'')^2]$ is presented in figure 6.6.9 for gels A (left panel a), B (right panel a), and C (panel b) at $k_t \approx 9$ μN m^{-1}. For gels (A,B,C), sweeping the frequency $f = (8, 16, 32, 64, 128)$ Hz results in $\eta_0/\eta_s \approx (500, 100, 30)$, $(100, 30, 10)$, $(30, 15, 5)$, $(9, 3, 2)$, and $(5, 2, -)$. Therefore, the interfacial zero-shear viscosity of the gels decrease when increasing the drive frequency (for a specified μ_g) or decreasing gel stiffness (for a given f), which can ultimately reach close values to the solvent viscosity in the vicinity of a gel wall. Furthermore, increasing the shear strain, as evidenced by right panel (b), decreases η_0 at a given frequency. It is shown in Appendix 6.B that the zero-shear viscosity directly affects the phase lag of a probe response to an external drive in active interfacial microrheology.

If a microsphere is optically trapped in a viscous solvent, *e.g.*, water, the phase lag of the particle response to an external oscillatory shear flow decreases when increasing the shear rate

$$\tan \phi_0 = \frac{k_t D_0}{2\pi f k_B T}, \tag{6.18}$$

where free transverse Brownian diffusion coefficient $D_0 = k_B T/(6\pi\eta_s R)$. As derived in Appendix 6.B, for a particle in a viscoelastic medium, *e.g.*, when adhered to an hydrogel

$$\frac{\tan \phi}{\tan \phi_0} = \frac{\tan \phi}{\frac{k_t}{12\pi^2 \eta_s R f}} \approx \frac{D_x}{D_0} \left(\frac{\eta'}{\eta_0} \right); \tag{6.19}$$

therefore, the particle phase lag when contacting a soft substrate

$$\tan \phi \approx \frac{k_t}{12\pi^2 \eta_s R f} \frac{9\pi R \eta_s}{2a\eta'} \left(\frac{\eta'}{\eta_0} \right) = \frac{3k_t}{8\pi a \eta_0 f}, \tag{6.20}$$

where a is the contact radius and η' and η_0 denote the substrate (gel) shear viscosity and zero-shear viscosity, respectively. Note that to obtain Eqn. 6.20 (Hill & Sheikhi, 2014)

$$\frac{D_x}{D_0} = \frac{\frac{k_B T}{4a\eta'/3}}{\frac{k_B T}{6\pi\eta_s R}} = \frac{9\pi R \eta_s}{2a\eta'}. \tag{6.21}$$

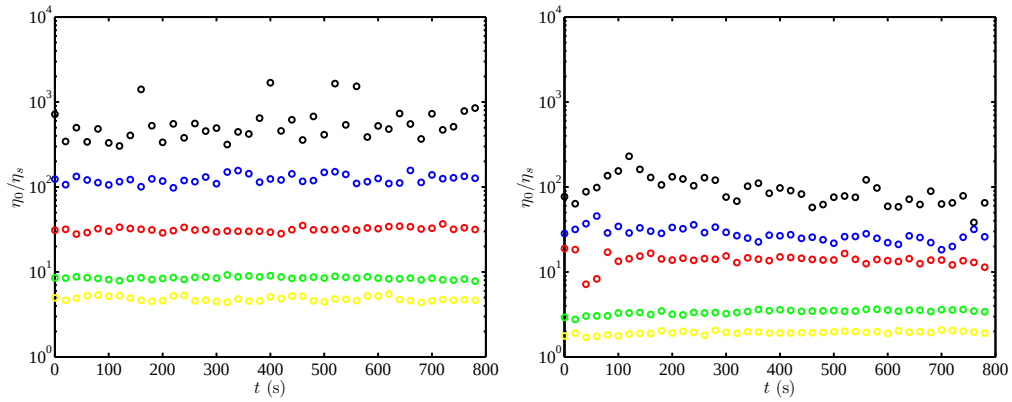

(a) Bare silica microsphere on PA hydrogel A (left panel) and B (right panel), $k_t \approx 9$ μN m^{-1}.

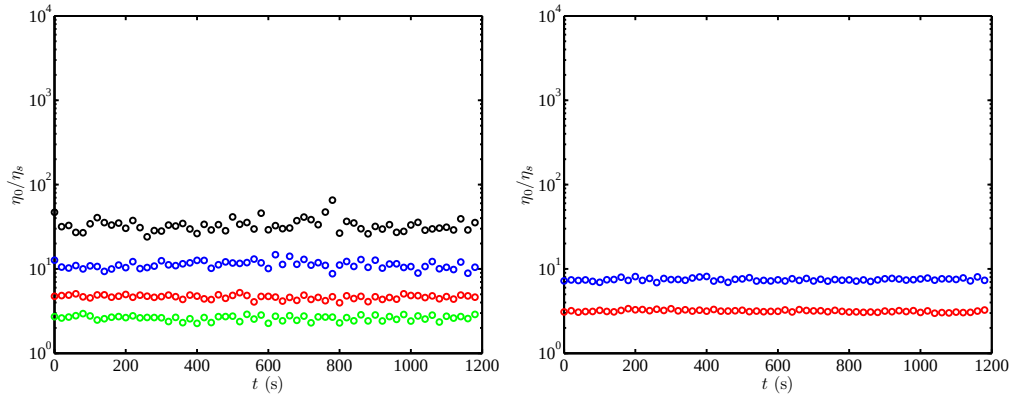

(b) Bare silica microsphere on PA hydrogel C with $|x_s| \approx 30$ nm (left panel) and 60 nm (right panel), $k_t \approx 9$ μN m^{-1}.

Figure 6.6.9: Interfacial zero-shear viscosity $\eta_0 = \eta' \left[1 + (G'/G'')^2\right]$ versus time t, furnished from active microrheology at $k_t \approx 9$ μN m^{-1} with a bare silica microsphere adhered to hydrogels A (left panel a), B (right panel a), and C (left panel b; $|x_s| \approx 30$ nm, right panel b; $|x_s| \approx 60$ nm). At a given frequency, a stiffer substrate results in an higher interfacial zero-shear viscosity. Also, η_0 decreases when increasing the shear rate and strain, which can ultimately reach the solvent viscosity near a gel film ($\approx 2\eta_s \approx 1.8$ cP) at high enough frequencies. Zero-shear viscosity at a low drive frequency, *e.g.*, $f = 8$ Hz, is higher than furnished by the passive interfacial microrheology (figure 5.6.8) for a given gel.

Accordingly, the phase lag decreases when increasing the contact radius, gel shear viscosity and stiffness, and drive frequency. The contact radius and interfacial shear and zero-shear viscosity are functions of drive frequency; therefore, it is not possible to decouple them from each other; however, the phase lag can furnish the transverse interfacial diffusion coefficient

defined as $D_x = k_B T/(6\pi\eta' R)$:

$$D_x \approx \frac{2\pi f k_B T \tan\phi}{k_t}\left(\frac{\eta_0}{\eta'}\right). \tag{6.22}$$

The effective transverse diffusion coefficient is obtained by taking the zero-shear viscosity into account

$$D_{x,eff} = \frac{k_B T}{6\pi\eta_0 R} = D_x\left(\frac{\eta'}{\eta_0}\right) \approx \frac{2\pi f k_B T \tan\phi}{k_t}, \tag{6.23}$$

which is of particular interest in this study, because it includes only one parameter from the active interfacial experiments (phase lag) and does not demand further position calibration. Moreover, it has the general form of the diffusion coefficient dependency on the phase lag in a pure viscous medium (compare to Eqn. 6.18). The subscript *eff* is dropped for simplicity in the effective diffusion coefficient figures in chapters 6 and 7.

The phase-sensitive measurements furnish the phase lag between an external oscillatory drive and a bare silica microsphere subject to that drive while adhered to the gel (figure 6.6.10, left panel). As can be seen in these figures, in contrast to the typical phase lag behavior of a microsphere in an unbound solvent (*i.e.*, a decreasing trend when increasing the frequency to maintain the diffusion coefficient constant, Eqn. 6.18), for all of the gels, the phase lag increases when increasing the shear rate up to a specific frequency, suggesting that the effective interfacial transverse diffusion coefficient increases by such an externally imposed stress. Moreover, comparing the phase lag values for gels A (panel a), B (panel b), and C (panel c) shows that $\tan\phi$ increases when decreasing the substrate stiffness (at a fixed f): the softer the gel, the higher the particle effective interfacial transverse diffusion coefficient. This is similar to the trend of passive microrheology diffusion results, discussed in figure 5.6.5. At an high frequency, *e.g.*, $f = 128$ Hz, the phase lag drops, because the inclusion undergoes a close-to-viscous coupling, which results in phase lag attenuation by increasing the frequency, so that the diffusion coefficient does not exceed its bulk ($z > 0$) value.

The loss tangent, defined as $\tan\delta = G''/G'$ is independent of the trap stiffness calibration. For a pure elastic solid (viscous fluid), $\tan\delta \approx 0$ (∞). This parameter, which is a dimensionless representative of viscoelastic damping in a linear material, is presented in figure 6.6.10, right panel. The loss tangent linearly grows with the frequency for all the gels up to a specific frequency, indicating that the interfacial inclusions undergo much viscous-like coupling when increasing the shear rate. Substrate stiffness has a reverse effect on the loss tangent: decreasing the bulk gel shear modulus increases G''/G' at a given shear rate, as compared in panels (a), (b), and (c). An estimation of the loss tangent for an optically trapped particle in unbound water is $\tan\delta = G''/G' \approx 2\pi f\eta_s/(k_t/6\pi R) \approx 0.011f$, with $k_t \approx 9$ μN m^{-1}. This results in water loss tangent $\approx$ 0.09, 0.19, 0.37, 0.75, and 1.49, at $f = 8$ Hz, 16 Hz, 32 Hz, 64 Hz, and 128 Hz, respectively. The reason that the loss tangent does not necessarily follow a linear dependency on the frequency at an high frequency, *e.g.*, $f = 128$ Hz, can be the adhesion regime transition. Remember that in the Nyquist plot of an ideal Maxwell material, by decreasing the storage modulus, the loss modulus initially increases and then levels off. Note that the reduced drive amplitude at an high frequency (Table 6.1) due to the experimental limitation may result in different physics at the interface. To compare the results of such an high frequency with lower frequencies, the effect of drive amplitude is taken into account to calculate the dissipation force, which will be presented in figure 6.6.14.

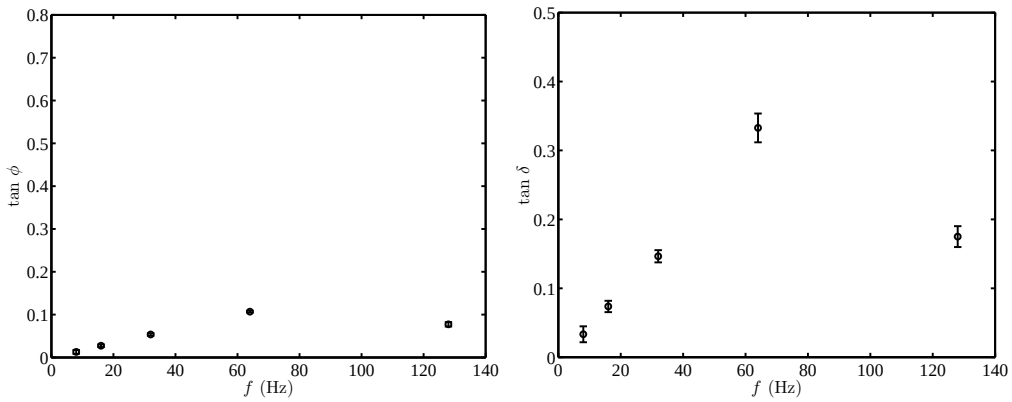

(a) Bare silica microsphere on PA hydrogel A, $k_t \approx 9$ μN m^{-1}.

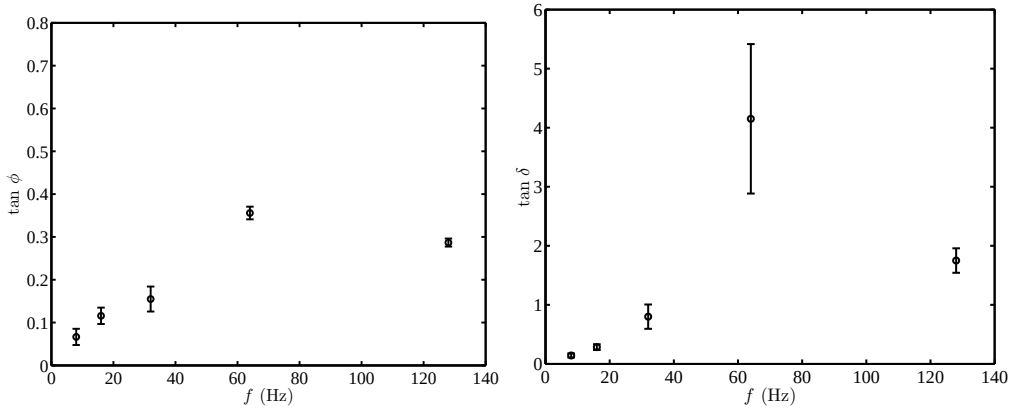

(b) Bare silica microsphere on PA hydrogel B, $k_t \approx 9$ μN m^{-1}.

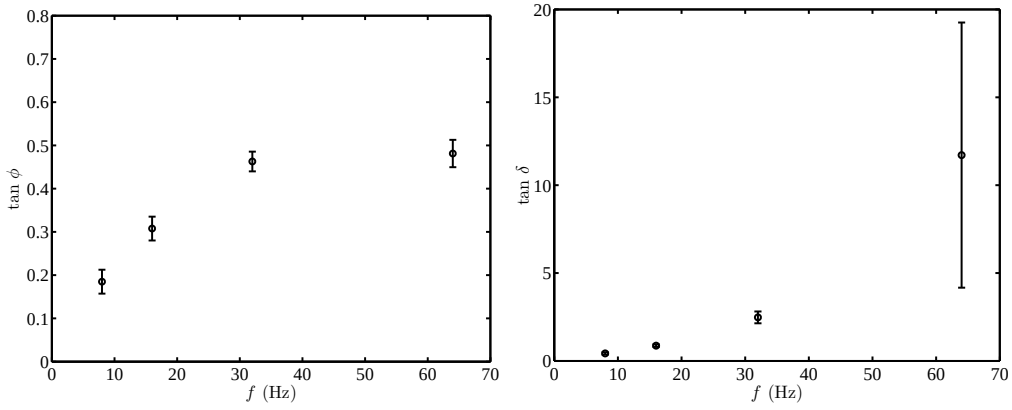

(c) Bare silica microsphere on PA hydrogel C, $k_t \approx 9$ μN m^{-1}.

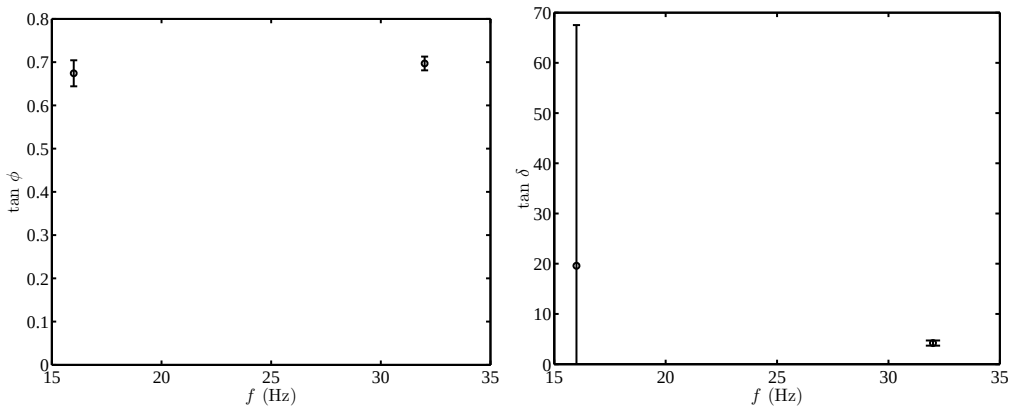

(d) Bare silica microsphere on PA hydrogel C, $k_t \approx 9$ μN m^{-1}, $|x_s| \approx 60$ nm.

Figure 6.6.10 *(previous page)*: Phase lag of an optically trapped bare silica microsphere probe response, adhered to hydrogels A (panel a), B (panel b), and C (panel c for the same drive amplitude as panels a and b, and panel d with a doubled amplitude) in TAE buffer (pH = 8.3, ionic strength 41 mmol l^{-1}), to an external sinusoidal shear $\tan\phi$ (left panel) and loss tangent $\tan\delta$ (right panel) versus drive frequency f, obtained from active interfacial microrheology. All experimental parameters are the same as figure 6.6.7. The values are averaged over the sampling time (shown in figure 6.6.7), and the error bars are time standard deviation. A stiffer hydrogel and/or a lower shear rate or strain results in a smaller phase lag and loss tangent, which shifts the adhesion toward the elastic binding. Also, at low enough frequencies, the phase lag and loss tangent increase linearly with the shear rate.

The effective interfacial transverse diffusion coefficients obtained from the phase lags (figure 6.6.10) using Eqn. 6.23 are presented in figure 6.6.11. When a bare silica microsphere adheres to a relatively stiff substrate, *e.g.*, gel A, the diffusion coefficient is attenuated almost two orders of magnitude (relative to the hindered diffusion close to a rigid wall) at a low frequency, *e.g.*, $f = 8$ Hz. This is smaller than the diffusion coefficient attenuation furnished from the passive interfacial microrheology (figure 5.6.5), which is due to the zero-shear viscosity contribution, affected by the interface storage modulus. Inducing oscillatory shear decreases the local viscosity (as evidenced by the interfacial and bulk experiments), which is expected to increase the particle diffusion coefficient. The viscosity decrease results in an increased contact area between the microsphere and the gel surface, which, indeed, decreases the diffusion coefficient. The tradeoff between these two phenomena defines the

extent to which the diffusion coefficient is attenuated.

Moreover, a gel, as a Brinkman medium, induces a non-zero slip velocity on the interface (Damiano *et al.*, 2004), which depends on the Brinkman screening length. This velocity depends on the drive frequency and can reduce the symmetry-breaking effect of the wall and increase the microsphere diffusion coefficient at high enough shear rates. As an example, for gel B, to furnish $D_x/D_0 \approx 0.4$ at $f = 128$ Hz, presented in Figure 6.6.11, according to Faxen (1923), the equivalent microsphere distance from a rigid wall needs to be ≈ 60 nm. Increasing the shear strain has, also, a similar effect on increasing the interfacial diffusion coefficient. As can be observed in figure 6.6.11 (red squares), doubling the shear strain at $f = 16$ Hz (32 Hz), increases the microsphere diffusivity on gel C from $D_x/D_0 \approx 0.06$ (0.18) to $D_x/D_0 \approx 0.12$ (0.26).

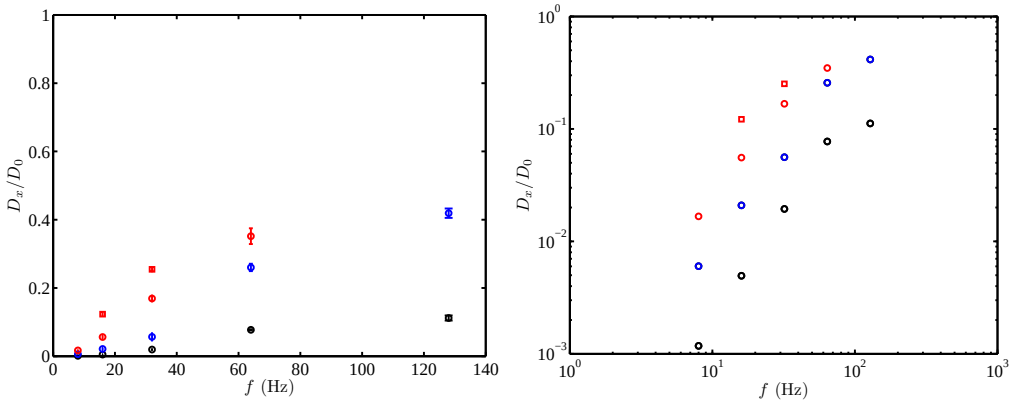

Figure 6.6.11: Effective interfacial transverse diffusion coefficient $D_x = 2\pi f k_B T \tan(\phi)/k_t$ versus drive frequency f, furnished from active microrheology at $k_t \approx 9$ μN m^{-1} with a bare silica microsphere, adhered to hydrogels A (black symbols), B (blue symbols), and C (red circles: $|x_s| \approx 30$ nm, red squares: $|x_s| \approx 60$ nm). At a specified frequency, a stiff substrate attenuates the effective transverse diffusion coefficient more than a soft gel. Also, the diffusion coefficient depends on the drive frequency and amplitude, which can ultimately reach values close to the free Brownian diffusion coefficient close to a rigid wall in an unbound solvent at high enough frequencies. The free diffusion coefficient of a silica microsphere in unbound water $D_0 \approx 0.25$ μm^2 s^{-1} at $T \approx 23$°C. The right panel is a logarithmic presentation of the same data.

It was shown that the interfacial viscoelastic properties depend on the adhesion strength; therefore, the storage and loss moduli are altered by changing the shear rate (or shear strain

for a soft enough substrate). The interfacial viscoelasticity can be incorporated into a general framework to furnish characteristic properties of the underlying gel through the standard linear solid (SLS, in case of highly elastic adhesion: $\omega\tau \gg 1$) or extended standard linear solid (ESLS, in case of viscoelastic adhesion) models. Storage (left panel) and loss (right panel) moduli versus the dimensionless Maxwell relaxation time $\omega\tau = G'/G''$ are plotted in figure 6.6.12 for gels A (panel a), B (panel b), and C (panel c). For each gel, if the adhesion is located in the elastic-coupling (viscous-coupling) region, the dimensionless relaxation time $\omega\tau > 1$ ($\omega\tau < 1$). For all the gels, increasing the shear rate decreases the dimensionless Maxwell relaxation time (as evidenced by left panel), resulting in a systematic change in the viscoelastic properties, which can be explained by simultaneous fits of G' and G'' to the SLS or ESLS models. If the adhesion is highly elastic, *i.e.*, $\omega\tau >> 1$ (panel a), both SLS and ESLS models result in similar high-$\omega\tau$ fits; however, the SLS model furnishes $k_e \approx 0$ for all the gels showing its impotence in capturing the interfacial behavior at low $\omega\tau$. For a relatively weak adhesion, *e.g.*, viscoelastic coupling (panels b and c), the loss modulus approaches that of unbound fluid at a specified (high) frequency, which demands the ESLS model to furnish accurate fits.

Similar to packed systems subject to glass transition (Sharma *et al.*, 2008) in which decreasing temperature attenuates the dynamics by increasing the relaxation time and viscosity while keeping the ratio almost constant, the interfacial adhesion of a bare silica microsphere on PA gels seems to follow the same trend: the fit parameter $(\eta/\tau)/(0.001\mu_g) \approx 0.23$, 0.33, and 0.74 for gels A (SLS model), B (ESLS model), and C (ESLS model), respectively. This indicates that PA hydrogel as a soft substrate can attenuate the microsphere dynamics with an approximately constant $\eta/(\tau\mu_g)$ ratio, which increases when increasing the gel stiffness. This can be of interest in designing soft substrates for interfacial cell growth and differentiation, where a specific stress is needed to be applied to a species to initiate a desired bioprocess. Moreover, the normalized elastic stress with bulk gel shear modulus decreases when increasing the crosslinker concentration, which suggests that the gel interfacial prop-

erties are affected by the bulk properties in a non-linear manner.

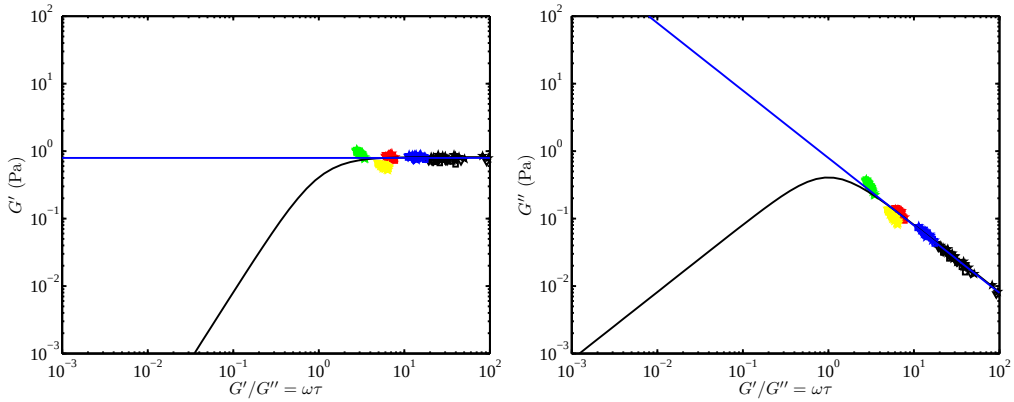

(a) Bare silica microsphere on PA hydrogel A, $k_t \approx 9$ μN m^{-1}.

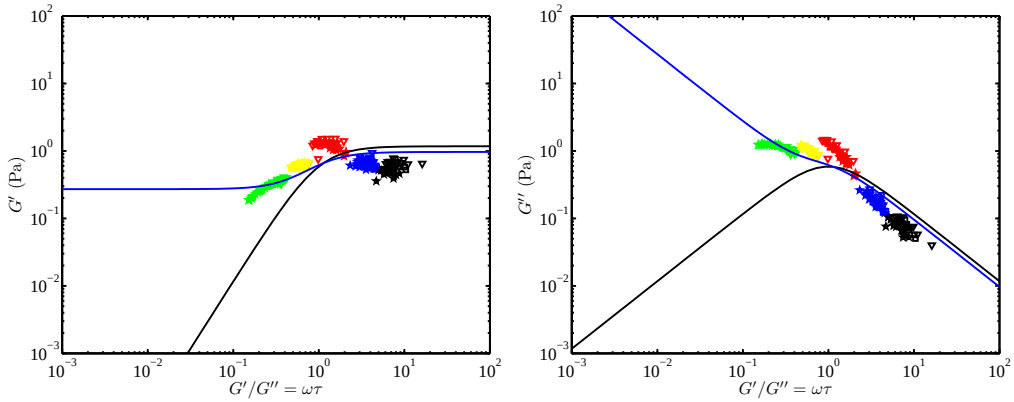

(b) Bare silica microsphere on PA hydrogel B, $k_t \approx 9$ μN m^{-1}.

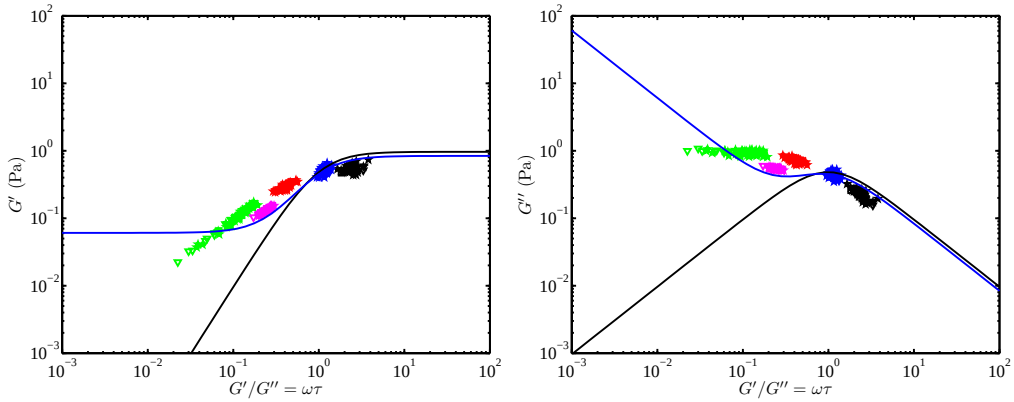

(c) Bare silica microsphere on PA hydrogel C, $k_t \approx 9$ μN m^{-1}.

Figure 6.6.12 *(previous page)*: Storage (left panel) and loss (right panel) moduli versus dimensionless Maxwell relaxation time $G'/G'' = \omega\tau$ with a simultaneous least-squares best fit to the standard linear solid (SLS, black line) and extended standard linear solid (ESLS, blue line) models for gels A, B, and C, furnished from active interfacial microrheology with a bare silica microsphere at $k_t \approx 9$ μN m^{-1}. Fit parameter η/τ in the SLS model: $G' = k_e + (\eta/\tau)\frac{(\omega\tau)^2}{1+(\omega\tau)^2}$ and $G'' = (\eta/\tau)\frac{\omega\tau}{1+(\omega\tau)^2}$ for gels A, B, and C is 0.82 Pa, 1.17 Pa, and 0.99 Pa, respectively, and for all cases, $k_e \approx 0$, which brings about $(\eta/\tau)/(0.001\mu_g) \approx 0.23$, 0.56, and 0.93, respectively; however, the fit is accurate only if the particle is in the elastic adhesion regime and deviates from the experimental G'' at low $\omega\tau$, because at such condition, the loss modulus tends to that of the solvent. The ESLS model, $G' = k_e + (\eta/\tau)\frac{(\omega\tau)^2}{1+(\omega\tau)^2}$ and $G'' = (\eta/\tau)\frac{\omega\tau}{1+(\omega\tau)^2} + k_e/(\omega\tau_e)$, furnishes more accurate fits for gels B and C. The ESLS model parameters (all in Pa) for gels A: $\eta/\tau \approx 0, k_e \approx 0.79$, B: $\eta/\tau \approx 0.69, k_e \approx 0.27$, and C: $\eta/\tau \approx 0.78, k_e \approx 0.06$, which bring about $(\eta/\tau)/(0.001\mu_g) \approx 0.23$, 0.33, and 0.74 for gels A, B, and C, respectively. In panel c, the data acquired with $|x_s| \approx 60$ nm are shown with magenta ($f = 32$ Hz) color. Data for gel A are for one microsphere, for gel B are for 5 microspheres, and for gel C are for one microsphere. All experimental parameters are the same as figure 6.6.7.

In the glassy systems (*e.g.*, glass-forming liquids), decreasing the temperature shifts the material state from a low-molecular relaxation time liquid to an high-molecular relaxation time solid (Debenedetti & Stillinger, 2001). The dynamics of such systems are manifested in their viscosity evolution versus external stimuli, such as temperature. At low temperatures (*e.g.*, close to the glass transition temperature), the liquid and its dynamics are termed *strong* and Arrhenius, and at high temperatures, they are called *fragile* and non-Arrhenius (Mauro *et al.*, 2009). The Arrhenius liquid viscosity is well described by the Vogel-Fulcher-Tammann (VFT) equation (Fulcher, 1925; Scherer, 1992), which is also known as Williams-Landel-Ferry (WLF) equation

$$\log_{10}\eta = \log_{10}\eta_\infty + \frac{A}{T - T_0}, \tag{6.24}$$

where η_∞, A, and B are experimental parameters, and the non-Arrhenius (fragile) liquid viscosity is successfully described by Avramov-Milchev (AM) equation (Avramov & Milchev, 1988)

$$\log_{10}\eta = \log_{10}\eta_\infty + \left(\frac{\tau}{T}\right)^\alpha, \tag{6.25}$$

with experimental parameters: η_∞, τ, and α. All the parameters in Eqns. 6.24 and 6.25 are only functions of material composition.

The analogy between the viscoelastic evolution of interfacial bare silica microsphere-PA hydrogel inclusions and the glass transition process in the packed, many-body systems, is investigated by studying the Maxwell relaxation time τ and zero-shear viscosity η_0 versus the external frequency f, shown in figure 6.6.13. While in glassy systems, increasing the temperature decreases the viscosity, in the interfacial sticking system, increasing the external shear rate has a similar effect. Resembled to Eqn. 6.24, single relaxation functions

$$\tau = \tau_\infty e^{\frac{f_\tau}{f}}, \text{ and } \frac{\eta_0}{\eta_s} = \frac{\eta_{0,\infty}}{\eta_s} e^{\frac{f_{\eta_0}}{f}} \tag{6.26}$$

fitted the Maxwell relaxation time and zero-shear viscosity well, furnishing the relaxation time at infinite frequency $\tau_\infty \approx 6.4$, 0.7, and 0.3 ms, for gels A, B, and C. The normalized zero shear viscosity at infinite frequency $\eta_{0,\infty}/\eta_s \approx 5.7$, 2.6, and 2.2 for gels A, B, and C, respectively. Interestingly, the characteristic relaxation frequency of τ and η_0, namely f_τ and f_{η_0} adopt similar values, $f_\tau \approx 40.3$ Hz and $f_{\eta_0} \approx 40.2$ Hz, for the stiffest gel, where the adhesion is dominated by the storage modulus at all the frequencies. Decreasing the gel bulk shear modulus results in much deviation between f_τ and f_{η_0}: for gel B, $f_\tau \approx 47.1$ Hz and $f_{\eta_0} \approx 31.2$ Hz, and for gel C, $f_\tau \approx 43.2$ Hz and $f_{\eta_0} \approx 22.6$ Hz. The deviation between the characteristic relaxation frequencies is associated with the inclusions on gels B and C undergoing adhesion regime transition at intermediate frequencies. The relaxation time $\tau = 1/(2\pi f)$ below which the coupling regime is transferred from elastic to viscous is shown with dashed blue line in figure 6.6.13.

To decrease the zero-shear viscosity, an activation barrier energy (Sharma *et al.*, 2008) relevant to the particle-hydrogel adhesion potential must be overcome. The exponential

decay of the zero-shear viscosity suggests

$$\frac{\eta_0}{\eta_s} = \frac{\eta_{0,\infty}}{\eta_s} e^{\frac{\Psi}{k_B T}}, \tag{6.27}$$

where Ψ is the activation energy, which is a function of the external stimuli on the microsphere, namely drive frequency, gel crosslinker concentration c, and trap stiffness: $\Psi = \Psi(f, c, k_t)$. At a constant trap stiffness and crosslinker concentration, comparing Eqn. 6.26 with Eqn. 6.28 suggests

$$\frac{\Psi}{k_B T} = \frac{f_{\eta_0}}{f}. \tag{6.28}$$

Accordingly, $\Psi = k_B T f_{\eta_0}/f$, which results in $\Psi \approx 40.2 k_B T/f$, $31.2 k_B T/f$, and $22.6 k_B T/f$ for gels A, B, and C, respectively, at $k_t \approx 9$ μN m^{-1}; therefore, the activation barrier is larger for a stiffer gel. The dependency of the activation barrier on the gel crosslinker concentration c can be inferred from plots of f_{η_0} versus bis-acrylamide concentration. This is shown in figure 6.6.13 (b), which, interestingly, implies a linear correlation $f_{\eta_0} = 87.56c + 18.23$ with $R^2 \approx 1$; therefore,

$$\Psi = \frac{k_B T}{f} (\alpha c + \beta), \tag{6.29}$$

where the constants $\alpha = 87.56$ Hz (w/v %)$^{-1}$ and $\beta = 18.23$ Hz are obtained from figure 6.6.13 (b). Note that despite the good linear fit in panel (b), each point is obtained from a fitting in panel (a) with a certain error.

As discussed earlier, the interfacial loss modulus is a function of shear rate and shear strain. The experimental limitation (nano-positioning stage control system) imposes inevitable drive amplitude attenuation at an high frequency (refer to Table 6.1), which makes it inaccurate to compare the furnished viscoelastic moduli at $f = 128$ Hz with the low-frequency data. The interfacial dissipation force per cycle $F_d = \pi |x_s|^2 G''$ (compare to Eqn. 3.68) permits to take the extension reduction into account. Interfacial dissipation force per cycle, presented in figure 6.6.14 for gels A and B (panel a) and C (panel b) versus frequency follows a similar trend as observed in figure 6.6.12, right panel, *i.e.*, it increases

with increasing drive frequency in case of an elastic adhesion, and relaxes when the adhesion is viscosity-dominant. For comparatively stiff gels, *e.g.*, gels A and B, the maximum normalized dissipation force occurs at an intermediate frequency, which depends on the gel shear modulus: the stiffer the gel, the higher the required drive frequency to achieve the maximum dimensionless dissipation force. For a soft gel, *e.g.*, gel C, the dissipation force decreases when increasing the drive frequency by sweeping the drive frequency from 8 to 64 Hz. Such decrease can also be a result of an increased shear strain (extension), as illustrated in figure 6.6.14, right panel (b). Note that, here, F_d is normalized with the drive frequency; therefore, the absolute dissipation force increases by increasing the drive frequency, while the normalized F_d remains in the range $0.001 - 0.04$ for all gels at all drive frequencies.

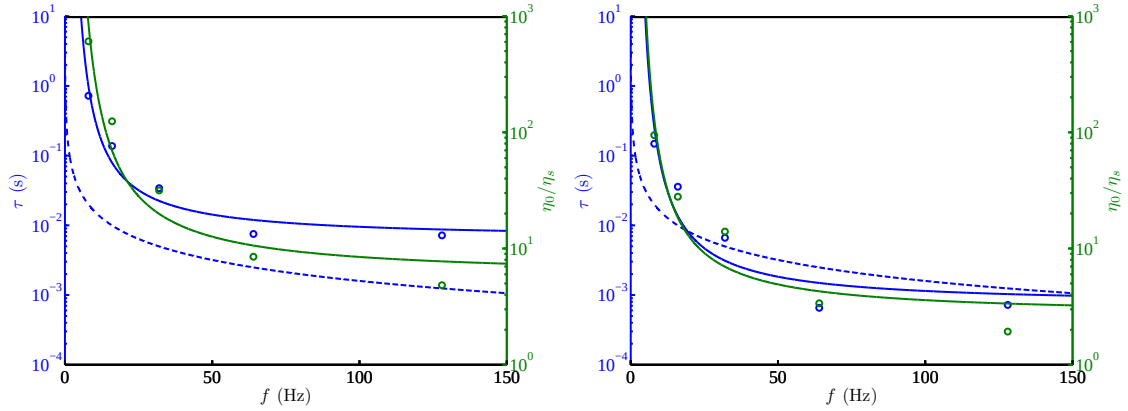

(a) Bare silica microsphere on PA hydrogels A and B at $k_t \approx 9$ μN m^{-1}.

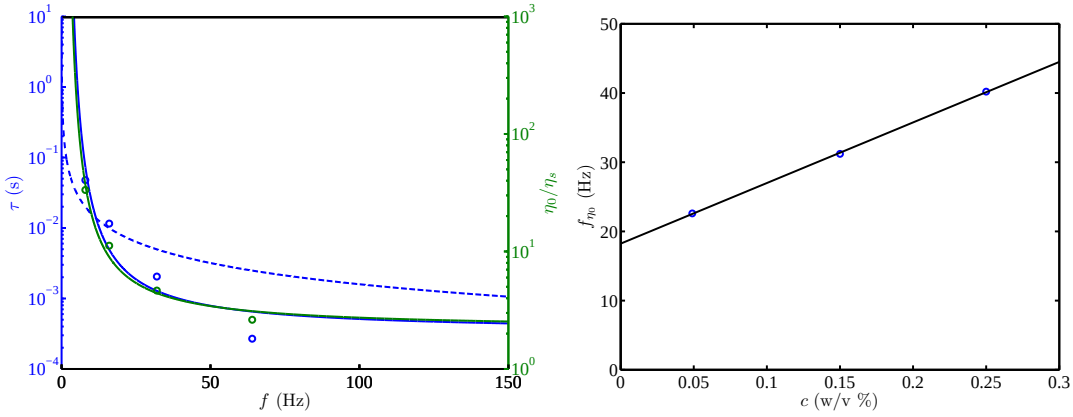

(b) (left panel) Bare silica microsphere on PA hydrogel C at $k_t \approx 9$ μN m^{-1}. (right panel) Zero-shear characteristic frequency f_{η_0} versus gel C, B, and A crosslinker concentrations c at $k_t \approx 9$ μN m^{-1}.

Figure 6.6.13: (panel a and left panel b) Maxwell relaxation time $\tau = G'/(G''\omega)$ (shown with blue symbols) and zero-shear viscosity $\eta_0 = \eta' \left[1 + (\omega\tau)^2\right]$ (shown with green symbols) versus external drive frequency f with the corresponding exponential relaxation fits to τ (blue line) and η_0/η_s (green line) according to Eqn. 6.26 for gels A (left panel a), B (right panel a), and C (left panel b), furnished from bare silica microsphere active interfacial microrheology at low k_t. The fit parameters $(\tau_\infty, \eta_{0,\infty}/\eta_s, f_\tau, f_{\eta_0})$ with units (ms,-,Hz,Hz) for gels A, B, and C are $(6.4, 5.7, 40.3, 40.2)$, $(0.7, 2.6, 47.1, 31.2)$, and $(0.3, 2.2, 43.2, 22.6)$, respectively, all with $R^2 \gtrsim 0.97$. The relaxation time below which the adhesion regime undergoes transition from elastic to viscous coupling $\tau = 1/(2\pi f)$ is shown with blue dashed line. While on gel A, at all the frequencies, τ remains higher than the blue dashed line, decreasing gel stiffness shifts the relaxation times below it, resulting in deviation between the characteristic frequencies of relaxation time f_τ and zero-shear viscosity f_{η_0}. (right panel b) Zero-shear characteristic frequency f_{η_0} versus gel crosslinker concentration c.

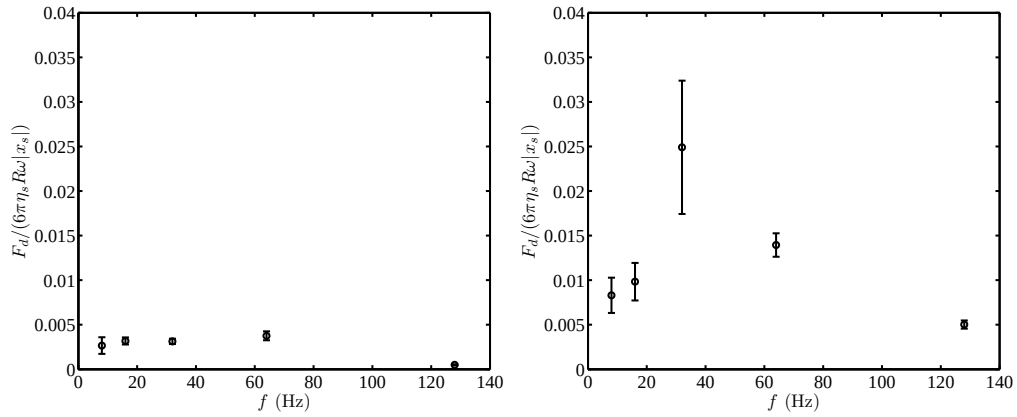

(a) Bare silica microsphere on PA hydrogel A (left panel) and B (right panel), $k_t \approx 9\ \mu\text{N m}^{-1}$.

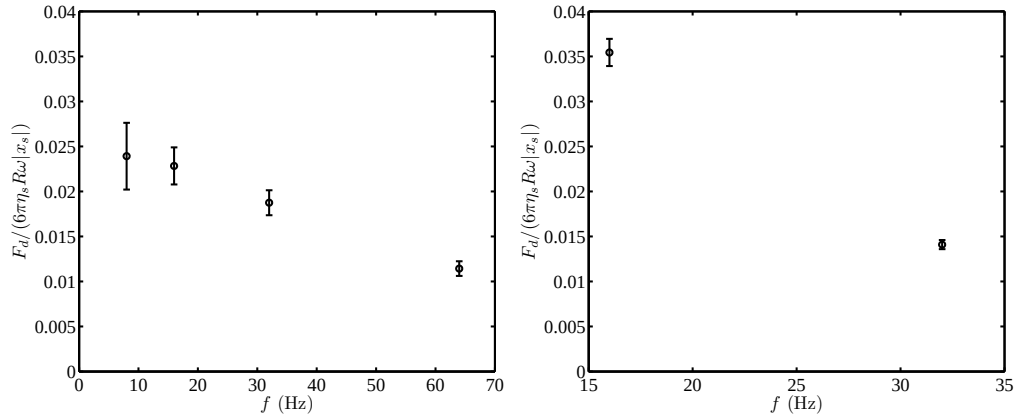

(b) Bare silica microsphere on PA hydrogel C with $|x_s| \approx 30$ nm (left panel) and 60 nm (right panel), $k_t \approx 9\ \mu\text{N m}^{-1}$.

Figure 6.6.14: Dissipation force per cycle $F_d = \pi |x_s|^2 G''$, normalized with the Stokes drag force $6\pi\eta_s R\omega |x_s|$ versus drive frequency f, furnished from active interfacial microrheology at $k_t \approx 9\ \mu\text{N m}^{-1}$ with a bare silica microsphere, adhered to hydrogels A (left panel a), B (right panel a), and C (panel b) in TAE buffer. The interfacial loss modulus is inversely correlated with the bulk gel shear modulus (shown in figure 6.6.7); therefore, a stiffer gel brings about a smaller dissipation force at a given drive frequency. The normalized dissipation force increases when increasing the drive frequency only if the adhesion is in the elastic regime. When the probe particle is in the elastic coupling mode, the dissipation force adopts relatively smaller values compared to the viscous coupling. Moreover, for a viscous coupling, the normalized dissipation force decreases when increasing the frequency. Such behavior is also observed for the bulk gel (figure 5.B.5): G''/ω decreases when increasing ω. The error bars show the standard deviation over sampling times.

The microsphere-hydrogel interaction can be tuned by subjecting the probe to an high optical restoring force. The physics of this process is as follows: while the particle is attached to an horizontal optical spring, it adheres to the substrate. If the spring constant tends to infinity, resembling an attached fixed rigid rod to the microsphere, the particle cannot move with the substrate movement; therefore, the broken bonds between the particle and the substrate cannot be reformed, and the particle detaches. To examine this hypothesis, active interfacial experiments with an high optical trap stiffness were conducted using a bare silica microsphere adhering to gels A ($k_t \approx$ 24 μN m^{-1}) and B ($k_t \approx$ 27 μN m^{-1}). The experimental repeats are also presented in Appendix 6.C.

At an high optical force, there is an higher probability for decoupling the microsphere from the substrate. The Cole-Cole plots for gels A and B are presented in figure 6.6.15. In this figure, the drive frequency effect is the same as $k_t \approx 9$ μN m^{-1} (figure 6.6.7): increasing the shear rate, modifies the adhesion viscoelastic properties such that the inclusion tends to behave as a fluid. For gel A, the adhesion remained in the elastic-coupling region at $k_t \approx 9$ μN m^{-1} at all frequencies (figure 6.6.7); however, at an high optical force, it is shifted to the viscous-coupling region at high frequencies (f = 64 Hz and 128 Hz) as observed in figure 6.6.15, panel a (green and yellow symbols).

Interestingly, decreasing the gel stiffness (gel B), presented in figure 6.6.15 (b), results in prevailing loss moduli against storage moduli ($G'' > G'$) at all the experimented frequencies. Recall that at such condition with $k_t \approx 9$ μN m^{-1} (figure 6.6.7b), the adhesion resides in the elastic-coupling region at low frequencies ($f \leq$ 32 Hz). Normalizing the viscoelastic moduli with the gel shear modulus (right panel) results in the similar range of $G/\mu_g \approx 0.4 \times 10^{-3} - 1 \times 10^{-3}$ to gel A at $k_t \approx 9$ μN m^{-1} at $f \leq 32$ Hz (elastic coupling), showing that the trap stiffness increase is not adequate to significantly shift the coupling mode; however, for the loss modulus-dominant adhesion to gel A at high frequencies as well as all the cases for gel B, the storage modulus attains relatively small values $G'/\mu_g \leq 0.3 \times 10^{-3}$ at the high trap stiffness. At such an high trap stiffness, the microspheres do not adhere to

gel C.

Interfacial dynamic viscosity (presented in figure 6.6.16, left panel) at an high trap stiffness shows that for gel A, when the microsphere is in the elastic adhesion region ($f \leq 32$ Hz), the viscosity ($\eta'/\eta_s \approx 3$) is higher than that furnished with $k_t \approx 9$ μN m^{-1} ($\eta'/\eta_s \approx 0.8$), indicating that the high trap restoring force is able to increase the interfacial loss modulus at a specified drive frequency. As expected, increasing the drive frequency, decreases the interfacial dynamic viscosity for both gels only if the particle adhesion is not strongly dominated by the elastic forces, *i.e.*, gel A at high frequencies (panel a, green $f = 64$ Hz and yellow $f = 128$ Hz symbols) and gel B (panel b, at all frequencies). The dynamic viscosity (η'/η_s), furnished from active interfacial microrheology on gel B at $k_t \approx 27$ μN m^{-1} adopts values between $\approx 2.5 - 5$ (figure 6.6.16, left panel b), which is higher than furnished with $k_t \approx 9$ μN m^{-1} (between $\approx 1 - 3$, figure 6.6.8, left panel b). Moreover, if the adhesion resides in the elastic region, the out-of-phase viscosity (figure 6.6.16, right panel a) for a specified gel at an high trap stiffness is close to that at a low trap stiffness, because in both cases the trap (decoupling) force is weaker than the intefacial elastic force. Regardless of the trap stiffness, the out-of-phase viscosity is higher for elastic adhesion compared to viscous attachment at a given frequency.

The zero-shear viscosity of an elastically-coupled inclusion, furnished from the dynamic and out-of-phase viscosity, presented in figure 6.6.17, decreases when increasing the drive frequency: a behavior similar to the low trap stiffness, shown in figure 6.6.9. For gel A, the zero-shear viscosity, furnished at high (figure 6.6.17) and low (figure 6.6.9) trap stiffnesses are very close; however, η_0 in a viscous coupling is lower than an elastic adhesion. Zero-shear viscosity of gel B (right panel) attains values close to the solvent viscosity, which has weaker dependency on the external drive.

Figure 6.6.18 presents the phase lag (left panel) and loss tangent (right panel) for a bare silica microsphere, adhered to gels A (panel a, $k_t \approx 24$ μN m^{-1}) and B (panel b, $k_t \approx 27$ μN m^{-1}). The phase lag for gel A at low frequencies ($f \leq 32$ Hz, elastic adhesion) adopts

small values, which are still larger than furnished with $k_t \approx 9$ μN m^{-1} (see figure 6.6.10, left panel a). This is expected, because an higher restoring force helps the microsphere partially detach from the gel; however, as soon as the particle adhesion falls into the viscous region ($f > 32$ Hz), the phase lag, as evidenced by figure 6.6.18, left panel (a), increases sharply, *e.g.*, for gel A at $f = 64$ Hz, $\tan\phi \approx 0.5$ at $k_t \approx 24$ μN m^{-1} while $\tan\phi \approx 0.1$ at $k_t \approx 9$ μN m^{-1}. For a semi-stiff gel (B) at $k_t \approx 27$ μN m^{-1}, all the phase lags stand tremendously higher than at $k_t \approx 9$ μN m^{-1} and become attenuated with the drive frequency (similar to the behavior of an optically trapped particle in bulk electrolyte), which suggests that the particle is much mobile in the former (high k_t) condition.

The boundary of viscous and elastic coupling is indicated by $\tan\delta = 1$. The loss-to-storage moduli ratio (loss tangent, shown in figure 6.6.18, right panel) follows a similar trend as the phase lag. When the adhesion is elastically stiff, the loss tangent is smaller than 1; however, comparing $k_t \approx 24$ μN m^{-1} to $k_t \approx 9$ μN m^{-1} (figure 6.6.10), the loss tangent adopts higher values at an higher trap stiffness. The abrupt increase in the loss tangent is evident by figure 6.6.18, panel (a), when the adhesion regime changes. For gel B (panel b), the loss tangent at low frequencies is higher than both gel A at the same trap stiffness and gel B at $k_t \approx 9$ μN m^{-1}.

Employing the phase lags, the effective transverse diffusion coefficients are calculated according to Eqn. 6.23 and shown in figure 6.6.19. The trend is similar to that at $k_t \approx 9$ μN m^{-1}, *i.e.*, the diffusion coefficient increases when increasing the shear rate for both gels, while the diffusion on a softer gel (B, blue symbols) is faster than that on a stiffer gel (A, black symbols). Comparing figure 6.6.19 with figure 6.6.11 shows that when the particle-hydrogel adhesion is elastically firm ($G' > G''$), the increase in trap stiffness is not able to affect the interacting surfaces significantly, and the effective lateral diffusion coefficient remains similar at both k_t; however, when the coupling is dominated by the viscous stresses, *e.g.*, gel B, it is more susceptible to the restoring force, which brings about faster diffusion at an higher trap stiffness.

The SLS and ESLS models are examined to fit the storage and loss moduli, acquired at an high trap stiffness, which are illustrated in figure 6.6.20. The storage modulus (left panel a) remains almost unchanged by decreasing $\omega\tau$ if the adhesion is dominated by the elastic stresses, *i.e.*, large $\omega\tau$. At this condition, the loss modulus (right panel a) increases when decreasing $\omega\tau$. This is a typical behavior of a Maxwell viscoelastic material. However, when the microsphere undergoes viscous coupling to the gel, *i.e.*, low $\omega\tau$, the storage modulus is more affected by the trap stiffness, tending to small values, and the loss modulus, in contrast to a typical Maxwell material, increases with decreasing $\omega\tau$. Similar to $k_t \approx 9$ μN m^{-1} (figure 6.6.12), the SLS model furnishes $k_e \approx 0$ for both gels, showing its inability to describe the low-$\omega\tau$ behavior. The ESLS model, however, furnishes much accurate fits for gels A and B, because at such an high trap stiffness, the microsphere is partially decoupled from the gel and experiences a wide range of $\omega\tau$, from $0.01 - 10$. The ESLS fit parameter for gels A and B, $\eta/(0.001\tau\mu_g) \approx 0.58$ and 0.24, which are comparable to that furnished previously with $k_t \approx 9$ μN m^{-1} (A: 0.23, and B: 0.33). The elastic contribution of the trap can be considered by normalizing the fit parameter $(\eta/\tau)/(k_t/R) \approx 0.087$ (0.02) and ≈ 0.091 (0.077) for gel A (B) at the high or low trap stiffness, respectively. It can be concluded that if the adhesion is elastic, η/τ remains comparable when normalized with the trap spring constant; however, for weak adhesion, it decreases by changing the adhesion regime from elastic to viscous. All the experiments on gel B at such an high trap stiffness adopt viscous binding; therefore, lack of data at $\omega\tau > 1$ reduces the SLS model (black line) fit accuracy, as presented in figure 6.6.20, panel (b).

The dissipation force at the high trap stiffness is presented in figure 6.6.21 for gels A (left panel) and B (right panel). Similarly to the gel A interfacial inclusion behavior at $k_t \approx 9$ μN m^{-1} (figure 6.6.14), there exists a maximum value for the normalized dissipation force if the coupling is dominated by the elasticity, which occurs at intermediate drive frequencies (left panel). Further increase in the shear rate results in a level-off in the dynamic viscosity, and, consequently, the normalized dissipation force decreases. The high-frequency

dissipation, here, is slightly larger than $k_t \approx 9$ μN m^{-1}, because subjecting the microsphere to the high restoring force resulted in higher binding loss modulus at the gel interface. Moreover, at the low trap stiffness and $f \leq 32$ Hz, where the coupling is dominated by the elastic stresses, the dissipation force is smaller ($k_t \approx 9$ μN m^{-1}, figure 6.6.14, right panel a) than here, while it adopts similar values at high frequencies for both gels, which suggests that the particle-hydrogel inclusions experience similar interfacial viscous evolution.

The interfacial adhesion phase diagram, in which the adhesion is divided into three main categories, namely elastic ($G' > G''$), aging (transition from $G'' > G'$ to $G' > G''$), and viscous ($G'' > G'$) coupling, is constructed by comparing G' and G'' at various operating conditions, including trap stiffness, drive frequency, and substrate stiffness. The interfacial adhesion phase diagrams for gels A, B, and C are presented in figure 6.6.22. As can be seen in this figure, for gel A (left panel), regardless of the optical trap stiffness, presented as $k_t^* = k_t/(R\mu_g)$, at low frequencies (shown as the Roshko number: Ro $= fR^2\rho_s/\eta_s$), a bare microsphere adheres elastically to gel A. Increasing the frequency and trap stiffness is not able to change the adhesion region until $k_t^*/10^{-3} \approx 6.8$, after which the coupling is dominated by the viscosity. Decreasing the gel stiffness (gel B: middle panel and gel C: right panel) facilitates viscous adhesion at a given trap stiffness and drive frequency, as evidenced by the wide operating condition at which the adhesion is dominated by the viscous stresses, *e.g.*, data points shown with squares.

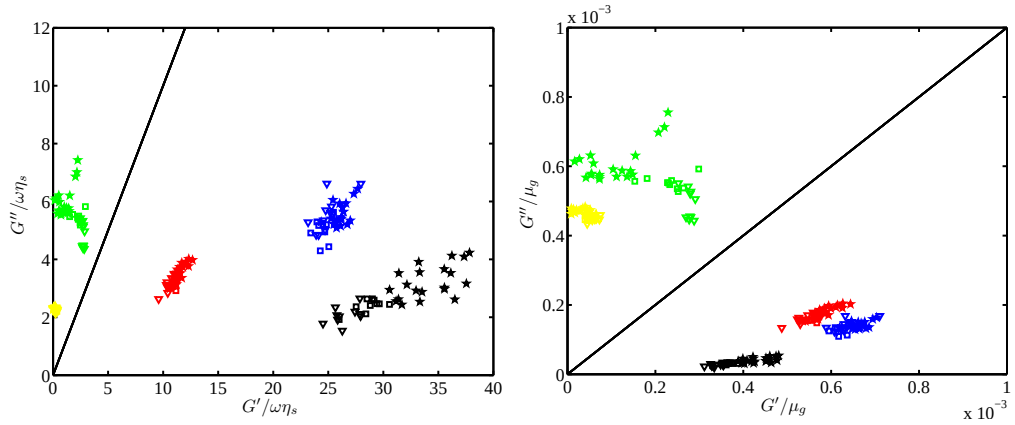

(a) Bare silica microsphere on PA hydrogel A, $k_t \approx 24$ μN m^{-1}.

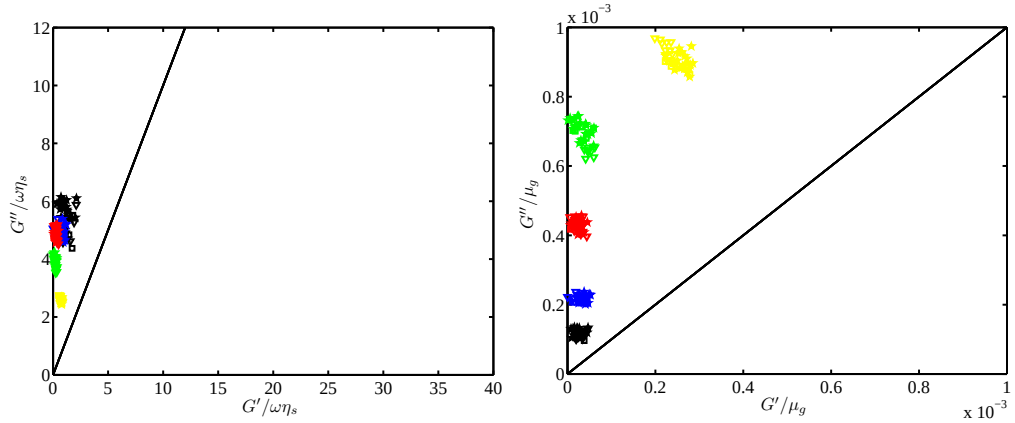

(b) Bare silica microsphere on PA hydrogel B, $k_t \approx 27$ μN m^{-1}.

Figure 6.6.15: Loss modulus G'' versus storage modulus G' (Cole-Cole plots), normalized with solvent viscosity ($\eta_s \approx 0.9$ cP), presented in left panel, or gel shear modulus μ_g, shown in right panel, for a bare silica microsphere adhered to PA hydrogels A (panel a, $k_t \approx 24$ μN m^{-1}) and B (panel b, $k_t \approx 27$ μN m^{-1}) in TAE buffer (pH = 8.3, ionic strength 41 mmol l^{-1}), furnished from active interfacial microrheology. The boundary of the viscous ($G'' > G'$)-to-elastic ($G' > G''$) transition (*i.e.*, $G'' = G'$) is indicated with the solid line. The stage (and consequently the probe particle) is subject to a small-amplitude ($|x_s| \approx 30$ nm, see table 6.1) sinusoidal displacement with an oscillatory shear frequency $f \approx 8$ Hz (black symbols), 16 Hz (blue symbols), 32 Hz (red symbols), 64 Hz (green symbols), and 128 Hz (yellow symbols), shown with triangles ($t \leq 180$ s), squares ($180 < t \leq 360$ s), and pentagons ($t > 360$ s). Despite employing such an high trap stiffness, gel A can still keep the particle in the elastic coupling mode at low enough frequencies ($f \leq 32$ Hz). A semi-stiff gel (B) storage modulus is relatively smaller than the stiffer one (A) at a given drive frequency. An high enough drive frequency or low enough substrate stiffness can shift the coupling towards the viscous region. Data for gels A and B are for various microspheres.

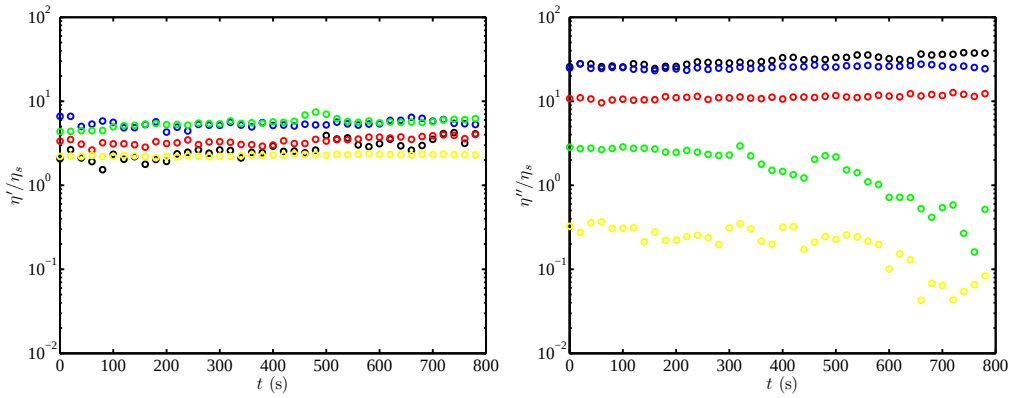

(a) Bare silica microsphere on PA hydrogel A, $k_t \approx 24$ μN m^{-1}.

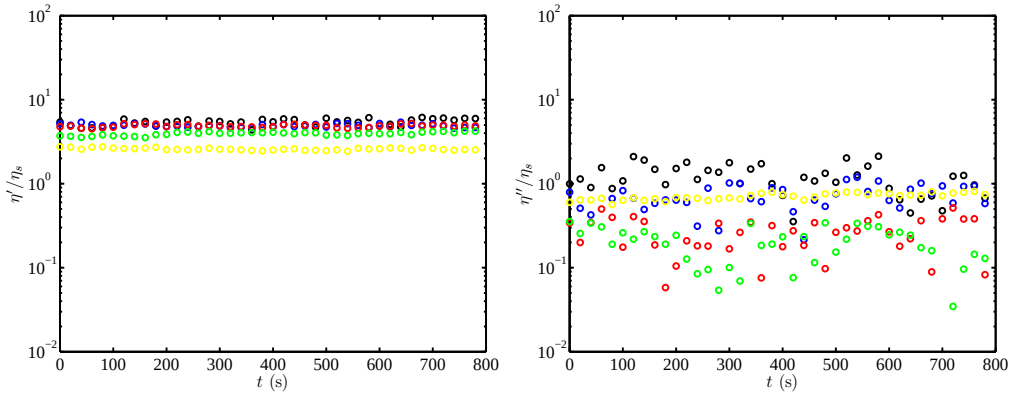

(b) Bare silica microsphere on PA hydrogel B, $k_t \approx 27$ μN m^{-1}.

Figure 6.6.16: Interfacial dynamic viscosity $\eta' = G''/\omega$ (left panel) and out-of-phase viscosity $\eta'' = G'/\omega$ (right panel) versus time t for a bare silica microsphere on PA hydrogels A (panel a, $k_t \approx 24$ μN m^{-1}) and B (panel b, $k_t \approx 27$ μN m^{-1}) in TAE buffer (pH = 8.3, ionic strength 41 mmol l^{-1}), furnished from active interfacial microrheology. All experimental parameters are the same as figure 6.6.15. The oscillatory shear frequency $f \approx 8$ Hz (black symbols), 16 Hz (blue symbols), 32 Hz (red symbols), 64 Hz (green symbols), and 128 Hz (yellow symbols). The acquired interfacial dynamic viscosity at low frequencies fluctuates around $\eta'/\eta_s \approx 3$ and 5 for gels A and B, respectively, which are smaller than the values obtained from the passive interfacial microrheology (figure 5.6.8). The gel A and B interfacial dynamic viscosity are higher than obtained in figure 6.6.8, because the particle is whether no longer in the elastic adhesion region or it is closer to a viscous binding mode. Such an high trap stiffness can partially decouple the particle from the substrate, resulting in decreased elastic and increased loss moduli. An high enough drive frequency or low enough substrate stiffness can decrease the dynamic viscosity down to solvent viscosity probed near the gel wall (see figure 6.6.5). Moreover, the stiffer the substrate, the higher the out-of-phase viscosity at a given frequency (see right panel).

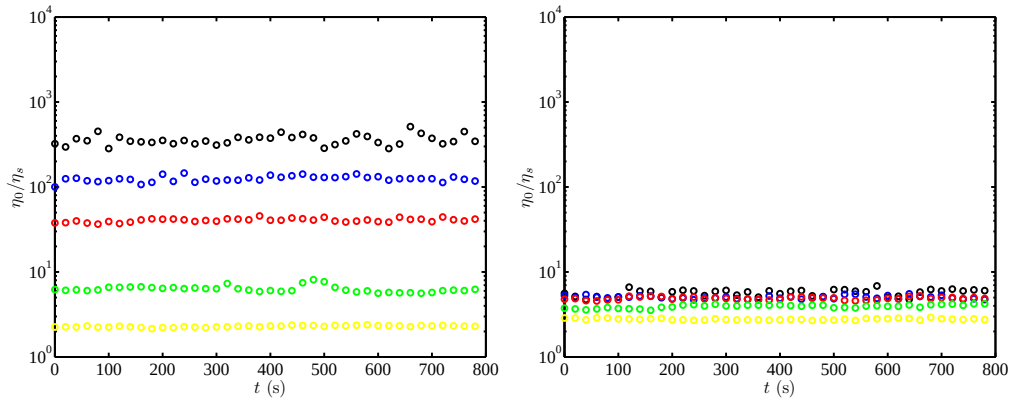

Figure 6.6.17: Interfacial zero-shear viscosity $\eta_0 = \eta' \left[1 + (G'/G'')^2\right]$ versus time t, furnished from active interfacial microrheology with a bare silica microsphere, adhered to PA hydrogels A (left panel, $k_t \approx 24$ μN m^{-1}) and B (right panel, $k_t \approx 27$ μN m^{-1}). At a given frequency, a stiffer substrate results in an higher interfacial zero-shear viscosity. Also, η_0 decreases when increasing the shear rate, which can ultimately reach the solvent viscosity near a gel film ($\approx 2\eta_s \approx 1.8$ cP) at high enough frequencies (see yellow symbols in the left panel). The zero-shear viscosity at a low drive frequency, *e.g.*, $f = 8$ Hz, is higher than the dynamic viscosity, furnished by the passive interfacial microrheology (figure 5.6.8) for a specified gel. Compared to a low trap stiffness ($k_t \approx 9$ μN m^{-1}, figure 6.6.9), the zero-shear viscosity is comparable for gel A at $f \leq 32$ Hz, *i.e.*, elastic adhesion between the probe particle and the gel, and is slightly decreased at $f > 32$ Hz, *i.e.*, viscous coupling. For gel B, η_0 is attenuated at all the frequencies, because the particle is more susceptible to the trap restoring force when it is in the viscous coupling (weaker adhesion) region.

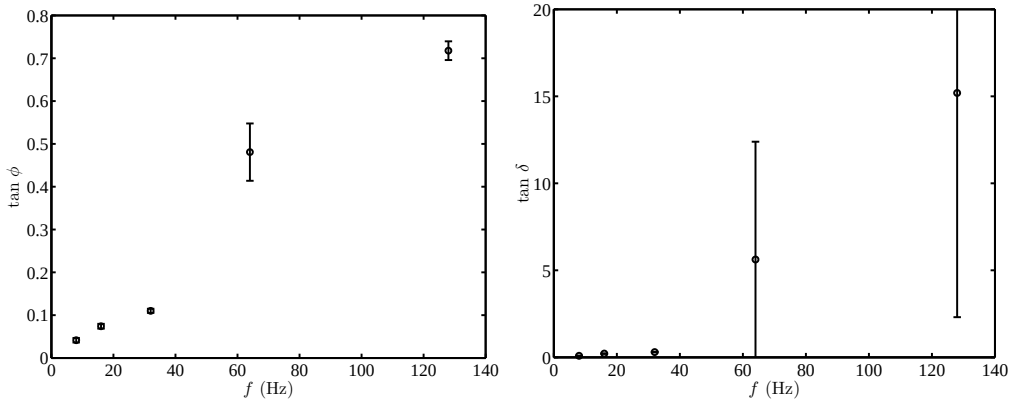

(a) Bare silica microsphere on PA hydrogel A, $k_t \approx 24$ μN m^{-1}.

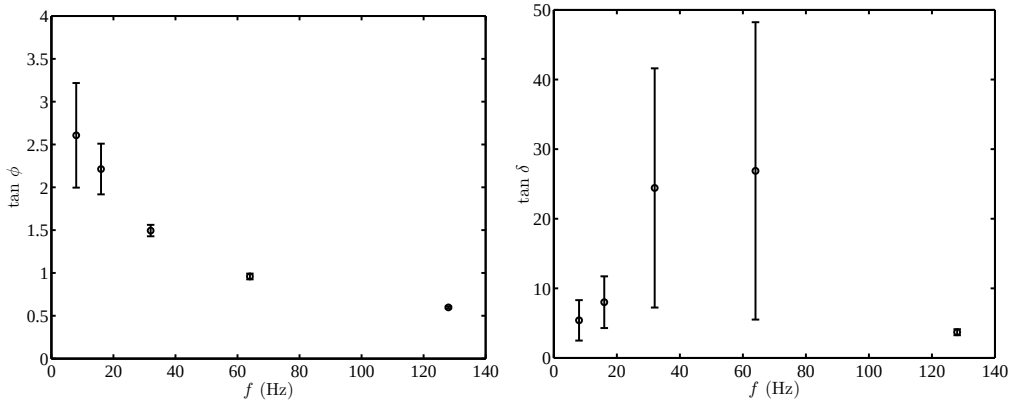

(b) Bare silica microsphere on PA hydrogel B, $k_t \approx 27$ μN m^{-1}.

Figure 6.6.18: Phase lag of a bare silica microsphere probe response to an external sinusoidal shear $\tan\phi$ (left panel) and loss tangent $\tan\delta$ (right panel) versus drive frequency f while the microsphere is attached to PA hydrogels A (panel a, $k_t \approx 24$ μN m^{-1}) and B (panel b, $k_t \approx 27$ μN m^{-1}) in TAE buffer (pH = 8.3, ionic strength 41 mmol l^{-1}), obtained from active interfacial microrheology. All experimental parameters are the same as figure 6.6.15. The values are averaged over the sampling time shown in figure 6.6.15. Despite an high optical trap stiffness, while the particle is in the elastic coupling region (panel a, $f \leq 32$ Hz), the phase lag adopts relatively small values, which linearly increases with f; however, when the particle is decoupled from the gel surface (panel b, $f \geq 16$ Hz), phase lags adopt relatively high values and decrease with increasing f. Compared to figure 6.6.10, an high trap stiffness results in an higher loss tangent, because it shifts the binding toward the viscous region. Note that the positive and negative error bars, representing the standard deviation, are equal; however, they are partially shown in panel a to maintain the readability of low-frequency data.

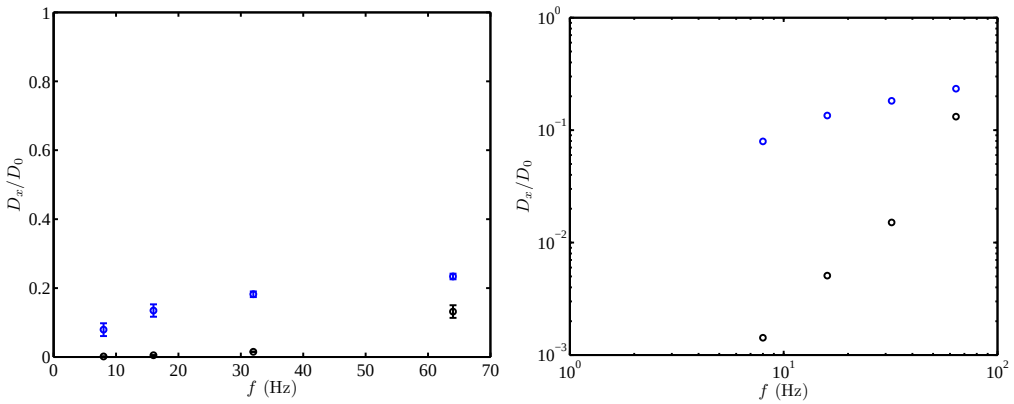

Figure 6.6.19: Effective interfacial transverse diffusion coefficient $D_x = 2\pi f k_B T \tan(\phi)/k_t$ versus drive frequency f, furnished from active microrheology with a bare silica microsphere, adhered to PA hydrogels A (black symbols, $k_t \approx 24$ μN m^{-1}) and B (blue symbols, $k_t \approx 27$ μN m^{-1}). At a given frequency, a stiffer substrate attenuates the effective transverse diffusion coefficient more than a softer gel. Also, the diffusion coefficient depends on the drive frequency and can reach values close to the free diffusion coefficient near a rigid wall in an unbound solvent at high enough frequencies. The free diffusion coefficient of a silica microsphere in unbound water $D_0 \approx 0.25$ μm^2 s^{-1} at $T \approx 23$°C. Compared to $k_t \approx 9$ μN m^{-1} (figure 6.6.11), an higher restoring force on the microsphere increases the effective transverse diffusion coefficient when the coupling is dominated by the viscous stresses. The right panel is a logarithmic presentation of the same data.

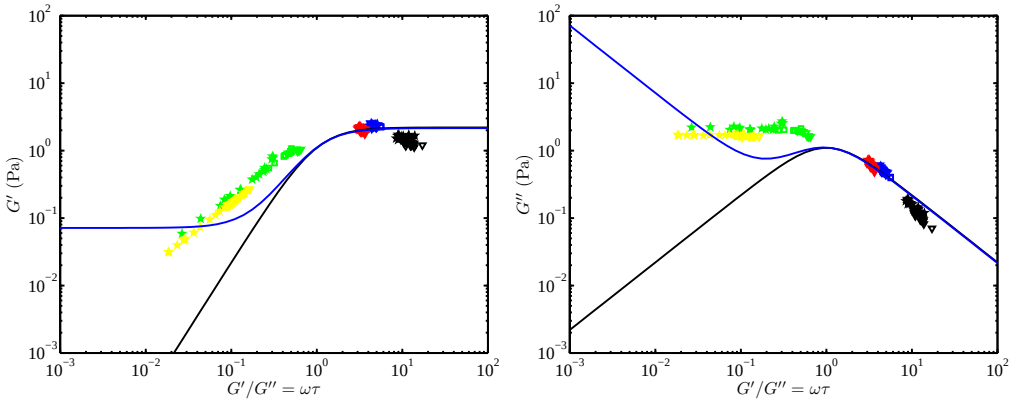

(a) Bare silica microsphere on PA hydrogel A, $k_t \approx 24$ μN m^{-1}.

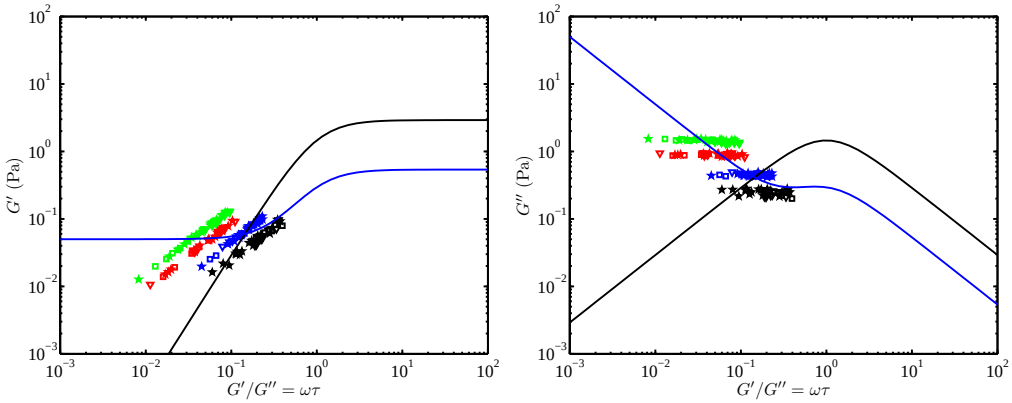

(b) Bare silica microsphere on PA hydrogel B, $k_t \approx 27$ μN m^{-1}.

Figure 6.6.20: Storage (left panel) and loss (right panel) moduli versus dimensionless relaxation time $G'/G'' = \omega\tau$ with a simultaneous least-squares best fit to the standard linear solid (SLS, black line) and extended standard linear solid (ESLS, blue line) models for gels A (panel a, $k_t \approx 24$ μN m^{-1}) and B (panel b, $k_t \approx 27$ μN m^{-1}). Fit parameter η/τ in the SLS model: $G' = k_e + (\eta/\tau)\frac{(\omega\tau)^2}{1+(\omega\tau)^2}$ and $G'' = (\eta/\tau)\frac{\omega\tau}{1+(\omega\tau)^2}$ for gels A and B is 2.20 and 2.91, respectively, resulting in $\eta/(0.001\tau\mu_g) \approx 0.61$ and 1.4, and $\eta/\tau/(k_t/R) \approx 0.092$ and 0.108, respectively. Normalizing the fit parameter with the trap stiffness allows the comparison with other trap stiffnesses, *e.g.*, for gel A, at $k_t \approx 9$ μN m^{-1}, $\eta/\tau/(k_t/R) \approx 0.091$, which is in close agreement with the value furnished at $k_t \approx 24$ μN m^{-1}. Lack of elastic coupling data for gel B prevents the fit from being accurate. For all cases, $k_e \approx 0$. The ESLS model, $G' = k_e + (\eta/\tau)\frac{(\omega\tau)^2}{1+(\omega\tau)^2}$ and $G'' = (\eta/\tau)\frac{\omega\tau}{1+(\omega\tau)^2} + k_e/(\omega\tau_e)$, furnishes much accurate fits for gel B. The ESLS model parameters (all in Pa) for gels A, $\eta/\tau \approx 2.08, k_e \approx 0.07$, and B, $\eta/\tau \approx 0.49, k_e \approx 0.05$, which bring about $(\eta/\tau)/(0.001\mu_g) \approx 0.58$ and 0.24 for gels A and B, respectively. Normalizing η/τ with the trap stiffness for gel A ($k_t \approx 24$ μN m^{-1}) and B ($k_t \approx 27$ μN m^{-1}) results in $\eta/\tau/(k_t/R) \approx 0.087$, and 0.02, which is close to the values furnished at $k_t \approx 9$ μN m^{-1} for gel A (0.091), and is lower than gel B (0.077). All experimental parameters are the same as figure 6.6.15.

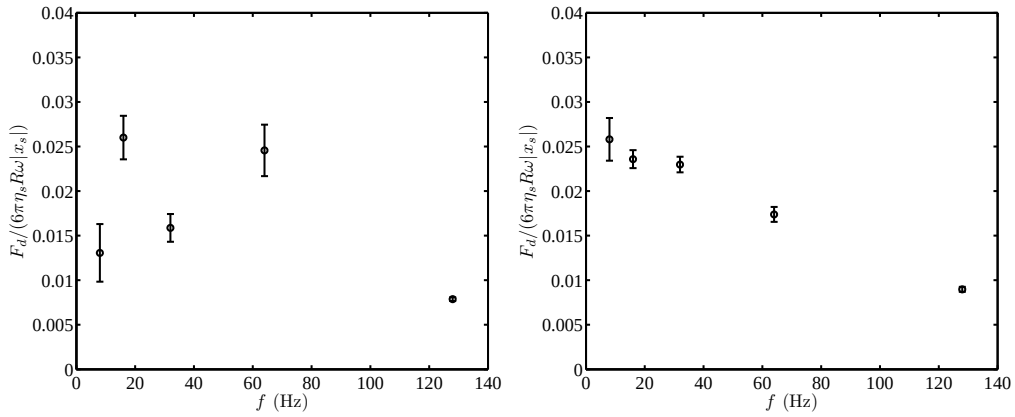

Figure 6.6.21: Dissipation force $F_d = \pi |x_s|^2 G''$, normalized with the Stokes drag force $6\pi\eta_s R\omega |x_s|$ versus drive frequency f, furnished from active interfacial microrheology with a bare silica microsphere adhered to hydrogels A (left panel, $k_t \approx 24$ μN m^{-1}) and B (right panel, $k_t \approx 27$ μN m^{-1}) in TAE buffer. Compared to a lower trap stiffness ($k_t \approx 9$ μN m^{-1}, 6.6.14, panel a), the dissipative force is higher at a specified frequency if the microsphere is elastically adhered to the gel. For the case of viscous adhesion, the dissipative force is not significantly affected by the trap stiffness. At such condition, *e.g.*, gel B (right panel), the dissipation force decreases when increasing the frequency, because the interfacial dynamic viscosity decreases (see figure 6.6.16, left panel b). Such behavior is also observed for the bulk gel (figure 5.B.5). The error bars show the standard deviation over sampling times.

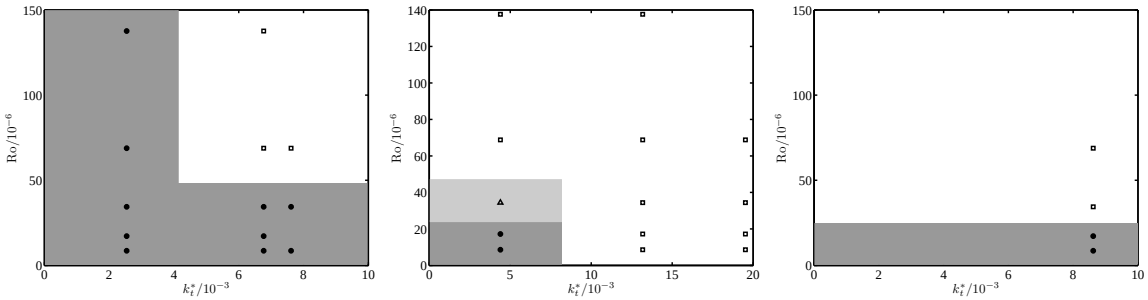

Figure 6.6.22: Interfacial adhesion phase diagram, furnished from active interfacial microrheology with a bare silica microsphere, coupled to PA hydrogels A (left panel), B (middle panel), and C (right panel), obtained by tuning the drive frequency, presented as Roshko number $\mathrm{Ro} = fR^2\rho_s/\eta_s$, and optical trap stiffness, presented as $k_t^* = k_t/(R\mu_g)$. Elastic adhesion ($G' > G''$) region is shown with dark gray color, distinguished by the experimental data points presented as filled circles. Viscous coupling ($G'' > G'$) region is illustrated with white color, distinguished by the experimental data points presented as squares. Aged coupling (transition from $G'' > G'$ to $G' > G''$) region is illustrated with light gray color, distinguished by the experimental data points presented as triangles.

6.7 Conclusions

The soft, wet adhesion of a bare silica microsphere to a PA hydrogel film has been addressed while the particle was subject to an external oscillatory shear. An active interfacial microrheology method is developed using custom-built optical tweezers combined with the back-focal plane interferometry and phase-sensitive measurements to furnish an optically trapped particle position fluctuations response to an external small-amplitude sinusoidal drive. The real and imaginary responses versus the microsphere height when elevated, and versus time while attached to a gel, are further used to calculate the viscoelastic properties of the microsphere-hydrogel interfacial inclusion in TAE buffer. The Nyquist analysis shows that the microsphere interfacial adhesion follows an abrupt transition from an-almost-pure viscous regime in the bulk electrolyte to an elastic coupling at low shear rates and optical restoring force and high substrate stiffness. The coupling is strongly affected by the underlying substrate shear modulus by which the microsphere dynamics become attenuated. Fixing the van der Waals attraction by using three PA gels with the same monomer concentration (5 %) and different crosslinker concentrations revealed that the lower the elastic stress, the weaker the adhesion. This may suggest that there are more dangling polymer chains on a stiffer gel surface, which can be adsorbed on bare silica microspheres. The equilibrium adsorbed chain number is, therefore, a function of operating condition, *e.g.*, at extreme shear rate or optical restoring force, the chain detachment from the particle may result in complete gel-particle decoupling. The interfacial loss and storage moduli data points are mostly clustered versus time, which is related to discrete interfacial adhesion energy metastable minima. The dynamics of interfacial viscoelasticity, viscosity, phase lag, and loss tangent, suggest that the substrate stiffness, external shear rate and extension, and optical restoring force can be employed to shift the interfacial energy minima, permitting the design of tunable soft adhesion platforms for controlled release and bioadhesion purposes. Future work seeks to study the effect of intermolecular forces on the interfacial soft adhesion dynamics by coating the bare silica microspheres.

Appendix

6.A Maxwell model derivation for linear viscoelasticity

To derive the constitutive equation governing the Maxwell model for a bead attached to a viscoelastic substrate, a spring (denoted by number 1 with spring stiffness per unit length k, which is related to substrate shear modulus μ) and a dash-pot (denoted by number 2 with viscosity η) as elastic and viscous elements, respectively, are considered to be connected in series. An applied stress σ to this system produces spring strain $\epsilon_1 = \sigma/k$ and dash-pot strain rate $\dot{\epsilon_2} = \sigma/\eta$; therefore,

$$\sigma = \sigma_1 = \sigma_2, \tag{6.30}$$

and

$$\epsilon = \epsilon_1 + \epsilon_2. \tag{6.31}$$

It follows that

$$\dot{\epsilon} = \dot{\epsilon_1} + \dot{\epsilon_2} = \frac{d}{dt}\left(\frac{\sigma}{k}\right) + \frac{\sigma}{\eta} = \frac{\dot{\sigma}}{k} + \frac{\sigma}{\eta} + \frac{\sigma\dot{k}}{k^2}, \tag{6.32}$$

so upon introducing a relaxation time $\tau = \eta/k$, we have

$$\frac{1}{\tau}\sigma + \dot{\sigma} + \frac{\sigma\dot{k}}{k} = k\dot{\epsilon}, \tag{6.33}$$

which reduces to Eqn. 6.9 when taking $\dot{k} = 0$. This demands the Young's modulus (spring stiffness) to be independent of time (which is the case for elastic materials, including hy-

drogels) and/or $\epsilon_1 \approx 0$. Note that this is the only assumption in deriving the Maxwell viscoelasticity model, which is adjusted to fit the active interfacial moduli. If this term is not neglected, for an oscillatory strain $\epsilon = \epsilon_0 \exp(i\omega t)$ [resulting in $\sigma = \sigma_0 \exp(i\omega t)$], the foregoing Maxwell model furnishes

$$G' = k\frac{(\omega\tau)^2}{1+(\omega\tau)^2+\frac{\tau\dot{k}}{k^2}}, \tag{6.34}$$

and

$$G'' = k\frac{\omega\tau(1+\frac{\tau\dot{k}}{k^2})}{1+(\omega\tau)^2+\frac{\tau\dot{k}}{k^2}}. \tag{6.35}$$

It is emphasized in the active microrheology of a silica microsphere-PA gel interfacial inclusion that the relaxation time changes when changing the drive frequency; however, the good fit of the high-$\omega\tau$ moduli to the Maxwell model with $\dot{k} = 0$ proves that the assumption of a constant τ in model is unnecessary. Moreover, $\tau\dot{k}/k^2 = \eta\dot{k}/k^3$, which is expected to be negligible for an elastic coupling due to an high k and low η.

6.B Viscoelasticity and diffusion coefficient from phase-sensitive measurements

From Eqn. 6.5,

$$\gamma^* = \frac{-k_t x_p}{\dot{x}_p - \dot{x}_s} = \frac{-k_t x_p}{i\omega\left[\hat{x}_p e^{i(\omega t+\phi)} - \hat{x}_s e^{i\omega t}\right]} = \frac{-k_t}{i\omega}\frac{\hat{x}_p e^{i\phi}}{\hat{x}_p e^{i\phi} - \hat{x}_s} = \frac{k_t}{i\omega}\frac{\hat{x}_p e^{i\phi}/\hat{x}_s}{1-\hat{x}_p e^{i\phi}/\hat{x}_s}, \tag{6.36}$$

or

$$\gamma^* = \frac{k_t}{i\omega}\frac{S^*}{1-S^*} \text{ with } S^* = \hat{x}_p e^{i\phi}/\hat{x}_s. \tag{6.37}$$

Accordingly,

$$\gamma^* = \frac{ik_t}{\omega}\frac{-\hat{x}_p e^{i\phi}}{\hat{x}_s - \hat{x}_p e^{i\phi}} = \frac{ik_t}{\omega}\frac{-\mathrm{Re}(x_p) - i\mathrm{Im}(x_p)}{\hat{x}_s - \mathrm{Re}(x_p) - i\mathrm{Im}(x_p)} \times \frac{\hat{x}_s - \mathrm{Re}(x_p) + i\mathrm{Im}(x_p)}{\hat{x}_s - \mathrm{Re}(x_p) + i\mathrm{Im}(x_p)} =$$
$$\frac{k_t}{\omega}\frac{-i\hat{x}_s\mathrm{Re}(x_p) + i\mathrm{Re}^2\left(x_\mathrm{p}\right) + \cancel{\mathrm{Re}(x_p)\mathrm{Im}(x_p)} + \hat{x}_s\mathrm{Im}(x_p) - \cancel{\mathrm{Im}(x_p)\mathrm{Re}(x_p)} + i\mathrm{Im}^2\left(x_\mathrm{p}\right)}{\left[\hat{x}_s - \mathrm{Re}(x_p)\right]^2 + \mathrm{Im}^2\left(x_\mathrm{p}\right)}$$
$$= \frac{k_t}{\omega}\frac{-i\left[\hat{x}_s\mathrm{Re}(x_p) - \mathrm{Re}^2\left(x_\mathrm{p}\right) - \mathrm{Im}^2\left(x_\mathrm{p}\right)\right] + \hat{x}_s\mathrm{Im}(x_p)}{\left[\hat{x}_s - \mathrm{Re}(x_p)\right]^2 + \mathrm{Im}^2\left(x_\mathrm{p}\right)} \tag{6.38}$$
$$= \frac{k_t}{\omega}\frac{-i\left[\hat{x}_s\mathrm{Re}(x_p) - \hat{x}_p^2\right] + \hat{x}_s\mathrm{Im}(x_p)}{\left[\hat{x}_s - \mathrm{Re}(x_p)\right]^2 + \mathrm{Im}^2\left(x_\mathrm{p}\right)}.$$

From Eqn. 6.7,

$$G' = \frac{k_t}{6\pi R}\frac{\hat{x}_s\mathrm{Re}(x_p) - \hat{x}_p^2}{\left[\hat{x}_s - \mathrm{Re}(x_p)\right]^2 + \mathrm{Im}^2\left(x_\mathrm{p}\right)}, \tag{6.39}$$

and

$$G'' = \frac{k_t}{6\pi R}\frac{\hat{x}_s\mathrm{Im}(x_p)}{\left[\hat{x}_s - \mathrm{Re}(x_p)\right]^2 + \mathrm{Im}^2\left(x_\mathrm{p}\right)}, \tag{6.40}$$

$$\gamma^* = \frac{6\pi R(G' + iG'')}{i\omega} = \frac{k_t}{i\omega}\frac{S^*}{1 - S^*}, \tag{6.41}$$

$$\frac{6\pi R}{k_t}(G' + iG'') = \frac{S^*(1 + S^*)}{1 - S^{*2}}, \tag{6.42}$$

$$\frac{6\pi R}{k_t}(1 - S^{*2})(G' + iG'') = S^*(1 + S^*) = S^* + S^{*2} = S' + iS'' + S^{*2}; \tag{6.43}$$

therefore,

$$S' = \frac{6\pi R}{k_t}(1 - S^{*2})G' - S^{*2}, \tag{6.44}$$

and

$$S'' = \frac{6\pi R}{k_t}(1 - S^{*2})G''. \tag{6.45}$$

Thus,

$$\tan\phi = \frac{S''}{S'} = \frac{1}{\frac{G'}{G''} - \frac{S^{*2}}{\frac{6\pi R}{k_t}(1-S^{*2})G''}}. \tag{6.46}$$

Equivalently, from the governing equation for a simple harmonic oscillator in a viscoelastic medium (complex viscosity $\eta^* = \eta' - i\eta''$ [1]) with a sinusoidal external drive x_s

$$6\pi\eta^* R(\dot{x}_p - \dot{x}_s) + k_t x_p = 0, \tag{6.47}$$

$$6\pi R\omega(\eta' - i\eta'')(x_p - x_s)i + k_t x_p = 0, \tag{6.48}$$

$$6\pi R\omega(\eta'' + i\eta')(\hat{x}_p e^{i\phi} - \hat{x}_s) + k_t \hat{x}_p e^{i\phi} = 0, \tag{6.49}$$

$$6\pi R\omega(\eta'' + i\eta')(\hat{x}_p\cos\phi + i\hat{x}_p\sin\phi - \hat{x}_s) + k_t\hat{x}_p\cos\phi + ik_t\hat{x}_p\sin\phi = 0, \tag{6.50}$$

which results in two governing equations with $A'' = 6\pi R\omega\eta''$ and $A' = 6\pi R\omega\eta'$:

$$A''(\hat{x}_p\cos\phi - \hat{x}_s) - A'\hat{x}_p\sin\phi + k_t\hat{x}_p\cos\phi = 0, \tag{6.51}$$

and

$$A'(\hat{x}_p\cos\phi - \hat{x}_s) + A''\hat{x}_p\sin\phi + k_t\hat{x}_p\sin\phi = 0. \tag{6.52}$$

For a viscous liquid $\eta'' = 0$; therefore, from Eqn. 6.51

$$\tan\phi = \frac{k_t}{A'} = \frac{k_t}{6\pi\eta' R\omega} = \frac{k_t D_0}{k_B T\omega}, \tag{6.53}$$

[1] The complex viscosity may be expressed in two forms: (i) taking the strain $\epsilon = \epsilon_0 e^{i\omega t}$, the complex shear modulus $G^* = G' + iG''$, which brings about $\eta^* = G^*/(i\omega) = \eta' - i\eta''$, and (ii) interchangeably, taking strain $\epsilon = \epsilon_0 e^{-i\omega t}$, the complex shear modulus $G^* = G' - iG''$, which gives $\eta^* = G^*/(-i\omega) = \eta' + i\eta''$.

which furnishes the particle diffusion coefficient in a viscous liquid D_0, and from Eqn. 6.52

$$\hat{x}_p = \hat{x}_s \frac{6\pi\eta' R\omega}{\sqrt{k_t^2 + (6\pi\eta' R\omega)^2}}, \tag{6.54}$$

a result used by Ghosh *et al.* (2007) without derivation. For a viscoelastic material, Eqn. 6.51 results in

$$\hat{x}_p = \frac{A''}{A'' \cos\phi - A' \sin\phi + k_t \cos\phi} \hat{x}_s, \tag{6.55}$$

and from Eqn. 6.52

$$\hat{x}_p = \frac{A'}{A' \cos\phi + A'' \sin\phi + k_t \sin\phi} \hat{x}_s. \tag{6.56}$$

These furnish

$$\tan\phi = \frac{A' k_t}{A'^2 + A''^2 + A'' k_t}, \tag{6.57}$$

which reduces to Eqn. 6.53 for a viscous medium ($A'' = 0$), also yielding $\phi = 0$ for an elastic medium ($A' = 0$). A rough approximation of Eqn. 6.57 for elasticity-dominant viscoelastic adhesion $A' \ll A''$ is $\tan\phi \approx (A'/A'')^2 \tan\phi_{viscous} = (\eta'/\eta'')^2 \tan\phi_{viscous}$.

It is necessary to derive a correlation between the transverse diffusion coefficient $D_x = k_B T/(6\pi\eta' R)$ and the phase lag in a viscoelastic medium. From Eqn. 6.57

$$\cot\phi = \frac{A'^2}{A' k_t} + \frac{A''^2}{A' k_t} + \frac{A''}{A'} = \frac{6\pi\eta' R\omega}{k_t} + \frac{6\pi R\omega \eta''^2}{\eta' k_t} + \frac{\eta''}{\eta'}, \tag{6.58}$$

so, substituting $6\pi\eta' R$ for $k_B T/D_x$ gives

$$\cot\phi = \frac{k_B T\omega}{D_x k_t} + \frac{k_B T\omega}{D_x k_t}\left(\frac{\eta''}{\eta'}\right)^2 + \left(\frac{\eta''}{\eta'}\right) = \frac{k_B T\omega}{D_x k_t}\left[1 + \left(\frac{\eta''}{\eta'}\right)^2\right] + \left(\frac{\eta''}{\eta'}\right). \tag{6.59}$$

Noting that $\eta_0/\eta' = \left[1 + \left(\frac{\eta''}{\eta'}\right)^2\right]$,

$$\cot\phi = \frac{k_B T\omega}{D_x k_t}\left(\frac{\eta_0}{\eta'}\right) + \left(\frac{\eta''}{\eta'}\right) = \frac{k_B T\omega\eta_0 + \eta'' D_x k_t}{D_x k_t \eta'}; \tag{6.60}$$

therefore,

$$D_x k_t \eta' \cot\phi - \eta'' D_x k_t = k_B T \omega \eta_0, \tag{6.61}$$

$$D_x = \frac{k_B T \omega \eta_0}{k_t \eta' \cot\phi - k_t \eta''} = \frac{k_B T \omega \tan\phi}{k_t \eta' - k_t \eta'' \tan\phi} \eta_0, \tag{6.62}$$

$$D_x = \frac{k_B T \omega \tan\phi}{k_t} \left(\frac{\eta_0}{\eta' - \eta'' \tan\phi} \right). \tag{6.63}$$

For either cases of viscous coupling ($\eta'' \approx 0$) or elastic coupling ($\tan\phi \approx 0$), $\eta'' \tan\phi \approx 0$; therefore,

$$D_x \approx \frac{k_B T \omega \tan\phi}{k_t} \left(\frac{\eta_0}{\eta'} \right). \tag{6.64}$$

If the effective diffusion coefficient is defined as $D_{x,eff} = k_B T/(6\pi\eta_0 R)$, then

$$D_{x,eff} = D_x \left(\frac{\eta'}{\eta_0} \right) \approx \frac{k_B T \omega \tan\phi}{k_t}, \tag{6.65}$$

which requires only a single parameter from the active interfacial microrheology, *i.e.*, phase lag, and does not require a position calibration. Importantly, Eqn. 6.65 proves that the methodology, suggested by Sharma *et al.* (2010*a*), to measure the transverse diffusion coefficient of an optically trapped particle near a plane wall is only valid if the medium is purely viscous, *i.e.*, $\eta_0 = \eta'$, which is not the case in biological systems.

Eqn. 6.64 results in an attenuation of the diffusion coefficient on the gel:

$$\frac{D_{x(z=0)}}{D_{x(z>0)}} \approx \frac{\tan\phi}{\tan\phi_{viscous}} \left(\frac{\eta_0}{\eta'} \right). \tag{6.66}$$

This suggests that the phase lag attenuation is inversely related to the zero-shear viscosity. Accordingly, similar to Eqn. 6.53, an approximate relationship between the phase lag and the medium viscosity $\tan\phi \approx k_t/(6\pi\eta_0 a\omega)$. Thus, the diffusion coefficient, furnished from the phase lag in the active interfacial experiments is with respect to the medium zero-shear

viscosity, instead of dynamic viscosity. Note that for an elevated particle $\eta' \approx \eta_0$; therefore, the furnished effective diffusion coefficient from the phase lag matches the prediction of the Einstein correlation. However, when the particle is attached to the gel, $\eta' \ll \eta_0$; therefore, the effective diffusion coefficient is lower than the passive interfacial microrheology one.

6.C Experimental repeats

This section presents active interfacial microrheology experimental repeats for a bare silica microsphere on PA hydrogels.

6.C.1 Gels A and B, $k_t \approx 9$ μN m^{-1}

Experimental repeats at $k_t \approx 9$ μN m^{-1} on PA gel A suggest that $G'/\mu_g \approx 0.3 \times 10^{-3}$ at all frequencies (figure 6.C.1), which is very close to $G'/\mu_g \approx 0.2 \times 10^{-3}$ furnished from figure 6.6.7. The loss modulus $G''/\mu_g \lesssim 0.25 \times 10^{-3}$ for both sets of experiments; however, figure 6.C.1 shows slightly greater loss moduli than figure 6.6.7 at a given frequency, while both show that the microsphere-hydrogel inclusion is in the elastic adhesion region. Repeated experiments on gel B (panel b) show that at all frequencies, after attachment to the gel, $G'/\mu_g \lesssim 0.5 \times 10^{-3}$ and $G''/\mu_g \lesssim 0.7 \times 10^{-3}$, which are both in good agreement with 6.6.7 (b). Also, at $f = 8$ Hz, $G' > G''$, at $f = 32$ Hz, $G'' \approx G'$, and at $f = 128$ Hz, $G'' > G'$, which agrees with 6.6.7 (b). Note that the initial contact of the microsphere with gel B at $f = 8$ Hz (black symbols) resulted in at least four times stronger adhesion, as measured by the storage modulus, which relaxed to a steady condition after ≈ 200 s. This may be because of a deep local penetration into the gel.

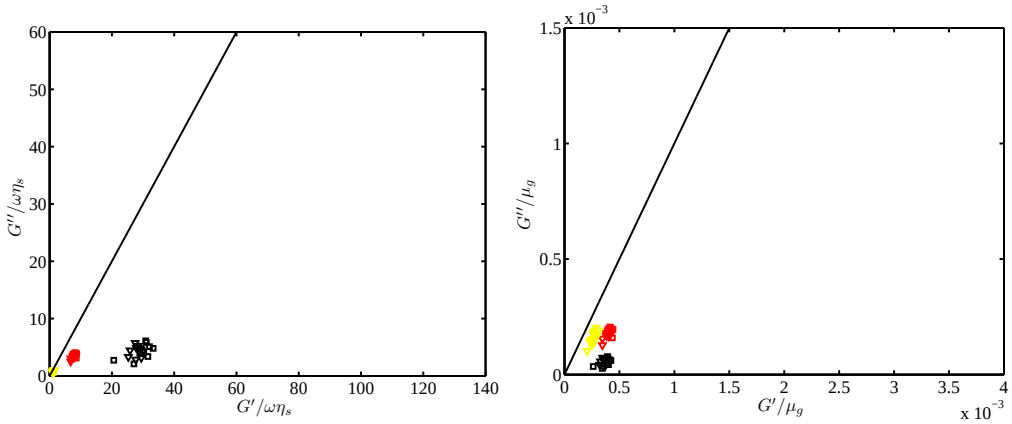

(a) Bare silica microsphere on PA hydrogel A, $k_t \approx 9$ μN m^{-1}.

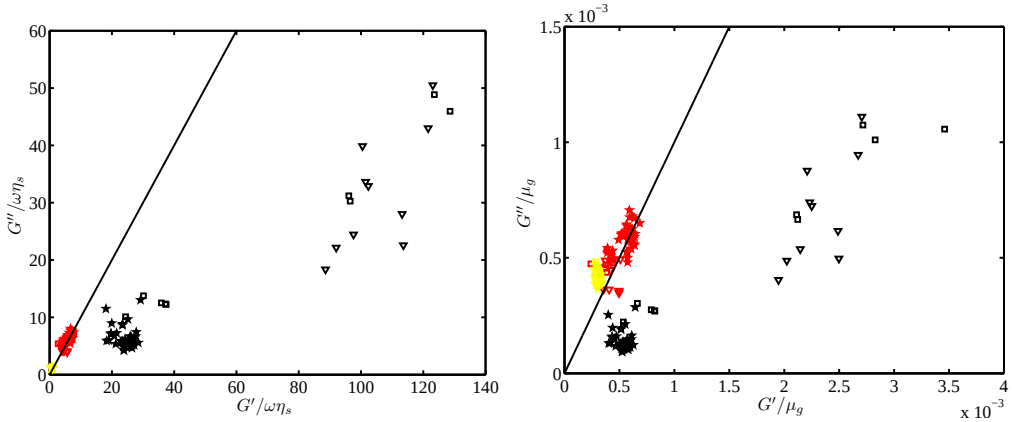

(b) Bare silica microsphere on PA hydrogel B, $k_t \approx 9$ μN m^{-1}.

Figure 6.C.1: Active interfacial microrheology experimental repeats: loss modulus G'' versus storage modulus G' (Cole-Cole plots), normalized with solvent viscosity ($\eta_s \approx 0.9$ cP), shown in left panel, or gel shear modulus μ_g, presented in right panel for a bare silica microsphere adhered to PA hydrogels A (panel a) and B (panel b). All experimental parameters and color legend are the same as figure 6.6.7. The storage and loss moduli behavior are in agreement with figure 6.6.7.

Interfacial dynamic viscosity of a bare silica microsphere-hydrogel inclusion (presented in figure 6.C.2, left panel) attains $\eta'/\eta_s \approx 3$ and 5 at low frequencies (black and red symbols) for gels A and B, respectively; these are slightly higher than the values furnished in figure 6.6.8, left panel, and the out-of-phase viscosity and its dependency on the drive frequency for both gels agree well with figure 6.6.8, right panel.

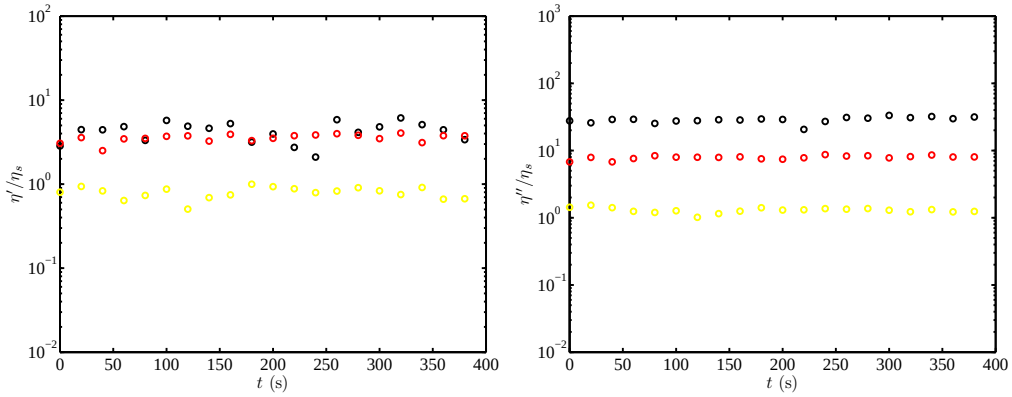

(a) Bare silica microsphere on PA hydrogel A, $k_t \approx 9$ μN m^{-1}.

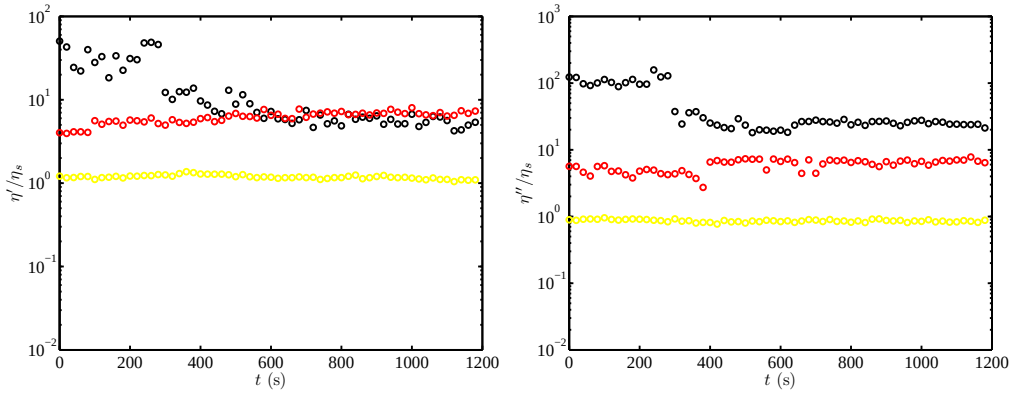

(b) Bare silica microsphere on PA hydrogel B, $k_t \approx 9$ μN m^{-1}.

Figure 6.C.2: Active interfacial microrheology experimental repeats: interfacial dynamic viscosity $\eta' = G''/\omega$ (left panel) and out-of-phase viscosity $\eta'' = G'/\omega$ (right panel) versus time t for a bare silica microsphere on PA hydrogels A (panel a) and B (panel b) in TAE buffer. All experimental parameters and color legend are the same as figure 6.6.7. The acquired interfacial dynamic viscosity at low frequencies fluctuates around $\eta'/\eta_s \approx 3$ and 5 for gels A and B, respectively, which are smaller than the values furnished from passive interfacial microrheology (figure 5.6.8). Compared to figure 6.6.8, a slightly higher dynamic viscosity and very close out-of-phase viscosity are observed.

The zero-shear viscosity for gels A and B (figure 6.C.3) adopt values that are close to figure 6.6.9. For instance, at $f = 32$ Hz (red symbols), $\eta_0/\eta_s \approx 20$ and 10 for gels A and B, respectively, compared to ≈ 30 and ≈ 10 in figure 6.6.9.

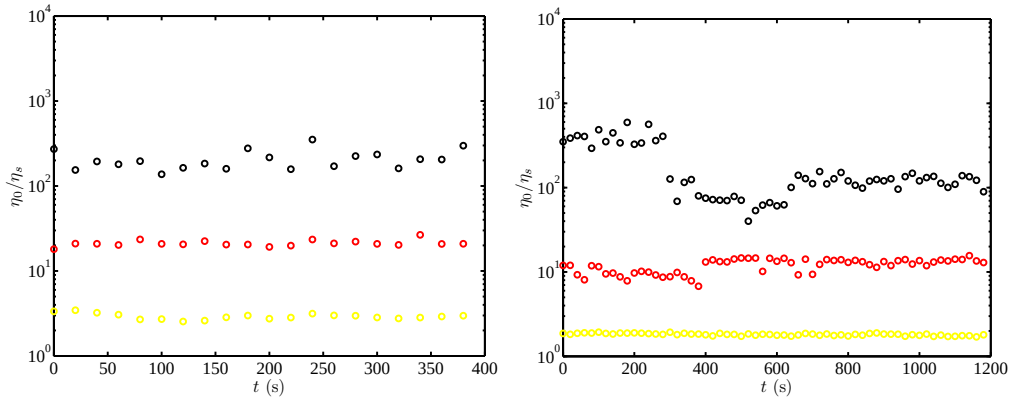

Figure 6.C.3: Active interfacial microrheology experimental repeats: interfacial zero-shear viscosity $\eta_0 = \eta' \left[1 + (\omega\tau)^2\right]$ versus time t for a bare silica microsphere on PA hydrogels A (left panel) and B (right panel) in TAE buffer. All experimental parameters and color legend are the same as figure 6.6.7. The acquired η_0 at low frequencies fluctuates around $\eta_0/\eta_s \approx 200$ and 100 for gels A and B, respectively, which are higher than the dynamic viscosity, furnished from the passive interfacial microrheology (figure 5.6.8).

In the experimental repeats, the phase lag at a given frequency is slightly higher (figure 6.C.4) compared to figure 6.6.10, suggesting an higher effective interfacial diffusivity. Similarly, at low frequencies, a linear phase lag growth versus frequency is observed, and the phase lag on gel A is smaller than on gel B at a given frequency, all consistent with figure 6.6.10. The low-frequency loss tangent (right panel) varies linearly with drive frequency such that zero-shear loss tangent adopts a value very close to zero. Compared to figure 6.6.10, right panel, the loss tangent is slightly higher, suggesting that the viscous contribution in the interfacial adhesion is slightly greater. Again, the loss tangent attenuation at $f = 128$ Hz may be the result of an unavoidable decrease in drive amplitude.

Using the phase lags, the effective interfacial transverse diffusion coefficients are calculated and shown in figure 6.C.5. Compared to figure 6.6.11, the diffusion is faster by almost a factor of two (three) for gel A (black symbols) at $f = 32$ and 128 Hz ($f = 8$ Hz) and is almost the same for gel B (blue symbols). At all frequencies, the diffusion coefficient of a

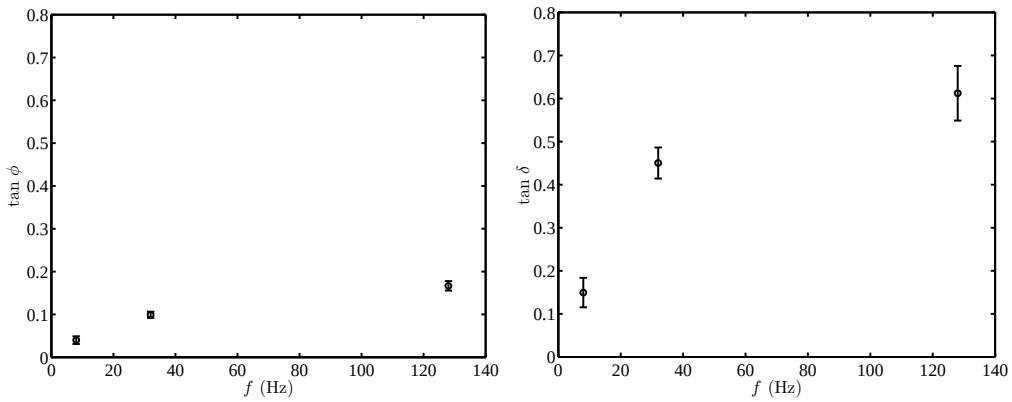

(a) Bare silica microsphere on PA hydrogel A, $k_t \approx 9$ μN m^{-1}.

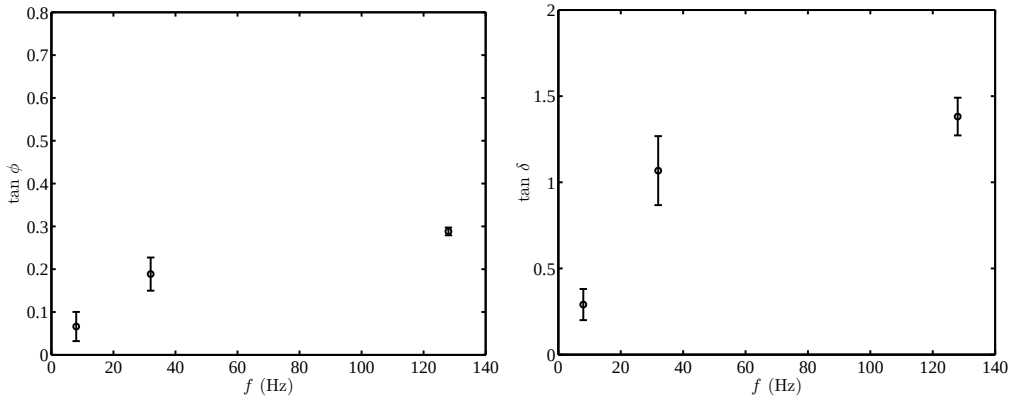

(b) Bare silica microsphere on PA hydrogel B, $k_t \approx 9$ μN m^{-1}.

Figure 6.C.4: Active interfacial microrheology experimental repeats: phase lag of a bare silica microsphere probe response to an external sinusoidal shear $\tan\phi$ (left panel) and loss tangent $\tan\delta$ (right panel) versus drive frequency f while the microsphere is adhered to hydrogels A (panel a) and B (panel b) in TAE buffer. All experimental parameters are the same as figure 6.6.7. The values are averaged over the sampling time shown in figure 6.C.1.

bare silica particle is higher on a softer gel.

The storage and loss moduli versus the dimensionless Maxwell relaxation time, presented in figure 6.C.6, suggest a slightly higher storage modulus plateau and loss modulus maximum for gel A, compared to figure 6.6.12 (a). These properties maintain close agreement with 6.6.12 (b), for gel B. The fits for the softer gel are not accurate, because the inclusion undergoes viscous binding when $\omega\tau \approx 1$.

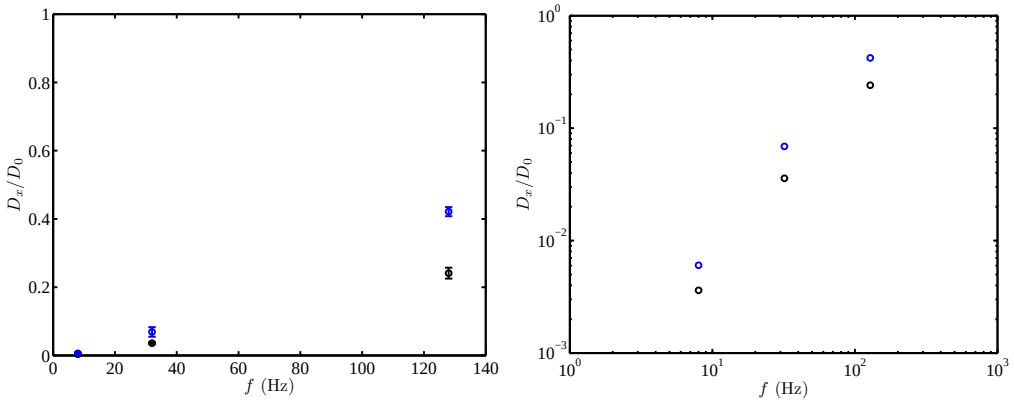

Figure 6.C.5: Active interfacial microrheology experimental repeats: the effective interfacial transverse diffusion coefficient $D_x = 2\pi f k_B T \tan(\phi)/k_t$ of a bare silica microsphere versus drive frequency f on hydrogels A (black symbols) and B (blue symbols) at $k_t \approx 9\ \mu\text{N m}^{-1}$. At a given frequency, a stiffer substrate attenuates the transverse diffusion coefficient more than a softer gel. Also, the diffusion coefficient depends on the drive frequency, reaching values close to the free diffusion coefficient near a rigid wall in an unbound solvent at high enough frequencies. The free Brownian diffusion coefficient of a silica microsphere in unbound water $D_0 \approx 0.25\ \mu\text{m}^2\ \text{s}^{-1}$ at $T \approx 23°\text{C}$. The right panel is a logarithmic presentation of the same data.

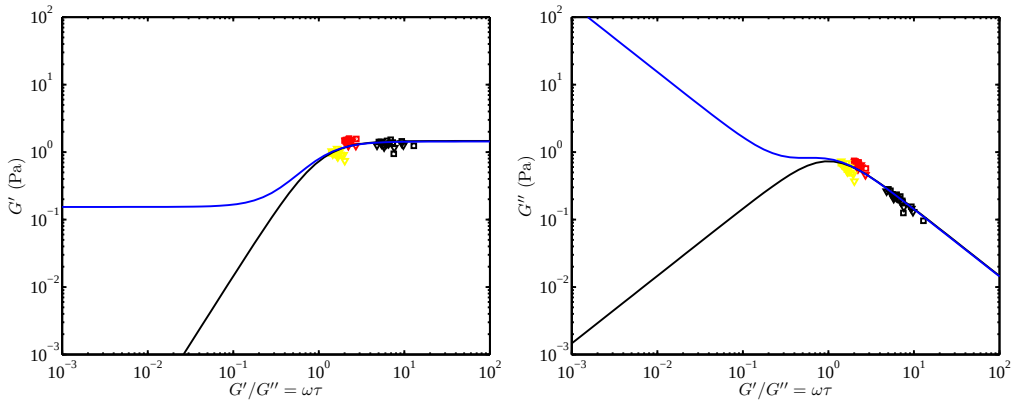

(a) Bare silica microsphere on PA hydrogel A, $k_t \approx 9$ μN m^{-1}.

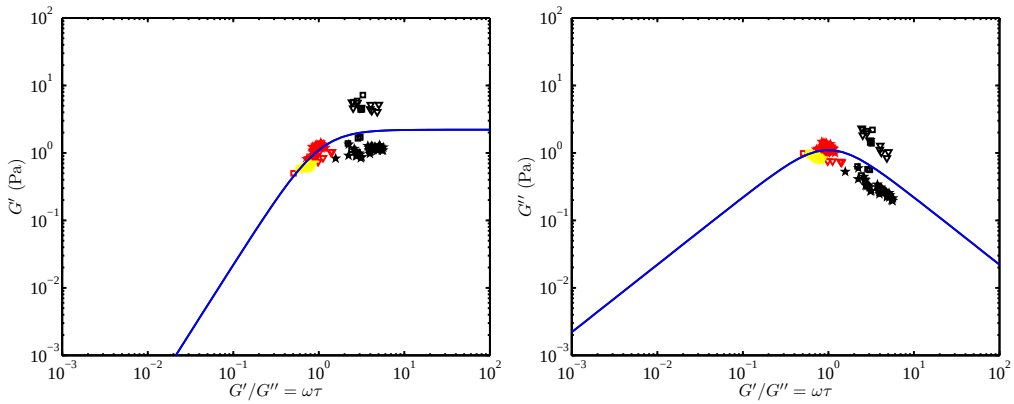

(b) Bare silica microsphere on PA hydrogel B, $k_t \approx 9$ μN m^{-1}.

Figure 6.C.6: Experimental repeats: storage (left panel) and loss (right panel) moduli versus dimensionless Maxwell relaxation time $G'/G'' = \omega\tau$ with a simultaneous least-squares best fit to the standard linear solid (SLS, black line) and extended standard linear solid (ESLS, blue line) models for gels A (panel a) and B (panels b). Fit parameter η/τ in the SLS model: $G' = k_e + (\eta/\tau)\frac{(\omega\tau)^2}{1+(\omega\tau)^2}$ and $G'' = (\eta/\tau)\frac{\omega\tau}{1+(\omega\tau)^2}$ for gels A and B is ≈ 1.5 (panel a) and ≈ 2.2 (panel b), respectively. For all cases, $k_e \approx 0$, which brings about $(\eta/\tau)/(0.001\mu_g) \approx 0.42$, 1.06, respectively. The fit parameters in the ESLS model: $G' = k_e + (\eta/\tau)\frac{(\omega\tau)^2}{1+(\omega\tau)^2}$ and $G'' = (\eta/\tau)\frac{\omega\tau}{1+(\omega\tau)^2} + k_e/(\omega\tau_e)$ for gels A: $\eta/\tau \approx 1.28, k_e \approx 0.15$, and B: $\eta/\tau \approx 2.2, k_e \approx 0$, bringing about $(\eta/\tau)/(0.001\mu_g) \approx 0.36$ and 1.06, respectively, which is close to the furnished value for gel A (figure 6.6.12). For gel B, the fits are not accurate, because most of the data are spread around $\omega\tau \approx 1$; however, taking the average $\eta/\tau \approx 1.2$ Pa at $f = 8$ Hz, η/τ agrees with figure 6.6.12b. All experimental parameters are the same as figure 6.C.1.

The interfacial dissipation force on gel A (figure 6.C.14, left panel) attains higher values (≈ 4 times) than figure 6.6.14, left panel (a). On gel B (right panel), the dissipation is higher at $f = 8$ Hz (≈ 6 times) and adopts values similar to those in figure 6.6.14, right panel (a), at higher frequencies. The discrepancy at $f = 8$ Hz is because the loss modulus is averaged over the whole experimental time, including the jump at $t \approx 200$ s (see figure 6.C.1).

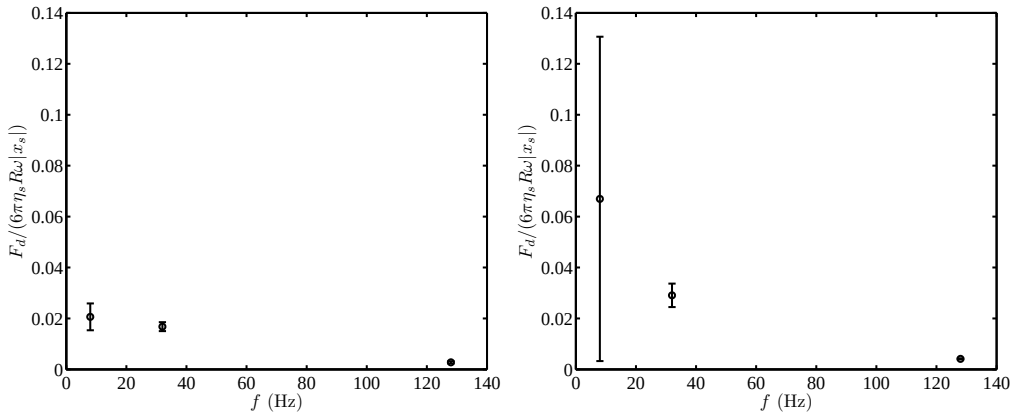

Figure 6.C.7: Experimental repeats: dissipation force per cycle $F_d = \pi |x_s|^2 G''$, normalized with the Stokes drag force $6\pi\eta_s R\omega |x_s|$ versus drive frequency f, furnished from active interfacial microrheology at $k_t \approx 9$ μN m^{-1} with a bare silica microsphere, adhered to hydrogels A (left panel) and B (right panel) in TAE buffer. The error bars show the standard deviation over the sampling time.

6.C.2 Gels A ($k_t \approx 28$ μN m^{-1}) and B ($k_t \approx 40$ μN m^{-1})

In this section, the experimental repeats at an high trap stiffness are discussed. The storage and loss moduli for gels A and B, as presented in figure 6.C.8, attain values that are close to figure 6.6.15: the normalized storage modulus with bulk gel shear modulus varies between $0.4 \times 10^{-3} - 0.6 \times 10^{-3}$ (0.1×10^{-3}) at low (high) frequencies, and $G''/\mu_g \lesssim 0.2 \times 10^{-3}$. The storage (loss) moduli, furnished in figure 6.C.8 (b), are slightly higher (lower) than figure 6.6.15, which can be because of the gel local properties; however, the overall adhesion regime is consistent with the experimental repeats.

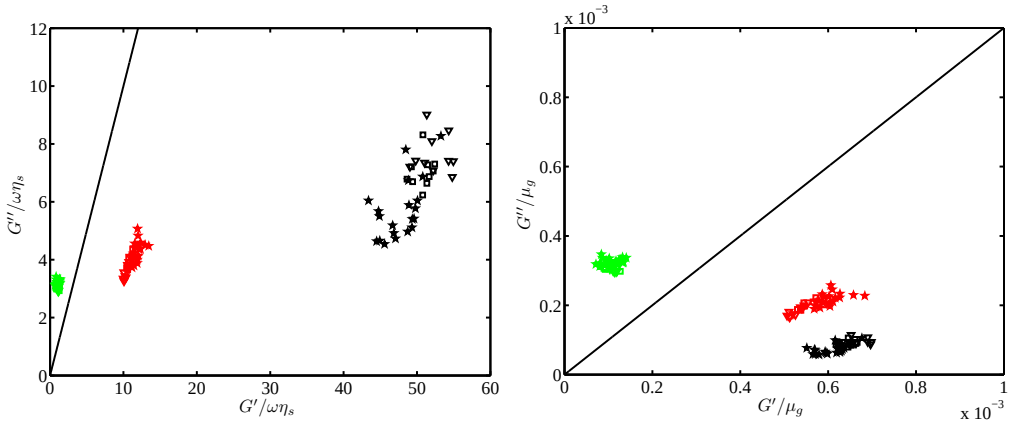

(a) Bare silica microsphere on PA hydrogel A, $k_t \approx 28$ μN m^{-1}.

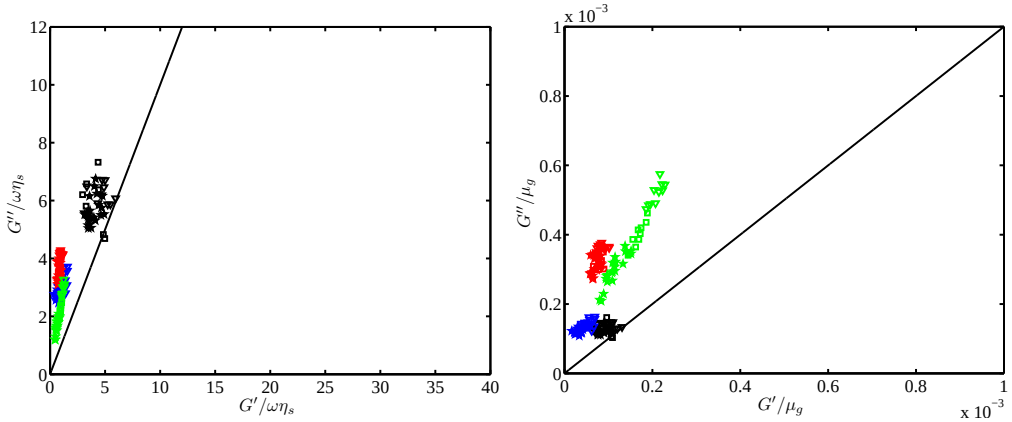

(b) Bare silica microsphere on PA hydrogel B, $k_t \approx 40$ μN m^{-1}.

Figure 6.C.8: Active interfacial microrheology experimental repeats: loss modulus G'' versus storage modulus G' (Cole-Cole plots), normalized with solvent viscosity ($\eta_s \approx 0.9$ cP), shown in left panel, or gel shear modulus μ_g, presented in right panel for a bare silica microsphere, adhered to PA hydrogels A ($k_t \approx 28$ μN m^{-1}, panel a) and B ($k_t \approx 40$ μN m^{-1}, panel b). All other experimental parameters and the color legend are the same as figure 6.6.15. Data correspond to different bare microspheres.

In terms of dynamic viscosity, figure 6.C.9 suggests good consistency in the repeated experiments on gels A (panel a) and B (panel b): average $\eta'/\eta_s \approx 4$ (3) and 5 (5) in figure 6.C.9 (figure 6.6.16) for gels A and B, respectively. Also, the out-of-phase viscosity, furnished in figure 6.C.9, agrees well with figure 6.6.16 (shown in parentheses): $\eta''/\eta_s \approx$ 40 (30), 10 (10), and 1 (1) at $f = 8$ Hz, 32 Hz, and 64 Hz, respectively, for gel A, and ≈ 3 (1), 1 (0.3), and 1 (0.3), respectively, for gel B.

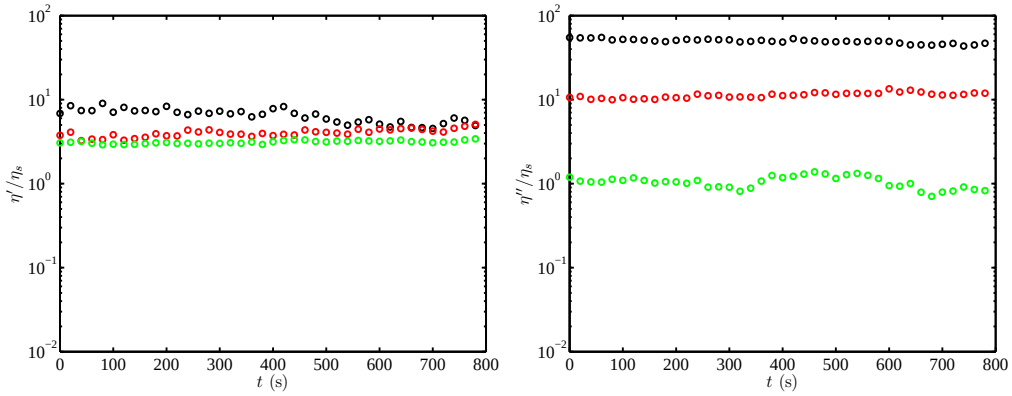

(a) Bare silica microsphere on PA hydrogel A, $k_t \approx 28$ μN m^{-1}.

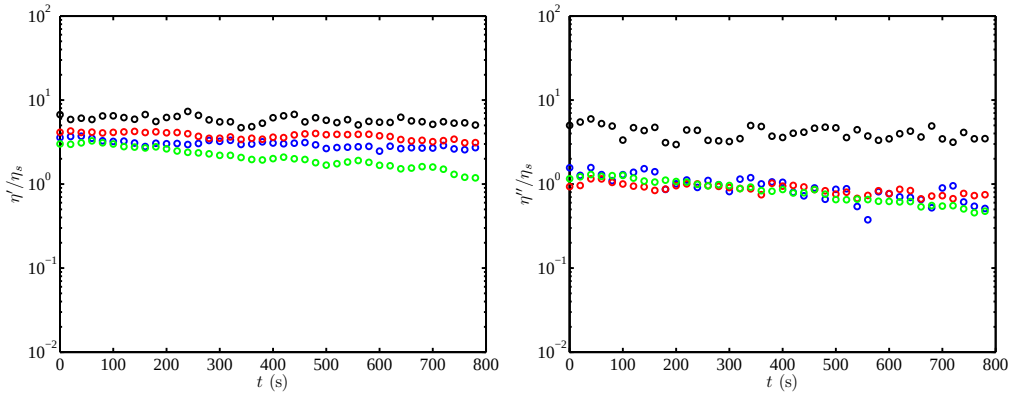

(b) Bare silica microsphere on PA hydrogel B, $k_t \approx 40$ μN m^{-1}.

Figure 6.C.9: Active interfacial microrheology experimental repeats: interfacial dynamic viscosity $\eta' = G''/\omega$ (left panel) and out-of-phase viscosity $\eta'' = G'/\omega$ (right panel) versus time t for a bare silica microsphere, coupled to PA hydrogels A ($k_t \approx 28$ μN m^{-1}, panel a) and B ($k_t \approx 40$ μN m^{-1}, panel b) in TAE buffer. All experimental parameters are the same as figure 6.C.8. The acquired interfacial dynamic viscosity at low frequencies fluctuates around $\eta'/\eta_s \approx 5$ for gels A and B, which is smaller than the values obtained from passive interfacial microrheology (figure 5.6.8).

The zero-shear viscosity from the experimental repeats at an high trap stiffness agrees well with figure 6.6.17 (values in parentheses): $\eta_0/\eta_s \approx 400$ (400), 30 (40), and 3 (6) at $f = 8$ Hz, 32 Hz, and 64 Hz, respectively, for gel A, and ≈ 10 (6), 3 (5), and 2 (4), respectively, for gel B.

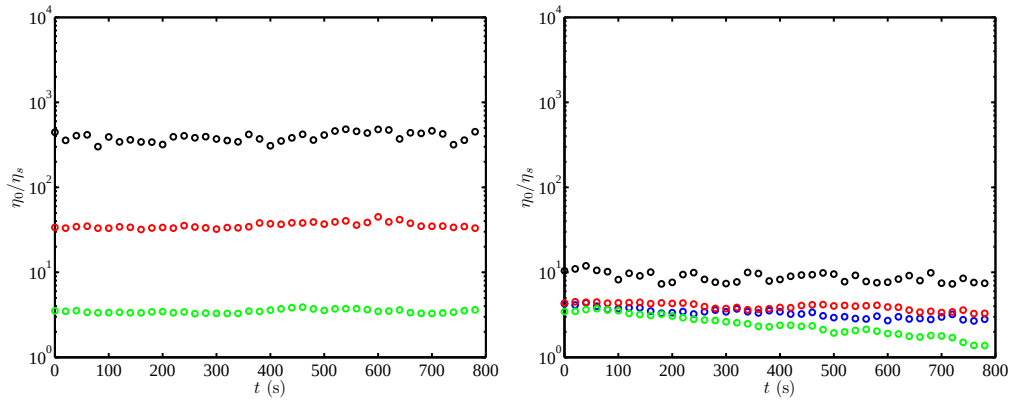

Figure 6.C.10: Active interfacial microrheology experimental repeats: interfacial zero-shear viscosity $\eta_0 = \eta' \left[1 + (\omega\tau)^2\right]$ versus time t for a bare silica microsphere on PA hydrogels A (left panel, $k_t \approx 28$ μN m^{-1}) and B (right panel, $k_t \approx 40$ μN m^{-1}) in TAE buffer. All experimental parameters and color legend are the same as figure 6.6.15. The acquired η_0 at low frequencies fluctuates around $\eta_0/\eta_s \approx 400$ and 10 for gels A and B, respectively, which are close to figure 6.6.17 and higher than the dynamic viscosity, furnished from the passive interfacial microrheology (figure 5.6.8).

A relatively small phase lag at low-frequencies on gel A (elastic adhesion) is evident from figure 6.C.11, left panel (a), which agrees with figure 6.6.18, left panel (a). Moreover, the phase lag on gel B attains values that are close to figure 6.6.18, left panel (b), excluding $f = 8$ Hz, in which, unexpectedly, the phase lag is smaller than figure 6.6.18, left panel (b). While the loss tangent of gel A is in very good agreement with figure 6.6.18, right panel (a), the loss tangent on gel B in figure 6.C.11, right panel b, adopts smaller values than figure 6.6.18, right panel (b), because the elastic adhesion contribution in the experimented location is more pronounced in figure 6.C.8 (b) compared to figure 6.6.15 (b).

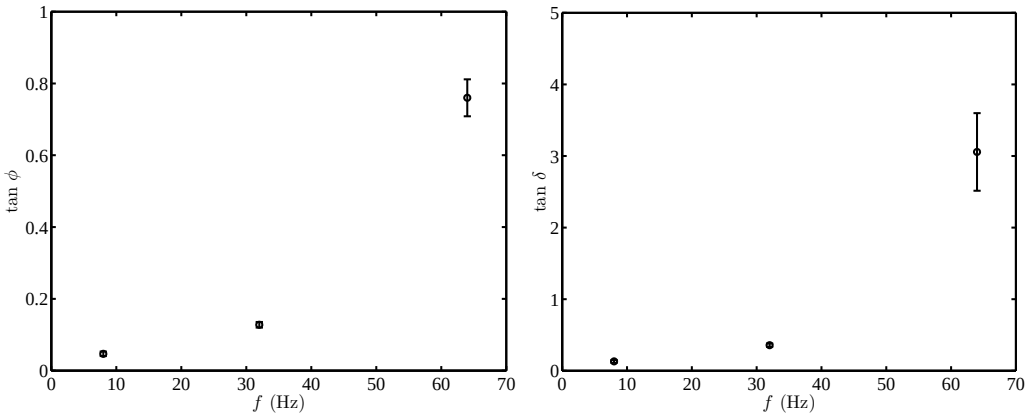

(a) Bare silica microsphere on PA hydrogel A, $k_t \approx 28$ μN m^{-1}.

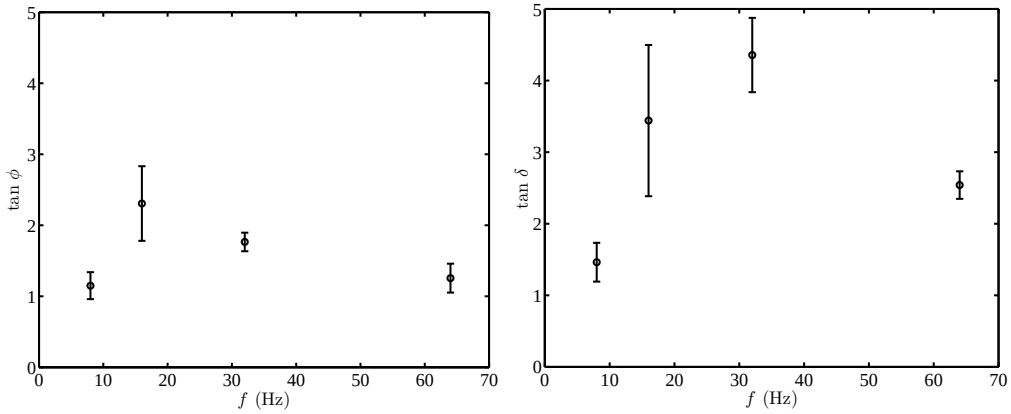

(b) Bare silica microsphere on PA hydrogel B, $k_t \approx 40$ μN m^{-1}.

Figure 6.C.11: Active interfacial microrheology experimental repeats: phase lag of a bare silica microsphere probe response to an external sinusoidal shear $\tan\phi$ (left panel) and loss tangent $\tan\delta$ (right panel) versus drive frequency f while the microsphere is attached to hydrogels A ($k_t \approx 28$ μN m^{-1}, panel a) and B ($k_t \approx 40$ μN m^{-1}, panel b) in TAE buffer. All experimental parameters are the same as figure 6.6.15. The values are averaged over the sampling time, shown in figure 6.C.8.

The effective interfacial transverse diffusion coefficient, furnished from the phase lag, is presented in figure 6.C.12. For gel A, it is in very good agreement with figure 6.6.19 (black symbols); however, for gel B, the diffusion coefficient at $f = 8$ Hz is smaller than figure 6.6.19 (blue symbols), and at other frequencies the values agree well.

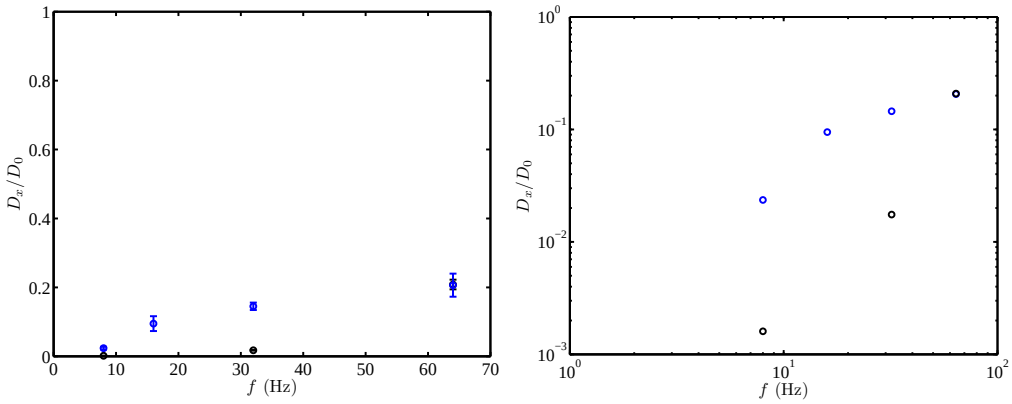

Figure 6.C.12: Experimental repeats: effective interfacial transverse diffusion coefficient $D_x = 2\pi f k_B T \tan(\phi)/k_t$ versus drive frequency f, furnished from active microrheology with a bare silica microsphere on hydrogels A (black symbols, $k_t \approx 28$ μN m^{-1}) and B (blue symbols, $k_t \approx 40$ μN m^{-1}). At a given frequency, a stiffer substrate attenuates the transverse diffusion coefficient more than a softer gel. Also, the diffusion coefficient depends on the drive frequency, which can reach values close to the free diffusion coefficient in an unbound solvent at high enough frequencies. The free diffusion coefficient of a silica microsphere in unbound water $D_0 \approx 0.25$ μm^2 s^{-1} at $T \approx 23$°C. Compared to $k_t \approx 9$ μN m^{-1} (figure 6.6.11), an high restoring force on the microsphere increases the effective transverse diffusion coefficient when the adhesion is dominated by the viscous stresses. The right panel is a logarithmic presentation of the same data.

A comparison of the storage and loss moduli versus the dimensionless Maxwell relaxation time shows that there is good compatibility between the repeated experiments (figures 6.C.13 and figures 6.6.20), furnishing $\eta/\tau \approx 2$ (0.5) Pa for gel A (B).

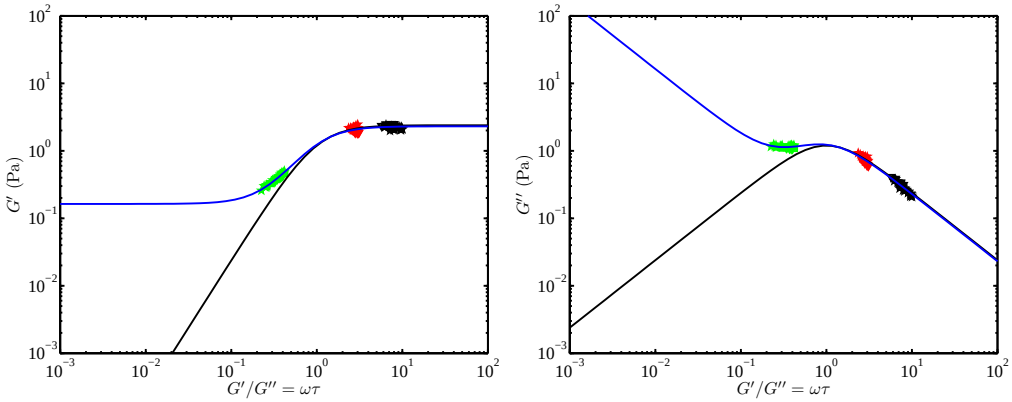

(a) Bare silica microsphere on PA hydrogel A, $k_t \approx 28$ μN m^{-1}.

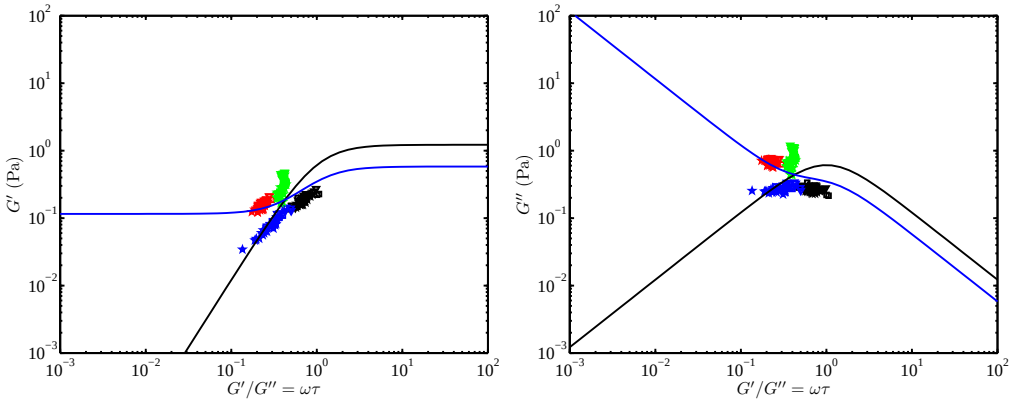

(b) Bare silica microsphere on PA hydrogel B, $k_t \approx 40$ μN m^{-1}.

Figure 6.C.13: Experimental repeats: storage (left panel) and loss (right panel) moduli versus dimensionless Maxwell relaxation time $G'/G'' = \omega\tau$ with a simultaneous least-squares best fit to the standard linear solid (SLS) and extended standard linear solid (ESLS) models for gels A ($k_t \approx 28$ μN m^{-1}, panel a) and B ($k_t \approx 40$ μN m^{-1}, panel b). Fit parameter in the SLS model: η/τ in $G' = k_e + (\eta/\tau)\frac{(\omega\tau)^2}{1+(\omega\tau)^2}$ and $G'' = (\eta/\tau)\frac{\omega\tau}{1+(\omega\tau)^2}$, for gels A and B is ≈ 2.4 (panel a) and ≈ 1.2 (panel b), respectively. For all cases, $k_e \approx 0$, which brings about $(\eta/\tau)/(0.001\mu_g) \approx 0.67$ and 0.58, respectively. The ESLS model, $G' = k_e + (\eta/\tau)\frac{(\omega\tau)^2}{1+(\omega\tau)^2}$ and $G'' = (\eta/\tau)\frac{\omega\tau}{1+(\omega\tau)^2} + k_e/(\omega\tau_e)$, furnishes $\eta/\tau \approx 2.14, k_e \approx 0.16$, for gel A, and $\eta/\tau \approx 0.47, k_e \approx 0.12$, for gel B, which bring about $(\eta/\tau)/(0.001\mu_g) \approx 0.59$ and 0.23 for gels A and B, respectively. All experimental parameters are the same as figure 6.C.8. The furnished η/τ for gels A and B are in close agreement with figure 6.6.20.

Finally, the dissipation force per cycle on gels A and B at the high trap stiffnesses (figure 6.C.14) attains values close to figure 6.6.21, suggesting a decrease in the normalized dissipation force from ≈ 0.03 to 0.01 when increasing the frequency from 8 Hz to 64 Hz.

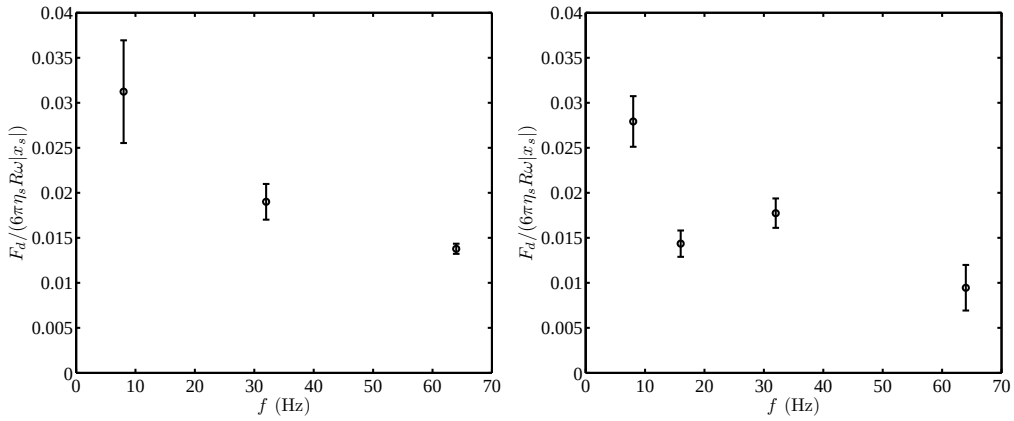

Figure 6.C.14: Active interfacial microrheology experimental repeats: dissipation force per cycle $F_d = \pi |x_s|^2 G''$, normalized with the Stokes drag force $6\pi\eta_s R\omega |x_s|$ versus drive frequency f, furnished with a bare silica microsphere adhered to hydrogels A (left panel, $k_t \approx 28$ μN m^{-1}) and B (right panel, $k_t \approx 40$ μN m^{-1}) in TAE buffer. The error bars show the standard deviation over the sampling time. The results are in agreement with figure 6.6.21.

Chapter 7

Passive and active interfacial microrheology for quantifying coated silica microsphere adhesion to polyacrylamide hydrogels

7.1 Preface

Amir Sheikhi designed and conducted the experiments and analyzed the data. In this chapter, the dynamics of lipid bilayer (DOPC) and lipopolymer-doped lipid bilayer (DSPE-PEG2k/DOPC, termed as DSPE)-coated silica microspheres at an hydrogel-electrolyte interface are studied using passive and active interfacial microrheology technique. The objective is to shed light on the interfacial influence of supported lipid bilayers (SLBs) or grated polymer chains (polyethylene glycol, PEG) on the coated particle behavior on a PA gel. Such coatings have been widely used to modify drug carriers recently without thorough understanding of their adhesive properties on soft tissues while they are subject to the thermal and/or shear forces.

7.2 Abstract

Colloidal drug carriers are coated with lipid bilayers to prevent drug leakage, or lipopolymer-doped lipid bilayers to enhance their biocompatibility. Although these particles are widely used for drug delivery to tissues, there has been no single-particle study on their behavior at a soft, sticky interface, such as an hydrogel. In this study, silica microspheres are coated with lipid bilayers (DOPC) or polyethylene glycol (PEG, $M_w = 2000$)-doped lipid bilayers (DSPE-PEG2k/DOPC, termed as DSPE) via a self-assembly approach, and their dynamics at a polyacrylamide (PA) hydrogel-TAE buffer interface are studied using novel passive and active interfacial microrheology techniques. While a bare silica microsphere presents a strong adhesive affinity to PA hydrogels (as discussed in chapters 5 and 6), DOPC-coated silica particles show no trace of interfacial adhesion, providing a neutral sensor to measure the solvent rheological properties in hydrogel contact proximity. Having a DOPC-coated microsphere decoupled from the gel, the pure effect of DOPC-embedded PEG chains on the DSPE-coated particle adhesion to the PA gels is characterized in terms of passive interfacial diffusion coefficient, binding stiffness, and viscoelastic properties, as well as frequency-dependent interfacial storage and loss moduli, viscosity, loss tangent, and dissipation force. The passive adhesion energy between a DSPE-coated microsphere and a PA gel is three times smaller than a bare silica microsphere. Accordingly, the adhesion is found to be more susceptible to external decoupling forces, resulting in a smaller interfacial storage modulus than a bare silica microsphere at a specified operating condition. Cole-Cole plots suggest that viscous coupling is easier to achieve for a DSPE-coated particle than a bare silica microsphere. Such adhesion-tunable micro-carriers can be used for advance drug delivery purposes and as biocompatible soft glues.

7.3 Introduction

Lipid bilayers are ready-to-fuse structures, which can be deposited on a planar or spherical solid support to from supported lipid bilayers (SLBs). Not only the support reinforces the bilayers, enabling them to mimic stable biomembranes, which provide a platform to study cell-level interactions, but also the bilayer coatings act as a barrier, preventing the encapsulated species from diffusing out of the underlying support (Chemburu *et al.*, 2010). A promising type of microsphere-SLBs, which is widely used as drug carriers, biosensors, and cell mimic, is known as biomimetic silica microspheres (Chemburu *et al.*, 2010).

Employing silica microspheres for drug delivery purposes demands non-toxicity, encapsulation and structural stability, targeted behavior, and an high circulation rate. Lipid bilayer-coated mesoporous silica nanoparticles carrying an anticancer drug provide an high uptake rate by the infected cells (Cauda *et al.*, 2010), while the coating stops premature release. Such a capping effect of the SLBs has been the focus of many recent studies: Bringas *et al.* (2012) introduced bilayer-capped magnetic silica particles ready to release their loaded drug upon exposure to an alternating magnetic field; Ashley *et al.* (2011) produced porous nanoparticle-supported lipid bilayers (protocells), benefited from an high loading capacity of multi-component anticancer cocktails, selectivity, stability, and targeted delivery ability. Targeted gene treatment was achieved owing to combinatorial properties of protocells encapsulating siRNA (Ashley *et al.*, 2012).

Bilayer coating enhanced the silica particle hemocompatibilty when interacting with red blood cells (Roggers *et al.*, 2014). Such a biocompatiblity is also reported by grafting polyethylene glycol on a surface (Guo *et al.*, 2009; Gulati *et al.*, 2010). Incorporating PEG-lipid conjugates into the lipid bilayers increased the lifetime of cisplatin, a chemotherapy agent, nanocapsules in mouse serum (Velinova *et al.*, 2004). Such a polymer conjugate enables a silica microsphere to benefit from the unique properties of sterically stabilized liposomes, such as biological stability and stealth, as discussed by Lasic (1994).

Hydrogels, hydrophilic crosslinked polymer networks, mimicking extracellular matrices

(ECMs) (Geckil *et al.*, 2010) and soft tissues, provide a platform to study tissue-cell or tissue-drug carrier systems when they contact SLBs on a silica microsphere. From a different point of view, biocompatible adhesive agents, to attach two slippery and non-adhesive tissues in wet milieu, have always been an important concern in regenerative medicine for self-healing purposes. As a recent example, Rose *et al.* (2014) have demonstrated that a layer of silica nanoparticles can instantly glue two pieces of polydimethylacrylamide (PDMA) hydrogels or liver tissues successfully.

The adhesive behavior of such coated microspheres at a single-particle level has not been understood yet. This study focuses on tuning the interfacial adhesion properties of a silica microsphere, which was previously found to adhere strongly to a PA gel (see chapters 5 and 6), by altering intermolecular forces using neutral (zwitterionic) DOPC bilayers. Moreover, by maintaining the ζ-potential of DSPE-coated silica microspheres similar to the DOPC-coated particles, the grafted-polymer (PEG) chain interfacial adhesion to a PA hydrogel is characterized via passive and active interfacial microrheology techniques.

7.4 Materials and methods

Bare silica microspheres and hydrogels were prepared following the methods described in chapter 5. To coat the cleaned microspheres with bilayers, the methodology explained in chapter 4 was closely followed. Final coated particles were diluted in TAE buffer (pH $\approx$ 8.3) and used in further gel interfacial microrheology experiments as a single probe. The same optical tweezers setup and procedure as chapter 6 was used to conduct passive and active interfacial microrheology experiments.

7.5 Theory

The same theoretical framework as chapter 6 is closely followed here.

7.6 Results and discussion

In this section, the interfacial behavior of a bilayer-coated silica microsphere in the absence (passive microrheology) or presence (active microrheology) of an external oscillatory shear force is discussed.

7.6.1 Passive interfacial microrheology

Brownian position time series, acquired from the optical tweezers back-focal-plane interferometry (see section 5.4.3), furnish short-time transverse diffusion coefficient D_x and long-time position fluctuation variance $\langle X^2 \rangle$, hinging on Eqn. 5.11. These parameters are presented in figure 7.6.1 for a DOPC-coated silica microsphere (panel a) and a DSPE-coated particle (panel b), when the particle is elevated from the gel interface ($z > 0$) or while it contacts it ($t > 0$). For both particles, decreasing particle height by vertically translating the nano-positioning stage toward the optically trapped microsphere decreases the transverse diffusion coefficient such that D_x follows the well-known hydrodynamic theories (shown with solid lines) for a translating sphere near a plane wall.

At a particle-gel gap $z \approx 40$ nm, a DOPC-coated particle adopts $D_x/D_0 \approx 0.45$, which corresponds to a theoretical gap approximately 100 nm. Such an high diffusion coefficient remains unchanged with time when the particle touches the gel. This is achieved by tuning the effective van der Waals attraction between the particle and the gel by decreasing Hamaker constant as follows: the Hamaker constant between silica and acrylamide monomer interacting through water $A_{s-w-a} \approx (\epsilon_s - \epsilon_w)(\epsilon_a - \epsilon_w)/[(\epsilon_s + \epsilon_w)(\epsilon_a + \epsilon_w)] \approx 10^{-20}$ J (Di Michele *et al.*, 2012). Accordingly, Hamaker constant for DOPC-water-acrylamide can be scaled as $A_{b-w-a}/A_{s-w-a} \approx (\epsilon_b - \epsilon_w)(\epsilon_s + \epsilon_w)/[(\epsilon_s - \epsilon_w)(\epsilon_b + \epsilon_w)] \approx 0.31$, considering DOPC, water, and silica dielectric constants $\epsilon_b \approx 45$ (Lomize *et al.*, 2011), $\epsilon_w \approx 80$, and $\epsilon_s \approx 4$ (Valle-Delgado *et al.*, 2005), respectively, which shows approximately 3 fold lower van der Waals attraction for the latter system. Note that this is just a rough estimation, because the

bilayer dielectric constant cannot be precisely determined, and, also, the hydrogel comprises 95 % water.

A DSPE-coated silica microsphere (7.6.1, left panel b), closely follows the theoretical diffusion coefficient prediction at $z \geq 20$ nm; however, at contact proximity, the transverse diffusion coefficient is attenuated to $D_x/D_0 \approx 0.09$, suggesting an increase in the interfacial viscosity. Moreover, the long-time Brownian position variance (7.6.1, right panel), which is inversely proportional to the binding stiffness (see Eqn. 5.9), does not change upon DOPC-coated particle-gel contact while a DSPE-coated microsphere attenuates $\langle X^2 \rangle$ to ≈ 10 % of bulk values, suggesting a strong adhesion between grafted PEG chains and a PA gel.

The passive interfacial experiments on a PA gel were repeated 3, 7, and 10 times with a DOPC, DSPE (2.5 %), or DSPE (0.5 %)-coated silica microsphere, respectively, and the diffusion coefficient and position variance are shown in figure 7.6.2. While a plain bilayer coating (panel a) provides a fast particle diffusion and low gel-binding affinity, PEG chain moieties with concentration as low as 0.5 mol % (panel c) attenuate the diffusion coefficient and position variance significantly. No significant aging is observed with time for all bilayer-coated particles (panels a, b, and c), and the PEG chain adhesion to a PA gel is spontaneous. The averaged D_x and $\langle X^2 \rangle$ with time ($z = 0$) are presented in figure 7.6.3. As evidenced by this figure, both 2.5% (panel b) and 0.5% (panel c) DSPE coatings similarly attenuate the interfacial transverse diffusion coefficient $D_x/D_0 \approx 0.12$ and increase the binding stiffness by a factor of 10. Apparently, a DSPE coating results in an intermediate adhesion strength compared to a DOPC-coated or bare silica microspheres, suggested by a lower (higher) diffusion coefficient and position variance than a DOPC-coated (bare, see figure 5.6.4, panel a) silica microsphere.

The effect of substrate stiffness on the bilayer-coated particle interfacial dynamics is investigated using a softer PA gel, *i.e.*, gel B. The DOPC-coated particle behavior (figure 7.6.4a) on gel B is similar to gel A with no evidence of interfacial entanglement. The diffusion coefficient of sticking particles (left panels b and c) are in the same range as gel A (shown in

figure 7.6.2) with slightly larger position variance (right panels b and c). The discontinuous dynamics of a DSPE (0.5 %)-coated particle on gel B (figure 7.6.4c, red symbols) can be due to possible bilayer imperfection or damage in case of a low DSPE content, resulting in partial contact of particle bare regions with the gel, or time-dependent diffusion of PEG moieties inside the fluid membrane coating toward the contact area, resulting in a spontaneous particle-gel attachment after approximately 800 s. Three types of dynamic behavior, namely spontaneous adhesion (blue symbols), discontinuous attachment (red symbols), and aged adhesion (black symbols) may be due to these phenomena.

The average particle diffusion coefficient and position variance on gel B is presented in figure 7.6.5. Compared to a bare silica microsphere on gel B (figure 5.6.4b), while ensuring the adhesion, DSPE-coated particles are more mobile, evidenced by higher interfacial diffusion coefficient and position variance. This suggests that a PEG-doped lipid bilayer coating can provide a tunable biocompatible glue to adhere colloidal particles to PA hydrogel or gel pieces together. An interesting study is to investigate the PEG-conjugated vesicle rupture and possible in vivo bioadhesion, which is out of the scope of this work.

The diffusion coefficient (left panel) and long-time position variance (right panel) of a DSPE-coated particle versus PA substrate stiffness is presented in figure 7.6.6. While the diffusion coefficient is almost independent of the gel stiffness and DSPE content, the position variance decreases when increasing the gel Young's modulus, furnishing an adhesion energy U almost three times lower than a bare silica microsphere on PA gel. Note that the interfacial contact area is calculated according to Eqn. 5.9, which is used to furnish the adhesion energy, hinging on Maugis (1995) theory.

The particle position time series can furnish the interfacial storage modulus and viscosity directly, using the general methodolgy suggested by Mason & Weitz (1995), as discussed in chapter 5 (see figure 5.6.7). Using the data presented in figures 7.6.2 and 7.6.4, G' and η are obtained from passive interfacial microrheology (figure 7.6.7). As expected, the acquired storage modulus with a DOPC-coated microsphere probe (left panel, black squares)

is independent of the gel stiffness, attaining a small value corresponding to the trap stiffness, while DSPE-coated particles bring about $1000G'/E \approx 0.7$, a value smaller than a bare silica mcirosphere on a PA gel ($1000G'/E \approx 1$, see figure 5.6.8, left panel). As explained in the caption, the corresponding $\langle X^2 \rangle$ to G' are in close agreement with the position variance, presented in figure 7.6.6. The interfacial viscosity (figure 7.6.7, right panel), furnished with a DOPC-coated microsphere represents water viscosity in plane wall vicinity, while $\eta/\eta_0 \approx 10$ for a PEG-conjugated DOPC-coated silica microsphere agrees with the diffusion coefficients in figure 7.6.6.

7.6.2 Active interfacial microrheology

In this section, the dynamics of a DOPC-coated silica microsphere, subject to an external oscillatory shear, at gel A or B interface in TAE electrolyte are discussed. The frequency-dependent behavior of a DSPE-coated silica microsphere at such interfaces is, then, characterized at various grafted PEG-bilayer conjugate (lipopolymer) concentration, gel stiffness, and optical restoring force.

The effect of substrate stiffness and oscillatory drive frequency on the interfacial storage and loss moduli of a PA gel, measured by a DOPC-coated microsphere, is presented in figure 7.6.8. As can be observed, regardless of the gel stiffness and drive frequency, the loss modulus is always grater than the storage modulus (viscous coupling), which is also attested by the passive experiments ($f = 0$ Hz). Left panels show that the normalized dynamic viscosity is more than 10 times higher than the normalized out-of-phase viscosity, while the right panel depicts the dependency of the loss modulus on the drive frequency. Such dependency is compatible with the typical behavior of an optically trapped microsphere in an unbound fluid, keeping the dynamic viscosity constant. The interfacial storage modulus is independent of the drive frequency, as expected for a trapped particle in a viscous medium. The slight increase in G' at $f = 64$ Hz (right panel, green symbols) can be due to the gel surface deformation at an high shear, resulting in a negligible physical binding.

Compared to an elastically-adhered bare silica microsphere to PA gel at a low (figure 6.6.7, panels a and b) or high (figure 6.6.15) trap stiffness, the storage modulus, measured with DOPC-coated probes, is more than one order of magnitude lower. However, the storage modulus measured with a bare silica microsphere at high enough shear rate and restoring force attains values that are close to a DOPC-coated microsphere. At such high external forces, the bonds between a bare silica microsphere and gel surface dangling polymer chains are partially broken, resulting in non-elastic (viscous) coupling, *e.g.*, at $f = 128$ Hz and $k_t \approx 24$ μN m^{-1} (see figure 6.6.15a, yellow symbols). Similarly, a DOPC coating prevents the bond formation between a silica particle and PA gel. A DOPC-coated microsphere remains in the viscous coupling region even at a low trap stiffness; therefore, studying the effect of increasing restoring force on the interfacial viscoelasticity is redundant.

The dynamic (left panel) and out-of-phase (right panel) viscosity, furnished with a DOPC-coated silica probe on a PA gel are presented in figure 7.6.9. The dynamic viscosity is independent of the drive frequency, reflecting water viscosity at a plane wall vicinity (provided that the effective particle size is twice as large as the nominal probe size at a particle-gel gap $z \approx 100$ nm). This proves that there exists no significant polymer partitioning between the gel and solvent. The out-of-phase viscosity is also independent of the gel stiffness and drive frequency, attaining small values compared to a bare silica microsphere (figure 6.6.8). Note that applying a strong restoring force to a bare silica microsphere adhered to a soft gel B (figure 6.6.16b), results in comparable η'' to a DOPC-coated particle, suggesting that increasing the external forces on an adhesive particle has the same effect as decreasing the gel-particle intermolecular attraction force by coating it with zwitterionic bilayers.

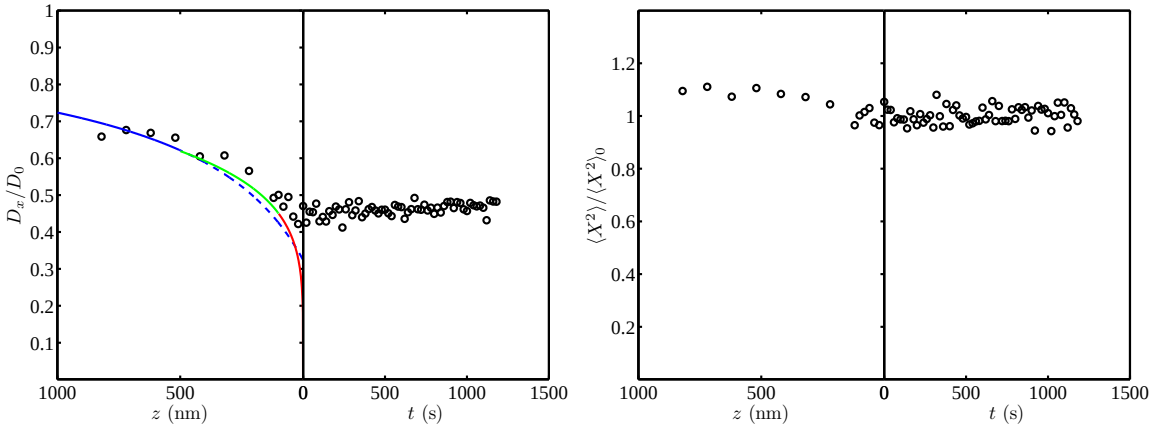

(a) DOPC-coated silica microsphere on PA hydrogel A.

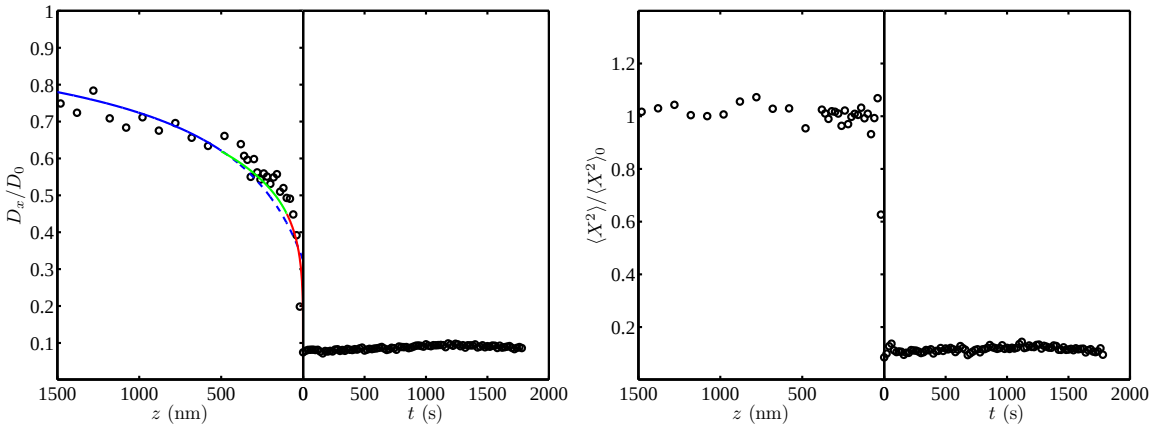

(b) DSPE (2.5 %)-coated silica microsphere on PA hydrogel A.

Figure 7.6.1: Short-time diffusion coefficient D_x (left panel) and long-time Brownian position fluctuation variance $\langle X^2\rangle$ (right panel), furnished from passive interfacial microrheology with optical tweezers and back-focal-plane interferometry position detection for a DOPC-coated (panel a) and DSPE (2.5 %)-coated (panel b) silica microsphere ($2R \approx 1.97$ μm) on PA hydrogel A. The particle is brought in contact with the PA hydrogel planar layer by vertically translating the sample in 20 nm increments, using a piezo-electric nano-positioning stage. The diffusion coefficients and the (long-time) variance of transverse Brownian position fluctuations are plotted versus the particle-hydrogel gap height z, for an elevated particle, and versus time t, once the particle adheres to the interface. Lines in the left panel are the Faxen (1923) (solid and dashed, blue), O'Neill (1964) (green), and Goldman *et al.* (1967) (red) hydrodynamic theories for the translation of a sphere parallel to a plane wall. Note that $\langle X^2\rangle$ and D_x are obtained by fitting a single exponential relaxation to plots of $\langle [X(t+\tau) - X(t)]^2\rangle$ versus the time lag τ (up to 5 s in panel (a) and 0.0234 s in panel (b), to eliminate any long-time drift): $D_0 \approx 0.25$ μm^2 s^{-1}, and $\langle X^2\rangle_0 \approx 493$ (panel a) and 584 (panel b) nm^2. The grafted PEG chain-mediated adhesion is evident by panel (b).

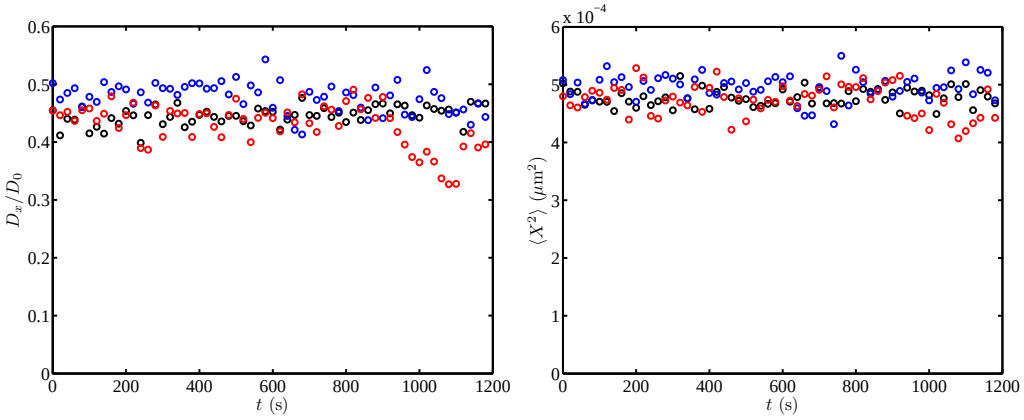

(a) DOPC-coated silica microsphere on PA hydrogel A.

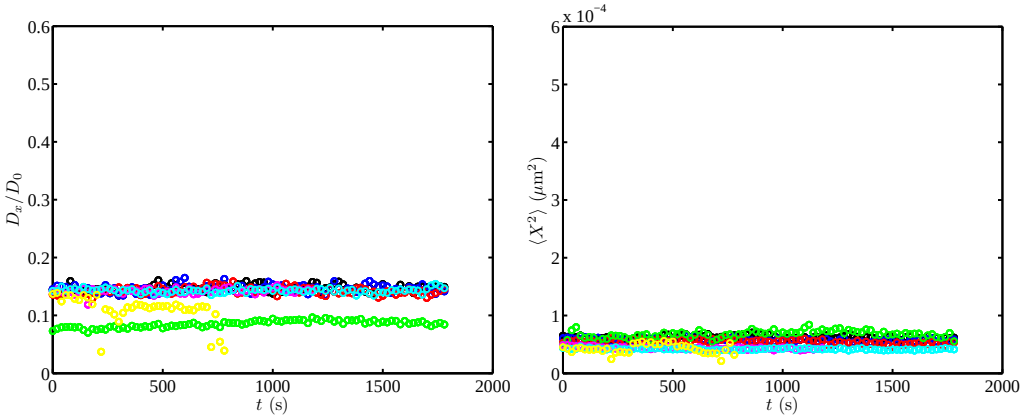

(b) DSPE (2.5 %)-coated silica microsphere on PA hydrogel A.

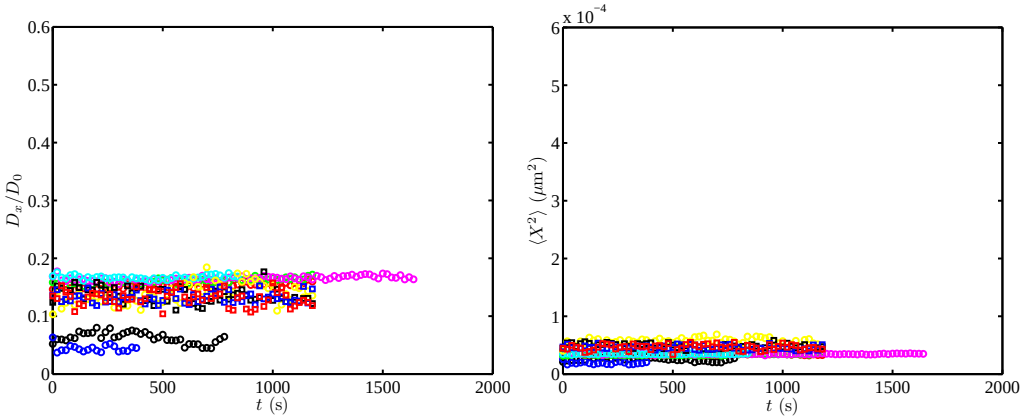

(c) DSPE (0.5 %)-coated silica microsphere on PA hydrogel A.

Figure 7.6.2 *(previous page)*: Short-time diffusion coefficient (left panel) and long-time Brownian position fluctuation variance (right panel) of DOPC (panel a), DSPE (2.5 %, panel b), and DSPE (0.5 %, panel c)-coated silica microspheres on a PA hydrogel A, furnished from passive interfacial microrheology. Note that $\langle X^2 \rangle$ and D_x are obtained by fitting a single exponential relaxation to plots of $\langle [X(t+\tau) - X(t)]^2 \rangle$ versus the time lag τ (up to 5 s in panel a and 0.0234 s in panels b and c, to eliminate any long-time drift): $D_0 \approx 0.25\ \mu\text{m}^2\ \text{s}^{-1}$. Each color represents properties acquired in one experiment on a gel, including 3, 7, and 10 experiments in panels (a), (b), and (c), respectively. Averaged values are presented in figure 7.6.3. While the DOPC-coated particles bring about diffusion coefficient (position variance) comparable to the diffusion coefficient of a non-sticking sphere close to a rigid wall (an optically trapped particle in an unbound fluid), the presence of as low as 2.5 or 0.5 % grafted PEG chains in the DOPC coating results in a significant attenuation of diffusion coefficient and position variance, suggesting a strong grafted-polymer induced interfacial adhesion.

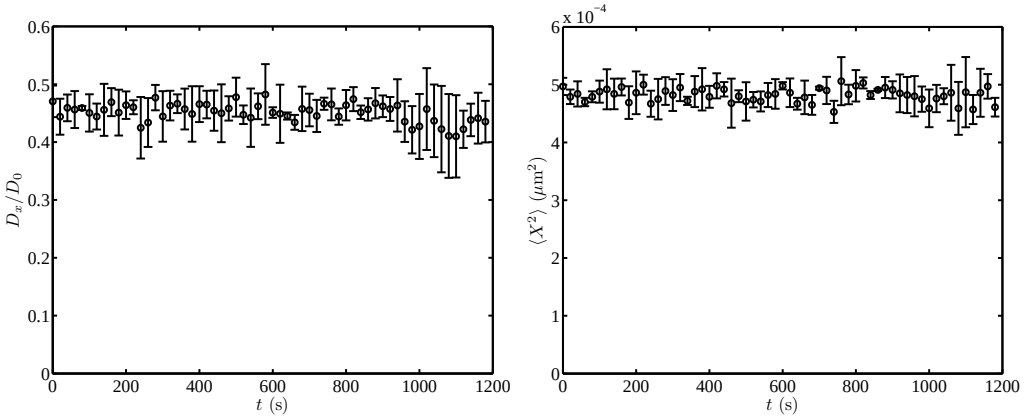

(a) DOPC-coated silica microsphere on PA hydrogel A.

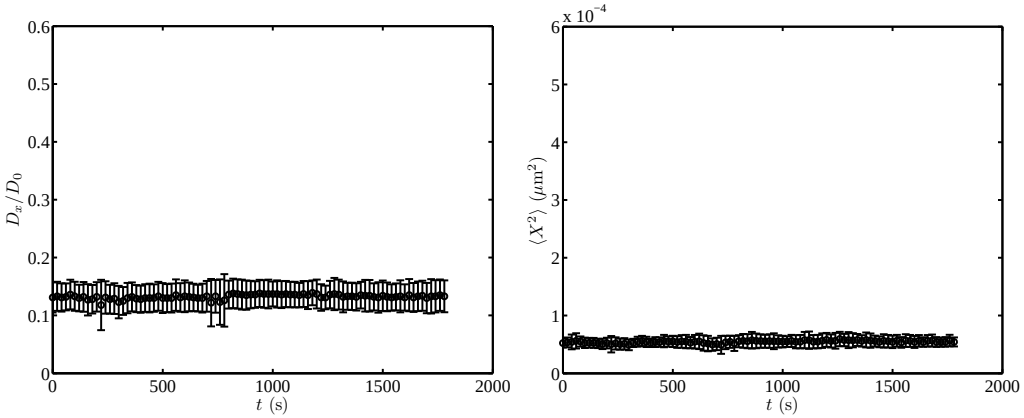

(b) DSPE (2.5 %)-coated silica microsphere on PA hydrogel A.

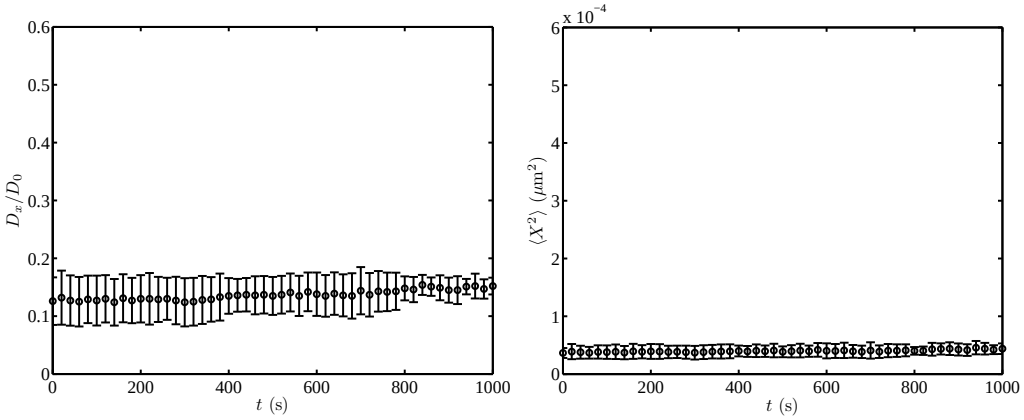

(c) DSPE (0.5 %)-coated silica microsphere on PA hydrogel A.

Figure 7.6.3 *(previous page)*: Average values of the short-time diffusion coefficient (left panel) and long-time Brownian position fluctuations variance (right panel) of DOPC (panel a), DSPE (2.5 %, panel b), and DSPE (0.5 %, panel c)-coated silica microspheres on a PA hydrogel A, presented in figure 7.6.2. The DOPC-coated particles undergo a free short-time Brownian diffusion, and no evidence of binding on the gel is observed, while the PEG chain-doped bilayer coatings (panels b and c) bind the particles to the gel-electrolyte interface, which is manifested in the attenuated diffusion coefficient and position variance. Compared to a bare silica microsphere (figure 5.6.5a), DSPE-coated particles adhere weaker to gel A, suggested by higher diffusion coefficient and position variance.

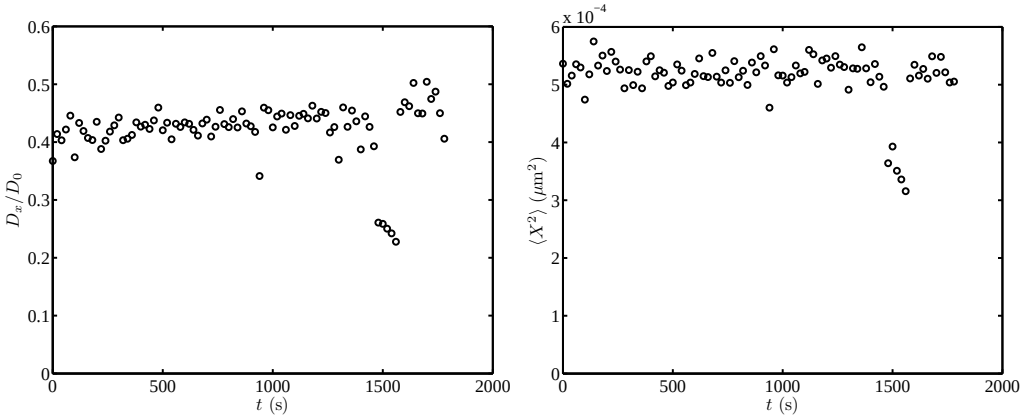

(a) DOPC-coated silica microsphere on PA hydrogel B.

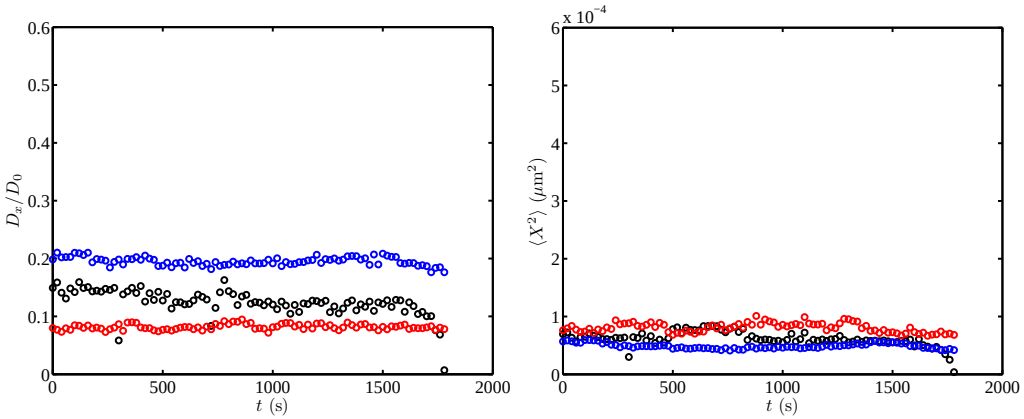

(b) DSPE (2.5 %)-coated silica microsphere on PA hydrogel B.

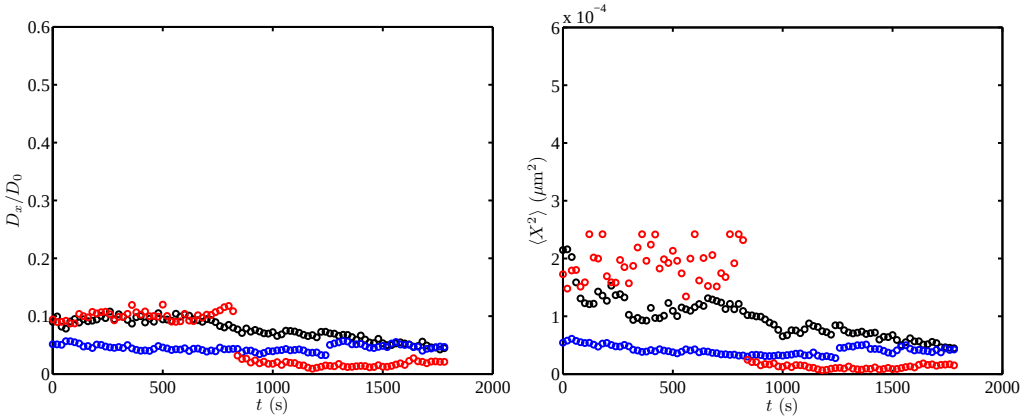

(c) DSPE (0.5 %)-coated silica microsphere on PA hydrogel B.

Figure 7.6.4 *(previous page)*: Short-time diffusion coefficient (left panel) and long-time Brownian position fluctuation variance (right panel) of DOPC (panel a), DSPE (2.5 %, panel b), and DSPE (0.5 %, panel c)-coated silica microspheres on a PA hydrogel B, furnished from passive interfacial microrheology. Note that $\langle X^2 \rangle$ and D_x are obtained by fitting a single exponential relaxation to plots of $\langle [X(t+\tau) - X(t)]^2 \rangle$ versus the time lag τ (up to 5 s in panel a and 0.1 s in panels b and c, to eliminate any long-time drift): $D_0 \approx 0.25\ \mu\text{m}^2\ \text{s}^{-1}$. Each color represents properties acquired in one experiment on the gel, including 1, 3, and 3 experiments in panels (a), (b), and (c), respectively. Averaged values are presented in figure 7.6.5. The DOPC-coated particles show similar behavior to PA hydrogel A (see figure 7.6.2a). The binding strength of the DSPE-coated particles (panels b and c) on this gel is comparable to gel A, manifested in close diffusion coefficient and position variance values.

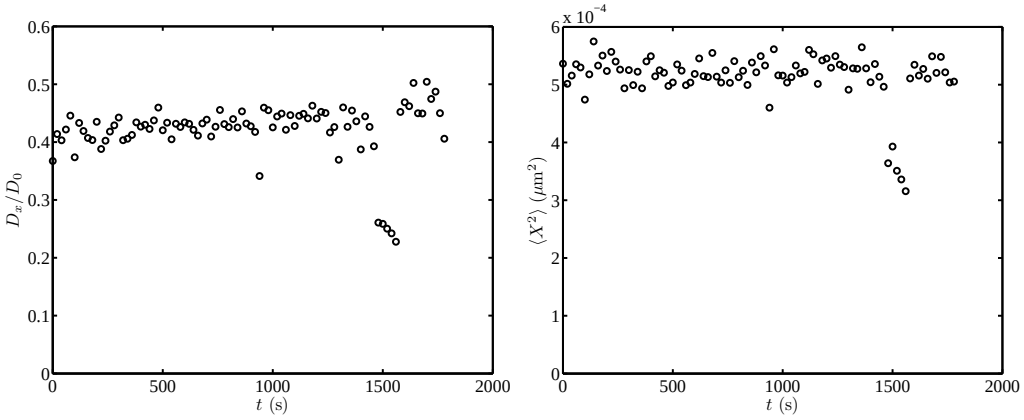

(a) DOPC-coated silica microsphere on PA hydrogel B.

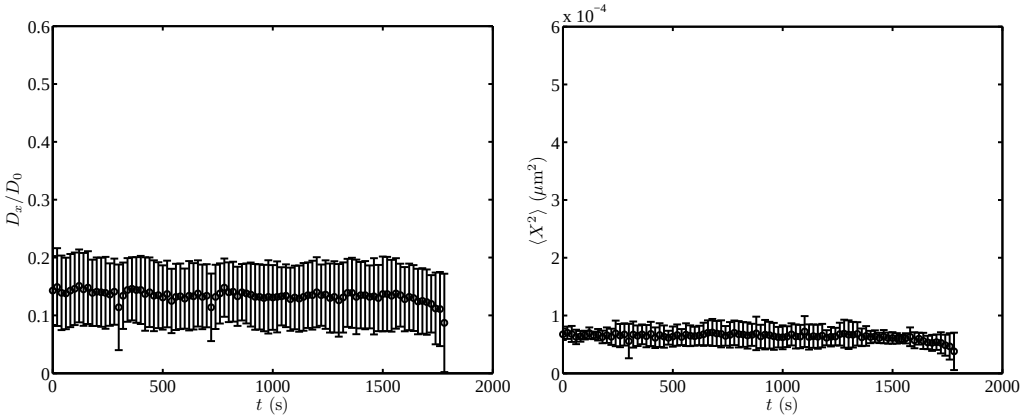

(b) DSPE (2.5 %)-coated silica microsphere on PA hydrogel B.

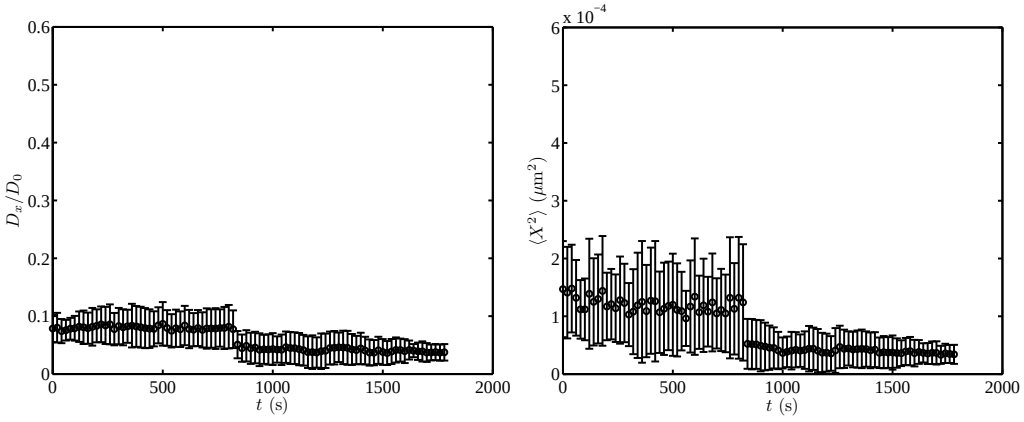

(c) DSPE (0.5 %)-coated silica microsphere on PA hydrogel B.

Figure 7.6.5 *(previous page)*: Average values of short-time diffusion coefficient (left panel) and long-time Brownian position fluctuation variance (right panel) of DOPC (panel a), DSPE (2.5 %, panel b), and DSPE (0.5 %, panel c)-coated silica microspheres on a PA hydrogel B, presented in figure 7.6.4. The interfacial dynamics of coated silica microspheres on gel B are similar to gel A (figure 7.6.5). Compared to a bare silica microsphere (figure 5.6.5a), DSPE-coated particles adhere weaker to gel B, manifested in higher diffusion coefficient and position variance.

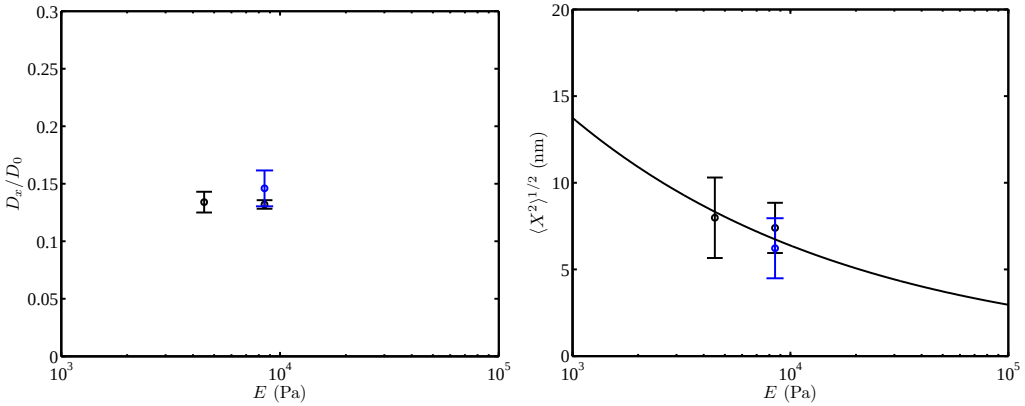

Figure 7.6.6: Substrate stiffness (AFM elastic modulus E) effect on the short-time diffusion coefficient (left panel) and Brownian position fluctuation variance (right panel) of a DSPE (2.5 %, black symbols or 0.5 %, blue symbols)-coated silica microsphere adhered to a PA hydrogel film with a controlled elasticity. Data points represent average values of particle steady state behavior. Theoretical prediction, using the contact area from Eqn. 5.9, is plotted with a solid line using Maugis (1995) adhesion energy per unit area $U \approx 1.79 \times 10^{-10}$ J m^{-2}. This results in adhesion energy $\pi a^2 U/(k_B T) \approx 1.36 \times 10^{-5}$, taking the contact radius $a \approx$ 10 nm (Refer to section 5.5 for details), which is $\approx$ 3 times smaller than a bare silica microsphere (figure 5.6.5).

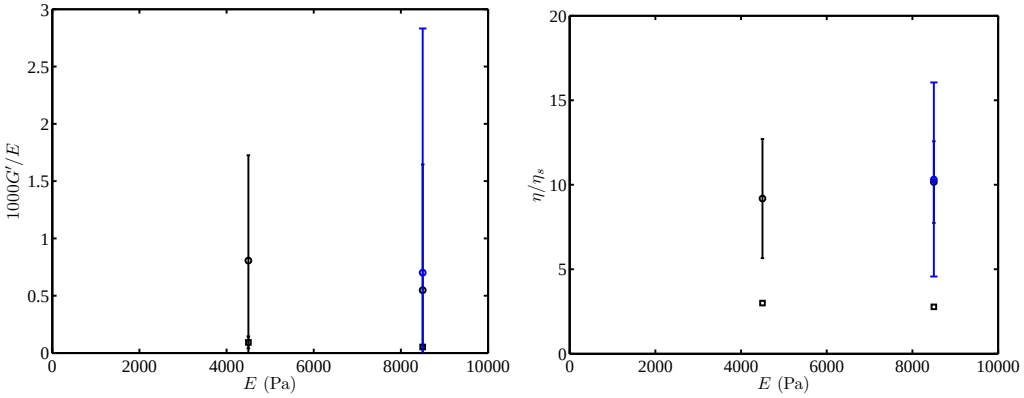

Figure 7.6.7: Interfacial storage modulus (left panel) and viscosity (right panel) versus AFM elastic modulus E, obtained from passive interfacial microrheology with a DOPC-coated (shown with black squares) or a DSPE (2.5 %, shown with black circles or 0.5 %, shown with blue circles) silica microsphere at a PA gel-electrolyte interface. Normalizing the storage moduli with gel AFM Young's modulus results in $1000G'/E \approx 0.7$, which is slightly smaller than a bare silica microsphere (≈ 1, figure 5.6.8). The viscosity is normalized with solvent (water) viscosity $\eta_s \approx 0.9$ mPa s, which slightly increases when increasing gel stiffness. Note that the data points (error bars) in both panels reflect the average (standard deviation) over all the samplings over all sampling times in figures 7.6.2 and 7.6.4 for DSPE-coated particles. According to Stokes-Einstein theory $D_x = k_B T/(6\pi\eta R)$, which suggests $D_x/D_0 \propto \eta_s/\eta$; therefore, the corresponding diffusion coefficients to the viscosity data (right panel) $D_x/D_0 \approx 0.1$, and 0.35 for a DSPE-coated and a DOPC-coated particle, respectively, which are in close agreement with figure 7.6.6; left panel: $D_x/D_0 \approx 0.13$. Also, the furnished storage moduli (left panel) for gels A and B, $G' \approx 4.7$ and 3.6 Pa bring about $\langle X^2 \rangle^{1/2} = (k_B T/6\pi R G')^{1/2} \approx 7$ and 8 nm, respectively, which agree with figure 7.6.6, right panel.

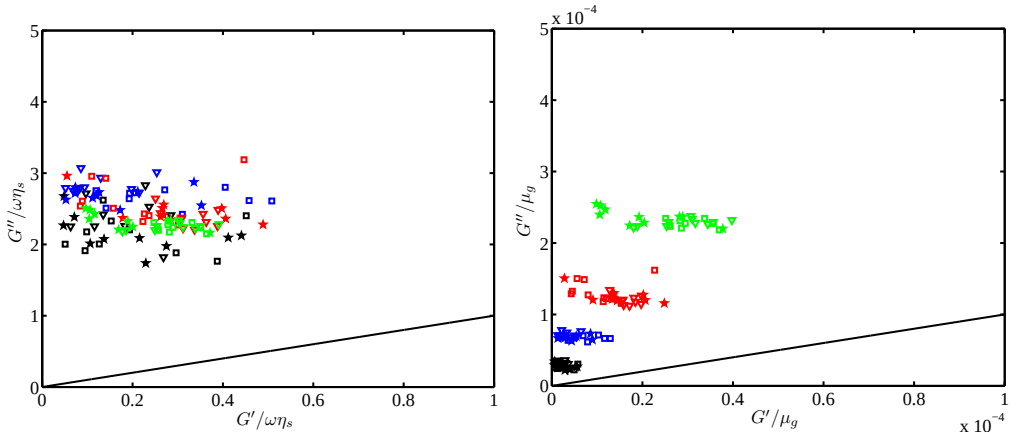

(a) DOPC-coated silica microsphere on PA hydrogel A, $k_t \approx 9$ μN m^{-1}.

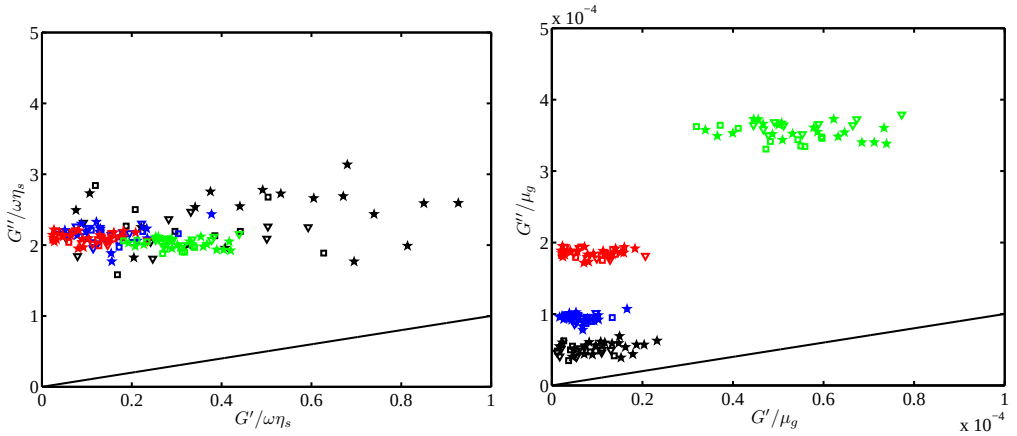

(b) DOPC-coated silica microsphere on PA hydrogel B, $k_t \approx 8.3$ μN m^{-1}.

Figure 7.6.8: Loss modulus G'' versus storage modulus G' (Cole-Cole plots) normalized with solvent viscosity ($\eta_s \approx 0.9$ mPa s, left panel) or bulk gel shear modulus μ_g (right panel) for a DOPC-coated silica microsphere on PA hydrogels A (panel a, $k_t \approx 9$ μN m^{-1}) and B (panel b, $k_t \approx 8.3$ μN m^{-1}) in TAE buffer (pH = 8.3, ionic strength 41 mmol l^{-1}), obtained from active interfacial microrheology. The boundary for the viscous ($G'' > G'$)-to-elastic ($G' > G''$) coupling transition (*i.e.*, $G'' = G'$) is presented with the solid line. The stage (and consequently the probe particle) is subject to a small-amplitude ($|x_s| \approx 30$ nm, see table 6.1) sinusoidal displacement with an oscillatory shear frequency $f \approx 8$ Hz (black symbols), 16 Hz (blue symbols), 32 Hz (red symbols), and 64 Hz (green symbols), shown with triangles ($t \leq 180$ s), squares ($180 < t \leq 360$ s), and pentagons ($t > 360$ s). In contrast to a bare silica microsphere, DOPC coating maintains a silica microsphere in the viscous coupling region on all the gel surfaces independent of the external drive frequency, reflecting the properties of the solvent in the gel vicinity. Compared to a bare silica microsphere (figure 6.6.7, panels a and b), DOPC coating decreased the measured interfacial storage modulus of the gels by more than one order of magnitude.

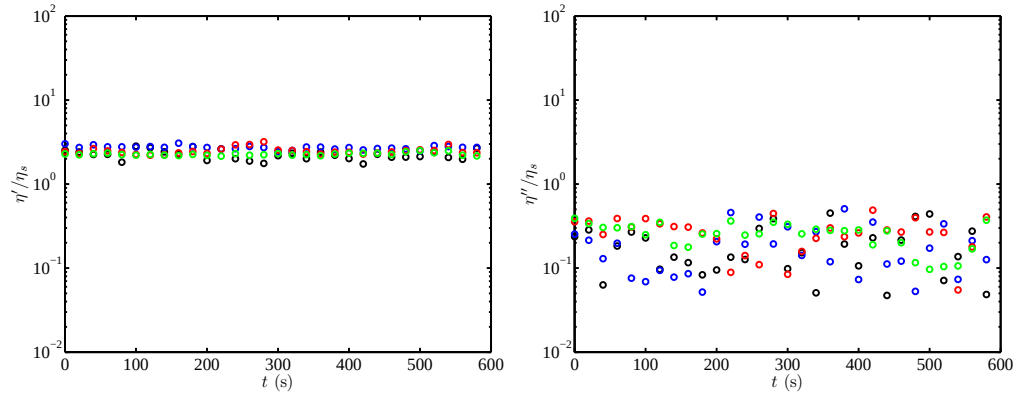

(a) DOPC-coated silica microsphere on PA hydrogel A, $k_t \approx 9$ μN m^{-1}.

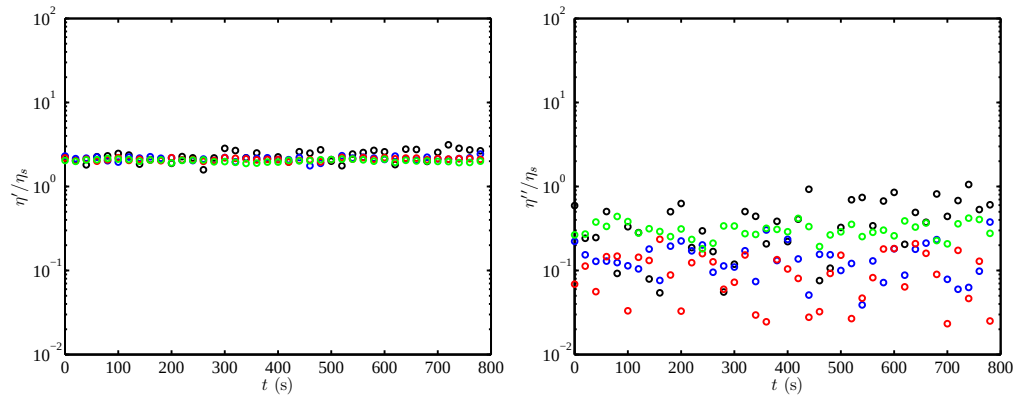

(b) DOPC-coated silica microsphere on PA hydrogel B, $k_t \approx 8.3$ μN m^{-1}.

Figure 7.6.9: Interfacial dynamic viscosity $\eta' = G''/\omega$ (left panel) and out-of-phase viscosity $\eta'' = G'/\omega$ (right panel) versus time t for a DOPC-coated silica microsphere on PA hydrogels A (panel a, $k_t \approx 9$ μN m^{-1}) and B (panel b, $k_t \approx 8.3$ μN m^{-1}) in TAE buffer (pH = 8.3, ionic strength 41 mmol l^{-1}), furnished from active interfacial microrheology. All experimental parameters are the same as figure 7.6.8. The oscillatory shear frequency $f \approx 8$ Hz (black symbols), 16 Hz (blue symbols), 32 Hz (red symbols), and 64 Hz (green symbols). The acquired interfacial dynamic viscosity reflects the solvent viscosity, which is independent of the external drive frequency. Moreover, regardless of the gel stiffness, the DOPC-coating prevents the microsphere from attaching to the gel; therefore, it cannot be employed to measure the gel-electrolyte microrheological properties. The out-of-phase viscosity is, accordingly, affected only by the trap stiffness, which adopts a relatively small value compared to the furnished values with a bare silica microsphere (figure 6.6.8) by as much as two orders of magnitude.

The interfacial zero-shear viscosity (shown in figure 7.6.10) furnished using a DOPC-coated silica microsphere probe adopts values close to the solvent dynamic viscosity (figure 7.6.9) due to a negligible elastic contribution from the substrate. Similar to the dynamic viscosity, η_0 is independent of the gel stiffness and external drive frequency, representing water viscosity near a plane wall. This is more than two orders of magnitude lower than the zero-shear viscosity furnished with a bare silica microsphere on gel A at low f and k_t (figure 6.6.9).

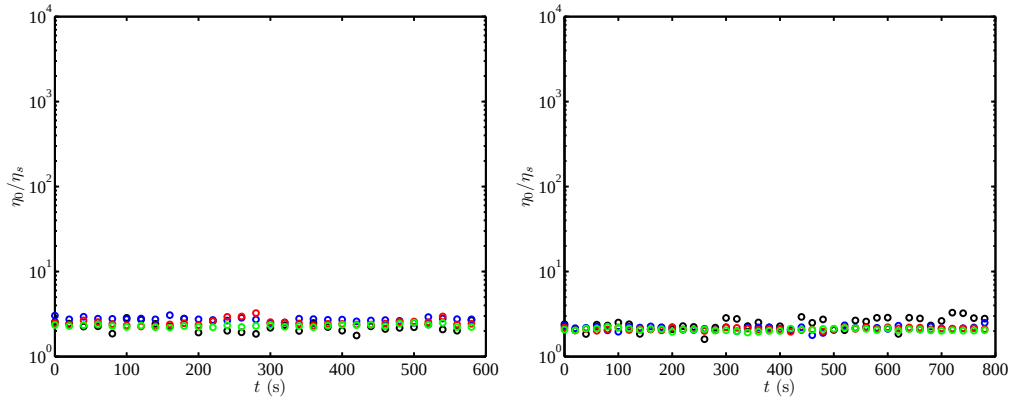

Figure 7.6.10: Interfacial zero-shear viscosity $\eta_0 = \eta' \left[1 + (G'/G'')^2\right]$ versus time t, furnished from active interfacial microrheology with a DOPC-coated silica microsphere on PA hydrogels A (left panel, $k_t \approx 9$ μN m^{-1}) and B (right panel, $k_t \approx 8.3$ μN m^{-1}). At all frequencies, regardless of the gel stiffness, the zero-shear viscosity adopts values close to the solvent viscosity, taking the effective hydrodynamic size of the probe particle close to a wall. The zero-shear viscosity, probed by a DOPC-coated particle, is close to the dynamic viscosity, furnished in figure 7.6.9, because the storage modulus and consequently the out-of-phase viscosity are negligible, suggesting an insignificant substrate elastic contribution.

The maximum stress response of a pure elastic material occurs exactly at the maximum small-amplitude oscillatory strain (to ensure linear viscoelasticity), *i.e.*, a completely in-phase response, whereas increasing viscous contribution dissipates stress, resulting in the maximum stress occurrence before the maximum strain, leading to a completely out-of-phase response for a pure viscous liquid. It was discussed in chapter 6 that the phase lag of an unbound colloidal probe in an optical trap decreases when increasing the external oscillatory drive (Eqn. 6.18), keeping the measured medium dynamic viscosity constant. For a DOPC-coated

silica microsphere on a PA gel, as shown in figure 7.6.11, the phase lag follows the same behavior as a particle in an unbound fluid, which is also similar to a bare silica particle on PA gel B at an high trap stiffness (figure 6.6.18b), *i.e.*, viscous coupling. The loss tangent (right panel) attains large values compared to the sticking cases, *e.g.*, a bare silica particle on a PA gel (figures 6.6.10). The large loss tangent is a result of small, fluctuating storage moduli, corresponding only to the trap stiffness.

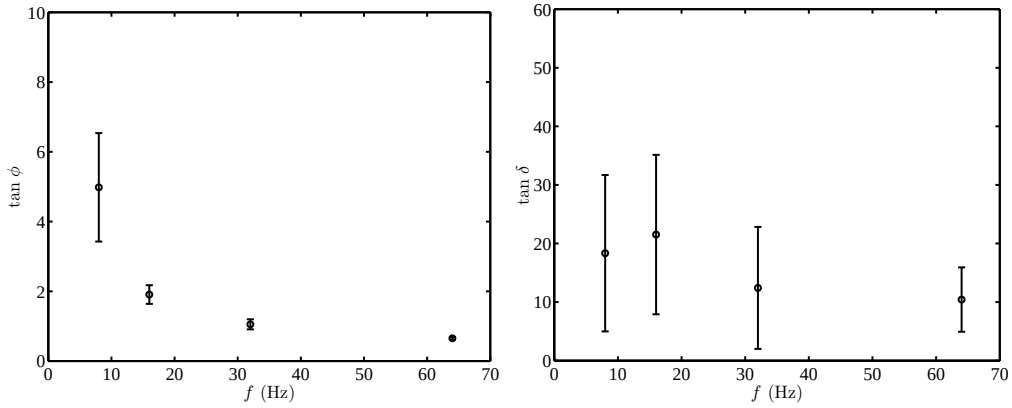

(a) DOPC-coated silica microsphere on PA hydrogel A, $k_t \approx 9$ μN m^{-1}.

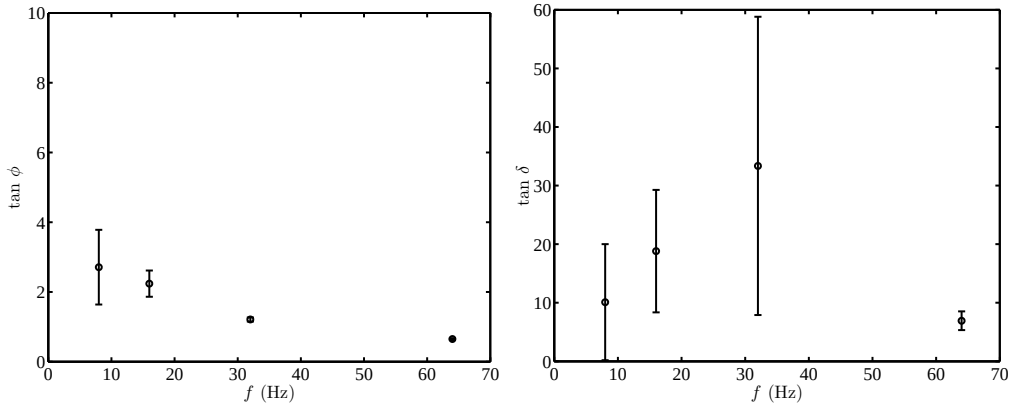

(b) DOPC-coated silica microsphere on PA hydrogel B, $k_t \approx 8.3$ μN m^{-1}.

Figure 7.6.11: Phase lag of a DOPC-coated silica microsphere probe response to an external sinusoidal shear $\tan\phi$ (left panel) and loss tangent $\tan\delta$ (right panel) versus drive frequency f while the microsphere is placed on PA hydrogels A (panel a, $k_t \approx 9$ μN m^{-1}) and B (panel b, $k_t \approx 8.3$ μN m^{-1}) in TAE buffer (pH = 8.3, ionic strength 41 mmol l^{-1}), obtained from active interfacial microrheology. All experimental parameters are the same as figure 7.6.8. The values are averaged over the sampling time, shown in figure 7.6.8. For both gels, the phase lag and loss tangent attain similar values at a given frequency. The decrease in phase lag (left panel) when increasing the frequency is compatible with the typical behavior of an optically trapped microsphere in an unbound solvent: $\tan\phi = k_t/(6\pi R\eta_s\omega)$, *e.g.*, doubling the drive frequency halves $\tan\phi$. The loss tangent adopt relatively high values (up to two orders of magnitude higher) compared to a bare silica microsphere on the gels (figure 6.6.10).

The effective interfacial transverse diffusion coefficient of a DOPC-coated silica microsphere on a PA gel is comparable to free Brownian diffusion coefficient in a bulk fluid close to a plane wall, as evidenced by figure 7.6.12. This is a result of negligible gel viscous and elastic contribution to the particle-gel inclusion, which is also previously confirmed by passive microrheology technique (see figure 7.6.2, left panel a).

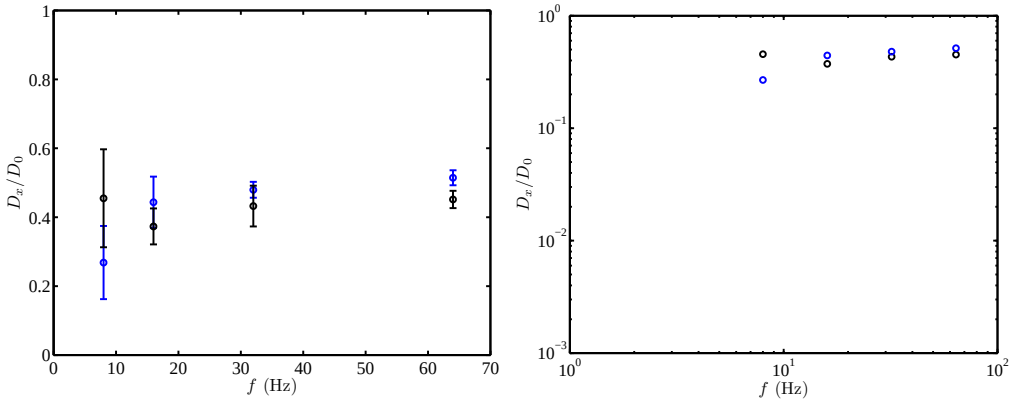

Figure 7.6.12: Effective interfacial transverse diffusion coefficient $D_x = 2\pi f k_B T \tan(\phi)/k_t$ versus drive frequency f, furnished from active microrheology with a DOPC-coated silica microsphere on PA hydrogels A (black symbols, $k_t \approx 9$ μN m^{-1}) and B (blue symbols, $k_t \approx 8.3$ μN m^{-1}). The diffusion coefficient is independent of both external drive frequency and gel stiffness, which attains values similar to the diffusion coefficient of a sphere close to a rigid wall with an height gap ≈ 130 nm according to the Faxen (1923) and ≈ 100 nm based on the Goldman *et al.* (1967) theories. The furnished effective diffusion coefficients are in close agreement with passive interfacial microrheology results, presented in figure 7.6.1, suggesting insignificant gel viscous and elastic contribution to the interfacial coupling. The right panel is a logarithmic presentation of the same data.

Lack of interfacial entanglement between a DOPC-coated particle and a PA gel results in low interfacial storage modulus, arising only from the optical trap; therefore, plotting storage and loss modulus versus $\omega\tau$ (figure 7.6.13) shows that G' and G'' are located at $\omega\tau < 1$, *i.e.*, viscous coupling region. The SLS and ESLS models, consequently, cannot furnish accurate fits for high-$\omega\tau$ ranges. The ESLS model yields an average $\eta/\tau \approx 2.5$ for panels (a) and (b), which brings about $\eta/\eta_0 \approx 2.7$, considering $\tau \approx 1$ ms (as furnished in figure 7.A.6). This is an acceptable estimation of water viscosity near a plane wall, which is compatible with the dynamic viscosity in figure 7.6.9.

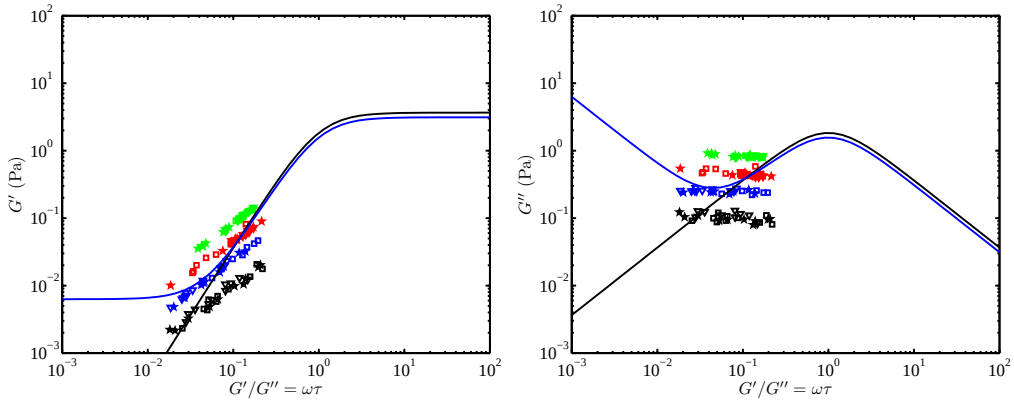

(a) DOPC-coated silica microsphere on PA hydrogel A, $k_t \approx 9$ μN m^{-1}.

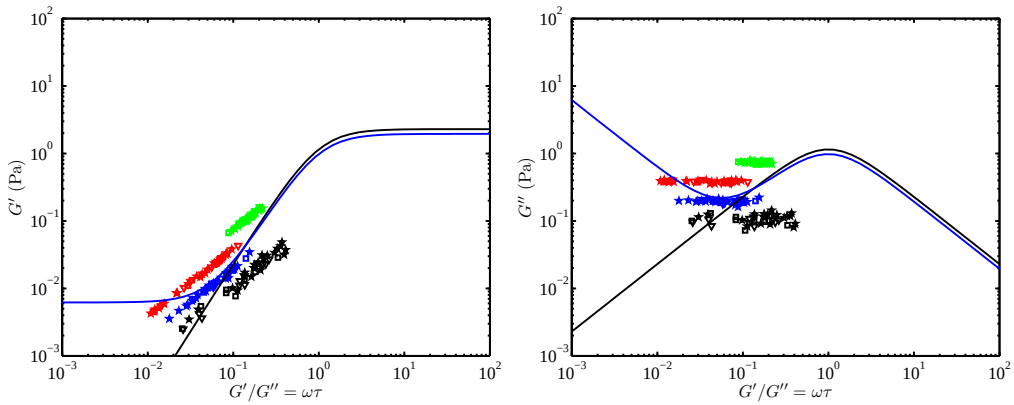

(b) DOPC-coated silica microsphere on PA hydrogel B, $k_t \approx 8.3$ μN m^{-1}.

Figure 7.6.13: Storage (left panel) and loss (right panel) moduli versus dimensionless relaxation time $G'/G'' = \omega\tau$ with a simultaneous least-squares best fit to the standard linear solid (SLS, black line) and extended standard linear solid (ESLS, blue line) models for gels A (panel a, $k_t \approx 9$ μN m^{-1}) and B (panel b, $k_t \approx 8.3$ μN m^{-1}), furnished from active interfacial microrheology with a DOPC-coated silica microsphere probe. Fit parameter η/τ in the SLS model: $G' = k_e + (\eta/\tau)\frac{(\omega\tau)^2}{1+(\omega\tau)^2}$ and $G'' = (\eta/\tau)\frac{\omega\tau}{1+(\omega\tau)^2}$ for gels A and B is 3.66 and 2.30, respectively, resulting in $\eta/(0.001\tau\mu_g) \approx 1.02$ and 1.11, and $\eta/\tau/(k_t/R) \approx 0.41$ and 0.25, respectively. Lack of elastic coupling data for gels A and B prevents the fit from predicting large-$\omega\tau$ moduli. For all cases, $k_e \approx 0$. The ESLS model, $G' = k_e + (\eta/\tau)\frac{(\omega\tau)^2}{1+(\omega\tau)^2}$ and $G'' = (\eta/\tau)\frac{\omega\tau}{1+(\omega\tau)^2} + k_e/(\omega\tau_e)$, furnishes more accurate fits for gels A and B. The ESLS model parameters (all in Pa) for gels A, $\eta/\tau \approx 3.12, k_e \approx 0.0063$, and B, $\eta/\tau \approx 1.95, k_e \approx 0.0062$, which bring about $(\eta/\tau)/(0.001\mu_g) \approx 0.87$ and 0.94 for gels A and B, respectively. Normalizing η/τ with the trap stiffness, for gel A ($k_t \approx 9$ μN m^{-1}) and B ($k_t \approx 8.3$ μN m^{-1}) results in $\eta/\tau/(k_t/R) \approx 0.35$, and 0.23, which are all representatives of solvent properties and trap stiffness. All experimental parameters are the same as figure 7.6.8.

The dissipation force per oscillation cycle of a DOPC-coated silica microsphere on a PA gel, shown in figure 7.6.14, suggests that regardless of the substrate stiffness, external drive frequency, and drive amplitude, the normalized $F_d \approx 0.01$. This is higher (lower) than the elastic (viscous) adhesion of a bare silica microsphere on PA gel A (B), as can be seen in figure 6.6.14 (a). Note that the dissipation force at an high frequency, *e.g.*, $f = 128$ Hz, with a reduced drive amplitude (see Table 6.1), remains comparable to the low-frequency data with a non-reduced drive amplitude. The constant normalized dissipation force is a result of constant dynamic viscosity, acquired with a DOPC-coated particle at the soft interfaces.

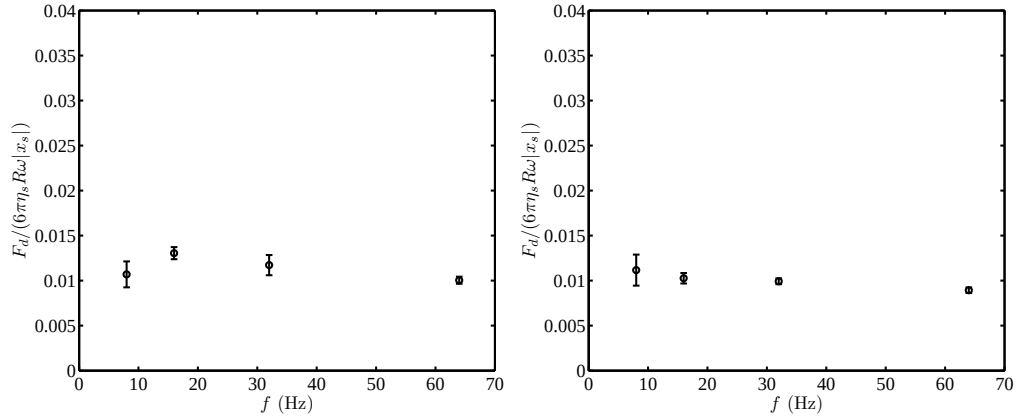

Figure 7.6.14: Dissipation force per cycle $F_d = \pi |x_s|^2 G''$, normalized with the Stokes drag force $6\pi\eta_s R\omega |x_s|$ versus drive frequency f, furnished from active interfacial microrheology with a DOPC-coated silica microsphere on PA hydrogels A (left panel, $k_t \approx 9$ μN m^{-1}) and B (right panel, $k_t \approx 8.3$ μN m^{-1}) in TAE buffer. Regardless of gel stiffness and shear rate, the dissipation force remains almost constant: normalized $F_d \approx 0.01$. The dissipation force of a DOPC-coated particle on a PA gel is higher than the elastic adhesion of a bare silica microsphere (gel A, figure 6.6.14, left panel), and is lower than bare silica particle viscous coupling (gel B: right panel in figure 6.6.14, and gel C: panel c in figure 6.6.14). The error bars show the standard deviation over the sampling time.

The interfacial adhesion phase diagram is constructed by comparing the interfacial storage and loss moduli (figure 7.6.8), which is shown in figure 7.6.15. A DOPC-coated silica microsphere-PA gel inclusion undergoes a viscous coupling ($G'' > G'$) with no significant elastic contribution of the gel substrate in the adhesion process.

Contrarily to DOPC-coated particles, by introducing the grafted PEG chains in the

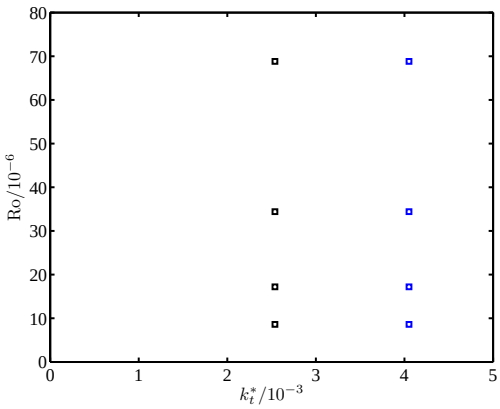

Figure 7.6.15: Interfacial adhesion phase diagram, furnished from active interfacial microrheology with a DOPC-coated silica microsphere on PA hydrogels A (black symbols) and B (blue symbols), obtained at a low trap stiffness, $k_t \approx 9$ μN m^{-1} for gel A and $k_t \approx 8.3$ μN m^{-1} for gel B, by altering the drive frequency, presented in terms of Roshko number $\mathrm{Ro} = fR^2\rho_s/\eta_s$ and dimensionless optical trap stiffness $k_t^* = k_t/(R\mu_g)$. DOPC coating results in microsphere-gel viscous coupling ($G'' > G'$) with negligible G', regardless of the gel stiffness and drive frequency.

DOPC coating, the resulted DSPE-coated silica microspheres were not able to be detached from the gel surface. Here, the adhesion between a DSPE-coated silica microsphere, originated exclusively from the PEG chains, and PA gels with a controlled stiffness is characterized. The interfacial behavior of a DSPE-coated silica microsphere with DSPE-PEG2k concentrations 2.5 or 0.5 mol % on PA gels A and B at low or high trap stiffness is discussed.

At a low trap stiffness, on a stiff PA gel (gel A), Cole-Cole plots of a DSPE-coated silica microsphere (figure 7.6.16) show that regardless of the DSPE content, the storage modulus at low frequencies is higher than the loss modulus, suggesting elastic adhesion. Increasing the drive frequency, increases the loss modulus while it has no significant effect on the storage modulus (see right panel), because at such a low trap stiffness, the shear force on the particle is not strong enough to deform the substrate and change the adhesion elasticity, similar to a bare silica particle on PA gels, as shown in figure 6.6.7. Normalizing the interfacial viscoelastic moduli with the drive frequency (left panel) shows a decrease in out-of-phase viscosity $\eta'' = G'/\omega$ when increasing the drive frequency, *i.e.*, constant G', while the dynamic viscosity $\eta' = G''/\omega$ remains almost constant until the adhesion regime is

changed from elastic $G' > G''$ to viscous $G'' > G'$ (*e.g.*, $f = 128$ Hz, yellow symbols in panel a).

At an high enough shear rate, *e.g.*, $f = 128$ Hz for 2.5 % DSPE and $f = 64$ Hz for 0.5 % DSPE concentrations, the loss modulus becomes greater than the storage modulus, suggesting viscous coupling. At a given frequency, the storage (loss) modulus, furnished with an higher DSPE content, is higher (almost unchanged). This, interestingly, suggests that the viscoelastic properties of the inclusion can be tuned, ranging from an almost-pure elastic (at high DSPE content) to an almost-viscous (at low DSPE content, *e.g.*, pure DOPC when DSPE concentration is zero); however, 0.5 % DSPE seems to be adequate to give rise to strong elastic particle-gel adhesion at low external forces. Moreover, the storage modulus, furnished with a DSPE (2.5 %)-coated particle, is similar to a bare silica microsphere on PA gel A (figure 6.6.7), while the loss modulus is higher. This suggests that the grafted PEG chains at such a concentration result in almost as strong elastic adhesion as a bare silica microsphere with much viscous contribution.

The interfacial dynamic (left panel) and out-of-phase viscosity (right panel), corresponding to the Cole-Cole data, are presented in figure 7.6.17. The dynamic viscosity fluctuates around $\eta'/\eta_0 \approx 2$ independently from the drive frequency and DSPE content as long as the adhesion resides in the elastic region. Although the dynamic viscosity, furnished with a sticking (DSPE-coated) particle is close to a non-stuck (DOPC-coated, figure 7.6.8) particle, the out-of-phase viscosity can be several orders of magnitude higher (compare right panel of figures 7.6.16 and 7.6.8), because the former particle reflects the interface properties while the latter is not significantly affected by the interface. The out-of-phase viscosity, in contrast to the dynamic viscosity, depends on the drive frequency: the higher the shear rate, the lower η'', similar to the sticking bare silica microsphere on PA gels. Moreover, comparing panels (a) and (b) suggests that a lower DSPE content results in a slightly lower out-of-phase viscosity at a given drive frequency. This is expected, because the DSPE coating acts as the binding agent and provides adhesive moieties. η' and η'' do not change with time.

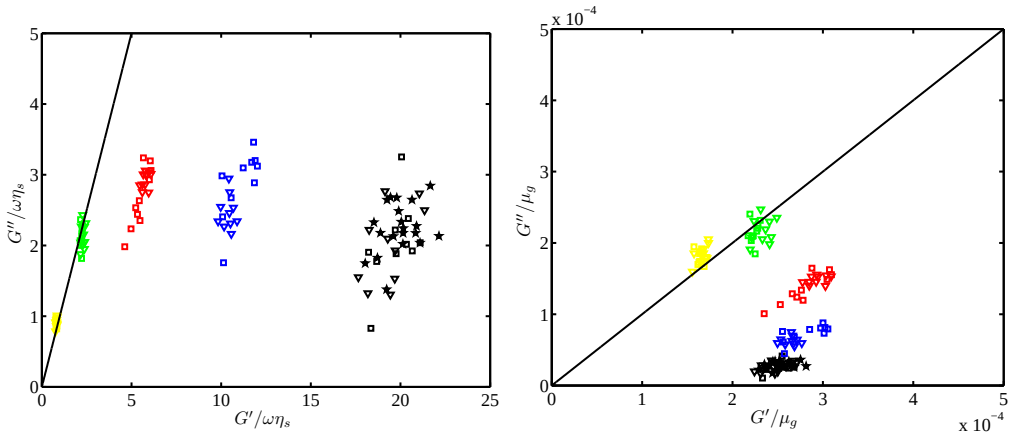

(a) DSPE (2.5 %)-coated silica microsphere on PA hydrogel A, $k_t \approx 7.6$ μN m^{-1}.

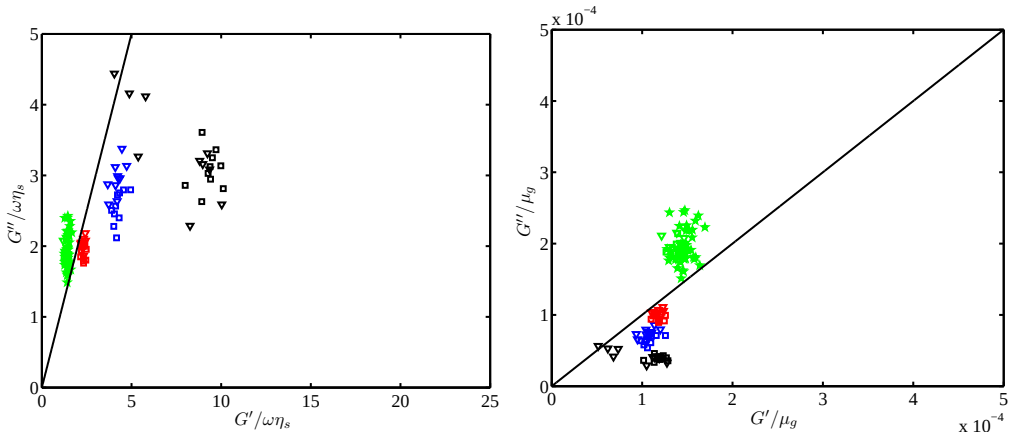

(b) DSPE (0.5 %)-coated silica microsphere on PA hydrogel A, $k_t \approx 8.2$ μN m^{-1}.

Figure 7.6.16: Loss modulus G'' versus storage modulus G' (Cole-Cole plots), normalized with solvent viscosity ($\eta_s \approx 0.9$ cP, left panel) or bulk gel shear modulus μ_g (right panel) for a DSPE (2.5 %)-coated (panel a) or a DSPE (0.5 %)-coated (panel b) silica microsphere on PA hydrogel A in TAE buffer (pH = 8.3, ionic strength 41 mmol l^{-1}), furnished from active interfacial microrheology with a low trap stiffness. The boundary for the viscous ($G'' > G'$)-to-elastic ($G' > G''$) transition (*i.e.*, $G'' = G'$) is presented with the solid line. The stage (and consequently the probe particle) is subject to a small-amplitude ($|x_s| \approx 30$ nm, see table 6.1) sinusoidal displacement with an oscillatory shear frequency $f \approx 8$ Hz (black symbols), 16 Hz (blue symbols), 32 Hz (red symbols), 64 Hz (green symbols), and 128 Hz (yellow symbols), shown with triangles ($t \leq 180$ s), squares ($180 < t \leq 360$ s), and pentagons ($t > 360$ s). Similar to a bare silica microsphere, DSPE-coated microspheres adhere firmly to the gel at a low enough shear rate. Comparing panels (a) and (b) suggests that (i) even a very low PEG content in the lipid bilayer coating can result in a firm interfacial adhesion, and (ii) decreasing the PEG content by a factor of 5 slightly decreases the storage modulus while the loss modulus remains almost unchanged at a given frequency. Compared to a bare silica microsphere (figure 6.6.7), a DSPE-coated microsphere brings about a similar interfacial storage modulus while the coupling is more viscous, as evidenced by greater loss moduli. This is consistent with the passive interfacial microrheology data (compare figures 7.6.3b with 5.6.4a).

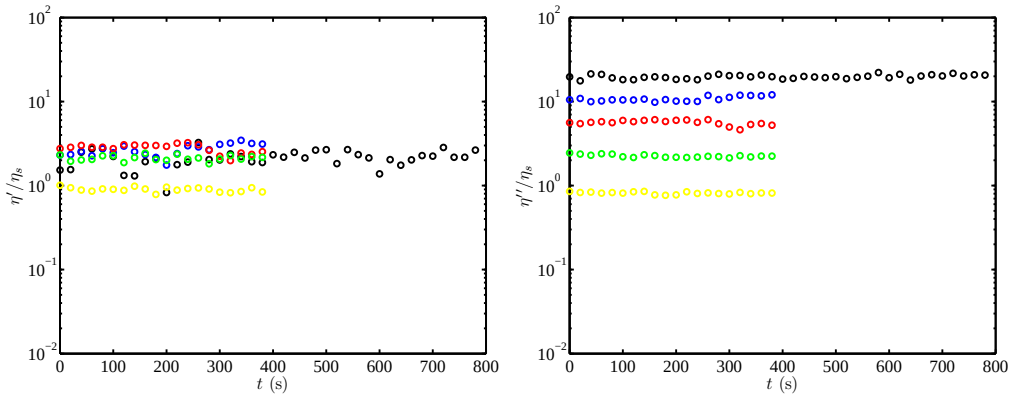

(a) DSPE (2.5 %)-coated silica microsphere on PA hydrogel A, $k_t \approx 7.6$ μN m^{-1}.

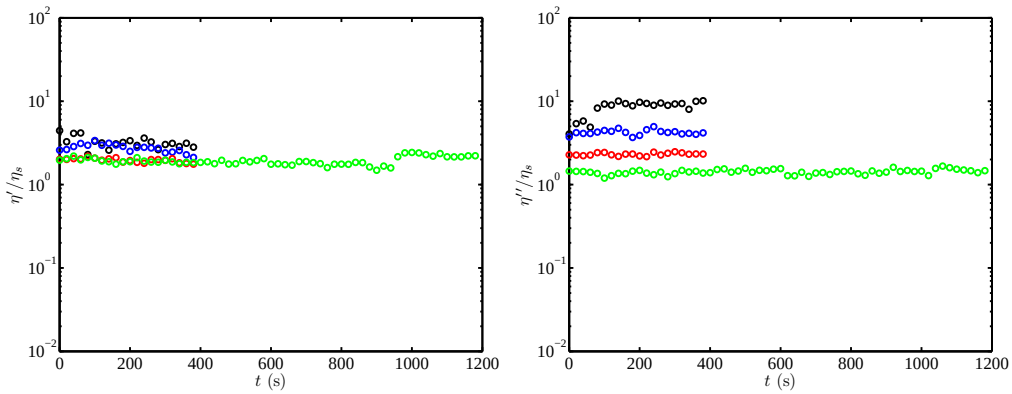

(b) DSPE (0.5 %)-coated silica microsphere on PA hydrogel A, $k_t \approx 8.2$ μN m^{-1}.

Figure 7.6.17: Interfacial dynamic viscosity $\eta' = G''/\omega$ (left panel) and out-of-phase viscosity $\eta'' = G'/\omega$ (right panel) versus time t for a DSPE (2.5 %)-coated (panel a) or a DSPE (0.5 %)-coated (panel b) silica microsphere on PA hydrogel A in TAE buffer (pH = 8.3, ionic strength 41 mmol l^{-1}), furnished from active interfacial microrheology with a low trap stiffness. All experimental parameters are the same as figure 7.6.16. The oscillatory shear frequency $f \approx 8$ Hz (black symbols), 16 Hz (blue symbols), 32 Hz (red symbols), 64 Hz (green symbols), and 128 Hz (yellow symbols). The interfacial dynamic viscosity is almost independent of the drive frequency and DSPE content, attaining values close to DOPC-coated particles (see figure 7.6.9), while the out-of-phase viscosity (i) decreases systematically when increasing the drive frequency at a given DSPE content, (ii) is slightly higher for an higher DSPE content at a given drive frequency, (iii) is higher than furnished with a DOPC-coated probe by several orders of magnitude (compare to figure 7.6.9, left panel), and (iv) adopts similar values to the experiments with a bare silica microsphere (see figure 6.6.8, right panel a).

The zero-shear viscosity, furnished from the dynamic and out-of-phase viscosity, versus time is shown in figure 7.6.18 for a DSPE (2.5 %, left panel, or 0.5 %, right panel)-coated silica microsphere on PA gel A. For these cases, the zero-shear viscosity at $f = 8$ Hz is approximately 200 and 40 times higher than water viscosity, respectively. This is slightly lower than the zero-shear viscosity furnished with a bare silica microsphere on PA gel A (figure 6.6.9, left panel a). Also, increasing the oscillatory drive frequency decreases η_0 due to a decrease in G'. At a specified drive frequency, the zero-shear viscosity is higher for an higher DSPE content. The furnished η_0 with a bare silica microsphere on gels A (B) are higher (lower) than a DSPE (0.5 %)-coated particle on gel A.

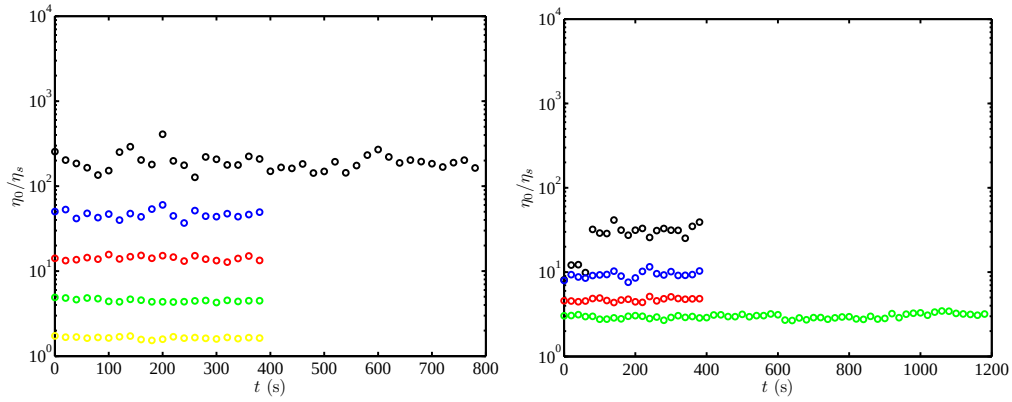

Figure 7.6.18: Interfacial zero-shear viscosity $\eta_0 = \eta' \left[1 + (G'/G'')^2\right]$ versus time t, furnished from active interfacial microrheology with a DSPE (2.5 %)-coated (left panel, $k_t \approx 7.6$ μN m^{-1}) or DSPE (0.5 %)-coated (right panel, $k_t \approx 8.2$ μN m^{-1}) silica microsphere on PA hydrogel A. The zero-shear viscosity decreases systematically when increasing the drive frequency for both high and low DSPE contents; however, at a given drive frequency, an higher DSPE content results in greater η_0. Compared to a bare silica microsphere on gel A (figure 6.6.9, left panel a), η_0 is smaller for a DSPE-coated particle at a specified shear rate. Also, here, the zero-shear viscosity is greater than a DOPC-coated particle, which reflects the favored effect of PEG chains on the microsphere-gel A interfacial adhesion.

The phase lag (left panel) and loss tangent (right panel) of a DSPE-coated silica microsphere, adhered to a PA gel A, are presented in figure 7.6.19. As can be seen in panel (a), for a DSPE (2.5 %)-coated silica microsphere, the phase lag and loss tangent, at low enough frequencies (*e.g.*, $f \leq 64$ Hz), increase linearly when increasing the drive frequency, indicating that the PA hydrogel-particle inclusions behave as a viscoelastic material with

higher viscous contribution at higher frequencies. In other words, they respond to the strain perturbation slower (with higher lag) at higher frequencies. Comparing panels (a) and (b) reveals that at a given frequency, the phase lag and loss tangent with an higher DSPE content is lower. Interestingly, $\tan\phi$ and $\tan\delta$ are both higher than a bare silica microsphere on PA gel A (figure 6.6.10a), because while a bare silica microsphere is affected by its whole contact area, providing much elastic adhesion, a DSPE-coated particle has fewer adhesive sites, *i.e.*, grafted PEG chains.

The number of grafted PEG chains, interacting with the gel, can be obtained using the mushroom-to-brush regime transition critical lipopolymer concentration. A DSPE-coated particle radius $R \approx$ 1000 nm, and polymer chain area $A_{\text{chain}} = \pi\ R_f^2 = \pi\ N^{6/5} a_p^2 = 36$ nm^2, with PEG degree of polymerization $N = 44$ and polymer chain radius $a_p = 0.35$ nm. Here, R_f is PEG Flory radius. Considering mushroom-to-brush regime transition concentration approximately 4 mol % (Noppl-Simson & Needham, 1996), if a polymer-coated microsphere has a zero nm^2 contact area with the substrate, and if a single PEG chain has length $l_c = 3.5$ nm, the polymer coating contact area with the substrate will be $A_p = \pi(2Rl_c - l_c^2) =$ 6240 nm^2. This is equivalent to $\approx$ 173 polymer chains at the regime transition point. Therefore, for 2.5 % and 0.5 % lipopolymer concentrations, there will be at least 108 and 22 polymer chains interacting with the underlying substrate, corresponding to grafting density approximately 0.0173 and 0.0035 nm^{-2}, respectively.

The effective interfacial transverse diffusion coefficient of a DSPE-coated silica microsphere on PA gel A is shown in figure 7.6.20. The diffusion coefficient increases linearly when increasing the drive frequency for both high (black symbols) and low (blue symbols) DSPE contents; however, an higher DSPE content results in a slightly lower diffusion coefficient. At an high enough shear rate (*e.g.*, $f = 128$ Hz), D_x attains a value close to a free diffusion case, such as a DOPC-coated microsphere (see figure 7.6.12), suggesting a faded inclusion elastic contribution. A DSPE-coated silica particle, as evidenced by figure 7.6.20 compared to figure 6.6.11, diffuses faster than a bare particle on PA gel A, while its effective

diffusion coefficient is smaller than a DOPC-coated particle by several orders of magnitude, as can be seen in figure 7.6.12.

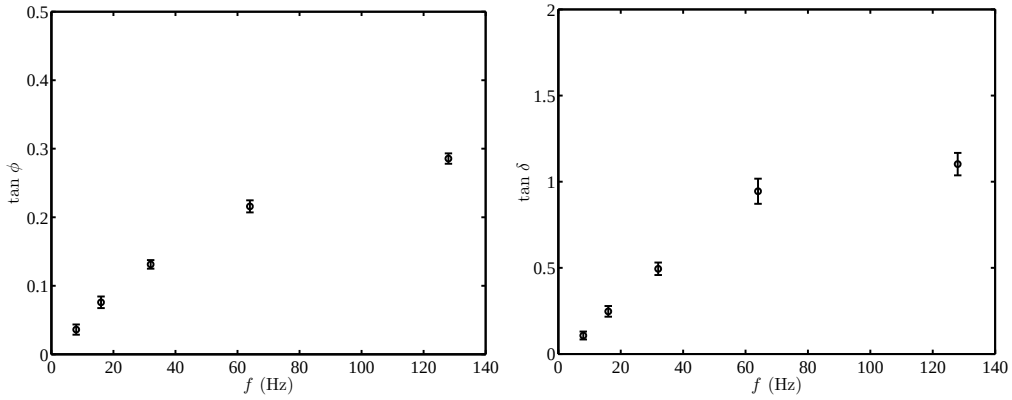

(a) DSPE (2.5 %)-coated silica microsphere on PA hydrogel A, $k_t \approx 7.6$ μN m^{-1}.

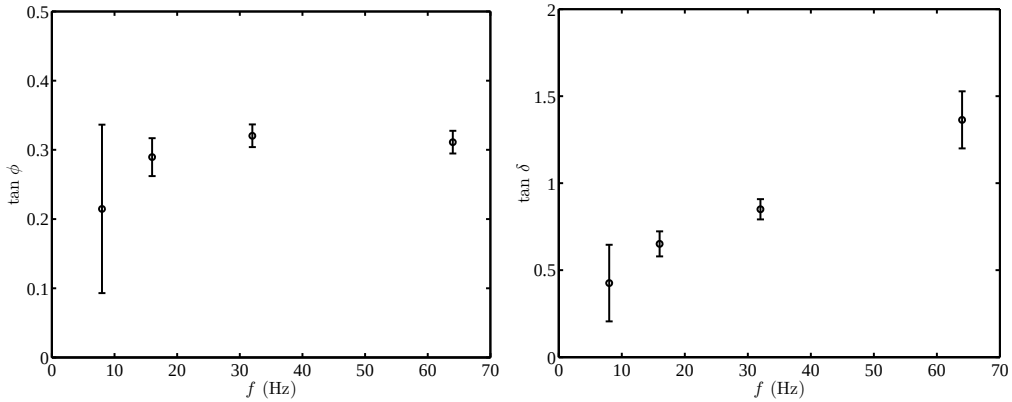

(b) DSPE (0.5 %)-coated silica microsphere on PA hydrogel A, $k_t \approx 8.2$ μN m^{-1}.

Figure 7.6.19: Phase lag of a DSPE (2.5 %)-coated (panel a) or a DSPE (0.5 %)-coated (panel b) silica microsphere probe response to an external sinusoidal shear $\tan\phi$ (left panel) and loss tangent $\tan\delta$ (right panel) versus drive frequency f while the microsphere is placed on PA hydrogel A in TAE buffer, obtained from active interfacial microrheology at a low trap stiffness. All experimental parameters are the same as figure 7.6.16. The values are averaged over the sampling time, shown in figure 7.6.16. The phase lag and loss tangent for both high and low DSPE contents are significantly smaller than DOPC-coated particles (figure 7.6.11); however, an higher DSPE content (panel a) results in a slightly lower phase lag and loss tangent, suggesting a slower effective interfacial diffusion and much elastic adhesion. Also, the phase lag and loss tangent are slightly greater than a bare silica microsphere (compared to figure 6.6.10a).

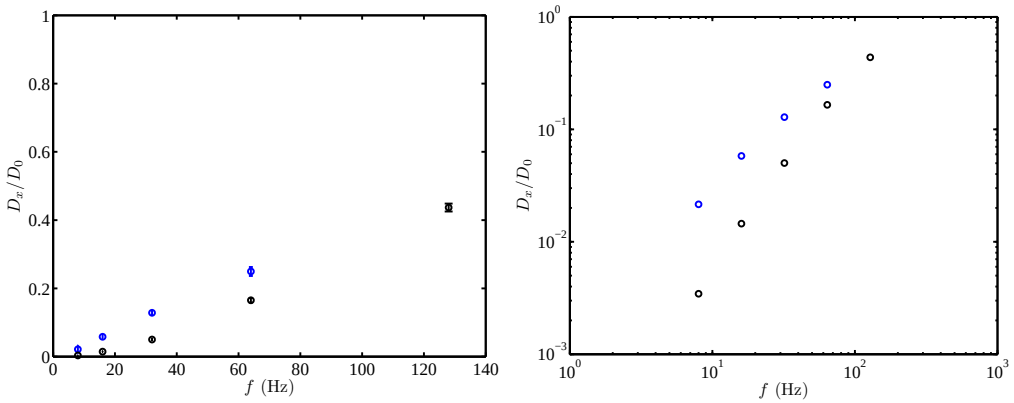

Figure 7.6.20: Effective interfacial transverse diffusion coefficient $D_x = 2\pi f k_B T \tan(\phi)/k_t$ versus drive frequency f, furnished from active microrheology with a DSPE (2.5 %)-coated (black symbols, $k_t \approx 7.6$ μN m^{-1}) or a DSPE (0.5 %)-coated (blue symbols, $k_t \approx 8.2$ μN m^{-1}) silica microsphere on PA hydrogel A. In contrast to DOPC-coated silica microspheres (figure 7.6.12), the conjugated PEG chains in the DOPC bilayer (*i.e.*, DSPE coating) attenuate the effective diffusion coefficient by several orders of magnitude, resulting in a frequency-dependent diffusion coefficient. Also, an higher DSPE content (black symbols) results in a slower diffusion due to higher elastic contribution. Compared to a bare silica microsphere (figure 6.6.11), DSPE-coating brings about a faster effective interfacial diffusion. The right panel is a logarithmic presentation of the same data.

The storage and loss moduli of PA gel A, furnished with a DSPE-coated silica microsphere, are plotted versus $\omega\tau$ in figure 7.6.21. The viscoelastic moduli fall in the $\omega\tau > 1$ region except at $f = 128$ Hz (64 Hz) for 2.5 % (0.5 %) DSPE coating due to viscous coupling at such high shear rates. Interestingly, the storage and loss moduli behavior at high $\omega\tau$ (elastic coupling) is similar to a Maxwell viscoelastic material. The SLS and ESLS models provide accurate fits for high-$\omega\tau$ data, furnishing $\eta/\tau/(0.001\mu_g) \approx 0.14$ and $k_e \approx 0.45$, values close to a bare silica microsphere: 0.23 and 0.79 (see figure 6.6.12), respectively. The low DSPE content results in inaccurate fits, because the data are mostly scattered around $\omega\tau \approx 1$. Compared to a DOPC-coated particle (figure 7.6.13), k_e is higher for a DSPE-coated particle. Note that high-$\omega\tau$ data for the DOPC-coated particle is not available; therefore, comparing η/τ, here, is not useful.

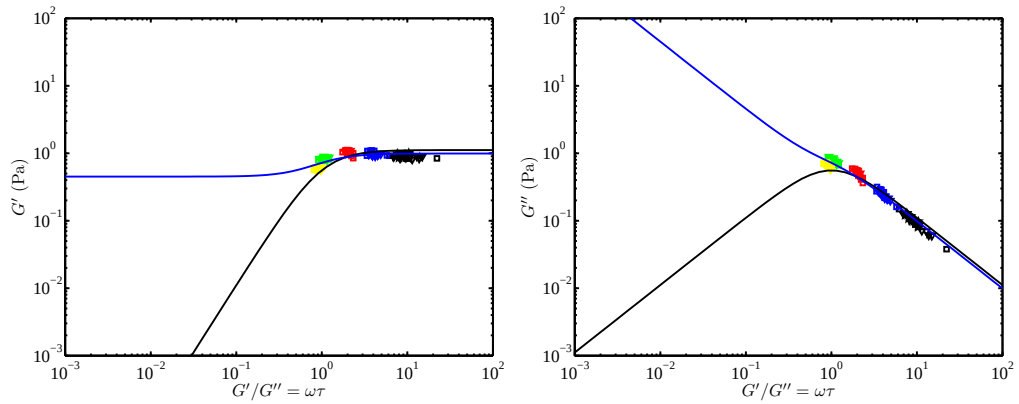

(a) DSPE(2.5 %)-coated silica microsphere on PA hydrogel A, $k_t \approx 7.6$ μN m^{-1}.

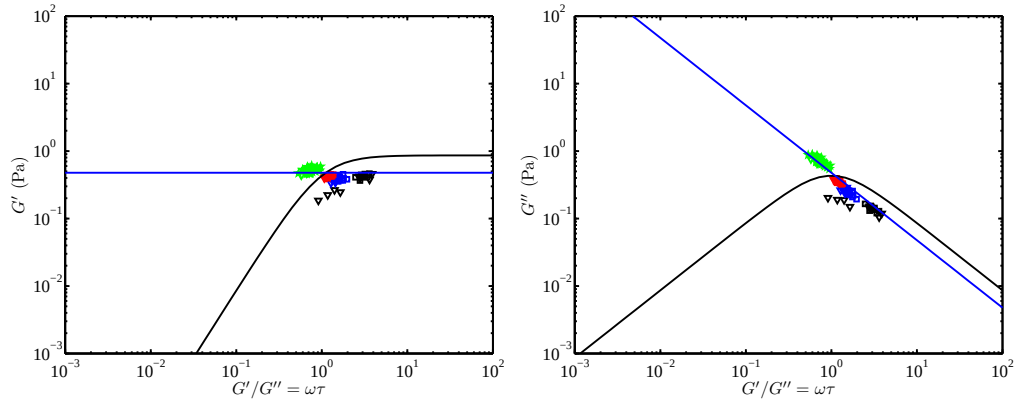

(b) DSPE (0.5 %)-coated silica microsphere on PA hydrogel A, $k_t \approx 8.2$ μN m^{-1}.

Figure 7.6.21: Storage (left panel) and loss (right panel) moduli versus dimensionless relaxation time $G'/G'' = \omega\tau$ with a simultaneous least-squares best fit to the standard linear solid (SLS, black line) and extended standard linear solid (ESLS, blue line) models for gel A, furnished from active interfacial microrheology with a DSPE (2.5 %)-coated (panel a, $k_t \approx 7.6$ μN m^{-1}) or DSPE (0.5 %)-coated (panel b, $k_t \approx 8.2$ μN m^{-1}) silica microsphere probe. Fit parameter η/τ in the SLS model: $G' = k_e + (\eta/\tau)\frac{(\omega\tau)^2}{1+(\omega\tau)^2}$ and $G'' = (\eta/\tau)\frac{\omega\tau}{1+(\omega\tau)^2}$ for panels (a) and (b) is 1.11 and 0.86, respectively, resulting in $\eta/(0.001\tau\mu_g) \approx 0.29$ and 0.23, and $\eta/\tau/(k_t/R) \approx 0.15$ and 0.11, respectively. For all cases, $k_e \approx 0$. The ESLS model, $G' = k_e + (\eta/\tau)\frac{(\omega\tau)^2}{1+(\omega\tau)^2}$ and $G'' = (\eta/\tau)\frac{\omega\tau}{1+(\omega\tau)^2} + k_e/(\omega\tau_e)$, furnishes much accurate fits. The ESLS model parameters (all in Pa) for panel (a), $\eta/\tau \approx 0.54, k_e \approx 0.45$, and panel (b), $\eta/\tau \approx 0, k_e \approx 0.48$, which bring about $(\eta/\tau)/(0.001\mu_g) \approx 0.14$ and 0 for panels (a) and (b), respectively. Normalizing the η/τ with the trap stiffness results in $\eta/\tau/(k_t/R) \approx 0.071$, a value close to that furnished with a bare silica microsphere (figure 6.6.20). Lack of viscous coupling data prevents the fit from predicting small-$\omega\tau$ moduli. All experimental parameters are the same as figure 7.6.16.

The dissipation force per oscillation cycle of a DSPE-coated silica microsphere on PA gel A is plotted in figure 7.6.22 for high (left panel) and low (right panel) DSPE contents. At an high DSPE content, *i.e.*, relatively stronger adhesion, the dissipative force first increases with drive frequency (up to $f = 32$ Hz) and then decreases to values comparable to a DOPC-coated particle. A low DSPE content results in comparable dissipation force to the high DSPE content case. Compared to a bare silica microsphere (figure 6.6.14, left panel a), regardless of the drive frequency and DSEP content, F_d is significantly larger.

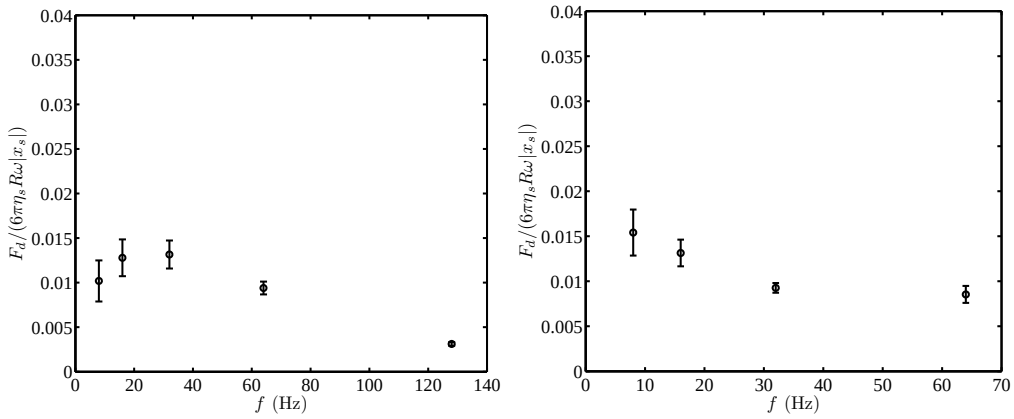

Figure 7.6.22: Dissipation force per cycle $F_d = \pi |x_s|^2 G''$, normalized with the Stokes drag force $6\pi\eta_s R\omega |x_s|$ versus drive frequency f, furnished from active interfacial microrheology with a DSPE (2.5 %)-coated (left panel, $k_t \approx 7.6$ μN m^{-1}) or a DSPE (0.5 %)-coated (right panel, $k_t \approx 8.2$ μN m^{-1}) silica microsphere on PA hydrogel A in TAE buffer. Regardless of DSPE content in the bilayer coating, the dissipation force adopts values close to a DOPC-coated particle (figure 7.6.14), which is higher than a bare silica microsphere on gel A (figure 6.6.14, left panel a).

The active interfacial experiments with the DSPE-coated silica microsphere probes were conducted on gel B to study the effect of substrate stiffness. The Cole-Cole plots, presenting the loss and storage moduli versus each other are illustrated in figure 7.6.23 (left panel: normalized with the drive frequency and solvent viscosity, right panel: normalized with the bulk gel shear modulus). With a DSPE (2.5 %)-coated particle (panel a), at all external drive frequencies, the steady-state storage modulus is higher than the loss modulus; however, at an high drive frequency ($f = 128$ Hz, yellow symbols), aging can be observed. The normalized storage moduli (panel a) with the bulk gel shear modulus remain $(0.2-0.6)\times 10^{-3}$, which are

similar to a bare silica microsphere on PA gel B (figure 7.6.23b). By decreasing the DSPE content (panel b), the interfacial storage moduli decrease, leading to the viscous coupling at $f \geq 16$ Hz. Similar to the stiffer gel (gel A; figure 7.6.16), at an high DSPE content, the interfacial storage modulus seems to be scalable with the gel shear modulus, which is also similar to a bare silica microsphere.

The interfacial dynamic viscosity of gel B, furnished with a DSPE-coated particle (shown in figure 7.6.24, left panel) are fluctuating around $\eta'/\eta_0 \approx 2$, while the out-of-phase viscosity at an high DSPE content (right panel a) decreases when increasing the drive frequency and attains values higher than the low-DSPE (right panel b) probe. The dynamic viscosity, furnished with both particles is similar to gel A (figure 7.6.17); however, the out-of-phase viscosity is lower than gel A at a specified drive frequency. Moreover, the dynamic and out-of-phase viscosity with a DSPE (2.5 %)-coated silica are close to a bare silica microsphere (figure 6.6.8b).

The zero-shear viscosity of gel B from active interfacial microrheology with the DSPE-coated particles are presented in figure 7.6.25. The zero-shear viscosity, furnished with an high DSPE content is higher than the low-DSPE particle, because the high grafting density of the adhesive moieties assures the particle-hydrogel elastic attachment, bringing about much accurate interfacial gel properties via the active experiments. Increasing the frequency decreases η_0, regardless of the DSPE content. Compared to gel A (figure 7.6.25), η_0 of gel B is lower, while it is close to the values furnished with a bare silica microsphere on gel B (figure 6.6.9) only if the coupling is dominated by the elasticity.

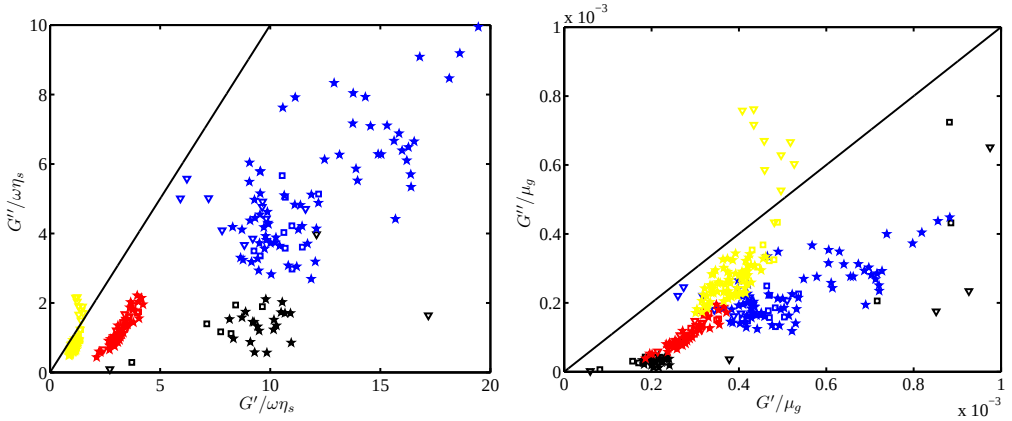

(a) DSPE (2.5 %)-coated silica microsphere on PA hydrogel B, $k_t \approx 8.2$ μN m^{-1}.

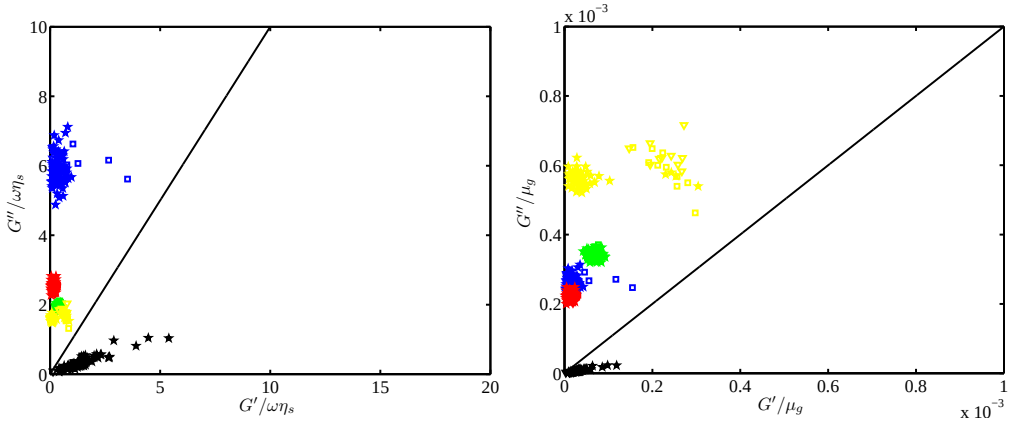

(b) DSPE (0.5 %)-coated silica microsphere on PA hydrogel B, $k_t \approx 8.8$ μN m^{-1}.

Figure 7.6.23: Loss modulus G'' versus storage modulus G' (Cole-Cole plots), normalized with solvent viscosity ($\eta_s \approx 0.9$ cP, left panel) or bulk gel shear modulus μ_g (right panel) for a DSPE (2.5 %)-coated (panel a) or a DSPE (0.5 %)-coated (panel b) silica microsphere on PA hydrogel B in TAE buffer (pH = 8.3, ionic strength 41 mmol l^{-1}), furnished from active interfacial microrheology at a low trap stiffness. The boundary for the viscous ($G'' > G'$)-to-elastic ($G' > G''$) transition (*i.e.*, $G'' = G'$) is presented with the solid line. The stage (and consequently the probe particle) is subject to a small-amplitude ($|x_s| \approx 30$ nm, see table 6.1) sinusoidal displacement with an oscillatory shear frequency $f \approx 8$ Hz (black symbols), 16 Hz (blue symbols), 32 Hz (red symbols), 64 Hz (green symbols), and 128 Hz (yellow symbols), shown with triangles ($t \leq 180$ s), squares ($180 < t \leq 360$ s), and pentagons ($t > 360$ s). Comparing panels (a) and (b) suggests that (i) regardless of the DSPE content, at a low enough frequency, *e.g.*, $f = 8$ Hz, the coupling is dominated by the elastic stresses, (ii) decreasing the PEG content decreases the storage modulus at a given frequency while the loss modulus does not change significantly. Compared to gel A (figure 7.6.16), at a given drive frequency and DSPE content, the interfacial storage modulus is smaller for a softer gel, which can be scaled with the bulk gel shear modulus if the adhesion resides in the elastic region.

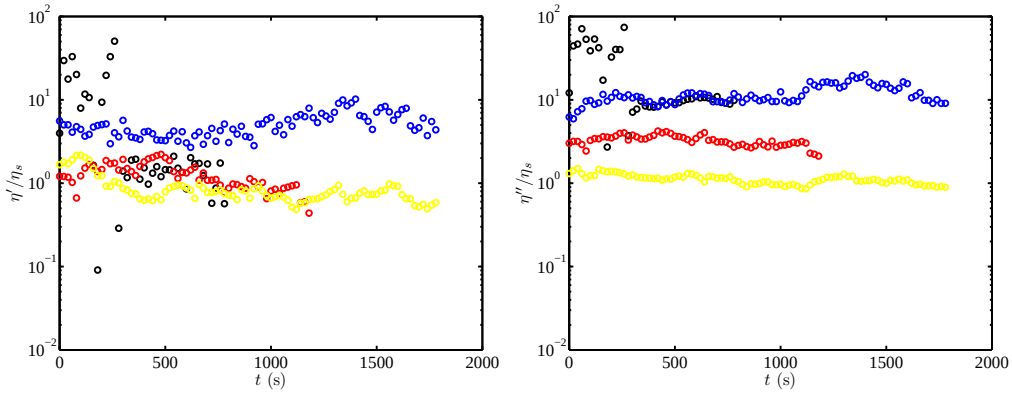

(a) DSPE (2.5 %)-coated silica microsphere on PA hydrogel B, $k_t \approx 8.2$ μN m^{-1}.

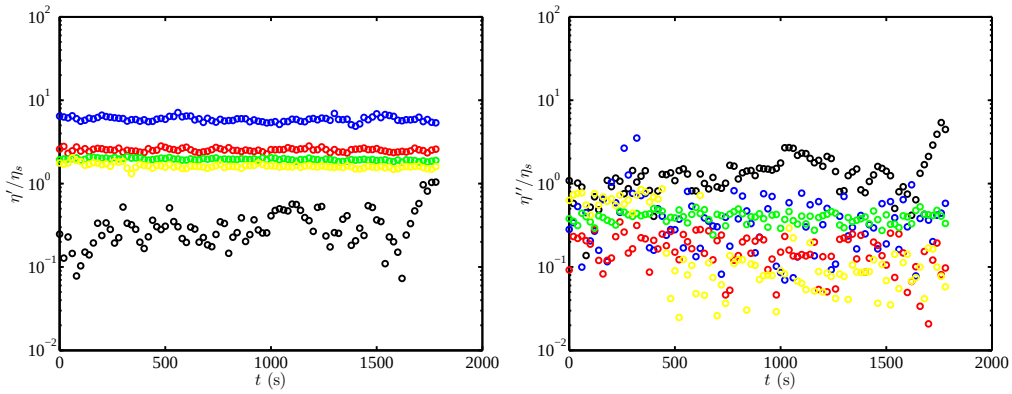

(b) DSPE (0.5 %)-coated silica microsphere on PA hydrogel B, $k_t \approx 8.8$ μN m^{-1}.

Figure 7.6.24: Interfacial dynamic viscosity $\eta' = G''/\omega$ (left panel) and out-of-phase viscosity $\eta'' = G'/\omega$ (right panel) versus time t for a DSPE (2.5 %)-coated (panel a) or a DSPE (0.5 %)-coated (panel b) silica microsphere on PA hydrogel B in TAE buffer (pH = 8.3, ionic strength 41 mmol l^{-1}), furnished from active interfacial microrheology at a low trap stiffness. All experimental parameters are the same as figure 7.6.23. The oscillatory shear frequency $f \approx 8$ Hz (black symbols), 16 Hz (blue symbols), 32 Hz (red symbols), 64 Hz (green symbols), and 128 Hz (yellow symbols). The interfacial dynamic viscosity in panels (a) and (b) are close to each other at a given frequency (excluding $f = 8$ Hz, *i.e.*, stuck case); however, the out-of-phase viscosity is higher for the larger DSPE content. Compared to gel A (figure 7.6.17), the dynamic (out-of-phase) viscosity are close (smaller) at given drive frequency and DSPE content for an elastic ($G' > G''$) adhesion.

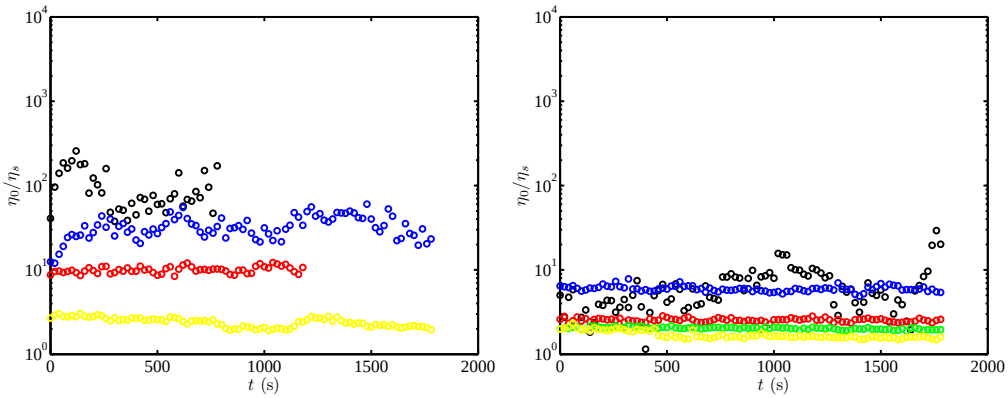

Figure 7.6.25: Interfacial zero-shear viscosity $\eta_0 = \eta' \left[1 + (G'/G'')^2\right]$ versus time t, furnished from active interfacial microrheology with a DSPE (2.5 %)-coated (left panel, $k_t \approx 8.2$ μN m^{-1}) or DSPE (0.5 %)-coated (right panel, $k_t \approx 8.8$ μN m^{-1}) silica microsphere on PA hydrogel B. Similar to gel A (figure 7.6.18), the zero-shear viscosity decreases systematically when increasing the drive frequency for both high and low DSPE contents; however, at a given drive frequency, an higher DSPE content results in a greater η_0. Compared to a bare silica microsphere on gel B (figure 6.6.9, right panel a), furnished η_0 with a DSPE-coated particle are close. Also, here, the zero-shear viscosity is smaller than gel A, which shows that the effect of substrate stiffness on PEG chain-mediated soft adhesion is weaker.

The phase lag and loss tangent, furnished with a DSPE-coated silica microsphere on gel B, shown in figure 7.6.26, increase linearly when increasing the shear rate on the high-DSPE content microsphere (panel a), attaining (small) values close to gel A (figure 7.6.19). Decreasing the DSPE content to 0.5 % results in higher phase lag and loss tangent (panel b), a behavior similar to a DOPC-coated microsphere (figure 7.6.11), *i.e.*, decrease in the phase lag when increasing the drive frequency as well as high $\tan\delta$. At an high DSPE content, the phase lag and loss tangent are close to a bare silica microspehre, while a low DSPE content results in higher $\tan\phi$ and $\tan\delta$ than a bare silica microsphere on gel B, *i.e.*, much viscous coupling. In fact, decreasing the gel stiffness, decreases the available ready-to-stick dangling polymer chains on the gel surface, resulting in lower probability of particle-gel attachment. While the high DSPE content, providing higher number of PEG chains, assures interfacial binding, decreasing the PEG content to 0.5 % eliminates strong interfacial attachment at high frequencies.

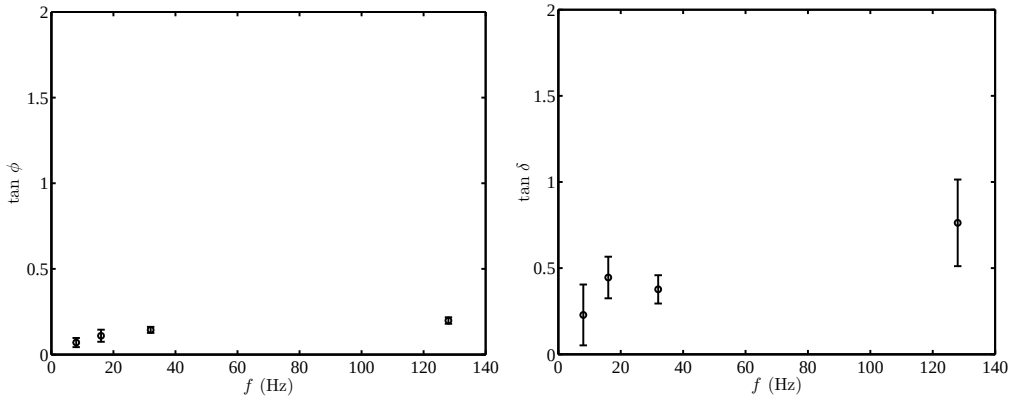

(a) DSPE (2.5 %)-coated silica microsphere on PA hydrogel B, $k_t \approx 8.2$ μN m^{-1}.

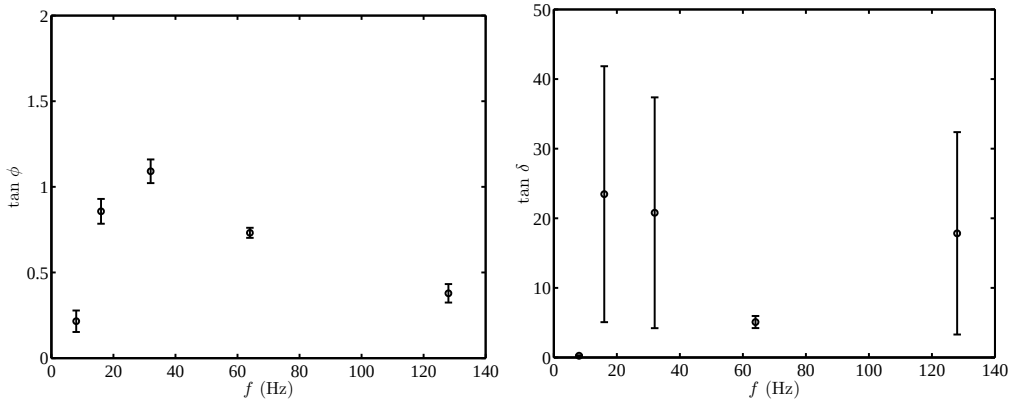

(b) DSPE (0.5 %)-coated silica microsphere on PA hydrogel B, $k_t \approx 8.8$ μN m^{-1}.

Figure 7.6.26: Phase lag of a DSPE (2.5 %)-coated (panel a) or a DSPE (0.5 %)-coated (panel b) silica microsphere probe response to an external sinusoidal shear $\tan\phi$ (left panel) and loss tangent $\tan\delta$ (right panel) versus drive frequency f, while the microsphere is placed on PA hydrogel B in TAE buffer, obtained from active interfacial microrheology at a low trap stiffness. All experimental parameters are the same as figure 7.6.23. The values are averaged over the sampling time, shown in figure 7.6.23. The phase lag and loss tangent for an high DSPE content are smaller than a low DSPE content, which suggests that the PEG chain concentration in the bilayer coating, acting as an adhesion agent, can control the adhesion properties. Compared to gel A (figure 7.6.26), DSPE (0.5 %)-coated particles can explore the viscous adhesion region, which brings about higher phase lag and loss tangent. Also, the phase lag and loss tangent in panel (a) are close to a bare silica microsphere (compare to figure 6.6.10b).

The effective transverse diffusion coefficient, furnished from the active interfacial microrheology with a DSPE-coated particle on gel B at a low trap stiffness, presented in figure 7.6.27, shows a linear dependency on the external drive frequency, similar to gel A. Decreasing the DSPE content increases the effective diffusion coefficient at a given frequency. Also, the diffusion coefficients are close to gel A, attaining values higher than a bare silica microsphere on gel B (figure 6.6.11). This suggests that the entangling PEG chains can control the effective interfacial diffusion coefficient of a microsphere on a PA gel, almost independent of the substrate stiffness (in the experimented stiffness range). The effective diffusion is, however, affected by the particle coating PEG content. Note that decreasing the PA stiffness (using gel C) resulted in no particle-hydrogel attachment, suggesting that soft enough interfaces can prevent grafted PEG chain-gel entanglement. Such an independency from the substrate stiffness is compatible with the passive interfacial microrheology diffusion coefficient (figure 7.6.6, left panel). Given that the effective diffusion coefficient depends on the local zero-shear viscosity, and that the dynamic viscosity is almost independent of the drive frequency (see figure 7.6.24, left panel), it can be concluded that (i) increasing the drive frequency decreases the contact area and weakens the elastic binding, and (ii) decreasing the DSPE content decreases the contact area, both resulting in an increase in D_x. The decrease in the contact area when increasing the drive frequency can be due to an increased rate of PEG chain-hydrogel bond breakage.

The loss and storage moduli are plotted versus the dimensionless Maxwell relaxation time $\omega\tau$ for a DSPE-coated microsphere on gel B in figure 7.6.28. At an high DSPE content (panel a), most of the data points fall within $\omega\tau \approx 1$, while decreasing the PEG chain concentration (panel b) results in $\omega\tau < 1$ at $f \geq 16$ Hz. The SLS model furnishes $\eta/(0.001\tau\mu_g \approx 0.51$ in panel (a), which is close to the bare silica microsphere on gel B (0.56, figure 7.6.28b). For a low DSPE content, providing viscous adhesion, the ESLS model furnishes $\eta/(0.001\mu_g\tau) \approx 0.04$ and $k_e \approx 0.02$, which are close to a bare silica microsphere on gel B: $\eta/(0.001\mu_g\tau) \approx 0.087$ and $k_e \approx 0.02$ at an high trap stiffness (figure 6.6.20). It should, however, be noted

that the fit is not as accurate as the case when both $\omega\tau > 1$ and $\omega\tau < 1$ data exist.

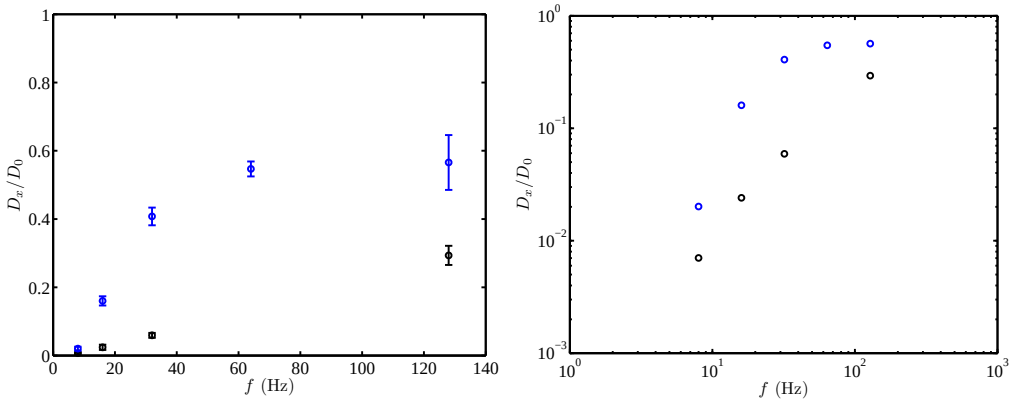

Figure 7.6.27: Effective interfacial transverse diffusion coefficient $D_x = 2\pi f k_B T \tan(\phi)/k_t$ versus drive frequency f, furnished from active microrheology with a DSPE (2.5 %)-coated (black symbols, $k_t \approx 8.2\ \mu\text{N m}^{-1}$) or a DSPE (0.5 %)-coated (blue symbols, $k_t \approx 8.8\ \mu\text{N m}^{-1}$) silica microsphere on PA hydrogel B. An higher DSPE content results in a slower effective interfacial diffusion. The effective diffusion coefficient at an high (low) DSPE content is slightly (significantly) greater than a bare silica microsphere on the same gel (figure 6.6.11). Also, compared to gel A (figure 7.6.20), the diffusion coefficient is greater on gel B at a given drive frequency and DSPE content. The right panel is a logarithmic presentation of the same data.

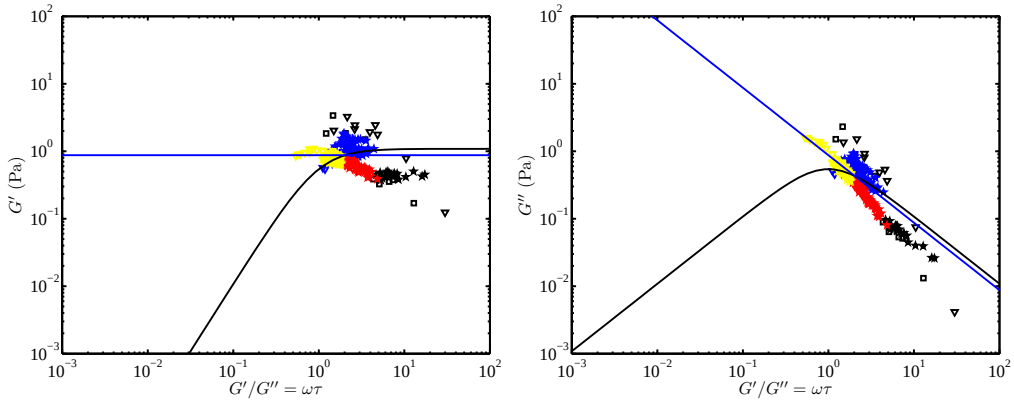

(a) DSPE (2.5 %)-coated silica microsphere on PA hydrogel B, $k_t \approx 8.2$ μN m^{-1}.

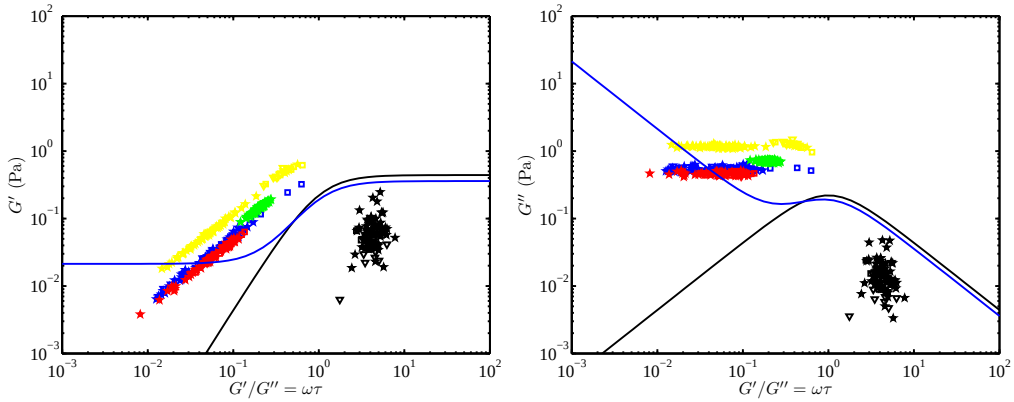

(b) DSPE (0.5 %)-coated silica microsphere on PA hydrogel B, $k_t \approx 8.8$ μN m^{-1}.

Figure 7.6.28: Storage (left panel) and loss (right panel) moduli versus dimensionless relaxation time $G'/G'' = \omega\tau$ with a simultaneous least-squares best fit to the standard linear solid (SLS, black line) and extended standard linear solid (ESLS, blue line) models for gel B, furnished from active interfacial microrheology with a DSPE (2.5 %)-coated (panel a, $k_t \approx 8.2$ μN m^{-1}) or DSPE (0.5 %)-coated (panel b, $k_t \approx 8.8$ μN m^{-1}) silica microsphere probe. Fit parameter η/τ in the SLS model: $G' = k_e + (\eta/\tau)\frac{(\omega\tau)^2}{1+(\omega\tau)^2}$ and $G'' = (\eta/\tau)\frac{\omega\tau}{1+(\omega\tau)^2}$ for panels (a) and (b) is 1.06 and 0.44, respectively, resulting in $\eta/(0.001\tau\mu_g) \approx 0.51$ and 0.21, and $\eta/\tau/(k_t/R) \approx 0.13$ and 0.05, respectively. For all cases, $k_e \approx 0$. The ESLS model, $G' = k_e + (\eta/\tau)\frac{(\omega\tau)^2}{1+(\omega\tau)^2}$ and $G'' = (\eta/\tau)\frac{\omega\tau}{1+(\omega\tau)^2} + k_e/(\omega\tau_e)$, furnishes much accurate fits. The ESLS model parameters (all in Pa) for panel (a), $\eta/\tau \approx 0, k_e \approx 0.87$, and panel (b), $\eta/\tau \approx 0.34, k_e \approx 0.02$, which bring about $(\eta/\tau)/(0.001\mu_g) \approx 0$ and 0.42 for panels (a) and (b), respectively. Normalizing the η/τ with the trap stiffness results in $\eta/\tau/(k_t/R) \approx 0.039$, a value close to a bare silica microsphere (figure 6.6.20). Lack of viscous coupling data in panel (a) prevents the fit from predicting small-$\omega\tau$ moduli. All experimental parameters are the same as figure 7.6.23.

The dissipation force per oscillation cycle of a DSPE-coated silica microsphere on PA gel B at a low trap stiffness is shown in figure 7.6.29. While a low DSEP content (right panel) results in similar F_d to a DOPC-coated particle (figure 7.6.14), an high DSPE content (left panel) results in slightly lower F_d at high frequencies, because the adhesion is less viscous than a DOPC-coated particle adhesion to PA gel. Large error bars show significant evolution in the interfacial loss modulus with time.

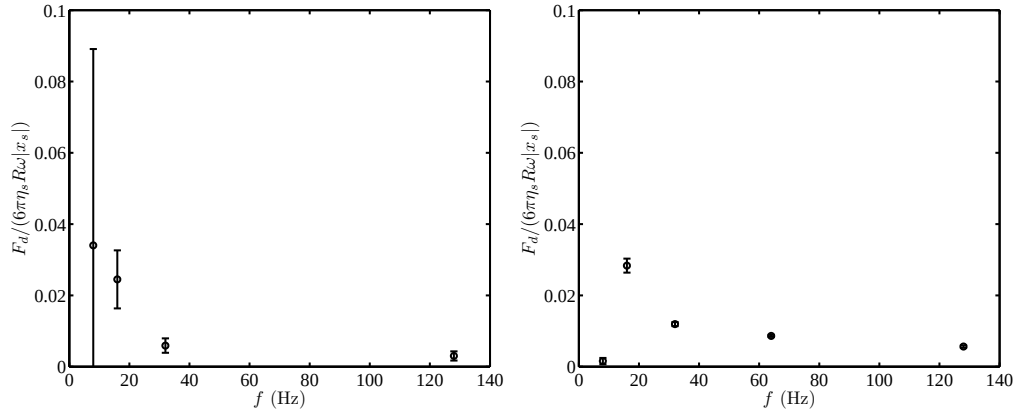

Figure 7.6.29: Dissipation force per cycle $F_d = \pi |x_s|^2 G''$, normalized with the Stokes drag force $6\pi\eta_s R\omega |x_s|$ versus drive frequency f, furnished from active interfacial microrheology with a DSPE (2.5 %)-coated (left panel, $k_t \approx 8.2$ μN m^{-1}) or a DSPE (0.5 %)-coated (right panel, $k_t \approx 8.8$ μN m^{-1}) silica microsphere on PA hydrogel B in TAE buffer. Regardless of the DSPE content in the bilayer coating, the dissipation force adopts values higher than (close to) a DOPC-coated particle (figure 7.6.14) at a low (high) frequency, which is comparable to a bare silica microsphere on gel B (figure 6.6.14, right panel a).

The effect of trap restoring force on the silica probe particle attachment to gels A and B at two DSPE coating concentrations are investigated. Cole-Cole plots for several combinations of DSPE concentration, gel stiffness, and trap stiffness are presented in figure 7.6.30. Regardless of the substrate stiffness and DSPE content, an high trap stiffness is able to shift the adhesion regime to the viscous coupling region. Decreasing the substrate stiffness and/or DSPE content, from left to right, increases the normalized loss modulus with the gel shear modulus (panel b) while the storage moduli remain comparably small. Contrarily, at a comparably high trap stiffness, a bare silica microsphere adheres elastically on PA gel A at low enough drive frequencies ($f \leq 32$ Hz), as shown in figure 6.6.15.

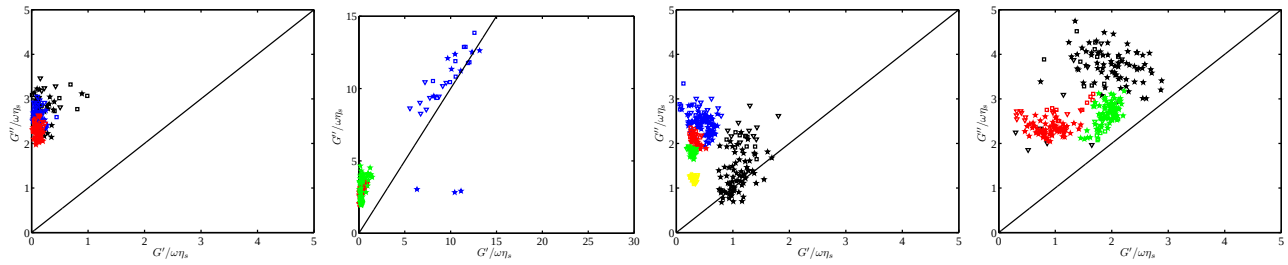

(a) Cole-Cole plots, normalized with $\omega\eta_s$: from left to right [DSPE %, gel, k_t (μN m^{-1})]: (2.5, A, 37), (0.5, A, 18), (2.5, B, 30), (0.5, B, 25).

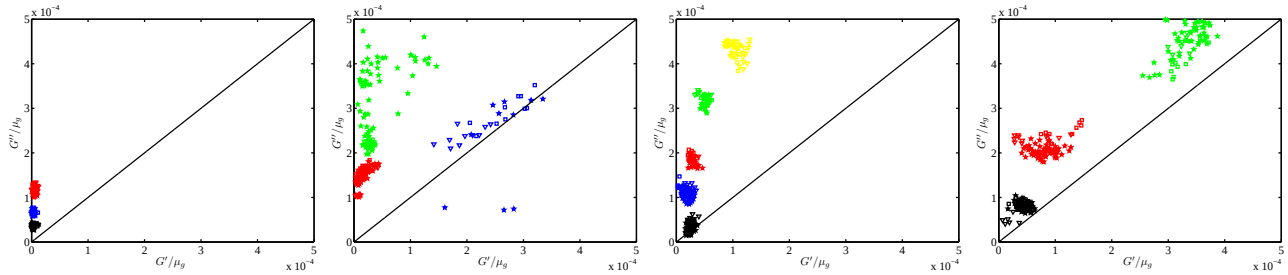

(b) Cole-Cole plots, normalized with μ_g: from left to right [DSPE %, gel, k_t (μN m^{-1})]: (2.5, A, 37), (0.5, A, 18), (2.5, B, 30), (0.5, B, 25).

Figure 7.6.30: Loss modulus G'' versus storage modulus G' (Cole-Cole plots) normalized with solvent viscosity ($\eta_s \approx 0.9$ cP, panel a) or bulk gel shear modulus μ_g (panel b) for a DSPE-coated silica microsphere on PA hydrogels A and B in TAE buffer (pH = 8.3, ionic strength 41 mmol l^{-1}), furnished from active interfacial microrheology with an high trap stiffness. The boundary for the viscous ($G'' > G'$)-to-elastic ($G' > G''$) transition (*i.e.*, $G'' = G'$) is presented with the solid line. The stage (and consequently the probe particle) is subject to a small-amplitude ($|x_s| \approx 30$ nm, see table 6.1) sinusoidal displacement with an oscillatory shear frequency $f \approx 8$ Hz (black symbols), 16 Hz (blue symbols), 32 Hz (red symbols), 64 Hz (green symbols), and 128 Hz (yellow symbols), shown with triangles ($t \leq 180$ s), squares ($180 < t \leq 360$ s), and pentagons ($t > 360$ s). At such an high restoring force exerted on the probe particle, the adhesion resides in the viscous coupling region, regardless of the DSPE content and gel stiffness. This suggests that a DSPE-coated microsphere undergoes weaker elastic adhesion to a PA hydrogel, compared to a bare silica particle (figure 6.6.15). Interestingly, the interfacial storage modulus remains within the same range for all the cases when it is normalized with the bulk gel shear modulus.

The dynamic and out-of-phase viscosity of gels A and B, furnished with a DSPE-coated silica microsphere at an high trap stiffness (shown in figure 7.6.31) suggests that regardless of the substrate stiffness, DSPE content, and drive frequency, $\eta'/\eta_s \approx 2$ while the out-of-phase viscosity fluctuates around small values due to low interfacial storage moduli. This

shows that the interfacial attachment between the grafted PEG chains on the particle and the PA chains on the gel can be attenuated by increasing the external force on the particle or decreasing the number of sticky moieties on the particle (by decreasing the DSPE content) or gel (by decreasing the crosslinking density).

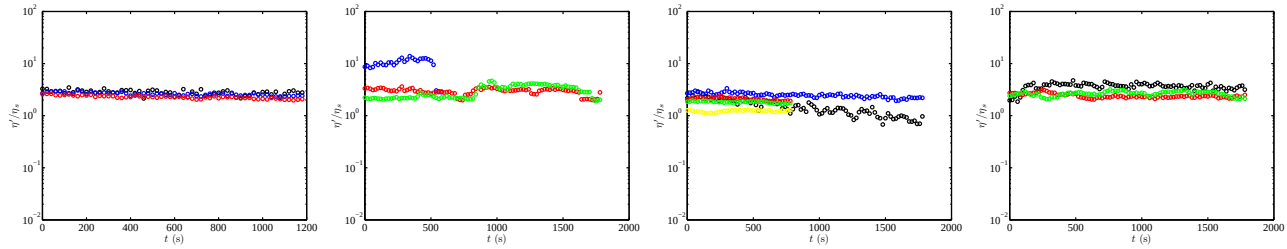

(a) Dynamic viscosity, from left to right [DSPE %, gel, k_t (μN m^{-1})]: (2.5, A, 37), (0.5, A, 18), (2.5, B, 30), (0.5, B, 25).

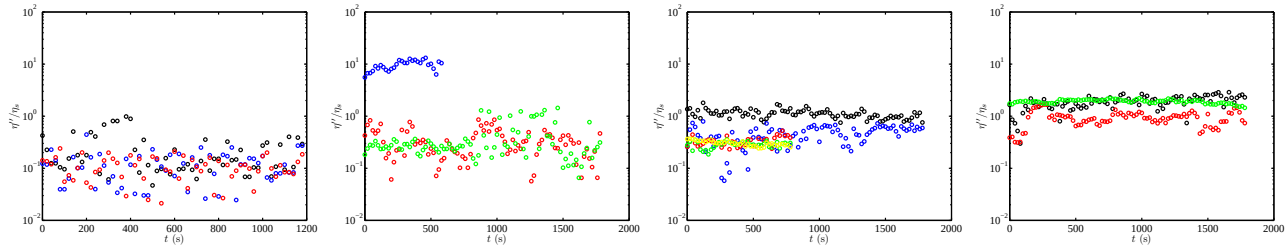

(b) Out-of-phase viscosity, from left to right [DSPE %, gel, k_t (μN m^{-1})]: (2.5, A, 37), (0.5, A, 18), (2.5, B, 30), (0.5, B, 25).

Figure 7.6.31: Interfacial dynamic viscosity $\eta' = G''/\omega$ (panel a) and out-of-phase viscosity $\eta'' = G'/\omega$ (panel b) versus time t for a DSPE-coated silica microsphere on PA hydrogels A and B in TAE buffer (pH = 8.3, ionic strength 41 mmol l^{-1}), furnished from active interfacial microrheology at an high trap stiffness. All experimental parameters are the same as figure 7.6.30. The oscillatory shear frequency $f \approx 8$ Hz (black symbols), 16 Hz (blue symbols), 32 Hz (red symbols), 64 Hz (green symbols), and 128 Hz (yellow symbols). Regardless of the drive frequency, DSPE content, and gel stiffness, the interfacial dynamic viscosity are close to each other, adopting similar values to water viscosity near a plane wall. The out-of-phase viscosity does not follow any significant frequency dependency, contrarily to the low trap stiffness (figure 7.6.17 and 7.6.24a). Compared to a bare silica microsphere, the behavior, here, is similar to the viscous coupling to hydrogel B at an high trap stiffness (figure 6.6.16b).

The zero-shear viscosity of gels A (panel a) and B (panel b), furnished from active interfacial microrheology with a DSPE-coated silica microsphere are presented in figure 7.6.32. At such an high trap stiffness, the zero-shear viscosity reflects values close to water viscosity, regardless of the substrate stiffness, gel stiffness, and drive frequency. This is because, in contrast to a low trap stiffness (*e.g.*, figure 7.6.18) where the particle can firmly stick to the gel, the high restoring force at high k_t decreases the number of particle adhesion bonds with the gel, resulting in low G'.

The phase lag of DSPE-coated particles on gels A and B at an high trap stiffness (shown in figure 7.6.33a) behaves similar to an optically trapped particle in an unbound fluid; however, the values depend on the trap stiffness and drive frequency, as discussed before. Such behavior is similar to a DOPC-coated silica microsphere on PA gels (figure 7.6.11), and a bare silica microsphere on gel B at an high trap stiffness (figure 6.6.18b). The loss tangent (shown in figure 7.6.33b) adopt similarly high values, independent of the gel stiffness and DSPE content, reflecting the ratio of solvent loss modulus to the trap elastic contribution.

The effective interfacial transverse diffusion coefficient of a DSPE-coated silica particle on PA gels A and B at an high trap stiffness, calculated from the phase lag, are presented in figure 7.6.34. At such an high trap stiffness, regardless of the DSPE content and gel stiffness, the diffusion coefficients D_x/D_0 are mostly higher than 0.2, suggesting that an high optical force can eventually decrease the particle-gel contact and zero-shear viscosity given that the interfacial dynamic viscosity remains almost constant (see figure 7.6.31).

The storage (panel a) and loss (panel b) moduli versus $\omega\tau$ are shown in figure 7.6.35. Small storage moduli, furnished at an high trap stiffness results in $\omega\tau < 1$ (viscous coupling) for almost all of the combinations of DSPE content, gel stiffness, and drive frequency. The ESLS model parameter η/τ in this case is higher than the low trap stiffness case (figure 7.6.32); however, the fits are not accurate enough, because most of the data are scattered at $\omega\tau \lesssim 1$. The relaxation time τ and zero-shear viscosity of a non-sticking inclusion (high k_t) are, generally, lower than a sticking (low k_t) case.

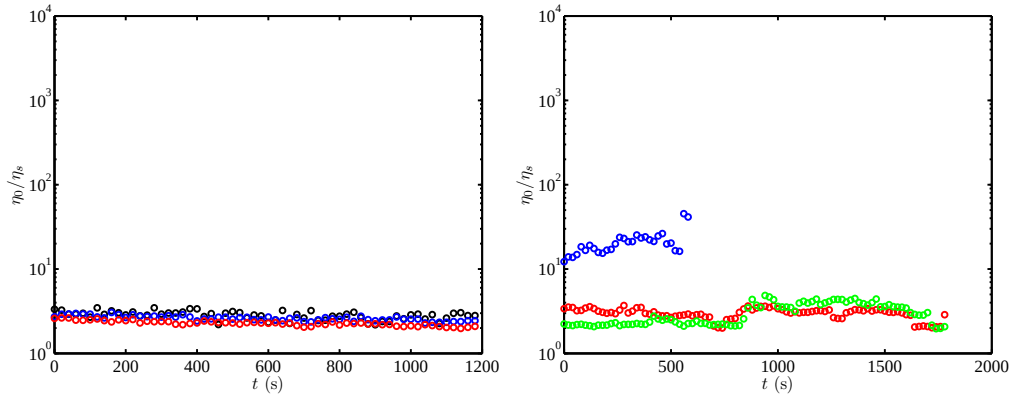

(a) [DSPE %, gel, k_t (μN m^{-1})]: (2.5, A, 37), (0.5, A, 18).

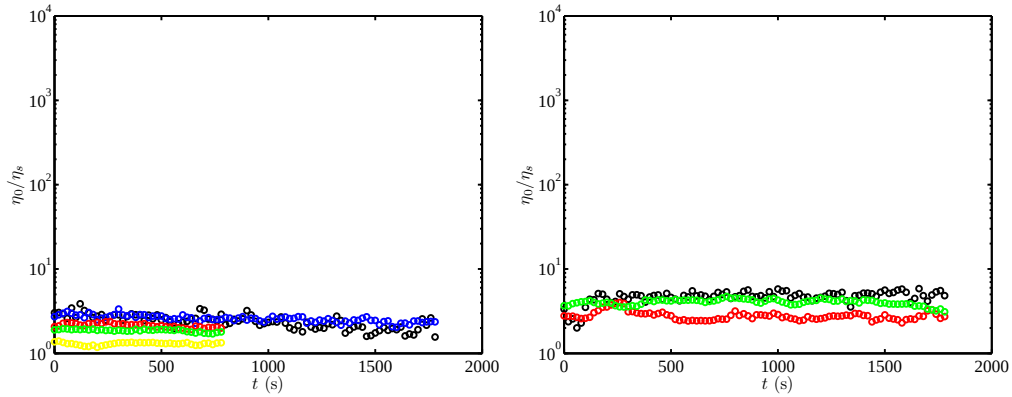

(b) [DSPE %, gel, k_t (μN m^{-1})]: (2.5, B, 30), (0.5, B, 25).

Figure 7.6.32: Interfacial zero-shear viscosity $\eta_0 = \eta' \left[1 + (G'/G'')^2\right]$ versus time t, furnished from active interfacial microrheology with a DSPE-coated silica microsphere on PA hydrogels A (panel a) and B (panel b). Similar to the dynamic viscosity (figure 7.6.31a), independent of the DSPE content, gel stiffness, and drive frequency, the zero-shear viscosity reflects water viscosity close to a plane wall due to small interfacial storage moduli. This is similar to a bare silica particle behavior on PA hydrogel B at an high trap stiffness, where the microsphere undergoes viscous coupling to the gel (figure 6.6.17, right panel).

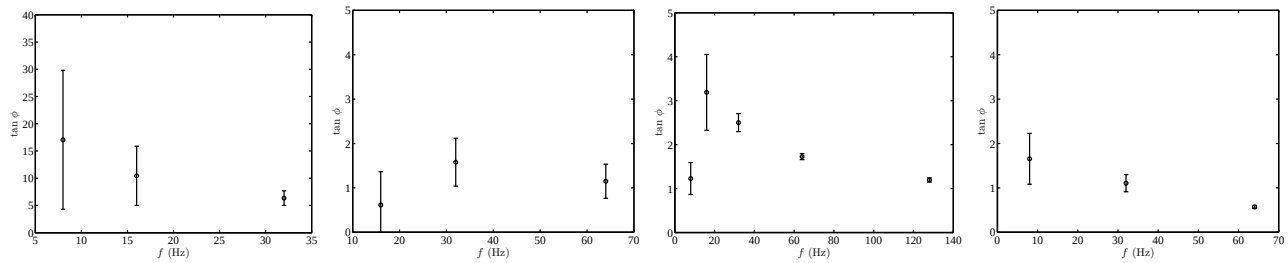

(a) Phase lag, from left to right [DSPE %, gel, k_t (μN m^{-1})]: (2.5, A, 37), (0.5, A, 18), (2.5, B, 30), (0.5, B, 25).

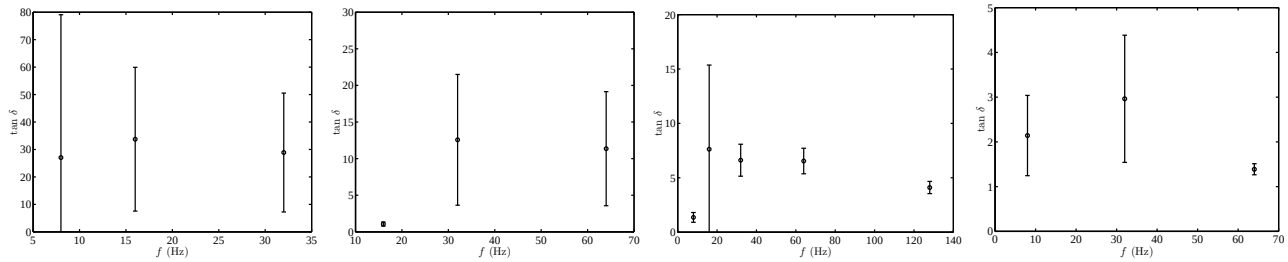

(b) Loss tangent, from left to right [DSPE %, gel, k_t (μN m^{-1})]: (2.5, A, 37), (0.5, A, 18), (2.5, B, 30), (0.5, B, 25).

Figure 7.6.33: Phase lag of a DSPE-coated silica microsphere probe response to an external sinusoidal shear $\tan\phi$ (panel a) and loss tangent $\tan\delta$ (panel b) versus drive frequency f, while the microsphere is placed on PA hydrogels A and B in TAE buffer, obtained from active interfacial microrheology at an high trap stiffness. All experimental parameters are the same as figure 7.6.30. The values are averaged over the sampling time, shown in figure 7.6.30. The phase lag and loss tangent adopt high values compared to the elastic adhesion of a DSPE-coated particle on PA gels at a low trap stiffness (figure 7.6.19 and 7.6.26), suggesting a weaker interaction between the substrate and the particle. The phase lag decrease when increasing the frequency is compatible with the behavior of a probe particle in an unbound solvent, as discussed in figure 7.6.11. Also, the phase lag and loss tangent are greater than (comparable to) bare silica microsphere elastic adhesion to gel A (viscous coupling to gel B) at an high trap stiffness (compared to figure 6.6.18).

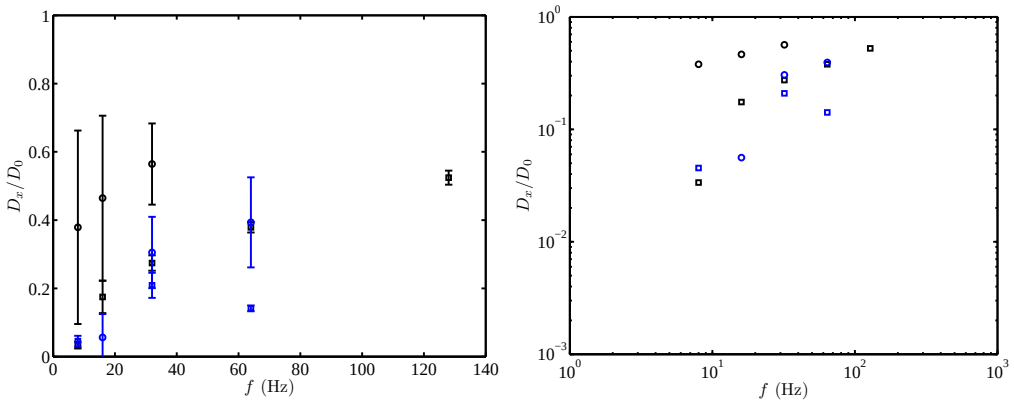

Figure 7.6.34: Effective interfacial transverse diffusion coefficient $D_x = 2\pi f k_B T \tan(\phi)/k_t$ versus drive frequency f, furnished from active microrheology with a DSPE-coated silica microsphere on PA hydrogels A and B: [DSPE %, gel, k_t (μN m^{-1})]: (2.5, A, 37), shown with black circles, (0.5, A, 18), shown with blue circles, (2.5, B, 30), shown with black squares, and (0.5, B, 25), shown with blue squares. At such high trap stiffnesses, the effective interfacial diffusion coefficient of DSPE-coated microspheres are mostly close to a DOPC-coated microsphere (figure 7.6.12), suggesting that the grafted PEG chain interaction with the PA gel substrate is not significant. The right panel is a logarithmic presentation of the same data.

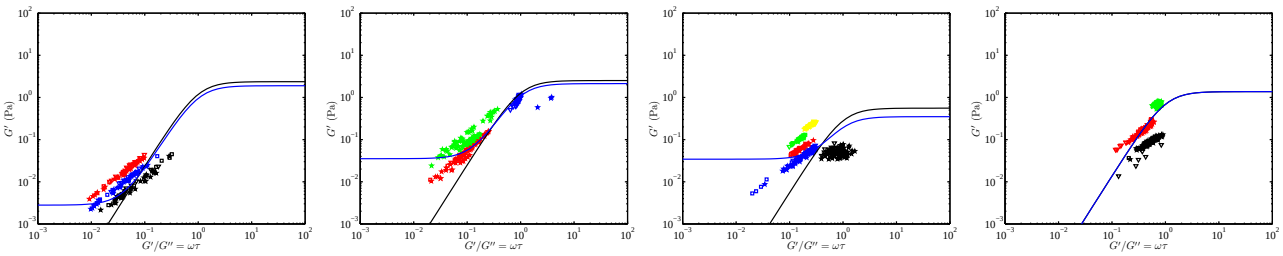

(a) G' versus $\omega\tau$, from left to right [DSPE %, gel, k_t (μN m^{-1})]: (2.5, A, 37), (0.5, A, 18), (2.5, B, 30), (0.5, B, 25).

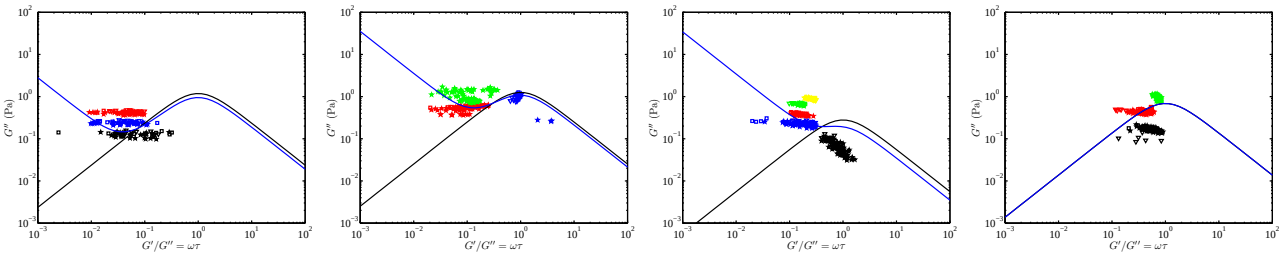

(b) G'' versus $\omega\tau$, from left to right [DSPE %, gel, k_t (μN m^{-1})]: (2.5, A, 37), (0.5, A, 18), (2.5, B, 30), (0.5, B, 25).

Figure 7.6.35: Storage (panel a) and loss (panel b) moduli versus dimensionless relaxation time $G'/G'' = \omega\tau$ with a simultaneous least-squares best fit to the standard linear solid (SLS, black line) and extended standard linear solid (ESLS, blue line) models for gels A and B, furnished from active interfacial microrheology with a DSPE-coated silica microsphere probe at an high trap stiffness. Fit parameter η/τ in the SLS model: $G' = k_e + (\eta/\tau)\frac{(\omega\tau)^2}{1+(\omega\tau)^2}$ and $G'' = (\eta/\tau)\frac{\omega\tau}{1+(\omega\tau)^2}$ from left to right is 2.36, 2.51, 0.56, and 1.37, respectively, resulting in $\eta/(0.001\tau\mu_g) \approx 0.66$, 0.7, 0.27, and 0.66, and $\eta/\tau/(k_t/R) \approx 0.06$, 0.14, 0.02, and 0.05, respectively. For all cases, $k_e \approx 0$. The ESLS model, $G' = k_e + (\eta/\tau)\frac{(\omega\tau)^2}{1+(\omega\tau)^2}$ and $G'' = (\eta/\tau)\frac{\omega\tau}{1+(\omega\tau)^2} + k_e/(\omega\tau_e)$, furnishes much accurate fits. The ESLS model parameters (all in Pa) from left to right, $\eta/\tau \approx 1.89$, 2.09, 0.32, and 1.37, and $k_e \approx 0.0028$, 0.0353, 0.0343, and 0, which bring about $(\eta/\tau)/(0.001\mu_g) \approx 0.53$, 0.58, 0.15, and 0.66 from left to right, respectively. Normalizing the η/τ with the trap stiffness results in $\eta/\tau/(k_t/R) \approx 0.05$, 0.12, 0.01, and 0.05. Lack of elastic coupling data prevents the fit from predicting large-$\omega\tau$ moduli. All experimental parameters are the same as figure 7.6.30.

The dissipation force per oscillation cycle of a DSPE-coated particle on PA gels A (panel a) and B (panel b) at high trap stiffnesses, shown in figure 7.6.36, is comparable to a DOPC-coated particle (figure 7.6.14) due to a similar viscous coupling to a PA gel. Note that F_d is normalized with the maximum oscillatory drag force on the particle.

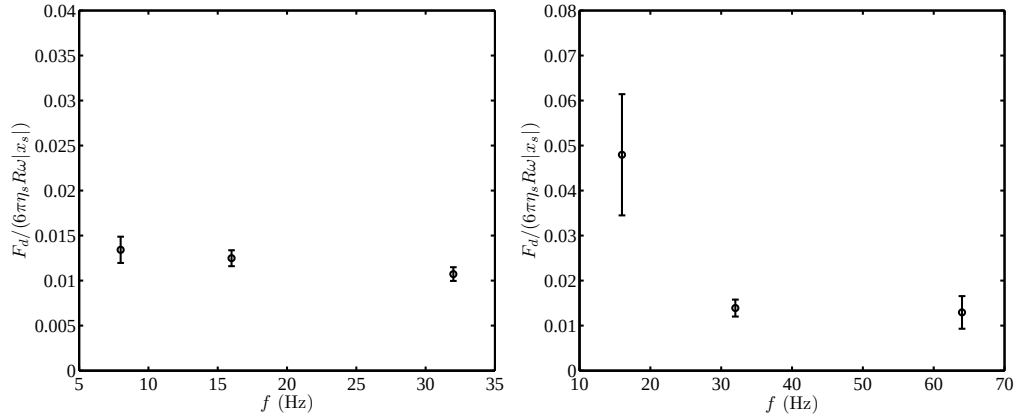

(a) [DSPE %, gel, k_t (μN m^{-1})]: (2.5, A, 37), (0.5, A, 18).

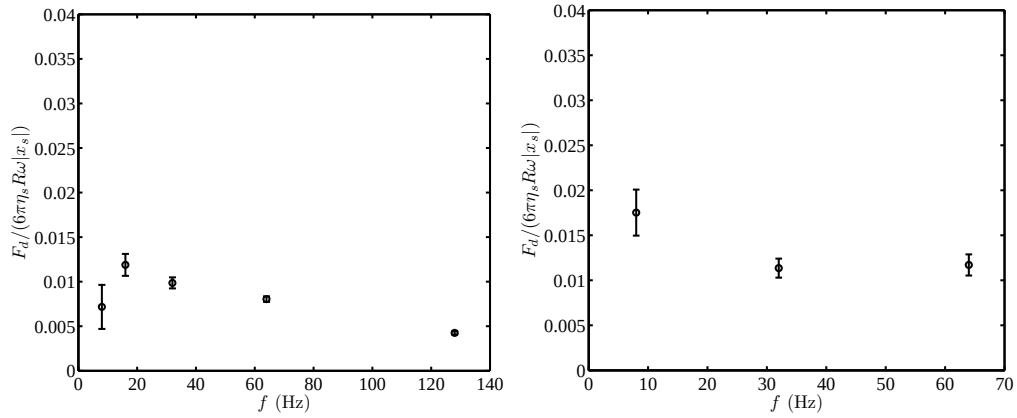

(b) [DSPE %, gel, k_t (μN m^{-1})]: (2.5, B, 30), (0.5, B, 25).

Figure 7.6.36: Dissipation force per cycle $F_d = \pi |x_s|^2 G''$, normalized with the Stokes drag force $6\pi\eta_s R\omega |x_s|$ versus drive frequency f, furnished from active interfacial microrheology with a DSPE-coated silica microsphere on PA hydrogels A and B in TAE buffer. Regardless of the drive frequency, gel stiffness, and DSPE content in the bilayer coating, the dissipation force at such an high trap stiffness adopts values close to a DOPC-coated particle (figure 7.6.14).

The interfacial adhesion phase diagram of a DSPE-coated silica microsphere and a PA gel is constructed from the Cole-Cole plots and presented in figure 7.6.37. When the drive

frequency and optical stiffness is low, the DSPE-coated particle adheres elastically ($G' > G''$) to the PA gels (shown with circles); however, by increasing the shear rate and/or restoring force, the interfacial coupling tends to become viscosity dominated ($G'' > G'$, shown with squares). Shifting the adhesion energy minima of a DSPE-coated particle on PA gels is easier than a bare silica microsphere due to the lower DSPE-PA interfacial energy.

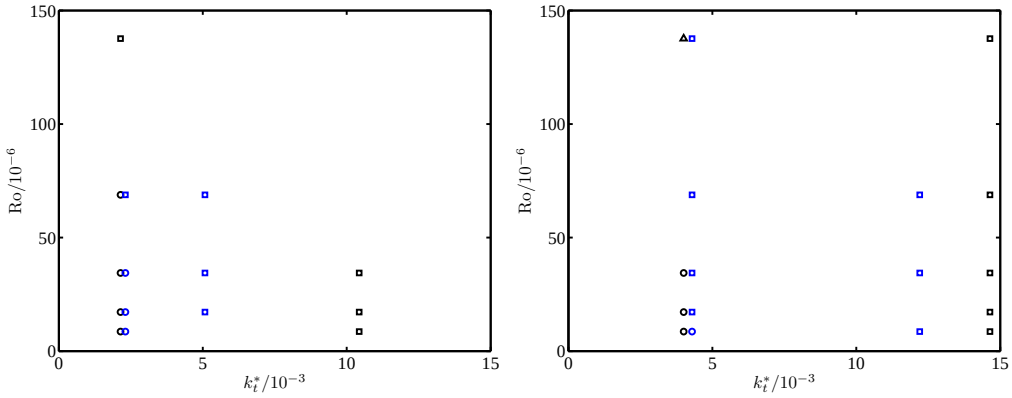

Figure 7.6.37: Interfacial adhesion phase diagram, furnished from active interfacial microrheology with a DSPE-coated silica microsphere on PA hydrogels A (left panel) and B (right panel), constructed from the Cole-Cole plots, presented in terms of Roshko number $\mathrm{Ro} = fR^2\rho_s/\eta_s$ and dimensionless optical trap stiffness $k_t^* = k_t/(R\mu_g)$. Black and blue symbols correspond to DSPE (2.5 %) and DSPE (0.5 %), respectively. Circles, triangles, and squares show elastic adhesion, aging, and viscous coupling, respectively. On a PA gel, low trap stiffness and drive frequency result in elastic adhesion, regardless of the DSPE content. Compared to a bare silica particle on PA gel (figure 6.6.22), lower restoring force and/or drive frequency is required to shift the interfacial coupling from elastic to viscous.

7.7 Conclusions

A strongly sticking bare silica microsphere to a PA hydrogel is successfully modified by coating the particle with lipid bilayers (DOPC), forming a biomimetic silica microsphere, to eliminate adhesion energy minima, resulting in a non-adhesive interfacial inclusion. Passive and active microrheology, using silica microsphere-supported lipid bilayers (SLBs), proved that there exists no significant adhesion affinity to a PA gel. Accordingly, silica-SLBs are used as a sensor to probe the possible interaction between the embedded species in the bilayer

and the soft gel. The DOPC bilayers were doped with polyethylene glycol (PEG2k)-grafted lipid bilayers (known as DSPE lipopolymer) to study the interfacial interaction of grafted polymers and PA hydrogels at a controlled substrate stiffness. A similar ζ-potential of DOPC and DSPE-coated particles proves that the strong attraction between DSPE-coated particles and a PA gel is mainly due to the van der Waals forces. Passive interfacial microrheology shows that there is a remarkable adhesion affinity between PEG chains and a PA gel even at as low DSPE concentration as 0.5 mol % in the DOPC coating; however, the adhesion energy is almost three times lower than a bare silica particle on a PA gel. Active interfacial microrheology furnished frequency-dependent viscoelastic moduli, suggesting tunable interfacial properties. The adhesion energy minima can be shifted to modify an elastic adhesion to a viscous coupling by increasing the drive frequency and trap stiffness, and decreasing the DSPE content and bulk gel stiffness. Hinging on the Cole-Cole plots, the interfacial adhesion maps for silica microsphere-SLBs on PA hydrogels are constructed. Such probe particles can be used to measure isolated interfacial forces between grafted moieties at a single-particle level. Accordingly, lipopolymer-doped lipid bilayers can be used as biocompatible, ready-to-fuse candidates to adhere soft and non-sticky materials, such as tissues.

Appendix

7.A Non-adhesive behavior of a DOPC-coated silica microsphere in PA hydrogel vicinity

It was previously shown in this chapter that by coating a bare silica microsphere with zwitterionic DOPC lipid bilayers, the interfacial attraction to a PA gel vanishes. Such a silica-SLB is, therefore, a decent sensor to probe the viscoelastic properties of the solvent in gel contact proximity. In this section, active microrheology experiments using a silica-SLB probe are conducted, and the particle behavior is tracked when approaching the gel ($z > 0$) and while placed on the gel ($z = 0$ and $t \geq 0$).

Figure 7.A.1 presents the phase lag (left panel) and the corresponding effective interfacial transverse diffusion coefficient (right panel) of a DOPC-coated silica microsphere versus particle height (when elevated) and time (while placed on gel). As evidenced by this figure, decreasing the particle-gel gap, decreases the phase lag and diffusion coefficient as predicted by the hydrodynamic theories; however, the phase lag values are dependent on the trap stiffness: the higher the trap stiffness, the lower the phase lag at a given particle height. Once the particle touches the PA gel, the phase lag and diffusion coefficient remain constant and comparable to the bulk values, suggesting that there exist no significant interfacial entanglement and elastic contribution to the inclusion at any external drive frequency. The gel stiffness (high) and trap stiffness (low) are chosen in a way that maximum interfacial interaction is expected.

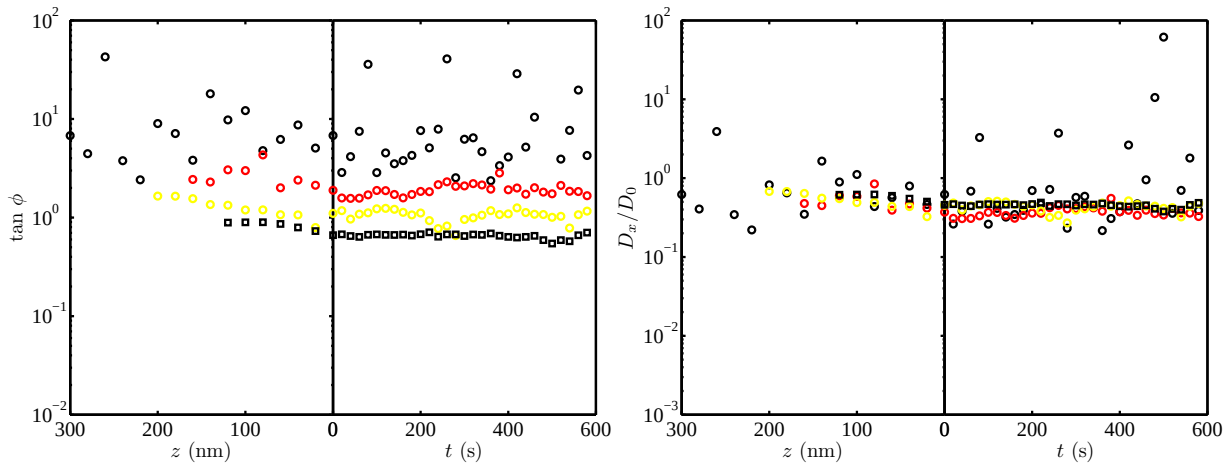

Figure 7.A.1: Examples of viscous coupling of a DOPC-coated silica microsphere and a PA gel film in terms of the phase lag (left panel) and effective transverse diffusion coefficient (right panel). An optically trapped bare silica microsphere (at a low trap stiffness $k_t \approx 8.7$ μN m^{-1} and $f = 8$ Hz: black circles, $f = 16$ Hz: red circles, $f = 32$ Hz: yellow circles, and $f = 64$ Hz: black squares) is brought in contact with PA gel A film, and the phase lag is furnished when approaching ($z > 0$) and while attached ($t > 0$) to the substrate. The microsphere response to an external oscillatory shear (with a specified drive frequency f) is recorded when it is brought to the hydrogel vicinity in 20 nm increments using a 3D nano-positioning stage, coupled with a feed-back control system. Upon touching the substrate, the stage height is fixed, and the particle response is acquired in terms of phase lag and amplitude via the phase-sensitive measurements. The solution comprised TAE buffer (pH $\approx$ 8.3, ionic strength 41 mmol l^{-1}). Regardless of the drive frequency, the behavior at $z > 0$ is similar to $t > 0$, suggesting non-adhesive behavior of DOPC-coated silica microspehres on the PA gel. An increased hydrodynamic drag on the microsphere, arising from the gel-electrolyte interface, reduces the diffusion coefficient (and phase lag), compared to the bulk values.

If the optically trapped particle is in a pure elastic (viscous) medium, the position response to an external oscillatory shear will be completely in-phase (out-of-phase) with the drive, resulting in two extremes, namely $\mathrm{Im}(x_p) = 0$ ($\mathrm{Re}(x_p) = 0$). Figure 7.A.2 illustrates the real and imaginary parts of the particle response to external oscillatory drives. As expected, for a DOPC-coated particle in an unbound fluid, the response real (left panel) and imaginary (right panel) parts remain unchanged after touching the gel, suggesting no significant elastic and viscous coupling.

The interfacial storage and loss moduli, furnished from the active interfacial microrheology with a silica-SLB probe is presented in figure 7.A.3. While the viscoelastic properties

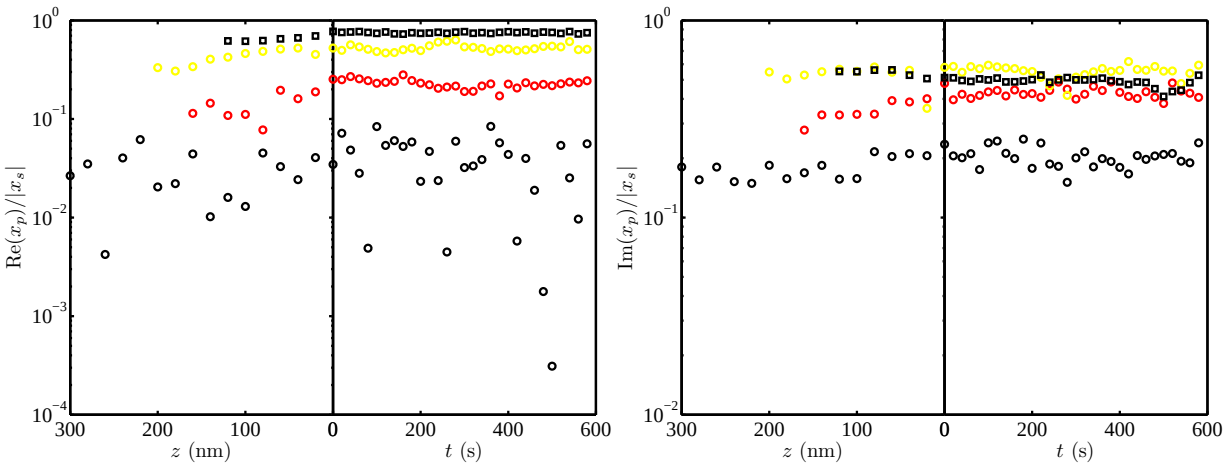

Figure 7.A.2: Examples of viscous coupling of a DOPC-coated silica microsphere to a PA gel film in terms of the (left panel) real (in-phase) and (right panel) imaginary (out-of-phase) parts of the position response to an external oscillatory shear, normalized with the stage small-amplitude sinusoidal input ($|x_s| \approx 30$ nm, see Table 6.1). The color legend is the same as figure 7.A.1. As soon as the particle contacts the hydrogel, independent of the drive frequency, the real and imaginary responses attain values similar to the bulk.

remain unchanged before and after touching the gel interface, the loss modulus (originated from the fluid) at a given frequency is remarkably larger than the storage modulus (originated from the trap), showing a viscosity-dominant coupling. The viscoelastic properties are also plotted versus the dimensionless relaxation time (figure 7.A.4), which clearly show that regardless of the drive frequency, $\omega\tau < 1$ or $G'' > G'$. The same results are observed for softer PA gels (results are not shown here).

The dynamic and out-of-phase viscosity are obtained from the viscoelastic moduli, which are presented in figure 7.A.5. At all drive frequencies, the dynamic viscosity (left panel), probed near a PA gel, is close to water viscosity, while the out-of-phase viscosity (right panel) remain frequency-independent and low. Interestingly, this suggests that the gel interface has no significant effect on the viscosity of neighboring fluid.

The zero-shear viscosity (left panel) and relaxation time (right panel) of a DOPC-PA gel inclusion are presented in figure 7.A.6. As expected, the zero-shear viscosity adopts values close to the dynamic viscosity of water near a plane wall at all frequencies when the

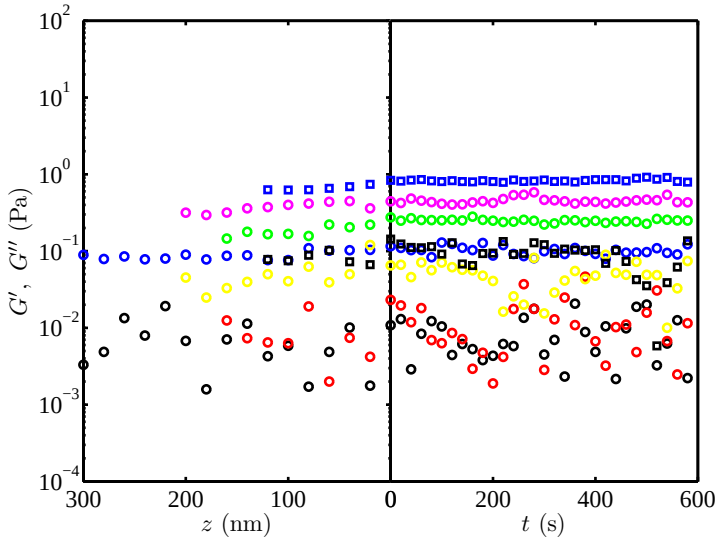

Figure 7.A.3: Examples of viscous coupling of a DOPC-coated silica microsphere and a PA gel film in terms of the interfacial storage G' (shown with black circles: $f = 8$ Hz, red symbols: $f = 16$ Hz, yellow symbols: $f = 32$ Hz, and black squares: $f = 64$ Hz) and loss G'' (shown with blue circles: $f = 8$ Hz, green symbols: $f = 16$ Hz, magenta symbols: $f = 32$ Hz, and blue squares: $f = 64$ Hz) moduli, furnished from active interfacial microrheology. The experimental parameters are the same as figure 7.A.1. The viscoelastic properties of a coupled DOPC-coated silica microsphere to the gel ($t > 0$) remains similar to those when coupled to the bulk environment (*i.e.*, electrolyte and optical trap, $z \geq 0$), suggesting no significant interaction between the soft substrate and the coated particle.

particle touches the gel. This is because the storage modulus is small, compared to the loss modulus, resulting in $\eta_0 \approx \eta'$. The relaxation time (right panel) is corresponding to the fluid environment ($\lesssim 1$ ms). Such a small relaxation time is a result of a small storage modulus, arising from the trap, and a relatively large loss modulus from the solvent.

7.B Electrokinetic and electrophoretic characterization

Prior to characterizing the colloidal interaction with the gel through the DLVO (Derjaguin-Landau-Verwey-Overbeek) interaction analysis, their surface potential is required to be measured. Microsphere ζ-potential is measured through the particle electrophoretic mobility, using a Zetasizer Nano ZS (Malvern Instruments, UK) instrument. Dynamic light scattering (DLS) technique is employed to acquire particle size, using the same instrument to investi-

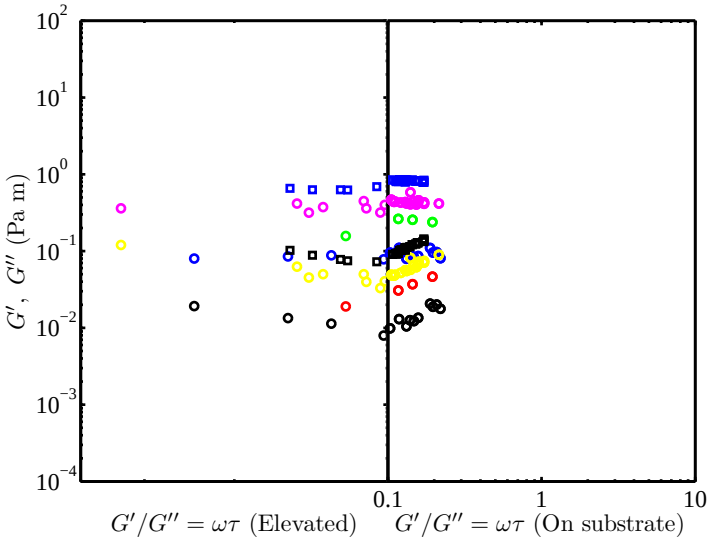

Figure 7.A.4: Examples of viscous coupling of a DOPC-coated silica microsphere and a PA gel film in terms of storage G' and loss G'' moduli versus the dimensionless Maxwell relaxation time $G'/G'' = \omega\tau$, furnished from active interfacial microrheology. Color legend is the same as figure 7.A.3. As expected, all the data fall in $\omega\tau < 1$ region, reflecting viscous (non-stuck, $G'' > G'$) coupling.

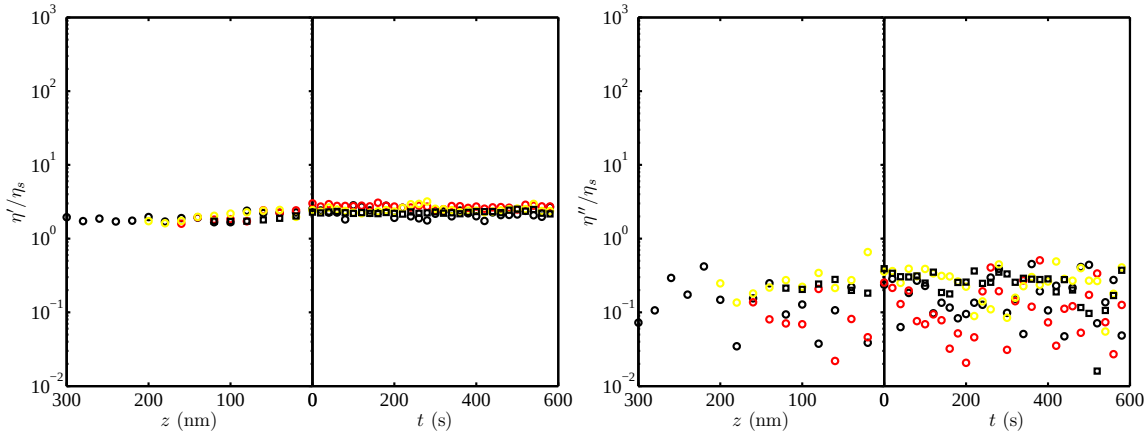

Figure 7.A.5: Examples of viscous coupling of a DOPC-coated silica microsphere and a PA gel film in terms of dynamic viscosity $\eta' = G''/\omega$ (left panel) and out-of-phase $\eta'' = G'/\omega$ (right panel) viscosity, furnished from active interfacial microrheology. The interfacial dynamic viscosity is similar to the solvent viscosity, accounting for the effective particle size near a plane wall ($\eta'/\eta_s \approx 2$) for an elevated particle ($100 \geq z \geq 0$) and when touching the gel ($t > 0$), which proves that there is no significant adhesion between the DOPC-coated particles and the PA gel. The out-of-phase viscosity for a particle on the gel remains comparable to an elevated particle, fluctuating $0.5 \leq \eta''/\eta_s \leq 0.05$ with no frequency dependency. The color legend is the same as figure 7.A.1.

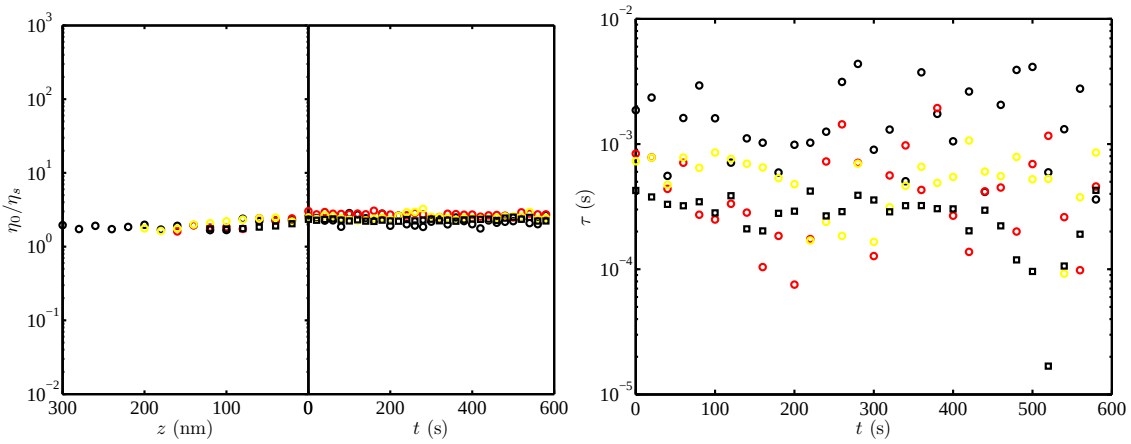

Figure 7.A.6: Examples of viscous coupling of a DOPC-coated silica microsphere and a PA gel film in terms of the zero-shear viscosity $\eta_0 = \eta' \left[1 + (\omega\tau)^2\right]$ (left panel) and Maxwell relaxation time $\tau = G'/(G''\omega)$ (right panel), furnished from active interfacial microrheology. The zero-shear viscosity attains values similar to the out-of-phase viscosity (figure 7.A.5, left panel) for both an elevated particle and a particle residing on the gel, guaranteeing no significant adhesion between a DOPC-coated particle and the PA gel. The Maxwell relaxation time is independent of the drive frequency (in contrast to a sticking transition, see figure 6.6.6), which fluctuates around $\tau \approx 1$ ms.

gate the effect of possible aggregation on the measured zeta potential. Results, presented in Table 7.B.1, elucidate that, as expected, by coating silica microspheres with DOPC bilayers, their ζ-potential decreases approximately 20 mV and reaches to about -30 mV. By doping DOPC with negatively-charged DSPE-PEG2k, the ζ-potential slightly increases to ≈ -40 mV for DSPE-PEG2k/DOPC (0.5 mol %)-coated silica microspheres. The lower surface coverage (0.5 mol %) resulted in a slightly higher mobility than the higher coverage (2.5 mol %), which is most probably because of an increased drag on the particle at an higher surface coverage. This can be the reason of the relatively similar passive binding stiffness of these particles onto the gels (see figures 7.6.3 and 7.6.5), although the 2.5 % coating has 5 times higher number of interacting polymer chains than the 0.5 % one. It is very important to note that the particle coating process, which takes place in an high ionic strength medium, involves particle aggregation. To prevent any possible damage to a bilayer coating around a particle, all the tests are conducted without any sonication. This is the reason that the DLS hydrodynamic size is greater than a single particle; however, here, by conducting

experiments on various aggregation sizes in the suspension, it is shown that there exists no significant effect of the aggregation size on the measured ζ-potential (see, for example, DOPC samples in Table 7.B.1). Theoretically, this is expected at large particle radius-to-diffuse layer thickness κR, where κ is the reciprocal Debye length. Therefore, the acquired ζ-potential can be safely employed to interpret the single particle interfacial microrheology experiments.

Table 7.B.1: Zeta-potential ζ, electrophoretic mobility μ_e, and DLS diameter $2R$ of coated silica microspheres ($2R \approx 1.97$ μm, from the supplier) in TAE buffer (pH ≈ 8.3 and ionic strength 41 mmol l^{-1}) at an ambient temperature.

Coating	ζ (mV)	μ_e (μm cm V^{-1} s^{-1})	$2R$ (μm)
Bare	-51.70 ± 0.75	-3.90 ± 0.06	1.90 ± 0.10
DOPC-sample # 1	-30.20 ± 0.66	-2.28 ± 0.05	1.94 ± 0.33
DOPC-sample # 2	-31.88 ± 1.12	-2.40 ± 0.08	5.05 ± 1.23
DSPE-PEG2k/DOPC (0.5 mol %) # 1	-39.96 ± 0.86	-3.01 ± 0.07	3.24 ± 0.44
DSPE-PEG2k/DOPC (0.5 mol %) # 2	-40.38 ± 0.77	-3.04 ± 0.06	4.31 ± 0.42
DSPE-PEG2k/DOPC (2.5 mol %) # 1	-30.2 ± 0.17	-2.28 ± 0.01	3.18 ± 0.63
DSPE-PEG2k/DOPC (2.5 mol %) # 2	-33.83 ± 0.2	-2.55 ± 0.15	-
DSPE-PEG2k/DOPC (2.5 mol %) # 3	-29.95 ± 0.64	-2.26 ± 0.05	5.31 ± 1.77
DSPE-PEG2k/DOPC (2.5 mol %) # 4	-35.37 ± 1.09	-2.67 ± 0.08	-
DSPE-PEG2k/DOPC (2.5 mol %) # 5	-31.28 ± 1.05	-2.36 ± 0.08	-
DSPE-PEG2k/DOPC (2.5 mol %) # 6	-33.48 ± 1.23	-2.52 ± 0.09	7.11 ± 1.64

Using an electrokinetic analyzer (Anton Paar, Graz, Austria), mounted with an asymmetric clamping cell, and in general accordance to Walker *et al.* (2002), the ζ-potential of an acetone-cleaned cover glass (top cover glass in the microrheology experiments), a silane-functionalized cover glass, and a PA hydrogel A-coated silane-functioanlized cover glass are measured. In brief, average streaming potential of a grooved poly(methyl methacrylate) (PMMA) spacer is measured as a reference, and the sample ζ-potential is obtained according to the modified Smoluchowski-Helmholtz equation (Walker *et al.*, 2002).

For 6 measurements of the cleaned non-functionalized cover glass, 3 for the silane-functionalized cover glass, and 6 for two separately-prepared PA hydrogel (A)-coated silane-functionalized cover glasses in TAE buffer, the ζ-potential is presented in Table 7.B.2. By functionalizing a cleaned cover glass with aminosilane (see section 7.4), the surface ζ-

potential is reduced to approximately zero due to the presence of positive amine groups on the negatively-charged silica surface; however, coating the functionalized cover glass with PA gel film results in a positive zeta potential in TAE buffer, which is of a surprise, considering the neutral nature of a PA gel. Experiments on two separately-prepared gel-coated cover glasses show a repeatable positive ζ-potential. Interestingly, according to Yezek & van Leeuwen (2004), zeta potential of a PA gel (prepared in DI water and swelled in DI water with added NaCl)-coated cover glasses are measured based on their streaming potentials, which suggested dependency on the medium ionic strength, changing from ≈ -30 mV at 0.05 mmol l^{-1} NaCl to ≈ -12 mV at 5 mmol l^{-1} NaCl. These values are very close to 0.2 % Na-acrylate-doped PA gels, even though Na-acrylate moieties introduce structural charge to the gel skeleton. Moreover, the PA gel streaming potential (in DI water with added NaCl) is reported to be higher than a charged PA gel doped with Na-acrylate (Yezek & van Leeuwen, 2004; Yezek *et al.*, 2005).

All these interesting observations are assumed to be related to: non-zero fixed-charge density on gels, even with no introduced charged groups, resulted from the ionic initiator, acrylamide hydrolysis, and/or unsymmetrical ion adsorption from a solution (Yezek *et al.*, 2005). Donnan potential (instead of ζ-potential) is more favorable in soft surface potential characterization (Yezek & van Leeuwen, 2004) due to the hydrogel ion permeability, which results in potential gradient inside the gel up to an equilibrium depth.

To test the idea of an uneven ion adsorption from the solution on the gel, several sets of experiments were performed, including a PA gel A (prepared at various pH/ionic strengths)-coated cover glass and swelled/rinsed in a specified electrolyte, which are presented in Table 7.B.2. Changing the bound electrolyte from PBS to NaCl (41 mmol l^{-1}) increased the potential from ≈ 0 to ≈ 5 mV, which suggests no significant sensitivity to the unbound fluid (solvent) ionic strength (5.3 mV for 41 mmol l^{-1} NaCl compared to 4.3 mV for 4.1 mmol l^{-1} NaCl).

It can be concluded from Table 7.B.2 that while the solution, used to prepare a gel (bound

electrolyte) has minor effect on the measured potential, the surrounding medium (unbound electrolyte) dictates the potential. To observe how fast the ions partition on a gel, a sample is prepared and swelled in 41 mmol l^{-1} NaCl in RO water (pH $\approx$ 5.8, potential $\approx$ 5 mV), and rinsed in TAE buffer while performing streaming potential experiments within $\lesssim$ 2 hours. This results in an high positive potential $\approx$ 21.5 mV, which suggests a fast ion adsorption on the gel. Also, the Trizma acetate component of the TAE buffer (provided as a powder form, Sigma-Aldrich, MO, U.S.A.) is replaced with acetic acid (provided as a solution form TAE, Sigma-Aldrich, MO, U.S.A.) to see the effect of these species. The results suggest that the acetic acid containing buffer brings about an higher zeta potential $\approx$ 41.8 mV, which can be because of the cation adsorption on the gel surface.

The streaming potential should be modeled based on the Donnan potential and the electrical and physical properties of the interface (Yezek & van Leeuwen, 2004). Moreover, defining the exact interface location for a gel-electrolyte system is challenging. It is assumed that the polymer layer thins out within a narrow layer at the gel-electrolyte interface, bringing the polymer density, and hence, polymer volume fraction, from the bulk value to zero. This transition was considered to be a step function from early attempts in the Oshima-Kondo theory, or, in a more realistic scheme, an hyperbolic tangent function (Yezek *et al.*, 2005). The streaming potential is resulted from the contribution of the bulk gel, the interfacial layer, and the electrolyte (Yezek *et al.*, 2005).

The presence of a porous ion-penetrable layer at the interface with an unbound electrolyte can deviate the ζ-potential, furnished from Walker *et al.* (2002) method for hard interfaces. An ion-permeable layer results in an extended fixed charge layer (known as Stern layer for hard interfaces) within distances comparable to the Debye length (Duval & Van Leeuwen, 2004). A thin crosslinked layer, confined on an impenetrable plate (such as a cover glass) and immersed in an electrolyte is assumed by Duval & Van Leeuwen (2004) to comprise (i) bulk gel (with polymer concentration ϕ), and (ii) an interfacial soft layer with complex properties, dependent on the interactions between the polymer chains, electrolyte

ions and solvent molecules (with a polymer concentration gradient from the bulk gel ϕ to bulk electrolyte $\phi = 0$). The same gradient as ϕ is expected for the fixed-charge density profile if the charged sites are distributed uniformly along the polymer segments. Accordingly, the measured streaming potential is the summation of three contributions, namely bulk gel layer, interfacial gel layer, and the solution (Duval & Van Leeuwen, 2004). The so-called Helmholtz-Smoluchowski equation (Walker *et al.*, 2002) is a reduced form of the electrokinetic equation when the interfacial gel layer does not exist.

Table 7.B.2: ζ-potential of a treated cover glass in TAE buffer (pH $\approx 8.3, 41$ mmol l^{-1}), PBS (pH $\approx 7.4, 164$ mmol l^{-1}), or NaCl in RO water (pH ≈ 5.8).

Cover glass coating	ζ (mV)
Acetone cleaned bare in TAE	-21.62 ± 3.71
Silane-functionalized in TAE	-0.48 ± 2.23
PA A, p.* in PBS, s.* in TAE, sample # 1	27.01 ± 1.97
PA A, p. in PBS, s. in TAE, sample # 2	27.02 ± 6.14
PA A, p. in PBS, s. in NaCl 41 mmol l^{-1}	0.20 ± 1.00
PA A, p. and s. in NaCl 41 mmol l^{-1}	5.30 ± 1.50
PA A, p. and s. in NaCl 41 mmol l^{-1}, rinsed in TAE	21.54 ± 3.65
PA A, p. in PBS, s. in TAE-solution form	41.84 ± 4.71
PA A, p. in PBS, s. in TAE-solution form, rinsed in NaCl 4.1 mmol l^{-1}	4.32 ± 0.56

*p. and s. stand for "prepared" and "swelled", respectively.

When the surface of a charged object, immersed in an electrolyte, is ion penetrable (*e.g.*, a membrane, hydrogel, or grafted polymer layer), the term ζ-potential is no longer a proper way of defining the surface potential, because the fixed charges are distributed within a layer with a finite thickness rather than being in an almost-zero thickness layer (known as Stern layer for rigid bodies). The equilibrium between the interfacial penetrable fixed-charge layer and the solution introduces a potential called Donnan potential, which usually has a lower magnitude than the ζ (surface)-potential, due to the potential decay in the fixed-charge layer. Upon particle-hydrogel contact, as discussed earlier, the interface deforms, and the particle-hydrogel interaction can be treated as a plate-plate interaction with surfaces equal to the particle-gel contact area.

The electrical potential, force, and energy between a plate of the same material as

the microspheres used in this study, *i.e.*, bare silica ($\psi \approx -50$ mV), DOPC-coated and DSPEPEG2k/DOPC-coated silica ($\psi \approx -30$ mV) and the gel surface ($\psi \approx 30$ mV) are calculated. The potential between the gel and plate placed at positions $x = -d_1$ and $x = h + d_2$, respectively, with a fixed-charge layer thickness $d_1 \approx \kappa^{-1} \approx 1.5$ nm and $d_2 \approx 0.1$ nm, respectively, in a $z - z$ electrolyte (schematic is presented in figure 7.B.1) can be calculated as follows (Ohshima *et al.*, 1987):

$$\psi(x) = \frac{k_B T}{2n\nu^2 e} \frac{\{-z_1 N_1 \sinh[\kappa(h + d_2)] + z_2 N_2 \sinh(\kappa d_2)\} \cosh[\kappa(x + d_1)]}{\sinh[\kappa(h + d_1 + d_2)]} + z_1 N_1, \qquad (7.1)$$

$$-d_1 \leq x \leq 0$$

$$\psi(x) = \frac{k_B T}{2n\nu^2 e} \frac{z_1 N_1 \sinh(\kappa d_1) \cosh[\kappa(h + d_2 - x)] + z_2 N_2 \sinh(\kappa d_2) \cosh[\kappa(x + d_1)]}{\sinh[\kappa(h + d_1 + d_2)]},$$

$$0 \leq x \leq h$$

$$\psi(x) = \frac{k_B T}{2n\nu^2 e} \frac{\{-z_2 N_2 \sinh[\kappa(h + d_1)] + z_1 N_1 \sinh(\kappa d_1)\} \cosh[\kappa(h + d_2 - x)]}{\sinh[\kappa(h + d_1 + d_2)]} + z_2 N_2,$$

$$h \leq x \leq h + d_2$$

where ψ, k_B, T, n, ν, e, z, and N are potential, Boltzmann constant, temperature, bulk ion concentration ($= n^1 = n^2 = n^\infty$ for a $1 - 1$ electrolyte), bulk ion valence ($= 1$ for a $1 - 1$ electrolyte), elementary charge, fixed-charge valence, and fixed-charge density, respectively. Also, the reciprocal Debye length

$$\kappa = \left(\frac{2n\nu^2 e^2}{\epsilon \epsilon_0 k_B T} \right)^{1/2}, \qquad (7.2)$$

where ϵ and ϵ_0 are the medium relative dielectric constant (relative permittivity) and vacuum permittivity, respectively.

Accordingly, potential (ψ, top panel), force (f, left bottom panel), and electrostatic potential energy (U, right bottom panel) are presented in figure 7.B.2. Note that in these calculations, it is assumed that gel concentration follows a step function ($\phi = 1$ to 0) at the interface. Also, it is assumed that the plate and gel fixed-charge layer thickness ≈ 0 and $\approx$ Debye length, respectively. Taking the predicted contact radius approximately 10 nm into

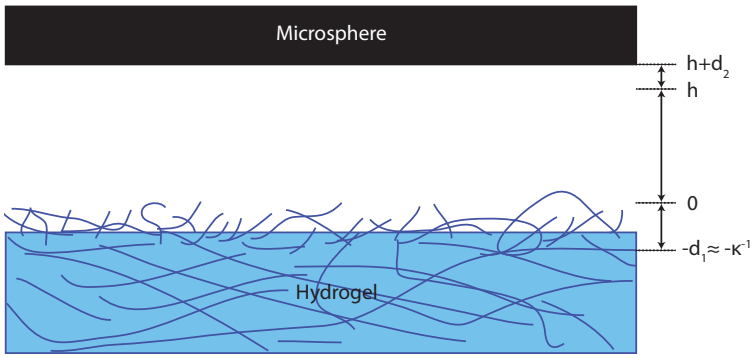

Figure 7.B.1: Schematic of hydrogel and microsphere positioning with their surface charge layers, presenting Eqn. 7.1.

account (Refer to section 5.5 for details), the attractive electrical force ≈ 10 pN, which is approximately two orders of magnitude higher than the optical force exerted on a microsphere in a bulk fluid. Noteworthy is that the presence of vdW attraction force, which can also induce tangential force (Czarnecki & Warszynski, 1987) due to surface roughness and the lack of knowledge about the exact particle-gel separation gap make further analysis difficult.

To acquire the potential between a sphere and a plate from the plate-plate (s-s) potential, Derjaguin (1934) suggested that the interaction is distributed through rings of different width on the sphere. The summation of ring-plate potentials furnishes the particle-substrate (p-s) potential (Derjaguin, 1934; Hoek & Agarwal, 2006)

$$U_{p-s} = 2\pi R \int_h^\infty U_{s-s}(x)dx, \tag{7.3}$$

where h is the minimum particle-plate separation, and x is the distance between a desired ring on the particle and the plate. This approximation is valid when a small area around the minimum separation point is responsible for all the potential, and the potential decays fast with h (White, 1983). Accordingly, the particle-substrate vdW energy and electrostatic energy can be calculated using Eqns. 3.5 and 3.16, respectively, which are shown with blue and red colors in figure 7.B.3. Note that to obtain the vdW energy, hydrogel polymer concentration ($\phi = 0.05$) is multiplied by Eqn. 3.5. The acid-base interaction between a

silica microsphere and a planar uncrosslinked polyacrylamide layer is, also, calculated, using Eqn. 3.17 and surface energetics in Table 7.B.3. Interestingly, the total potential energy between silica and uncrosslinked PA is dictated by the attractive potentials at $h \gtrsim 2.5$ nm, whereas repulsive AB interactions result in particle-polymer layer repulsion at $h \lesssim 2.5$ nm. It should be noted that the water contact angle on an uncrosslinked PA film is approximately 23.6° (Wu & Shanks, 2004), while on PA hydrogel, it is almost zero. This shows the difference between the surface energetics of an uncrosslinked PA layer and a PA hydrogel film, and accordingly dissimilar AB interactions.

Table 7.B.3: Surface energetics of silica microsphere, uncrosslinked polyacrylamide, and water, used in Eqn. 3.17.

	Silica	uncrosslinked polyacrylamide	water
γ^+ (mJ m^{-2})	1.04	1.88	25.5
γ^- (mJ m^{-2})	31.72	38.56	25.5
Reference	(Brant & Childress, 2002)	(Wu & Shanks, 2004)	(Brant & Childress, 2002)

For a small enough separation between a rigid body (*e.g.*, a plate) and a soft substrate (*e.g.*, constrained hydrogel layer on a cover slip), surface instabilities can occur due to the intermolecular interactions (Chen *et al.*, 2012; He, 2013). For silicon rubber films at contact proximity with a glass slide in air, spontaneous undulations were reported to occur, independent of the approaching body, but dependent on the film thickness (Monch & Herminghaus, 2001). The instability wave numbers ≈ 100 and 40 mm^{-1} for a rubber film ($E \approx 1$ MPa, $\gamma \approx 0.02$ N m^{-1}) with thickness $\approx$ 20 and 60 μm, respectively. For such system, including a film with thickness ≈ 10 μm, the critical distance to have the instability is 15 nm.

Another concern is the (unavoidable) possible deformation, caused by the residual stress, implied on the gel surface by removing the upper cover glass after gelation (see section 7.4). Hinging on linear elasticity, this problem is solved theoretically by Lin *et al.* (2008), studying the instability, induced by the contact between a rigid substrate and an elastic film. As the possible surface modulation length is unknown, two extreme cases are considered: (i) an

elastic half-space and (ii) an elastic thin film, according to Lin *et al.* (2008). In either case, surface modulation frequency ω is related to the substrate shear modulus $G = \mu_g$, Poisson ratio ν, and apparent surface stress $k = \sigma_r + \gamma$, where σ_r is the residual surface traction, and γ is the surface energy. In the later case, the film thickness h is also effective: Case (i): $\omega = G/(\nu k - k)$, and case (ii): $\omega = [2G(\nu - 1)/(hk - 2\nu hk)]^{1/2}$ for $\nu \neq 0.5$ and $\omega = [3G(\nu - 1)/kh^3]^{1/4}$ for $\nu = 0.5$. In the current study: $\sigma_r = m_c g/h \approx 16$ N m^{-1} for gels A, B, and C, respectively, considering the circular (12 mm diameter) top cover glass mass $m_c \approx 0.041$ g and $h \approx 25$ μm, using AFM shear moduli. This traction acts opposite to the surface tension resulting in a negative k, which ensures the surface instability formation Lin *et al.* (2008). Therefore, the spatial wavelength $2\pi/\omega$ for gels A, B, and C in case (i): ≈ 18.6, 33.5, and 100.6 mm, respectively, and in case (ii): 0.73, 0.85, and 1.12 mm, respectively. These values are more than 3 orders of magnitude higher than the particle size, thus their effect on the particle attachment is negligible.

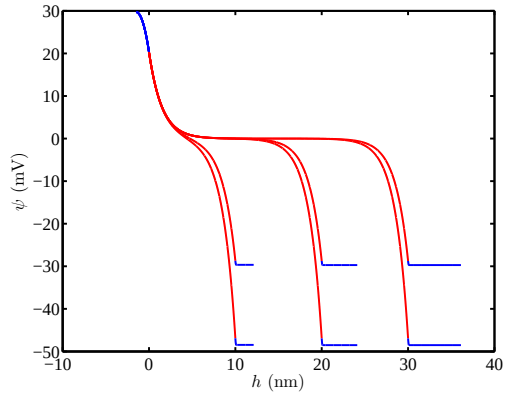

(a) Electrostatic potential according to Eqn. 7.1 between a planar PA hydrogel layer (placed at $x = -\kappa \approx -1.5$ nm) and a silica or a bilayer-coated plate (at $x = 10 + 0.1$, $20 + 0.1$, or $30 + 0.1$ nm).

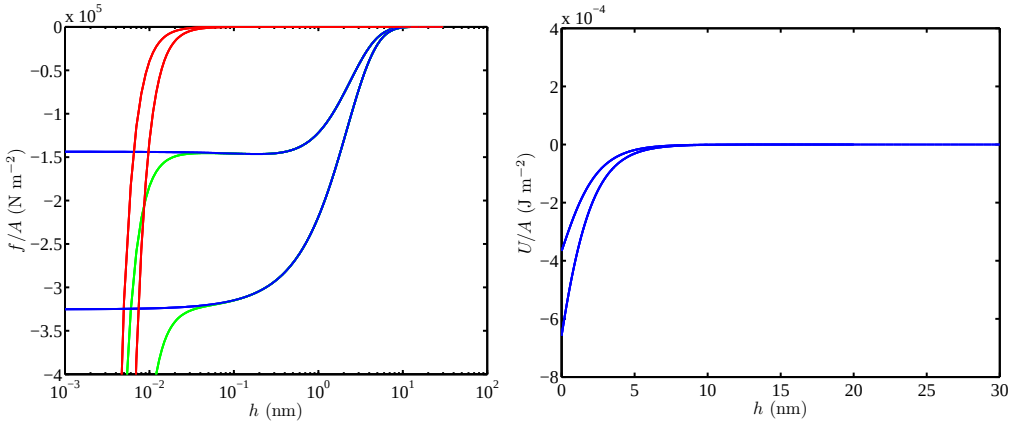

(b) Force (vdW and ES, left panel) and energy (ES, right panel) per unit area for the same system as (a).

Figure 7.B.2: Electrostatic potential ψ (panel a) between a PA hydrogel planar layer ($\psi \approx 30$ mV) and a silica plate ($\psi \approx -50$ mV) or a bilayer-coated silica plate ($\psi \approx -30$ mV) versus the separation gap h. The gel is located at $x = -\kappa^{-1} \approx -1.5$ nm with a fixed-charge layer thickness $d_1 = \kappa^{-1}$. Here, x is the distance from the location where the polymer concentration is zero (see figure 7.B.1). The fixed-charge layer on the plate is assumed to have a thickness $d_2 \approx 0.1$ nm. The fixed-charge layer potential is shown with blue in (a). The total force and electrostatic energy per unit area are shown in bottom left and right panels, respectively. Electrostatic force (bottom left panel) is shown with blue, and the van der Waals (vdW) force $f_{\text{vdW}} = -\phi A_H/(12\pi h^3 k_B T I N_A)$, where ϕ, I and N_A are polymer concentration in the hydrogel (5 %), ionic strength, and Avogadro's number, respectively, is shown with red taking $A_{H,g-s-p} \approx 3A_{H,g-s-b} \approx 10^{-20}$ J, where g, s, p, and b stand for gel, solvent, silica particle, and bilayer, respectively. The total force, defined as the summation of the electrostatic and vdW forces, is shown in green.

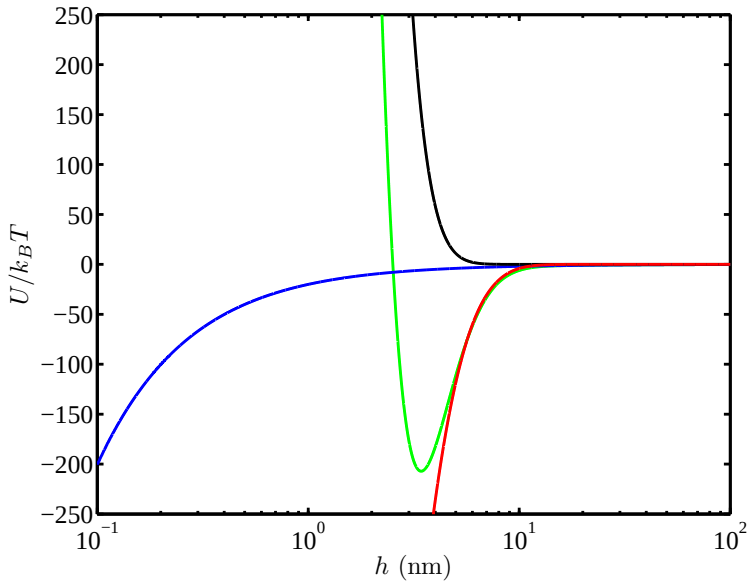

Figure 7.B.3: XDLVO interaction potential comprising the vdW attraction $U_{vdw} = -\phi A_H R/(6h)$ (shown with blue), where the planar layer polymer concentration $\phi = 0.05$, the electrostatic potential (U_{ES}, according to Eqn. 3.16 wih $\psi_p \approx -50$ mV and $\psi_s \approx 30$ mV), shown with red, and acid-base potential (U_{AB}, according to Eqn. 3.17), shown with black, between a silica microsphere with a planar layer of uncrosslinked polyacrylamide. The surface energetic parameters, used in Eqn. 3.17, are summarized in Table 7.B.3. Interestingly, the total energy $U_{tot} = U_{vdw} + U_{ES} + U_{AB}$, shown with green, indicates that for particle-substrate separation $h \gtrsim 2.5$ nm, the attractive interactions dominate, while at $h \lesssim 2.5$ nm, despite attractive electrostatic and vdW interactions, the acid-base repulsion dominates the system. The acid-base interaction for a PA hydrogel film is not calculated due to the lack of surface energetic parameters; however, possible hydrogen bonding between polyacrylamide hydrogel and a silica microsphere can result in negative U_{AB}.

Chapter 8

Conclusions and contribution to knowledge

The well-understood dynamics of silica microspheres in simple media, such as an electrolyte, are affected when the particles are subject to interacting interfaces with attractive or repulsive forces. Interfacial self-diffusion of silica microspheres with lipid bilayer or polymer coatings on coated flat substrates showed how the particle dynamics are affected by the soft interactions. Systematically decreasing the ζ-potential of surfaces by coating them with DOPC (a lipid bilayer) decreased the diffusion coefficient, and introducing conjugated PEG (polyethylene glycol) chains in the bilayers resulted in non-Brownian (anomalous) diffusion. PEG hydrogels were able to adsorb silica microspheres on their surface regardless of particle coating and medium ionic strength, providing a platform for particle separation. Negatively-charged agarose hydrogels, as a soft cushion, selectively adsorbed conjugated PEG-coated particles while keeping bare or DOPC bilayer-coated particles mobile on their surface.

Despite a wide application horizon of colloidal particle-hydrogel inclusions, such as soft, wet silica particle-mediated gluing of hydrogels, biofilm formation, and biofouling, little is known about how a single microsphere adheres to a compliant substrate. This problem is of great importance in colloidal-based drug delivery given that hydrogels, as hydrophilic

polymer networks comprising an high water content, are excellent model systems for soft tissues. It has not been well understood how the dynamics of a sticky colloidal particle, contacting a soft substrate, were affected by the viscoelastic properties of the interface.

Optical tweezers combined with nanometer accuracy position acquisition back-focal-plane interferometry and phase-sensitive detection are used to conduct two types of experimental measurements on the deformation and flow properties of polyacrylamide (PA) hydrogel-electrolyte interfaces, employing various types of probe microspheres. Passive and active optical tweezers microrheology experiments were conducted in which the behavior of a single optically trapped colloidal particle was probed at the PA gel vicinity in the absence or presence of external forces, such as an oscillatory shear drive.

Passive interfacial microrheology with a bare silica microsphere at a PA gel-tris acetate EDTA (TAE) electrolyte revealed that while an elevated probe behavior is similar to that near a rigid wall, the particle dynamics are highly attenuated once it contacts the soft substrate. This is manifested in the short-time lag Brownian diffusion coefficient attenuation by a factor of ≈ 6, 3, and 2 compared to the predictions by continuum hydrodynamic theories at a particle-gel gap $z \approx 20$ nm for PA hydrogels A, B, and C with Young's moduli 10.9, 6.3, and 3.2 kPa, respectively. This suggested ≈ 5, 10, and 15 fold interfacial viscosity increase for the aforementioned gels, compared to the viscosity of electrolyte. The long-time Brownian position variance, as a representative of the reciprocal binding stiffness, decreased by increasing the gel stiffness, which was fitted well by the Maugis (1995) adhesion energy using the contact radii predicted by the Hill & Sheikhi (2014) theory; however, the implausibly low adhesion energy suggests that (i) the effective gel surface stiffness at length scales comparable to a $2R \approx 1.97$ μm microsphere may be several times lower than the bulk elastic modulus, and (ii) the particle may be affected by the gel thermal fluctuations. Moreover, the attenuated dynamics of a bare silica microsphere on a PA gel took place abruptly when the bulk gel shear modulus $\mu_g \gtrsim 2$ kPa, while aging was observed for a softer gel, suggesting a gradual increase of the contact area. The passive interfacial storage modulus G' was

well-scaled with the gel AFM Young's modulus E: $1000G'/E \approx 1$.

The effect of external forces on the rheological behavior of PA hydrogel-TAE electrolyte interfaces was investigated through active optical tweezers microrheology, in which the position response of a bare silica probe particle to an external oscillatory shear was used to furnish the viscoelastic properties of the interface. It was observed that the interfacial viscoelasticity is affected by the external drive frequency, dictating the shear force on the probe, optical tweezers spring constant, manipulating the spring force on the particle, and the substrate stiffness. The interfacial storage G' and loss G'' moduli were used to define the bare silica microsphere-hydrogel coupling modes within the Cole-Cole formalism. It was concluded that by increasing the external forces (*e.g.*, oscillatory shear and optical trap force) on the particle or decreasing the substrate stiffness, a weaker elastic coupling was achieved. Given that the active microrheology experiments are conducted with a small amplitude perturbation ≈ 30 nm, the particle is expected to rock on the gel. The adhesion strength of such a rocking system is dictated by the equilibrium between the attaching polymer tethers, located on the gel surface, to the particle when advancing and detaching when receding. The experiments imply that the equilibrium number of bonds between a bare silica microsphere and PA gel can be decreased by increasing the external force or decreasing the gel crosslinking density.

The next goal of the current research was to isolate the hydrogel-attachment capability of grafted polymer chains (*e.g.*, polyethylene glycol, as one of the most abundantly used coatings in particle-based drug delivery applications). To accomplish this, first, the adhesive affinity of a bare silica microsphere was screened and eliminated by a phospholipid bilayer (DOPC, a biocompatible zwitterionic fluid lipid membrane) coating. Passive microrheology using such silica microsphere-supported lipid bilayers (SLBs) on a PA gel resulted in comparable short-time diffusion coefficient and long-time position variance to the bulk fluid, suggesting no remarkable interfacial adhesion. These non-adhesive particles, served as suitable colloidal probes to measure the solvent properties at a PA gel-electrolyte interface contact proximity,

indicated no sign of polymer release from the gel into the neighboring fluid.

Introducing grafted PEG chains into the DOPC coating resulted in lipopolymer-doped lipid bilayer (DSPE-PEG2k/DOPC, termed as DSPE)-coated silica microspheres, which tend to adhere to the PA hydrogels A and B. Noteworthy is that the presence of as low lipopolymer concentration as 0.5 or 2.5 mol % showed promising adhesion capability. A DSPE-coated silica microsphere was used as a colloidal probe to conduct passive and active interfacial microrheology. The former suggested that the adhesion energy between a DSPE-coated particle and PA gel is almost 1/3 of a bare silica adhesion. Also, the interfacial storage modulus $1000G'/E \approx 0.7$. Interestingly, in case of a low lipopolymer concentration (0.5 %) and a soft hydrogel B, three typical adhesive behavior, namely stuck, aging, and discontinuous sticking were observed. No significant adhesion was detected on gel C, even after a long contact time.

Active interfacial microrheology with DSPE-coated silica microspheres elucidated that the particle-hydrogel interfacial viscoelastic properties can be manipulated by the external forces easier than a bare particle due to weaker adhesion. The inclusion viscoelasticity was shifted from a high-G' to a low-G' coupling mode by increasing the drive frequency, trap stiffness, and/or decreasing the gel stiffness and DSPE content. At a specified operating condition (trap stiffness, drive frequency, substrate stiffness) the storage and loss moduli are clustered (not scattered) in the Cole-Cole plots, suggesting that the adhesion is achieved through discrete interfacial energy minima. Despite the clustered viscoelasticity, increasing the exerted force on the particle can spontaneously change the adhesion potential. Weaker adhesion (*e.g.*, softer gel or lower DSPE content) accompanied much scattered viscoelasticity, suggesting an higher particle-hydrogel degree of freedom.

In designing the drug delivery systems, the outcome of this thesis may be helpful for determining the local adhesion strength of a colloidal carrier on a soft tissue and its dependency on the external forces, such as blood shear flow. The rate of drug release can, then, be precisely acquired as a function of local viscoelastic properties. Moreover, coating a drug

carrier with DOPC can result in longer circulation time inside the body due to the minimized adhesion tendency. This is interesting that despite an expected high electrostatic attraction between the negatively-charged DOPC-coated silica particles and the gel positively-charged surface, such a coating eliminates the adhesion, regardless of the substrate stiffness and external forces. Furthermore, doping a DOPC-coated particle with a desired amount of PEG moieties can provide a customized local adhesion. This can be further used for bioadhesion applications, such as biocompatible in vivo stitching of damaged tissues.

Bibliography

Adamczyk, Z. 2006 *Particles at Interfaces: Interactions, Deposition, Structure*. Elsevier Ltd.

Ahuja, A., Khar, R. & Ali, J. 1997 Mucoadhesive drug delivery systems. *Drug Dev. Ind. Pharm.* **23**, 489–515.

Akhmanova, A. & Steinmetz, M. 2008 Tracking the ends: A dynamic protein network controls the fate of microtubule tips. *Nat. Rev. Mol. Cell Biol.* **9**, 309–322.

Anderson, A. M. & Worster, M. G. 2012 Periodic ice banding in freezing colloidal dispersions. *Langmuir* **28**, 16512–16523.

Angelini, T., Hannezo, E., Trepatc, X., Marquez, M., Fredberg, J. & Weitz, D. 2011 Glass-like dynamics of collective cell migration. *Proc. Natl. Acad. Sci. U.S.A.* **108**, 4714–4719.

Arai, Y., Yasuda, R., Akashi, K.-I., Harada, Y., Miyata, H., Kinosita Jr., K. & Itoh, H. 1999 Tying a molecular knot with optical tweezers. *Nature* **399**, 446–448.

Arzt, E., Gorb, S. & Spolenak, R. 2003 From micro to nano contacts in biological attachment devices. *Proc. Natl. Acad. Sci. U.S.A.* **100**, 10603–10606.

Ashkin, A. 1992 Forces of a single-beam gradient laser trap on a dielectric sphere in the ray optics regime. *Biophys. J.* **61**, 569–582.

Ashkin, A., Dziedzic, J., Bjorkholm, J. & Chu, S. 1986 Observation of a single-beam gradient force optical trap for dielectric particles. *Opt. Lett.* **11**, 288–290.

Ashley, C., Carnes, E., Phillips, G., Padilla, D., Durfee, P., Brown, P., Hanna, T., Liu, J., Phillips, B., Carter, M., Carroll, N., Jiang, X., Dunphy, D., Willman, C., Petsev, D., Evans, D., Parikh, A., Chackerian, B., Wharton, W., Peabody, D. & Brinker, C. 2011 The targeted delivery of multicomponent cargos to cancer cells by nanoporous particle–supported lipid bilayers. *Nat. Mater.* **10**, 389–397.

Ashley, C. E., Carnes, E. C., Epler, K. E., Padilla, D. P., Phillips, G. K., Castillo, R. E., Wilkinson, D. C., Wilkinson, B. S., Burgard, C. A., Kalinich, R. M., Townson, J. L., Chackerian, B., Willman, C. L., Peabody, D. S., Wharton, W. & Brinker, C. J. 2012 Delivery of small interfering RNA by peptide-targeted mesoporous silica nanoparticle-supported lipid bilayers. *ACS Nano* **6**, 2174–2188.

Autumn, K., Liang, Y., Hsieh, S., Zesch, W., Chan, W., Kenny, T., Fearing, R. & Full, R. 2000 Adhesive force of a single gecko foot-hair. *Nature* **405**, 681–685.

Avramov, I. & Milchev, A. 1988 Effect of disorder on diffusion and viscosity in condensed systems. *J. Non-Cryst. Solids* **104**, 253–260.

Baker, J. & Dudley, L. 1998 Biofouling in membrane systems–a review. *Desalination* **118**, 81–89.

Baksh, M., Jaros, M. & Groves, J. 2004 Detection of molecular interactions at membrane surfaces through colloid phase transitions. *Nature* **427**, 139–141.

Ballesta, P., Duri, A. & Cipelletti, L. 2008 Unexpected drop of dynamical heterogeneities in colloidal suspensions approaching the jamming transition. *Nat. Phys.* **4**, 550–554.

Barbe, C., Bartlett, J., Kong, L., Finnie, K., Lin, H., Larkin, M., Calleja, S., Bush, A. & Calleja, G. 2004 Silica particles: A novel drug-delivery system. *Adv. Mater.* **16**, 1959–1966.

Barton, J., Alexander, D. & Schaub, S. 1988 Internal and near-surface electromagnetic fields for a spherical particle irradiated by a focused laser beam. *J. Appl. Phys.* **64**, 1632–1639.

Beebe, D., Moore, J., Bauer, J., Yu, Q., Liu, R., Devadoss, C. & Jo, B.-H. 2000 Functional hydrogel structures for autonomous flow control inside microfluidic channels. *Nature* **404**, 588–590.

Behrens, S. & Grier, D. 2001 The charge of glass and silica surfaces. *J. Chem. Phys.* **115**, 6716–6721.

Beningo, K. & Wang, Y.-L. 2002 Fc-receptor-mediated phagocytosis is regulated by mechanical properties of the target. *J. Cell Sci.* **115**, 849–856.

Berg-Sørensen, K. & Flyvbjerg, H. 2004 Power spectrum analysis for optical tweezers. *Rev. Sci. Instrum.* **75**, 594–612.

Bhatia, S. K., Swers, J. S., Camphausen, R. T., Wittrup, K. D. & Hammer, D. A. 2003 Rolling adhesion kinematics of yeast engineered to express selectins. *Biotechnol. Progr.* **19**, 1033–1037.

Bhosale, P. S., Chun, J. & Berg, J. C. 2011 Electroacoustics of particles dispersed in polymer gel. *Langmuir* **27**, 7376–7379.

Bickel, T. 2007 Hindered mobility of a particle near a soft interface. *Phys. Rev. E* **75**, 041403.

Block, S., Blair, D. & Berg, H. 1989 Compliance of bacterial flagella measured with optical tweezers. *Nature* **338**, 514–518.

Bockelmann, U., Thomen, P., Essevaz-Roulet, B., Viasnoff, V. & Heslot, F. 2002 Unzipping DNA with optical tweezers: High sequence sensitivity and force flips. *Biophys. J.* **82**, 1537–1553.

Boudou, T., Ohayon, J., Arntz, Y., Finet, G., Picart, C. & Tracqui, P. 2006 An extended modeling of the micropipette aspiration experiment for the characterization of the Young's modulus and Poisson's ratio of adherent thin biological samples: Numerical and experimental studies. *J. Biomech.* **39**, 1677–1685.

Boussinesq, J. 1885 *Application des potentiels a l'etude de l'equilibre et du mouvement des solides elastiques*. Gauthier-Villars, Paris.

Bradley, R. S. 1932 The cohesive force between solid surfaces and the surface energy of solids. *Phil. Mag.* **13**, 853–862.

Brandenburg, B. & Zhuang, X. 2007 Virus trafficking - learning from single–virus tracking. *Nat. Rev. Microbiol.* **5**, 197–208.

Brant, J. & Childress, A. 2002 Assessing short-range membrane-colloid interactions using surface energetics. *J. Membr. Sci.* **203**, 257–273.

Brant, J. A. & Childress, A. E. 2004 Colloidal adhesion to hydrophilic membrane surfaces. *J. Membr. Sci.* **241**, 235–248.

Brau, R., Ferrer, J., Lee, H., Castro, C., Tam, B., Tarsa, P., Matsudaira, P., Boyce, M., Kamm, R. & Lang, M. 2007 Passive and active microrheology with optical tweezers. *J. Opt. A: Pure Appl. Opt.* **9**, S103–S112.

Bringas, E., Koysuren, O., Quach, D. V., Mahmoudi, M., Aznar, E., Roehling, J. D., Marcos, M. D., Martinez-Manez, R. & Stroeve, P. 2012 Triggered release in lipid bilayer-capped mesoporous silica nanoparticles containing SPION using an alternating magnetic field. *Chem. Commun.* **48**, 5647–5649.

Brunk, D. & Hammer, D. 1997 Quantifying rolling adhesion with a cell-free assay: E-selectin and its carbohydrate ligands. *Biophys. J.* **72**, 2820–2833.

Calvet, D., Wong, J. & Giasson, S. 2004 Rheological monitoring of polyacrylamide gelation: Importance of cross-link density and temperature. *Macromolecules* **37**, 7762–7771.

Caspi, A., Granek, R. & Elbaum, M. 2000 Enhanced diffusion in active intracellular transport. *Phys. Rev. Lett.* **85**, 5655–5658.

Castellana, E. T. & Cremer, P. S. 2006 Solid supported lipid bilayers: From biophysical studies to sensor design. *Surf. Sci. Rep.* **61**, 429–444.

Cauda, V., Engelke, H., Sauer, A., Arcizet, D., Brauchle, C., Radler, J. & Bein, T. 2010 Colchicine-loaded lipid bilayer-coated 50 nm mesoporous nanoparticles efficiently induce microtubule depolymerization upon cell uptake. *Nano Lett.* **10**, 2484–2492.

Chakrabarti, A. & Chaudhury, M. 2013 Direct measurement of the surface tension of a soft elastic hydrogel: Exploration of elastocapillary instability in adhesion. *Langmuir* **29**, 6926–6935.

Chang, K.-C. & Hammer, D. A. 1996 Influence of direction and type of applied force on the detachment of macromolecularly-bound particles from surfaces. *Langmuir* **12**, 2271–2282.

Chang, K.-C. & Hammer, D. A. 1999 The forward rate of binding of surface-tethered reactants: Effect of relative motion between two surfaces. *Biophys. J.* **76**, 1280–1292.

Chang, K.-C. & Hammer, D. A. 2000 Adhesive dynamics simulations of sialyl-lewisx/E-selectin-mediated rolling in a cell-free system. *Biophys. J.* **79**, 1891–1902.

Chapman, D. L. 1913 A contribution to the theory of electrocapillarity. *Lond. Edinb. Dublin Philos. Mag. J. Sci.* **25**, 475–481.

Chemburu, S., Fenton, K., Lopez, G. & Zeineldin, R. 2010 Biomimetic silica microspheres in biosensing. *Molecules* **15**, 1932–1957.

Chen, Y.-C., Fried, E. & Tortorelli, D. 2012 Stability of a thin elastic film close to a rigid plate. *J. Mech. Phys. Solids* **60**, 904–920.

Chenouard, N., Smal, I., de Chaumont, F., Maska, M., Sbalzarini, I. F., Gong, Y., Cardinale, J., Carthel, C., Coraluppi, S., Winter, M., Cohen, A. R., Godinez, W. J., Rohr, K., Kalaidzidis, Y., Liang, L., Duncan, J., Shen, H., Xu, Y., Magnusson, K. E. G., Jalden, J., Blau, H. M., Paul-Gilloteaux, P., Roudot, P., Kervrann, C., Waharte, F., Tinevez, J.-Y., Shorte, S. L., Willemse, J., Celler, K., van Wezel, G. P., Dan, H.-W., Tsai, Y.-S., de Solorzano, C. O., Olivo-Marin, J.-C. & Meijering, E. 2014 Objective comparison of particle tracking methods. *Nat. Methods* **11**, 281–289.

Cherukat, P., McLaughlin, J. & Graham, A. 1994 The inertial lift on a rigid sphere translating in a linear shear flow field. *Int. J. Multiphase Flow* **20**, 339–353.

Chin, H., Khayat, G. & Quinn, T. 2011 Improved characterization of cartilage mechanical properties using a combination of stress relaxation and creep. *J. Biomech.* **44**, 198–201.

Choi, M. J., Guntur, S. R., Lee, K. I., Paeng, D. G. & Coleman, A. 2013 A tissue mimicking polyacrylamide hydrogel phantom for visualizing thermal lesions generated by high intensity focused ultrasound. *Ultrasound Med. Biol.* **39**, 439–448.

Chu, C. T. W. & Chang, C. D. 1985 Isomorphous substitution in zeolite frameworks. 1. acidity of surface hydroxyls in [B]-, [Fe]-, [Ga]-, and [Al]-zsm-5. *J. Phys. Chem.* **89**, 1569–1571.

Cicuta, P. & Donald, A. 2007 Microrheology: A review of the method and applications. *Soft Matter* **3**, 1449–1455.

Clercx, H. & Schram, P. 1992 Brownian particles in shear flow and harmonic potentials: A study of long-time tails. *Phys. Rev. A* **46**, 1942–1950.

Cooley, M. D. A. & O'Neill, M. E. 1969 On the slow motion generated in a viscous fluid by the approach of a sphere to a plane wall or stationary sphere. *Mathematika* **16**, 37–49.

Corbin, E., Millet, L., Pikul, J., Johnson, C., Georgiadis, J., King, W. & Bashir, R. 2013 Micromechanical properties of hydrogels measured with mems resonant sensors. *Biomed. Microdevices* **15**, 311–319.

Cosgrove, T., ed. 2010 *Colloid Science: Principles, methods and applications, Second Edition*. John Wiley & Sons, Ltd.

Cremer, P. S. & Boxer, S. G. 1999 Formation and spreading of lipid bilayers on planar glass supports. *J. Phys. Chem. B* **103**, 2554–2559.

Crocker, J. & Grier, D. 1996 Methods of digital video microscopy for colloidal studies. *J. Colloid Interface Sci.* **179**, 298–310.

Crocker, J. C. 1999 Particle tracking using idl. http://www.physics.emory.edu/ weeks/idl/micrheo.html.

Czarnecki, J. & Warszynski, P. 1987 Evaluation of tangential forces due to surface inhomogeneities in the particle deposition process. *Colloids and surfaces* **22**, 207–214.

Damiano, E., Long, D., El-Khatib, F. & Stace, T. 2004 On the motion of a sphere in a Stokes flow parallel to a Brinkman half-space. *J. Fluid Mech.* **500**, 75–101.

Daniels, B. R., Masi, B. C. & Wirtz, D. 2006 Probing single-cell micromechanics in vivo: The microrheology of C. elegans developing embryos. *Biophys. J.* **90**, 4712–4719.

Day, J. & Robb, I. 1981 Thermodynamic parameters of polyacrylamides in water. *Polymer* **22**, 1530–1533.

Debenedetti, P. & Stillinger, F. 2001 Supercooled liquids and the glass transition. *Nature* **410**, 259–267.

Derjaguin, B. 1934 Kolloid z. *Kolloid Z.* **69**, 155–164.

Derjaguin, B. & Landau, L. 1941 *Acta Physicochim. URSS* pp. 633–662.

Derjaguin, B., Muller, V. & Toporov, Y. 1975 Effect of contact deformations on the adhesion of particles. *J. Colloid Interface Sci.* **53**, 314–326.

Di Michele, L., Yanagishima, T., Brewer, A., Kotar, J., Eiser, E. & Fraden, S. 2011 Interactions between colloids induced by a soft cross-linked polymer substrate. *Phys. Rev. Lett.* **107**.

Di Michele, L., Zaccone, A. & Eiser, E. 2012 Analytical theory of polymer-network-mediated interaction between colloidal particles. *Proc. Natl. Acad. Sci. U.S.A.* **109**, 10187–10192.

Ding, W., Zhang, H. & Cetinkaya, C. 2008 Rolling resistance moment-based adhesion characterization of microspheres. *J. Adhes.* **84**, 996–1006.

Doane, T. L., Chuang, C.-H., Hill, R. J. & Burda, C. 2012 Nanoparticle ζ-potentials. *Acc. Chem. Res.* **45**, 317–326.

Drozdov, A. D. 1998 *Viscoelastic Structures Mechanics of Growth and Aging*. Elsevier Inc.

Drury, J. L. & Mooney, D. J. 2003 Hydrogels for tissue engineering: scaffold design variables and applications. *Biomaterials* **24**, 4337–4351.

Duval, J. & Van Leeuwen, H. 2004 Electrokinetics of diffuse soft interfaces. 1. limit of low Donnan potentials. *Langmuir* **20**, 10324–10336.

Eddington, D. T. & Beebe, D. J. 2004 Flow control with hydrogels. *Adv. Drug Delivery Rev.* **56**, 199–210.

Ede, A. 2007 *The Rise and Decline of Colloid Science in North America, 1900-1935: The Neglected Dimension*. Ashgate Publishing, Ltd.

Einstein, A. 1905 On the movement of small particles suspended in stationary liquids required by the molecular-kinetic theory of heat. *Ann. Phys.* **17**, 549–560.

Engler, A., Bacakova, L., Newman, C., Hategan, A., Griffin, M. & Discher, D. 2004 Substrate compliance versus ligand density in cell on gel responses. *Biophys. J.* **86**, 617–628.

Ensign, L., Schneider, C., Suk, J., Cone, R. & Hanes, J. 2012 Mucus penetrating nanoparticles: Biophysical tool and method of drug and gene delivery. *Adv. Mater.* **24**, 3887–3894.

Eroshenko, N., Ramachandran, R., Yadavalli, V. & Rao, R. 2013 Effect of substrate stiffness on early human embryonic stem cell differentiation. *J. Biol. Eng.* **7**.

Everett, W. & Bevan, M. 2014 KT-scale interactions between supported lipid bilayers. *Soft Matter* **10**, 332–342.

Faraday, M. 1857 Experimental relations of gold (and other metals) to light. *Phil. Trans. R. Soc. London* **14**, 145–181.

Faxen, H. 1923 Die bewegung einer starren kugel lngs der achse eines mit zher flssigkeit gefllten rohres (the movement of a rigid sphere along the axis of the tube filled with viscous liquid). *Ark. Mat. Astron. Fys.* **18**, 1–28.

Ferry, J. D. 1980 *Viscoelastic properties of polymers (3rd edn)*. Wiley, New York.

Franklin, A. & Krizek, R. 1969 Complex viscosity of a kaolin clay. *Clays Clay Miner.* **17**, 101–110.

Fulcher, G. S. 1925 Analysis of recent measurements of the viscosity of glasses. *J. Am. Ceram. Soc.* **8**, 339–355.

Gady, B., Reifenberger, R., Schaefer, D., Bowen, R., Rimai, D., Demejo, L. & Vreeland, W. 1998 Particle adhesion to elastomeric substrates and elastomeric substrates with semi-rigid coatings. *J. Adhes.* **67**, 19–36.

Geckil, H., Xu, F., Zhang, X., Moon, S. & Demirci, U. 2010 Engineering hydrogels as extracellular matrix mimics. *Nanomedicine* **5**, 469–484.

Ghosh, S., Ashcraft, K., Jahid, M., April, C., Ghajar, C., Ruan, J., Wang, H., Foster, M., Hughes, D., Ramirez, A., Huang, T., Fan, J.-B., Hu, Y. & Li, R. 2013 Regulation of adipose oestrogen output by mechanical stress. *Nat. Commun.* **4**.

Ghosh, S., Sharma, P. & Bhattacharya, S. 2007 Surface modes of a sessile water drop: An optical tweezer based study. *Rev. Sci. Instrum.* **78**, 115110.

Gittes, F. & Schmidt, C. 1998 Interference model for back-focal-plane displacement detection in optical tweezers. *Opt. Lett.* **23**, 7–9.

Gniewek, P. & Kolinski, A. 2012 Coarse-grained modeling of mucus barrier properties. *Biophys. J.* **102**, 195–200.

Goldman, A., Cox, R. & Brenner, H. 1967 Slow viscous motion of a sphere parallel to a plane wall- motion through a quiescent fluid. *Chem. Eng. Sci.* **22**, 637–651.

Gong, J. 2006 Friction and lubrication of hydrogels - its richness and complexity. *Soft Matter* **2**, 544–552.

Goodwin, J. W. 2004 *Colloids and Interfaces with Surfactants and Polymers–An Introduction*. John Wiley & Sons Ltd.

Gopinath, A. & Mahadevan, L. 2011 Elastohydrodynamics of wet bristles, carpets and brushes. *Proc. R. Soc. A* **467**, 1665–1685.

Gouy, L. G. 1910 Sur la constitution de la charge electrique a la surface d'un electrolyte. *J. Phys. Theorique et Appliquee* **9**, 457–468.

Grahame, D. C. 1947 The electrical double layer and the theory of electrocapillarity. *Chem. Rev.* **41**, 441–501.

Grakoui, A., Bromley, S., Sumen, C., Davis, M., Shaw, A., Allen, P. & Dustin, M. 1999 The immunological synapse: A molecular machine controlling T cell activation. *Science* **285**, 221–227.

Griffith, A. A. 1921 The phenomena of rupture and flow in solids. *Phil. Trans. R. Soc. Lond. A* **221**, 163–198.

Gulati, N., Rastogi, R., Dinda, A. K., Saxena, R. & Koul, V. 2010 Characterization and cell material interactions of PEGylated PNIPAAM nanoparticles. *Colloids Surf., B* **79**, 164–173.

Guo, Z., Meng, S., Zhong, W., Du, Q. & Chou, L. L. 2009 Self-assembly of silanated poly(ethylene glycol) on silicon and glass surfaces for improved haemocompatibility. *Appl. Surf. Sci.* **255**, 6771–6780.

Haga, H., Irahara, C., Kobayashi, R., Nakagaki, T. & Kawabata, K. 2005 Collective movement of epithelial cells on a collagen gel substrate. *Biophys. J.* **88**, 2250–2256.

Hamaker, H. 1937 The London-van der Waals attraction between spherical particles. *Physica* **4**, 1058–1072.

Hammer, D. & Tirrell, M. 1996 Biological adhesion at interfaces. *Annu. Rev. Mater. Sci.* **26**, 651–691.

Harding, J. W. & Sneddon, I. N. 1945 The elastic stresses produced by the indentation of the plane surface of a semi-infinite elastic solid by a rigid punch. *Math. Proc. Cambridge Philos. Soc.* **41**, 16–26.

He, L. 2013 Stress and deformation in soft elastic bodies due to intermolecular forces. *J. Mech. Phys. Solids* **61**, 1377–1390.

van Heiningen, J. A., Mohammadi, A. & Hill, R. J. 2010 Dynamic electrical response of colloidal micro-spheres in compliant micro-channels from optical tweezers velocimetry. *Lab Chip* **10**, 1907–1921.

Hennink, W. & van Nostrum, C. 2012 Novel crosslinking methods to design hydrogels. *Adv. Drug Delivery Rev.* **64, Supplement**, 223–236.

Henon, S., Lenormand, G., Richert, A. & Gallet, F. 1999 A new determination of the shear modulus of the human erythrocyte membrane using optical tweezers. *Biophys. J.* **76**, 1145–1151.

Hertz, H. & Reine, J. 1882 On the contact of elastic solids. *Angew. Math.* **92**, 156.

Hida, T. 1980 Brownian motion. *Applications of Mathematics*, vol. 11, pp. 44–113. Springer US.

Hill, R. J. & Sheikhi, A. 2014 On the adhesion of a rigid colloidal sphere to an elastic plane. *To be submitted* .

Hoare, T. R. & Kohane, D. S. 2008 Hydrogels in drug delivery: Progress and challenges. *Polymer* **49**, 1993–2007.

Hoek, E. & Agarwal, G. 2006 Extended DLVO interactions between spherical particles and rough surfaces. *J. Colloid Interface Sci.* **298**, 50–58.

Hoffman, A. S. 2002 Hydrogels for biomedical applications. *Adv. Drug Delivery Rev.* **54**, 3–12.

Hogg, R., Healy, T. & Fuerstenau, D. 1966 Mutual coagulation of colloidal dispersions. *Trans. Faraday Soc.* **62**, 1638–1651.

Horn, R., Israelachvili, J. & Pribac, F. 1987 Measurement of the deformation and adhesion of solids in contact. *J. Colloid Interface Sci.* **115**, 480–492.

Hrning, M., Kidoaki, S., Kawano, T. & Yoshikawa, K. 2012 Rigidity matching between cells and the extracellular matrix leads to the stabilization of cardiac conduction. *Biophys. J.* **102**, 379–387.

Hu, D.-G. & Tsai, C.-E. 1996 Correlation between interfacial free energy and albumin adsorption in poly(acrylonitrile-acrylamide-acrylic acid) hydrogels. *J. Appl. Polym. Sci.* **59**, 1809–1817.

Hui, C.-Y., Baney, J. & Kramer, E. 1998 Contact mechanics and adhesion of viscoelastic spheres. *Langmuir* **14**, 6570–6578.

Israelachvili, J. N. 2011 *Intermolecular and Surface Forces, Third Edition*. Elsevier Inc.

Janmey, P., Winer, J., Murray, M. & Wen, Q. 2009 The hard life of soft cells. *Cell Motil. Cytoskeleton* **66**, 597–605.

Jannat, R., Robbins, G., Ricart, B., Dembo, M. & Hammer, D. 2010 Neutrophil adhesion and chemotaxis depend on substrate mechanics. *J. Phys. Condens Matter* **22**, 194117.

de Jesus, M., Morgan, J., Ahmed, R. & Rimai, D. 2007 The time dependence of the detachment force of ground micrometer-size particles from a planar substrate: Effect of particle rotation. *Part. Sci. Technol.* **25**, 107–116.

de Jesus, M., Rimai, D. & Quesnel, D. 2006 Effect of Young's modulus on the detachment force of 7 μm particles. *Langmuir* **22**, 729–735.

de Jesus, M., Rimai, D., Stelter, E., Tombs, T. & Weiss, D. 2008 Adhesion of silica-coated toner particles to bisphenol-a polycarbonate films. *J. Imaging Sci. Technol.* **52**, 010503–0105036.

Johansson, B. 1972 Agarose gel electrophoresis. *Scand. J. Clin. Lab. Inv.* **124**, 7–19.

Johnson, K. & Greenwood, J. 1997 An adhesion map for the contact of elastic spheres. *J. Colloid Interface Sci.* **192**, 326–333.

Johnson, L., Kendall, K. & Roberts, A. D. 1971 Surface energy and the contact of elastic solids. *Proc. R. Soc. A* **324**, 301–313.

Ju, Y.-E., Janmey, P., McCormick, M., Sawyer, E. & Flanagan, L. 2007 Enhanced neurite growth from mammalian neurons in three-dimensional salmon fibrin gels. *Biomaterials* **28**, 2097–2108.

Kabiri, K., Omidian, H., Hashemi, S. & Zohuriaan-Mehr, M. 2003 Synthesis of fast-swelling superabsorbent hydrogels: effect of crosslinker type and concentration on porosity and absorption rate. *Eur. Polym. J.* **39**, 1341–1348.

Kang, M. & Huang, R. 2010*a* Effect of surface tension on swell-induced surface instability of substrate-confined hydrogel layers. *Soft Matter* **6**, 5736–5742.

Kang, M. & Huang, R. 2010*b* Swell-induced surface instability of confined hydrogel layers on substrates. *J. Mech. Phys. Solids* **58**, 1582–1598.

Kappl, M. & Butt, H.-J. 2002 The colloidal probe technique and its application to adhesion force measurements. *Part. Part. Syst. Char.* **19**, 129–143.

Kemper, M., Spridon, D., van IJzendoorn, L. J. & Prins, M. W. J. 2012 Interactions between protein coated particles and polymer surfaces studied with the rotating particles probe. *Langmuir* **28**, 8149–8155.

Kendall, E. L., Mills, E., Liu, J., Jiang, X., Brinker, C. J. & Parikh, A. N. 2010 Salt-induced lipid transfer between colloidal supported lipid bilayers. *Soft Matter* **6**, 2628–2632.

Kilfoil, M. 2007 Matlab particle pretracking and tracking, and 2D feature finding.

Kim, D., You, E. & Rhee, S. 2012 Dynein regulates cell migration depending on substrate rigidity. *Int. J. Mol. Med.* **29**, 440–446.

Kloboucek, A., Behrisch, A., Faix, J. & Sackmann, E. 1999 Adhesion-induced receptor segregation and adhesion plaque formation: A model membrane study. *Biophysical Journal* **77**, 2311–2328.

Knopp, D., Tang, D. & Niessner, R. 2009 Review: Bioanalytical applications of biomolecule-functionalized nanometer-sized doped silica particles. *Anal. Chim. Acta* **647**, 14 – 30.

Krijt, S., Dominik, C. & Tielens, A. 2014 Rolling friction of adhesive microspheres. *J. Phys. D: Appl. Phys.* **47**.

Kumar, D., Bhattacharya, S. & Ghosh, S. 2013 Weak adhesion at the mesoscale: particles at an interface. *Soft Matter* **9**, 6618–6633.

Kumar, D., Ghosh, S. & Bhattacharya, S. 2012 Dynamical instabilities of a Brownian particle in weak adhesion. *J. Chem. Phys.* **137**.

Lai, S., Wang, Y.-Y., Hida, K., Cone, R. & Hanes, J. 2010 Nanoparticles reveal that human cervicovaginal mucus is riddled with pores larger than viruses. *Proc. Natl. Acad. Sci. U.S.A.* **107**, 598–603.

Lamblet, M., Delord, B., Johannes, L., van Effenterre, D. & Bassereau, P. 2008 Key role of receptor density in colloid/cell specific interaction: A quantitative biomimetic study on giant vesicles. *Eur. Phys. J. E* **26**, 205–216.

Landau, L. & Lifshitz, E. 1986 *Theory of Elasticity, vol. 7 of Course of Theoretial Physics*. Butterworth Heinmann.

Lasic, D. 1994 Sterically stabilized vesicles. *Angew. Chem. Int. Ed.* **33**, 1685–1698.

Lee, J. 2007 The use of gelatin substrates for traction force microscopy in rapidly moving cells. *Methods Cell Biol.* **83**, 295,297–312.

Lee, K. & Mooney, D. 2001 Hydrogels for tissue engineering. *Chem. Rev.* **101**, 1869–1879.

Leon-Morales, C., Leis, A., Strathmann, M. & Flemming, H.-C. 2004 Interactions between laponite and microbial biofilms in porous media: Implications for colloid transport and biofilm stability. *Water Res.* **38**, 3614–3626.

Leroueil, P. R., Berry, S. A., Duthie, K., Han, G., Rotello, V. M., McNerny, D. Q., Baker, J. R., Orr, B. G. & Banaszak Holl, M. M. 2008 Wide varieties of cationic nanoparticles induce defects in supported lipid bilayers. *Nano Letters* **8**, 420–424.

Leroueil, P. R., Hong, S., Mecke, A., Baker, J. R., Orr, B. G. & Banaszak Holl, M. M. 2007 Nanoparticle interaction with biological membranes: Does nanotechnology present a janus face? *Acc. Chem. Res.* **40**, 335–342.

Levental, I., Georges, P. & Janmey, P. 2007 Soft biological materials and their impact on cell function. *Soft Matter* **3**, 299–306.

Li, B., Cao, Y.-P., Feng, X.-Q. & Gao, H. 2012*a* Mechanics of morphological instabilities and surface wrinkling in soft materials: A review. *Soft Matter* **8**, 5728–5745.

Li, J., Hu, Y., Vlassak, J. & Suo, Z. 2012*b* Experimental determination of equations of state for ideal elastomeric gels. *Soft Matter* **8**, 8121–8128.

Lieleg, O., Vladescu, I. & Ribbeck, K. 2010 Characterization of particle translocation through mucin hydrogels. *Biophys. J.* **98**, 1782–1789.

Lin, C., Yang, F. & Lee, S. 2008 Surface wrinkling of an elastic film: Effect of residual surface stress. *Langmuir* **24**, 13627–13631.

Lin, Y. 2010 A model of cell motility leading to biphasic dependence of transport speed on adhesive strength. *J. Mech. Phys. Solids* **58**, 502–514.

Lin, Y., Hui, C. & Baney, J. 1999 Viscoelastic contract, work of adhesion and the JKR technique. *J. Phys. D: Appl. Phys.* **32**, 2250–2260.

van der Linden, H., Herber, S., Olthuis, W. & Bergveld, P. 2003 Stimulus-sensitive hydrogels and their applications in chemical (micro)analysis. *Analyst* **128**, 325–331.

Liu, J., Tan, Y., Zhang, H., Zhang, Y., Xu, P., Chen, J., Poh, Y.-C., Tang, K., Wang, N. & Huang, B. 2012 Soft fibrin gels promote selection and growth of tumorigenic cells. *Nat. Mater.* **11**, 734–741.

Ljung, L. 1999 *System Identification: Theory For the User, Second Edition*. Upper Saddle River, N.J: Prentice Hall.

Lo, C.-M., Wang, H.-B., Dembo, M. & Wang, Y.-L. 2000 Cell movement is guided by the rigidity of the substrate. *Biophys. J.* **79**, 144–152.

Lomize, A., Pogozheva, I. & Mosberg, H. 2011 Anisotropic solvent model of the lipid bilayer. 2. energetics of insertion of small molecules, peptides, and proteins in membranes. *J. Chem. Inf. Model.* **51**, 930–946.

Love, A. 1939 Boussinesq's problem for a rigid cone. *Q. J. Math.* **os-10**, 161–175.

Love, A. E. H. 1929 The stress produced in a semi-infinite solid by pressure on part of the boundary. *Phil. Trans. R. Soc. Lond. A* **228**, 377–420.

Macaya, D. & Spector, M. 2012 Injectable hydrogel materials for spinal cord regeneration: A review. *Biomed. Mater.* **7**.

Macdonald, J. 1992 Impedance spectroscopy. *Ann. Biomed. Eng.* **20**, 289–305.

Malkin, A. A. 1994 *Rheology fundamentals*. Toronto-Scarborough, Ont. : ChemTec Pub.

Mani, M., Gopinath, A. & Mahadevan, L. 2012 How things get stuck: Kinetics, elastohydrodynamics, and soft adhesion. *Phys. Rev. Lett.* **108**.

Marshall, B., Long, M., Piper, J., Yago, T., McEver, R. & Zhu, C. 2003 Direct observation of catch bonds involving cell-adhesion molecules. *Nature* **423**, 190–193.

Mason, T. & Weitz, D. 1995 Optical measurements of frequency-dependent linear viscoelastic moduli of complex fluids. *Phys. Rev. Lett.* **74**, 1250–1253.

Mason, T. G., Ganesan, K., van Zanten, J. H., Wirtz, D. & Kuo, S. C. 1997 Particle tracking microrheology of complex fluids. *Phys. Rev. Lett.* **79**, 3282–3285.

Maugis, D. 1992 Adhesion of spheres: The JKR-DMT transition using a dugdale model. *J. Colloid Interface Sci.* **150**, 243–269.

Maugis, D. 1995 Extension of the Johnson-Kendall-Roberts theory of the elastic contact of spheres to large contact radii. *Langmuir* **11**, 679–682.

Maugis, D. & Pollock, H. 1984 Surface forces, deformation and adherence at metal microcontacts. *Acta Metall.* **32**, 1323–1334.

Mauro, J., Yue, Y., Ellison, A., Gupta, P. & Allan, D. 2009 Viscosity of glass-forming liquids. *Proc. Natl. Acad. Sci. U.S.A.* **106**, 19780–19784.

Md, S., Singh, G., Ahuja, A., Khar, R., Baboota, S., Sahni, J. & Ali, J. 2012 Mucoadhesive microspheres as a controlled drug delivery system for gastroretention. *Sys Rev Pharm.* **3**, 4–14.

Moffitt, J., Chemla, Y., Smith, S. & Bustamante, C. 2008 Recent advances in optical tweezers. *Annu. Rev. Biochem.* **77**, 205–228.

Mohammadi, A. 2011 Dynamics of colloidal inclusions in hydrogels. PhD thesis, McGill University.

Monch, W. & Herminghaus, S. 2001 Elastic instability of rubber films between solid bodies. *Europhys. Lett.* **53**, 525–531.

Moorthy, J. 2012 *Smart Polymers: Applications in Biotechnology and Biomedicine, Second Edition*, chap. Hydrogels in Microfluidics, pp. 437–457. CRC Press.

Mornet, S., Lambert, O., Duguet, E. & Brisson, A. 2005 The formation of supported lipid bilayers on silica nanoparticles revealed by cryoelectron microscopy. *Nano Letters* **5**, 281–285.

Moshayedi, P., Da F Costa, L., Christ, A., Lacour, S., Fawcett, J., Guck, J. & Franze, K. 2010 Mechanosensitivity of astrocytes on optimized polyacrylamide gels analyzed by quantitative morphometry. *J. Phys. Condens Matter* **22**, 194114.

Murrell, M., Kamm, R. & Matsudaira, P. 2011 Substrate viscosity enhances correlation in epithelial sheet movement. *Biophys. J.* **101**, 297–306.

Murthy Peri, M. & Cetinkaya, C. 2005*a* Rolling resistance moment of microspheres on surfaces. *Philos. Mag.* **85**, 1347–1357.

Murthy Peri, M. & Cetinkaya, C. 2008 Adhesion characterization based on rolling resistance of individual microspheres on substrates: Review of recent experimental progress. *J. Adhes. Sci. Technol.* **22**, 507–528.

Murthy Peri, M. D. & Cetinkaya, C. 2005*b* Non-contact microsphere-surface adhesion measurement via acoustic base excitations. *J. Colloid Interface Sci.* **288**, 432–443.

Nagle, J. F. & Tristram-Nagle, S. 2000 Structure of lipid bilayers. *Biochim. Biophys. Acta, Rev. Biomembr.* **1469**, 159–195.

Nance, E., Woodworth, G., Sailor, K., Shih, T.-Y., Xu, Q., Swaminathan, G., Xiang, D., Eberhart, C. & Hanes, J. 2012 A dense poly(ethylene glycol) coating improves penetration of large polymeric nanoparticles within brain tissue. *Sci. Transl. Med.* **4**, 149ra119.

Neuman, K. & Nagy, A. 2008 Single-molecule force spectroscopy: Optical tweezers, magnetic tweezers and atomic force microscopy. *Nat. Methods* **5**, 491–505.

Neuman, K. C. & Block, S. M. 2004 Optical trapping. *Rev. Sci. Instrum.* **75**, 2787–2809.

Ng, M., Besser, A., Danuser, G. & Brugge, J. 2012 Substrate stiffness regulates cadherin-dependent collective migration through myosin-II contractility. *J. Cell Biol.* **199**, 545–563.

Ngai, K. 2000 Dynamic and thermodynamic properties of glass-forming substances. *J Non-Cryst Solids* **275**, 7–51.

Nguyen, V. T., Chia, T. W. R., Turner, M. S., Fegan, N. & Dykes, G. A. 2011 Quantification of acid-base interactions based on contact angle measurement allows XDLVO predictions to attachment of campylobacter jejuni but not salmonella. *J. Microbiol. Methods* **86**, 89–96.

Nicolson, P. C. & Vogt, J. 2001 Soft contact lens polymers: an evolution. *Biomaterials* **22**, 3273–3283.

Ninham, B. 1999 On progress in forces since the DLVO theory. *Adv. Colloid Interface Sci.* **83**, 1–17.

Noppl-Simson, D. & Needham, D. 1996 Avidin-biotin interactions at vesicle surfaces: Adsorption and binding, cross-bridge formation, and lateral interactions. *Biophys. J.* **70**, 1391–1401.

Normand, V., Lootens, D. L., Amici, E., Plucknett, K. P. & Aymard, P. 2000 New insight into agarose gel mechanical properties. *Biomacromolecules* **1**, 730–738.

Ohshima, H., Makino, K. & Kondo, T. 1987 Electrostatic interaction of two parallel plates with surface charge layers. *J. Colloid Interface Sci.* **116**, 196–199.

O'Neill, M. 1964 A slow motion of viscous liquid caused by a slowly moving solid sphere. *Mathematika* **11**, 67–74.

van Oss, C. J. 2006 *Interfacial forces in aqueous media, Second Edition*. CRC Press.

van Oss, C. J., Chaudhury, M. K. & Good, R. J. 1988*a* Interfacial Lifshitz-van der Waals and polar interactions in macroscopic systems. *Chem. Rev.* **88**, 927–941.

van Oss, C. J., Good, R. J. & Chaudhury, M. K. 1988*b* Additive and nonadditive surface tension components and the interpretation of contact angles. *Langmuir* **4**, 884–891.

O'Toole, M., Lamoureux, P. & Miller, K. 2008 A physical model of axonal elongation: Force, viscosity, and adhesions govern the mode of outgrowth. *Biophys. J.* **94**, 2610–2620.

Owens III, D. E. & Peppas, N. A. 2006 Opsonization, biodistribution, and pharmacokinetics of polymeric nanoparticles. *Int. J. Pharm.* **307**, 93–102.

Patel, N., Bole, M., Chen, C., Hardin, C., Kho, A., Mih, J., Deng, L., Butler, J., Tschumperlin, D., Fredberg, J., Krishnan, R. & Koziel, H. 2012 Cell elasticity determines macrophage function. *PLoS ONE* **7**.

Peak, C., Wilker, J. & Schmidt, G. 2013 A review on tough and sticky hydrogels. *Colloid. Polym. Sci.* **291**, 2031–2047.

Pecseli, H. L. 2000 *fluctuations in physical systems*. Cambridge University Press.

Peppas, N., Huang, Y., Torres-Lugo, M., Ward, J. & Zhang, J. 2000 Physicochemical foundations and structural design of hydrogels in medicine and biology. *Annu. Rev. Biomed. Eng.* **2**, 9–29.

Perschmann, N., Hellmann, J., Frischknecht, F. & Spatz, J. 2011 Induction of malaria parasite migration by synthetically tunable microenvironments. *Nano Lett.* **11**, 4468–4474.

Petersen, A., Joly, P., Bergmann, C., Korus, G. & Duda, G. 2012 The impact of substrate stiffness and mechanical loading on fibroblast-induced scaffold remodeling. *Tissue Eng. Part A* **18**, 1804–1817.

Plant, A. L. 1999 Supported hybrid bilayer membranes as rugged cell membrane mimics. *Langmuir* **15**, 5128–5135.

Plant, A. L., Bhadriraju, K., Spurlin, T. A. & Elliott, J. T. 2009 Cell response to matrix mechanics: Focus on collagen. *Biochim. Biophys. Acta, Mol. Cell. Res.* **1793**, 893–902.

Reed, J., Walczak, W., Petzold, O. & Gimzewski, J. 2009 In situ mechanical interferometry of matrigel films. *Langmuir* **25**, 36–39.

Richter, A., Paschew, G., Klatt, S., Lienig, J., Arndt, K.-F. & Adler, H.-J. 2008 Review on hydrogel-based pH sensors and microsensors. *Sensors* **8**, 561–581.

Richter, R. P., Berat, R. & Brisson, A. R. 2006 Formation of solid-supported lipid bilayers: An integrated view. *Langmuir* **22**, 3497–3505.

Rimai, D., Demejo, L. & Bowen, R. 1995 The adhesion of particles to polymer coated substrates. *J. Adhes.* **51:1-4**, 139–154.

Rimai, D., Demejo, L., Vreeland, W., Bowen, R., Gaboury, S. & Urban, M. 1992 The effect of Young's modulus on the surface-force-induced contact radius of spherical glass particles on polyurethane substrates. *J. Appl. Phys.* **71**, 2253–2258.

Rimai, D. & DeMejo, L. P. 1996 Physical interactions affecting the adhesion of dry particles. *Annu. Rev. Mater. Sci.* **26**, 21–41.

Rimai, D. & Quesnel, D. 2002 The adhesion of spherical particles: Contributions of van der Waals and electrostatic interactions. *J. Adhes.* **78**, 413–429.

Rimai, D., Quesnel, D. & Bowen, R. 2001 Particle adhesion to highly compliant substrates: Anomalous power-law dependence of the contact radius on particle radius. *Langmuir* **17**, 6946–6952.

Rimai, D., Schaefer, D., Bowen, R. & Quesnel, D. 2002 Time dependence of particle engulfment. *Langmuir* **18**, 4592–4597.

Rimai, D., Yang, H., Stelter, E., Tombs, T., Lambert, P. & Weiss, D. 2009 Adhesion of silica-coated toner particles to bisphenol-a polycarbonate films: Effect of toner charge. *J. Imaging Sci. Technol.* **53**.

Rimai, D. S., DeMejo, L. P., Vreeland, W. B. & Bowen, R. C. 1994 Adhesion induced deformations of a highly compliant elastomeric substrate in contact with rigid particles. *Langmuir* **10**, 4361–4366.

Roggers, R. A., Joglekar, M., Valenstein, J. S. & Trewyn, B. G. 2014 Mimicking red blood cell lipid membrane to enhance the hemocompatibility of large-pore mesoporous silica. *ACS Appl. Mater. Interfaces* **6**, 1675–1681.

Rose, S., Prevoteau, A., Elziere, P., Hourdet, D., Marcellan, A. & Leibler, L. 2014 Nanoparticle solutions as adhesives for gels and biological tissues. *Nature* **505**, 382–385.

Sackmann, E. & Tanaka, M. 2000 Supported membranes on soft polymer cushions: fabrication, characterization and applications. *Trends Biotechnol.* **18**, 58–64.

Sagle, A. C., Wagner, E. M. V., Ju, H., McCloskey, B. D., Freeman, B. D. & Sharma, M. M. 2009 PEG-coated reverse osmosis membranes: Desalination properties and fouling resistance. *J. Membr. Sci.* **340**, 92–108.

Sant, S., Hancock, M., Donnelly, J., Iyer, D. & Khademhosseini, A. 2010 Biomimetic gradient hydrogels for tissue engineering. *Can. J. Chem. Eng.* **88**, 899–911.

Sapuri, A. R., Baksh, M. M. & Groves, J. T. 2003 Electrostatically targeted intermembrane lipid exchange with micropatterned supported membranes. *Langmuir* **19**, 1606–1610.

Sarvestani, A. 2011 A model for cell motility on soft bio-adhesive substrates. *J. Biomech.* **44**, 755–758.

Saxton, M. 1997 Single-particle tracking: the distribution of diffusion coefficients. *Biophys. J.* **72**, 1744–1753.

Saxton, M. & Jacobson, K. 1997 Single-particle tracking: Applications to membrane dynamics. *Annu. Rev. Biophys. Biomol. Struct.* **26**, 373–399.

Scherer, G. W. 1992 Editorial comments on a paper by gordon s. fulcher. *Journal of the American Ceramic Society* **75**, 1060–1062.

Schuster, B., Suk, J., Woodworth, G. & Hanes, J. 2013 Nanoparticle diffusion in respiratory mucus from humans without lung disease. *Biomaterials* **34**, 3439–3446.

Sharma, P., Ghosh, S. & Bhattacharya, S. 2008 Microrheology of a sticking transition. *Nat. Phys.* **4**, 960–966.

Sharma, P., Ghosh, S. & Bhattacharya, S. 2010*a* A high-precision study of hindered diffusion near a wall. *Applied Phys. Lett.* **97**, 104101–1–104101–3.

Sharma, P., Ghosh, S. & Bhattacharya, S. 2010*b* A nyquist analysis of glassy dynamics, aging, and discrete basins of attraction in a small system. *J. Chem. Phys.* **133**, 144909.

Shull, K. R. 2002 Contact mechanics and the adhesion of soft solids. *Mater. Sci. Eng., R* **36**, 1–45.

Shull, K. R., Ahn, D., Chen, W.-L., Flanigan, C. M. & Crosby, A. J. 1998 Axisymmetric adhesion tests of soft materials. *Macromol. Chem. Phys.* **199**, 489–511.

Simhadri, J. J., Stretz, H. A., Oyanader, M. & Arce, P. E. 2010 Role of nanocomposite hydrogel morphology in the electrophoretic separation of biomolecules: A review. *Ind. Eng. Chem. Res.* **49**, 11866–11877.

Simons, K. & Vaz, W. 2004 Model systems, lipid rafts, and cell membranes. *Annu. Rev. Bioph. Biom.* **33**, 269–295.

Sneddon, I. N. 1960 The elementary solution of dual integral equations. *Glasgow Math. J.* **4**, 108–110.

Sneddon, I. N. 1965 The relation between load and penetration in the axisymmetric boussinesq problem for a punch of arbitrary profile. *Int. J. Eng. Sci.* **3**, 47–57.

Squires, T. & Mason, T. 2010 Fluid mechanics of microrheology. *Annu. Rev. Fluid Mech.* **42**, 413–438.

Stephens, D. & Allan, V. 2003 Light microscopy techniques for live cell imaging. *Science* **300**, 82–86.

Stern, O. Z. 1924 Zur theorie der elektrolytischen doppelschicht. *Z. Elktrochem. Angew. P* **30**, 508–516.

Storm, G., Belliot, S. O., Daemen, T. & Lasic, D. D. 1995 Surface modification of nanoparticles to oppose uptake by the mononuclear phagocyte system. *Advanced Drug Delivery Reviews* **17**, 31–48.

Style, R., Hyland, C., Boltyanskiy, R., Wettlaufer, J. & Dufresne, E. 2013 Surface tension and contact with soft elastic solids. *Nat. Commun.* **4**.

Suh, J., Wirtz, D. & Hanes, J. 2003 Efficient active transport of gene nanocarriers to the cell nucleus. *Proc. Natl. Acad. Sci. U.S.A.* **100**, 3878–3882.

Sunyer, R., Jin, A., Nossal, R. & Sackett, D. 2012 Fabrication of hydrogels with steep stiffness gradients for studying cell mechanical response. *PLoS ONE* **7**.

Sutherland, K., Madin, L. & Stocker, R. 2010 Filtration of submicrometer particles by pelagic tunicates. *Proc. Natl. Acad. Sci. U.S.A.* **107**, 15129–15134.

Suzuki, A., Yamazaki, M. & Kobiki, Y. 1996 Direct observation of polymer gel surfaces by atomic force microscopy. *J. Chem. Phys.* **104**, 1751–1757.

Suzuki, M., Yasukawa, T., Shiku, H. & Matsue, T. 2007 Negative dielectrophoretic patterning with colloidal particles and encapsulation into a hydrogel. *Langmuir* **23**, 4088–4094.

Tabor, D. 1977 Surface forces and surface interactions. *J. Colloid Interface Sci.* **58**, 2–13.

Takeuchi, H., Yamamoto, H. & Kawashima, Y. 2001 Mucoadhesive nanoparticulate systems for peptide drug delivery. *Adv. Drug Delivery Rev.* **47**, 39–54.

Tanaka, M. & Sackmann, E. 2005 Polymer-supported membranes as models of the cell surface. *Nature* **437**, 656–663.

Tee, S.-Y., Fu, J., Chen, C. & Janmey, P. 2011 Cell shape and substrate rigidity both regulate cell stiffness. *Biophys. J.* **100**, L25–L27.

Titchmarsh, E. 1937 *Introduction to the Theory of Fourier Integrals*. Clarendon Press, Oxford.

Tripathi, S., Champagne, D. & Tufenkji, N. 2012 Transport behavior of selected nanoparticles with different surface coatings in granular porous media coated with pseudomonas aeruginosa biofilm. *Environ. Sci. Technol.* **46**, 6942–6949.

Tse, J. & Engler, A. 2010 Preparation of hydrogel substrates with tunable mechanical properties. *Curr. Protoc. Cell Biol.* pp. 10.16.1–10.16.16.

Ulrich, T., De Juan Pardo, E. & Kumar, S. 2009 The mechanical rigidity of the extracellular matrix regulates the structure, motility, and proliferation of glioma cells. *Cancer Res.* **69**, 4167–4174.

Urzay, J., Llewellyn Smith, S. G. & Glover, B. J. 2007 The elastohydrodynamic force on a sphere near a soft wall. *Phys. Fluids* **19**, 103106.

Usta, O., Nayhouse, M., Alexeev, A. & Balazs, A. 2008 Designing patterned substrates to regulate the movement of capsules in microchannels. *J. Chem. Phys.* **128**, 235102–1–235102–8.

Valle-Delgado, J., Molina-Bolivar, J., Galisteo-Gonzalez, F., Galvez-Ruiz, M., Feiler, A. & Rutland, M. 2005 Hydration forces between silica surfaces: Experimental data and predictions from different theories. *J. Chem. Phys.* **123**, 034708–1–034708–12.

Vasir, J., Tambwekar, K. & Garg, S. 2003 Bioadhesive microspheres as a controlled drug delivery system. *Int. J. Pharm.* **255**, 13–32.

Velinova, M. J., Staffhorst, R. W., Mulder, W. J., Dries, A. S., Jansen, B. A., de Kruijff, B. & de Kroon, A. I. 2004 Preparation and stability of lipid-

coated nanocapsules of cisplatin: anionic phospholipid specificity. *Biochim. Biophys. Acta, Biomembr.* **1663**, 135–142.

Verhulsel, M., Vignes, M., Descroix, S., Malaquin, L., Vignjevic, D. M. & Viovy, J.-L. 2014 A review of microfabrication and hydrogel engineering for micro-organs on chips. *Biomaterials* **35**, 1816–1832.

Verwey, E. & Overbeek, J. 1946 Long distance forces acting between colloidal particles. *Trans. Faraday Soc.* **42**, B117–B123.

Verwey, E. J. W. 1947 Theory of the stability of lyophobic colloids. *J. Phys. Coll. Chem.* **51**, 631–636.

Verwey, W. & Overbeek, J. 1948 *Theory of the Stability of Lyophobic Colloids*. Elsevier.

Walker, S., Bhattacharjee, S., Hoek, E. & Elimelech, M. 2002 A novel asymmetric clamping cell for measuring streaming potential of flat surfaces. *Langmuir* **18**, 2193–2198.

Wang, M., Yin, H., Landick, R., Gelles, J. & Block, S. 1997 Stretching DNA with optical tweezers. *Biophys. J.* **72**, 1335–1346.

Wang, X.-D., Shen, Z.-X., Zhang, J.-L., Jiao, H.-F., Cheng, X.-B., Chen, L.-Y. & Wang, Z.-S. 2010 Submicrometer aluminum spheres' adhesion to planar silicon substrates. *Langmuir* **26**, 13903–13906.

Wang, Y. & Pelham, J. R. 1998 Preparation of a flexible, porous polyacrylamide substrate for mechanical studies of cultured cells. *Methods Enzymol.* **298**, 489–496.

Wang, Y., Wang, G., Luo, X., Qiu, J. & Tang, C. 2012 Substrate stiffness regulates the proliferation, migration, and differentiation of epidermal cells. *Burns* **38**, 414–420.

Wang, Y.-Y., Lai, S., So, C., Schneider, C., Cone, R. & Hanes, J. 2011 Mucoadhesive nanoparticles may disrupt the protective human mucus barrier by altering its microstructure. *PLoS ONE* **6**, e21547.

Weihs, D., Mason, T. G. & Teitell, M. A. 2006 Bio-microrheology: A frontier in microrheology. *Biophys. J.* **91**, 4296–4305.

White, L. R. 1983 On the deryaguin approximation for the interaction of macrobodies. *J. Colloid Interface Sci.* **95**, 286–288.

Willenbacher, N. & Oelschlaeger, C. 2007 Dynamics and structure of complex fluids from high frequency mechanical and optical rheometry. *Curr. Opin. Colloid Interface Sci.* **12**, 43–49.

Wilson, L. & Poon, W. 2011 Small-world rheology: An introduction to probe-based active microrheology. *Phys. Chem. Chem. Phys.* **13**, 10617–10630.

Winter, H. & Chambon, F. 1986 Analysis of linear viscoelasticity of a crosslinking polymer at the gel point. *J. Rheol.* **30**, 367–382.

Wirtz, D. 2009 Particle-tracking microrheology of living cells: Principles and applications. *Annu. Rev. Biophys.* **38**, 301–326.

Wu, S. & Shanks, R. 2004 Solubility study of polyacrylamide in polar solvents. *J. Appl. Polym. Sci.* **93**, 1493–1499.

Xinming, L., Yingde, C., Lloyd, A. W., Mikhalovsky, S. V., Sandeman, S. R., Howel, C. A. & Liewen, L. 2008 Polymeric hydrogels for novel contact lens-based ophthalmic drug delivery systems: A review. *Cont. Lens Anterior Eye* **31**, 57–64.

Yang, J., Deng, L.-H., Han, C.-R., Duan, J.-F., Ma, M.-G., Zhang, X.-M., Xu, F. & Sun, R.-C. 2013*a* Synthetic and viscoelastic behaviors of silica nanoparticle reinforced poly(acrylamide) core-shell nanocomposite hydrogels. *Soft Matter* **9**, 1220–1230.

Yang, J., Han, C.-R., Duan, J.-F., Xu, F. & Sun, R.-C. 2013*b* Interaction of silica nanoparticle/polymer nanocomposite cluster network structure: Revisiting the reinforcement mechanism. *J. Phys. Chem. C* **117**, 8223–8230.

Yang, J., Zhao, J.-J., Han, C.-R. & Duan, J.-F. 2014 Keys to enhancing mechanical properties of silica nanoparticle composites hydrogels: The role of network structure and interfacial interactions. *Compos. Sci. Technol.* **95**, 1–7.

Yang, T.-H. 2008 Recent applications of polyacrylamide as biomaterials. *Recent Patents on Materials Science* **1**, 29–40.

Yeung, T., Georges, P., Flanagan, L., Marg, B., Ortiz, M., Funaki, M., Zahir, N., Ming, W., Weaver, V. & Janmey, P. 2005 Effects of substrate stiffness on cell morphology, cytoskeletal structure, and adhesion. *Cell Motil. Cytoskeleton* **60**, 24–34.

Yezek, L., Duval, J. & Van Leeuwen, H. 2005 Electrokinetics of diffuse soft interfaces. iii. interpretation of data on the polyacrylamide/water interface. *Langmuir* **21**, 6220–6227.

Yezek, L. P. & van Leeuwen, H. P. 2004 An electrokinetic characterization of low charge density cross-linked polyacrylamide gels. *J. Colloid Interface Sci.* **278**, 243–250.

Yu, T., Malugin, A. & Ghandehari, H. 2011 Impact of silica nanoparticle design on cellular toxicity and hemolytic activity. *ACS Nano* **5**, 5717–5728.

Zeng, X. & Li, S. 2012 A three dimensional soft matter cell model for mechanotransduction. *Soft Matter* **8**, 5765–5776.

Zhang, H.-Y. & Hill, R. 2011 Concentration dependence of lipopolymer self-diffusion in supported bilayer membranes. *J. R. Soc. Interface* **8**, 127–143.

Zhang, M., Desai, T. & Ferrari, M. 1998 Proteins and cells on PEG immobilized silicon surfaces. *Biomaterials* **19**, 953–960.

Zhao, Y.-P., Wang, L. & Yu, T. 2003 Mechanics of adhesion in MEMS - a review. *J. Adhes. Sci. Technol.* **17**, 519–546.

Zhuravlev, L. 2000 The surface chemistry of amorphous silica. Zhuravlev model. *Colloids Surf., A* **173**, 1–38.